Ph. D Thesis

Development of UV-Vis-THz laser based pulsed photoacoustic pyrolysis technique for the study of thermal decomposition, stability mechanisms of high energy materials

Konda Srinivasa Rao

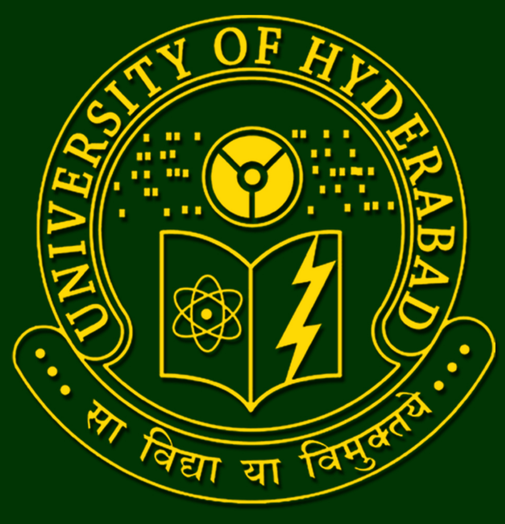

ACRHEM
School of Physics
University of Hyderabad
Hyderabad - 500046
Telangana, India

Thesis Supervisor
Dr. A. K. Chaudhary

Development of UV-Vis-THz laser based Pulsed Photoacoustic Pyrolysis Technique for the Study of Thermal Decomposition, Stability Mechanisms of High Energy Materials

A thesis submitted to University of Hyderabad for the award of

the degree of

Doctor of Philosophy

In

Physics

By

Konda Srinivasa Rao

Thesis supervisor

DR. A. K Chaudhary

Advanced Center of Research in High Energy Materials (ACRHEM)

School of Physics

University of Hyderabad, Hyderabad 500046

Telangana, India.

June 2016

Dedicated to...

My Father

Late. Sri Konda Ramulu

Declaration

I**, Konda Srinivasa Rao**, hereby declare that the work presented in this thesis entitled **"Development of UV-Vis-THz laser based Pulsed Photoacoustic Pyrolysis Technique for the Study of Thermal Decomposition, Stability Mechanisms of High Energy Materials"** has been carried out by me under the supervision of **Dr. A. K. Chaudhary**, Associate Professor, ACRHEM, School of Physics, University of Hyderabad, Hyderabad, India, as per the Ph.D. ordinances of the University, which is also free from plagiarism. I declare, to the best of my knowledge, that no part of this thesis has been submitted for the award of a research degree of any other University. I hereby agree that my thesis can be deposited in Shodhganga / NFLIBNET.

A report on plagiarism statistics from the University Librarian is enclosed.

(Konda Srinivasa Rao)

Reg. No: 10ACPP19

Dr. A. K. Chaudhary,
Associate professor (Physics)
Thesis Supervisor,
ACRHEM, School of Physics,
University of Hyderabad.

Dr. A.K. Chaudhary
Associate professor
Tel.: +91 40 23138807
Fax: +91 40 23012800
E-mail: anilphys@yahoo.com
akcphys@gmail.com

ACRHEM
School of Physics
University of Hyderabad
Prof. C. R. Rao Road,
Gachi Bowli
Hyderabad – 500 046, INDIA

Certificate

This is is to certify that the thesis entitled "**Development of UV-Vis-THz laser based Pulsed Photoacoustic Pyrolysis Technique for the Study of Thermal Decomposition, Stability Mechanisms of High Energy Materials**" being submitted to the University of Hyderabad by **Konda Srinivasa Rao** (Reg. No. 10ACPP19), for the award of the degree of Doctor of Philosophy in Physics, is a record of *bonafide* work carried out by him under my supervision and is free of plagiarism.

The matter embodied in this report has not been submitted to any other University or Institution for the award of any degree or diploma.

Dr. A. K. Chaudhary
(Supervisor)

Director
ACRHEM

Dean
School of Physics

A word of Gratitude

I would not have completed my research work and write this thesis without kind support and help of several people.

First, I would like to thank my thesis supervisor **Dr. A. K. Chaudhary** for his valuable guidance, scholarly inputs, and consistent moral encouragement received throughout the research work. This thesis would not have been possible without his support. I cannot thank him enough, and I am always grateful to him forever.

I would like to thank my doctoral committee members Dr. S. Venugopal Rao, Prof. M. Ghanashyam Krishna, for their valuable suggestions during the meetings.

I am thankful to Dr. K. V. Rao, Director, ACRHEM, for providing fellowship in extension period of course and for his moral encouragement. Thanks to Dean School of Physics for providing academic facilities. I also acknowledge DRDO for providing me fellowship throughout my Ph.D period.

I extend my gratitude to Dr. Fahem Yehya Bajash, Assistant Professor at Al Bayda University, Yemen, for the valuable academic discussions and suggestions. I also acknowledge him for providing me the opportunity and assisting with me to carry out my thesis work in initial days. I would like to extend my thank to Mr. M. Venkatesh for his support and encouragement throughout my Ph.D. career. I take this opportunity to thank Dr. S. Brahadeeswaran and his student K.Tirupugalmani, Bharathidasan Institute of Technology, Anna University, Tiruchirapalli for providing DAST crystal. I also acknowledge Prof. A. K. Sahoo and his students Dr. A Sudheer Kumar and Dr. K Nagarjuna for providing studied triazole derivatives. Also to Dr. D. Srinivas for providing samples. I extended my thanks to Prof. Durga Prasad and Dr, Saritha, school of Chemistry for teaching me Gaussian software.

I am so delighted to express my deep gratitude to the former directors of ACRHEM, Prof. S. P. Tewari, Dr. Sethuva for providing needful facilities. I also thank Dr. G. Manoj Kumar, P. Prem Kiran and Dr. G Vaitheeswaran, Dr. Anuj, Prof Ashok Chatterjee for their support. I wish to thank my seniors Dr. Syed Hamad, Dr. S. Appala Kondaiah, Dr. G. Krishna Podagatlapalli, Dr. S. Sreedhar, Dr. M. Ashwin Kumar, Dr. Ch. Leela, Dr. Ch. Bhem Lingam, Dr. K. Ramesh Babu, K. Nagendra, Dr. Debases for their help and support. It is pleasure to thank my batch mates E. Manikanta, V. Rakesh Kumar, E. Narasimha Rao, E. Nageswara Rao, N. Yedukondalu, Siva Kumar Anubham, Dr. Umar Pasha Shaik, L. Vinoth Kumar, S. Sai Siva, Naine Tarun Bharath, P. Venkateswarlu, Dr. Sachin Barthwal, Dr. P.T. Anusha, Santanu Kumar Padhi, T. Vikranth and J. Ramakrishna.

In this context, I would like to thank my group members Ganesh Damarla, Archana Kumari, M. Praveen Kumar and ACRHEM Colleagues: G. Nagaraju, B. Chandu, J. Rajendhar, S. Abdul Kalam, G. Chandra Shekar, M. Mahendhar, N. Linga Murthy, R. Mounika, Soma Datta Bhattacharya, M.S.S. Bharathi, P.L. Kameswari, G. Pratap, Moses Abraham, Adavaiah, Yellaiah, Ragavendhar, past Project Students: A.M. Reshma and Muntazir Gull. Colleagues from the school of physics, M. Sc and M. Tech classmates for their great cooperation and support. I express my sincere thanks to my friends G. Madhu Sudhan, J. Rajendra Prasad, P. Ramachandra Rao for their encouragement.

I would like to thank my cousin brother B. Venkateswara Rao, uncles: P. Ramesh Babu, P. Venkateswara Rao, P. Moshe, M. Sudharsana Rao and S. Rosaiah, also Sun-in-laws: G. Chiranjeevi, M. John Peter, S. Venkateswara Rao, S. Srinivasa Rao and their families for constant encouragement. I thank Sri V. Gandhi, Sri. Y. Vimala, Sri. Md. Riyaz, Sri. Md. Rafi, Sri. Md. Basiruddin, Sri S. Pullaiah, Sri. Ranga Nayakamma for preparing me well for the challenge of my High School, and Vidya Bharathi Junior college, Sathupalli, faculty and chairpersons: Sri G. Lingareddy, Sri. M. Satya Naraya, Sri. Veraiah and Sri. Venkateswara Rao for providing me residential facility. I thank my cousin sister B. Usharani, who carried my books and leave letters in school days. I thank J. Krishnaveni, because of her I spent most of the time on studies to achieve the challenging task. Also, thank my beloved friends K. Srujana, T. Roja Latha, N. Lalitha, B. Srinivasa Rao for their moral encouragement.

I feel it is a pleasant duty to express my regards to the non-teaching staff of ACRHEM, School of Physics, workshop, IGM Library and University of Hyderabad administration.

I am indebted to my family, Father: Ramulu (Late), Grand Mother: Suvarthamma (Late), they wake up me to study in the early morning in every day in school days. After that my mother: Lakshmi gave me the moral support for continuing my studies further. Sisters: Rajani and Sri Latha, brother's wife and his sons: Nirmala, Manvith Ram and Jevanth Ram for their unconditional love, sacrifices, and support. Finally, I express the gratitude my brother: Venkateswara Rao, is a person offered invaluable support and humor over the years. He is a friend, philosopher, Constance supporter. I am here to submit a thesis with the peaceful mind because of his motivation, encouragement. Words can't express how much I love you all and how grateful I am for your support. Without my family and Jesus Christ, I most certainly would not be where I am today.

Yours

Konda Srinivasa Rao

Contents

List of Figures

List of Tables

Symbols

ρ	Density
T_d	Decomposition temperature
r	Electro-optic coefficient
ΔH_f	Heat of formation
T_m	Melting temperature
d_{eff}	Non linear optical coefficient
kb	kilo barn
Q	Quality factor
n_{THz}	Terahertz refractive index

Abbreviations

DP	Detonation pressure
DAST	4-N, N-dimethylamino-4'-N'-methyl-stilbazoliumtoyslate
DSC	Differential scanning calorimetry/calorimeter
FTIR	Fourier transform infrared spectrometer
GC	Gas chromatography
GP	Graphite powder
MS	Mass spectrometer
PA	Photoacoustic
PAS	Photoacoustic spectroscopy
TG-DTA	Thermo gravimetric-differential thermal analysis
SHS	Second harmonic signal
PED	Pyro electric detector
VOD	Velocity of Detonation
$ZnGeP_2$	Zinc germanium phosphide
FWHM	Full width half max
SC	Sealed cell
DSC	Differential Scanning Calorimetry
CW	Continuous wave
PED	Pyroelectric Detector
GVM	Group Velocity mismatch
GVD	Group Velocity dispersion
BPF	Band Pass Filter
EO	Electro optic

Compounds

Benzyl series 1,2,3-triazoles

S_1	1-(2,4-dinitrobenzyl)-1H-1,2,3-triazole
S_2	1-(3,5-dinitrobenzyl)-1H-1,2,3-triazole
S_3	1-(2-methoxy-3,5-dinitrobenzyl)-1H-1,2,3-triazole
S_4	1-(4-methoxy-3,5-dinitrobenzyl)-1H-1,2,3-triazole
S_6	1-(2,4-dinitrobenzyl)-4-nitro-1H-1,2,3-triazole

Phenyl series 1,2,3-triazoles

S_5	1-(2-methoxy,-3,5-dinitrophenyl)-1H-1,2,3-triazole
S_{10}	1-(3-methoxy, 2, 6 dinitrophenyl) 1, 2, 3 triazole
S_8	1-(4-nitrophenyl)-1H-1,2,3-triazole
S_9	2,6-bis ((4-(nitromethyl)-1H-1,2,3-triazol-1-yl)methyl) pyridine

Phenyl series 1,2,4-triazoles

P-Me-DNPT	1-(4-Methyl-3,5-dinitrophenyl)-1H-1,2,4-triazole
P-OMe-DNPT	1-(4-Methoxy-3,5-dinitrophenyl)-1H-1,2,4-triazole
P-NH_2-DNPT	2,6-Dinitro-4-(1H-1,2,4-triazol-1-yl) aniline

Carbon blacks

GP	Graphite powder
DS	Diesel shoot
WB	wood black

Nitrogen-rich imidazole, 1, 2, 4-triazole and tetrazoles

DS51	1,1,3,3-tetra(1H-tetrazol-5-yl)propane
DS90	4-nitro-1H-imidazol-3-ium 3-(1H-tretrazol-1-yl)-1,2,4-triazole-1-ide
DS93	4-nitro-1H-imidazol-3-ium 5-amino -3-(1H-tretrazol-1-yl)-1,2,4-triazole-1-ide
DS99	3-(1H-tetrazol-1-yl)-1H-Cabohydrzidium ion
DS107	3,5-diamino-1H-1,2,4-triazol-4-ium-5,5',5",5'" -(propane-1,1,3,3-tetrayl-1-ide

Chapter 1

Introduction and Thesis overview

Abstract

This chapter deals with the classification of high energy materials, brief survey about photo acoustic spectroscopy, selection of excitation wavelengths amd Thermo gravimetric-Differential thermal analysis (TG-DTA) techniques. In addition to that, emphasis is given to general introduction about terahertz radiation, its generation and detection techniques. Finally summary and organization of thesis is presented.

1.1. Introduction

In present day, science and technology faces an open and formidable challenge of providing home land security by devising an efficient detection system for high energy materials (HEMs). The existence of a variety of HEMs, initiative of packing and transporting combined with the low vapor pressures of such materials makes the detection a convoluted task [1]. HEMs /explosive molecules are special in the sense that the rate of energy release is extremely abrupt as compared to other organic or inorganic molecules. The HEMs release several hazardous molecules into atmosphere when they are explored. These materials can be classified as thermally stable, high performance, melt-castable and insensitive explosives according to their chemical nature during the detonation process [2-6]. The study of thermal stability and decomposition mechanisms are essential to characterize the newly synthesized HEMs for their futuristic applications as explosives, propellants and rocket fuels.

1.2. Classification of high energy materials

HEMs is a common name used for the class of energetic materials known as explosives and propellants. An explosive material, is a reactive substance that contains a huge amount of potential energy that can produce an explosion if released suddenly, usually accompanied by the production of light, heat, sound and pressure. The organic explosive materials mainly consist of carbon, hydrogen, oxygen and nitrogen elements. Thus, combustion of organic explosive materials readily converts carbon to CO_2 and hydrogen to H_2O. Similarly, nitrogen translates to N_2 gas during detonation. As molecular nitrogen possesses low internal energy than the oxides of nitrogen (NO, NO_2 etc.). Therefore, -NO_2 groups are the source of oxygen in the molecule, which in turn significantly assists in detonation or combustion process [5-8].

An explosive charge is a measured quantity of energetic material. The potential energy stored in an explosive material are in the form of (a) chemical energy, such as nitroglycerin RDX, TNT etc. (b) pressurized gas, such as a gas cylinder or aerosol can (c) nuclear energy, such as in the fissile isotopes uranium-235 and plutonium-239. Explosive materials can further be categorized by the speed at which they expand with detonation velocity. Materials that detonate (the front of the chemical reaction moves faster through material than the speed of sound) are said to be high explosives and materials that deflagrate are said to be low explosives. Explosives are also be categorized according to their sensitivity. In sensitive materials the process of detonation is initiated by a relatively small amount of heat or pressure which is referred as primary explosives and materials that are relatively insensitive are treated as secondary or tertiary explosives. The classification of explosives according to their physical and chemical nature is shown in the form of flow chart in Fig.

1.1. Synthesis of novel energetic materials is highly requisite, as they are widely used in military and civilian applications such as explosives, rocket fuels and gun propellants [9]. Thus, the design of energetic materials is envisaged based on thermal stability, performance, high velocity of detonation, detonation pressure compared to the known standard energetic compounds. The novel energetic compounds can be synthesized including by following factors: the easy and cost-efficient, eco-friendly nature, production of non-toxic and non-hygroscopic byproducts during detonation, stability for long-time storage, insensitivity for safe transportation and handling, high enthalpy of formation, density and better oxygen balance which is required for complete combustion. Furthermore, effective application of thermally stable energetic materials to military and civilian use needs detailed investigation.

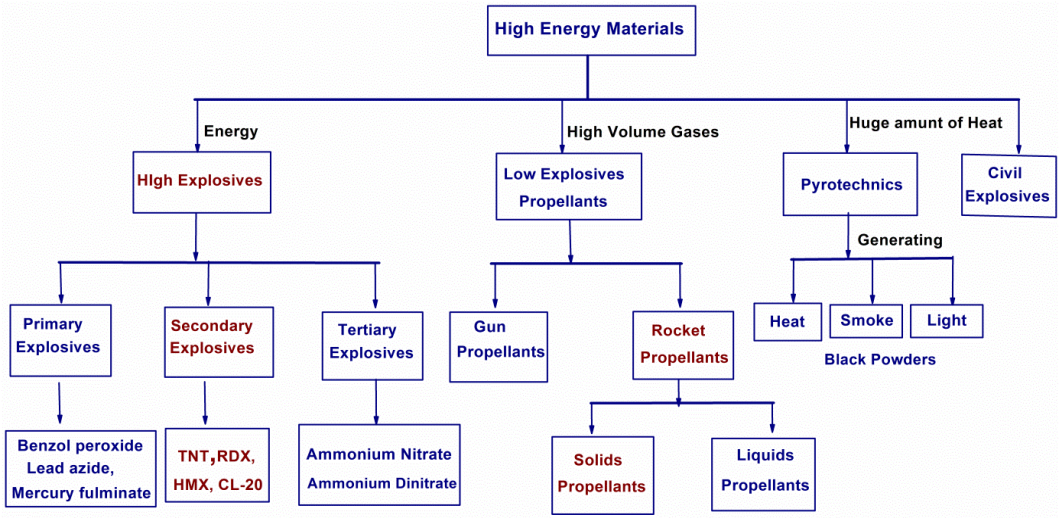

Figure 1.1: Classification of high energy materials [9].

Table 1.1: Energetic properties of some explosives.

Sample	Structure	Formula	ρ gm/cm^3	VOD km/s	DP GPa	ΔH_f kJ/mol	T_m ^{o}C	T_d ^{o}C	Explosive Nature
RDX	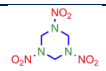	$C_3H_6N_6O_6$	1.82	8.7	35.17	83.82	205.5	234	Thermally stable
TATB	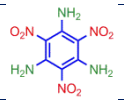	$C_3H_6N_6O_6$	1.94	8.11	31.1	-138	350		Thermally stable
HMX		$C_4H_8N_8O_8$	1.91	9.1	39.63	104.77	286.86		High performance
CL20	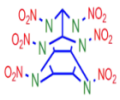	$C_6H_6N_{12}O_{12}$	2.04	9.4	46.6	454	245		High performance
TNT	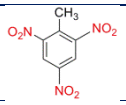	$C_7H_5N_3O_6$	1.65	6.95	19.5	-54.39	80.35	240	Melt-castable
MTNI	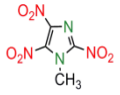	$C_4H_3N_5O_6$	1.76	8.17	35.58	--	82	295	Melt-castable

The benchmark secondary explosives such as RDX, TATB, HMX, CL20, TNT and MTNI are nitro rich energetic materials. The structures, chemical formulae and some of the important properties such as density (ρ), the velocity of detonation (VOD), detonation pressure (DP), the heat of formation (ΔH_f), melting temperature (T_m) and decomposition temperature (T_d) of these materials are comprised in Table. 1.1.

It is generally recognized that certain groups like nitro ($-NO_2$), nitrate ($-ONO_2$), and azide ($-N_3$), are intrinsically labile. Kinetically, there exists a low activation barrier to the decomposition reaction. Consequently, these compounds exhibit high sensitivity to flame or mechanical shock. The nitro group, attached to aromatic or aliphatic carbon is probably the most widely studied of the functional group and this is part used for 'explosophore' in many energetic materials [2]. The groups rapidly converted to gaseous products during detonation of the molecule are called explosophore [4]. The nitrogen and oxygen bearing nitro, nitroso, nitramine, nitrate ester and azido moieties belong to explosophore group. The oxygen content in the explosophore groups is useful for the conversion of molecular backbone to gaseous byproducts NO_2, CO_2, CO, and H_2O. There is a availability of various improvised spectroscopic techniques for the standoff and near-field detection of different HEMs [10]. No single technique has been found to be capable of detecting (i) all the explosives explicitly (ii) obscured/hidden explosives. They are either time consuming or involve sophisticated equipment along with tedious data analysis [11-14]. There is a requirement of identifying the pros and cons of each technique. Therefore, detailed study is required in order to investigate the new cross mechanism for achieving the optimum results. There are many methods to detect/identify explosive molecules based on their decomposition mechanisms as shown in the flow chart (Fig. 1.2).

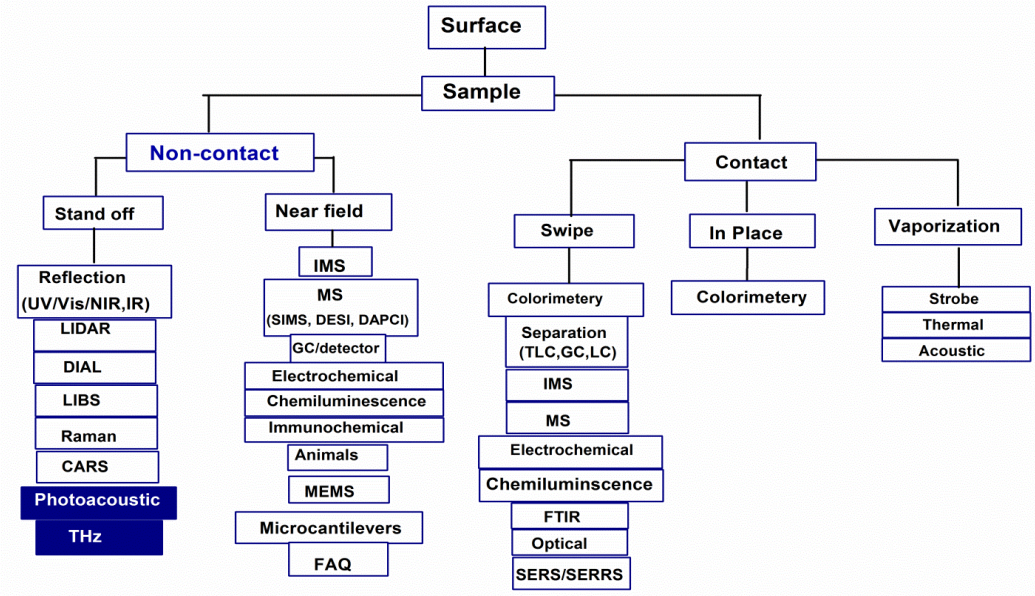

Figure 1.2: Detection schemes of high energy materials

Among many such identification techniques, photoacoustic spectroscopy [6] is a simple and suitable scheme, for detecting explosive molecules and their thermal decomposition process [15-17]. The identification, thermal decomposition and stability mechanism of HEMs are reported experimentally by several groups using TG-DSC/DTA coupled with Fourier transform infrared spectroscopy (FTIR) or Gas chromatography–mass spectrometry (GC-MS) [18-21]. However, Strachan et al. reported the thermal decomposition of solid RDX crystal at various temperatures and densities using reactive force field (ReaxFF) model, which is based on molecular dynamics as shown in Fig. 1.3 [22].

Table 1.2: Bond energies of some of weakest bonds.

Compound	Trigger linkage	Bond energy (kJ/mol)	Activation energy (kJ/mol)
Nitroarene	C-NO_2	305	293
Nitramine	N-NO_2	163	196
Nitrate Ester	CO-NO_2	222	167
Peroxide	CO-OC	142	146

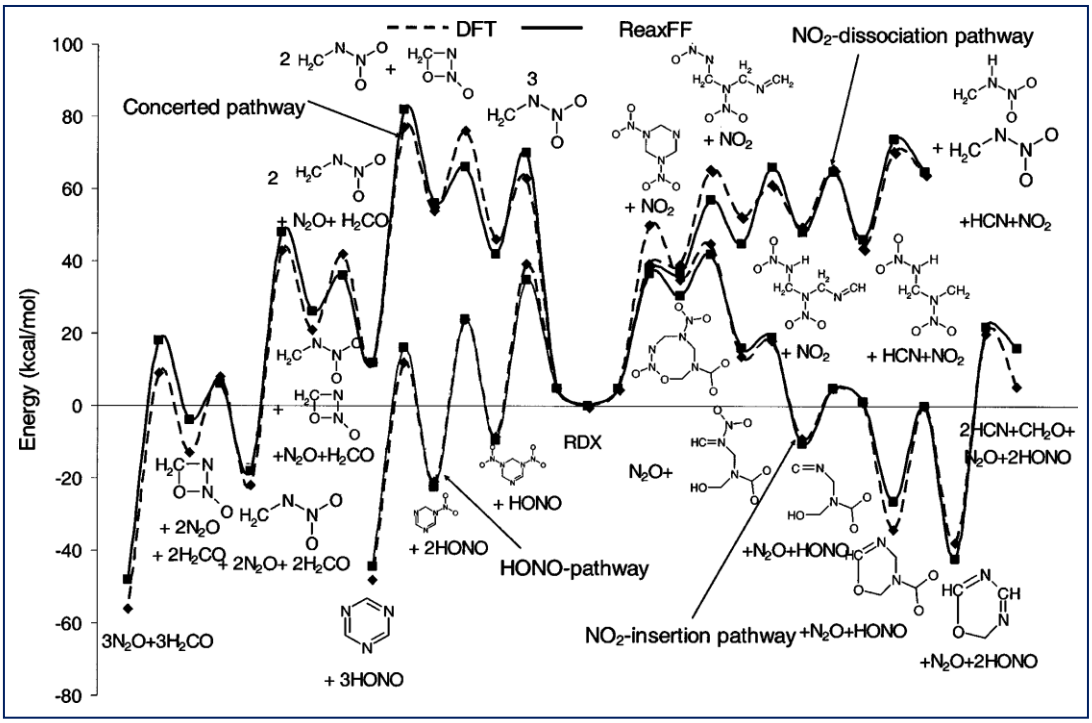

Figure 1.3: Energetics of unimolecular decomposition mechanisms in RDX obtained using the ReaxFF (full lines with filled symbols) and with QM (dashed lines with open symbols). Circles represent the sequential HONO elimination, triangles show the decomposition process following homolytic N–N bond breaking (NO_2 elimination), and diamonds represent the concerted ring-opening pathway. Intermediates and products are described in Ref. [32]. (Image and figure caption adopted from [22]).

The nitro rich energetic compounds contain C-NO_2 and N-NO_2 bonds, which depends upon their structures. The bond energies of these weakest bonds in HEMs compounds are comprised in Table 1.2. These experimental and theoretical studies show that NO_2 molecule is one of the principal by product gasses released by HEMs during the process of thermal decomposition The quantum chemistry based on new research has motivated the number of groups of a synthetic chemist to synthesize new, efficient and green high energy materials which might be a better alternative to the existing standard energetic materials [23-29]. In this series, the performance of some of the newly synthesized nitro rich benzyl series and phenyl series 1,2,3-triazoles and phenyl series 1,2,4-triazoles compounds were evaluated and compared with the benchmark explosives [30,31,46].

In the present research, we focused our study on examining the thermal decomposition mechanism, stability and efficiency of rocket fuels using pulsed photoacoustic technique, with excitation wavelengths of UV 266 nm and visible 532 nm, based on released quantity of gaseous molecules under controlled pyrolysis between 30-350 °C ranges. The results of PA technique are compared with Thermo gravimetric-differential thermal analysis (TG-DTA) technique to understand thermal decomposition mechanism of HEMs. Also, to detect the compounds, the time-resolved photoacoustic fingerprint spectra were recorded between the temperature range of 30-350 °C range. The study reveals that the positions of principal functional group -NO_2 in aromatic rings of compounds is a key factor in their thermal stability and efficiency as rocket fuels. The generated PA signal for 266 nm is total molecule vapor unlike for 532 nm wavelength where the signal is limited to NO_2 molecules. The present form of photoacoustic (PA) technique is based on 532 nm wavelength is not able to monitor the individual concentrations of byproduct gaseous molecules. However, we can monitor the release of NO_2 below the melting temperature to study the thermal stability of the compound.

1.3. Photoacoustic spectroscopy

Photoacoustic spectroscopy (PAS) is based on absorption of modulated/pulsed electromagnetic radiation by analyte molecules. The absorbed energy is then transformed into thermal energy through nonradiative relaxation (due to collisions of other molecules) process in the sample. When the modulated or pulsed laser radiation incident on the sample due to internal heating, an acoustic signal or short shock wave is generated this is detected using a sensitive microphone. The PAS has several added advantages over the conventional absorption spectroscopy such as effect of reflection, transmission and scattering are totally over ruled. As a result, the low absorption coefficient and opacity of the sample affects the transmitted signal but do not have any effect on PA signal. Therefore, it has tremendous applications in spectroscopy of solids, liquids, gasses, condensed

matter, nanoparticles and semiconducting materials etc. [33-42]. The PA technique offers several advantages such as high sensitivity, selectivity, simplicity and compact size, fast time response, non-destructive detection [43-48]. It is widely recognized for its excellent performance in trace gas detection from ppb to ppt level [49,50]. The PA signal generation mechanism varies from wavelength to wavelength. In case of UV range, it is attributed to electronic transition whereas in visible region it is due to vibronic modes of the molecules. However, in terahertz range the PA signal is generated due to excitation of weak vibrational-rotational lines of the molecules [51-59]. Fig. 1.4 shows the elementary processes for the generation of PA signal.

History: Alexander Graham Bell invented the photoacoustic effect in 1880 [60]; he discovered that thin discs emits sound when exposed to a rapidly interrupted beam of sunlight. The entire process is based on the absorption of modulated light/pulses by a gas/condensed sample. Viengerov (1938, 1940) has reported the first spectroscopy gas analysis, which is based on photoacoustic effect. He performed the spectroscopy analysis of gasses by using blackbody infrared as a source along with an electrostatic microphone as a detector [61-63].

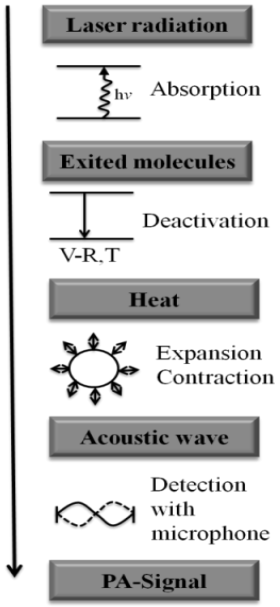

Figure 1.4: The processes for the generation of PA signal [64].

However, the actual application of PA effect was demonstrated in trace gas monitoring in the late 1960 due to the invention of the laser and highly sensitive microphones. Since that date, many scientists such as Kerr and Atwood employed the laser in photoacoustic spectroscopy (PAS) [65]. They have used CW (CO_2) laser to achieve the minimum detectable absorption coefficient α_{min} of the order 10^{-7} cm^{-1} for CO_2 buffered in N_2. Also, Kreuzer (1971) has reported the sensitive detection of (CH_4) in N_2 with lowest detection order of 10^{-8} (ppb) using He-Ne laser operating at 3.39 μm [66]. Patel demonstrated the technique's potential by measuring the NO and H_2O concentrations at an altitude of 28 kilometers with a balloon-borne spin-flip Raman laser [67], and also reported the

pulsed optoacoustic spectroscopy of condensed matter [68]. Rosencwaig in 1978 introduced an important theory called R-G theory explaining the mechanism of photoacoustic effect in condensed matter [69]. After that, several research groups focused on PAS in the field of trace gas detection, liquids and solids with environmental, biological and medical applications using different laser systems.

PA technique can be classified as continuous-wave (CW) modulation and pulsed modes. The duty cycle of the modulated beam is close to 50% in CW mode. As a duty, cycle of such size may produce counterfeit effects, such as heating of the sample and convection currents, the boundary conditions of the acoustic cell are important for the generation of the PA signal. The acoustic resonance of the cell can be used to maximize the PA signal response. Signal analysis is often performed in the frequency domain which convert time domain signal into frequency domain using fast Fourier transform. The CW mode suffers from apparent thermal diffusion in the generation of the PA response, thereby lowering its PA efficiency and sensitivity. To achieve highest PA response from a small quantity of samples, PA techniques utilize the pulsed excitation mode [45,70,71]. Pulsed PA technique uses a high power, low duty cycle optical source to excite a PA signal, because optical energy is deposited in the sample with relatively short time of the order 5 ns to 1 μs. The PA efficiency is greatly improved by ignoring the thermal diffusion effects. This results in eliminating the effects of sample heating and convection currents that usually occur in the CW excitation mode, due to the low average power of the pulsed source. For instance, Pulsed PA technique minimizes the noise that is produced by window absorption or light scattering and enhances the signal to noise ratio. As a result, the detection sensitivity is greatly improved, compared with the CW excitation mode. Furthermore, it should be noted that only the pulsed mode could be used in time-resolved PA spectroscopy.

The advantage of PAS is that it can be performed on all phases of matter. Therefore, it has tremendous applications in spectroscopy of solids, liquids, gases, condensed matter, nanoparticles study, semiconducting materials and electrodes devices etc. [33-42]. PAS is particularly useful technique for samples that are powdered (like catalysts), amorphous, or otherwise not conducive to reflective or transmission forms of optical spectroscopy. The photoacoustic effect is used to study biological samples such as blood, skin, eye lenses, tumors and drug-laced tissues. Several studies are available in which PA spectroscopy has been used to identify different types of bacteria. One useful aspect of photoacoustic spectroscopy of gases is that pulsed lasers can be used to detect very tiny concentrations of a particular gas of the order of parts per trillion. This makes photoacoustic spectroscopy very useful in following the concentrations of trace gases in mixtures, like soot in diesel exhaust or NO_x in the atmosphere.

Our group extended the potential use of photoacoustic spectroscopy in the field of HEMs, to study their decomposition mechanism, stability coupled with TG-DTA technique. We have also evaluated the efficiency of energetic materials as a rocket fuels under controlled pyrolysis process using UV-Visible laser pulses [15,57,72,]. The nitro rich HEMs release several gases as byproducts such as NO_2, NO, N_2O, CO, CO_2, HCN and H_2O etc. during the process of decomposition. Amongst, NO_2 is one of the major byproducts, which has strong absorption at 532 nm wavelength. However, the total molecule vapor and its byproducts have strong absorption at 266 nm wavelength. Therefore, we have chosen UV 266 nm and visible 532 nm of nanosecond pulses as an excitation source for recording the thermal PA spectra of reported compounds. Also, we have recorded the time-resolved PA spectra of some vapors using THz radiation.

1.3.1. Interaction of matter with electromagnetic radiation

The radiation from different parts of the electromagnetic spectrum has very different effects upon interaction with the matter. The energy of electromagnetic radiation increases as we move higher to lower wavelength region i.e. from the radio waves, microwaves and infrared to visible –UV light. Each portion of the electromagnetic spectrum has quantum energy which is quite sufficient appropriate for the excitation of certain types of physical processes. The energy levels for all physical processes at the atomic and molecular levels are quantized and if there are no available quantized energy levels with spacing, which match the quantum energy of the incident radiation, then the material will be transparent to that radiation and will pass through. If the electromagnetic energy is absorbed without ejecting electrons from the atoms of the material, then it is classified as non-ionizing radiation and will typically by just heating the material. Fig. 1.5 shows the interaction of matter with electromagnetic radiations and their physical process.

The physical process of each radiation is followed by:

Microwave Interactions: The quantum energy of microwaves is in the range of 0.00001 to 0.001 eV, this energy range separate the quantum states of molecular rotation and torsion. The interaction of microwaves with matter other than metallic conductors will be to rotate molecules and produce heat because of that molecular motion.

Infrared Interactions: The quantum energy of infrared waves is in the range of 0.001 to 1.7 eV, which is in the range of energies separating the quantum states of molecular vibrations. Infrared is absorbed more strongly than microwaves, but less strongly than visible light. The result of infrared absorption is heating of the samples since it increases molecular vibrational activity.

Visible Light Interactions: The primary mechanism for the absorption of visible light photons is the elevation of electrons to higher energy levels. There are many available states, so visible light is absorbed strongly.

Ultraviolet Interactions: UV photons above the ionization energy can disrupt atoms and molecules (photo ionization), while photons below the ionization energy is strongly absorbed in producing electronic transitions.

Terahertz Interactions: The microwaves and infrared radiations cause heat generation due to rotational and vibrations of molecules, respectively. However, Terahertz (THz) radiation lies between far infrared to microwaves resulting in the heat generation of molecules due to weak vibrational-rotational lines of matter.

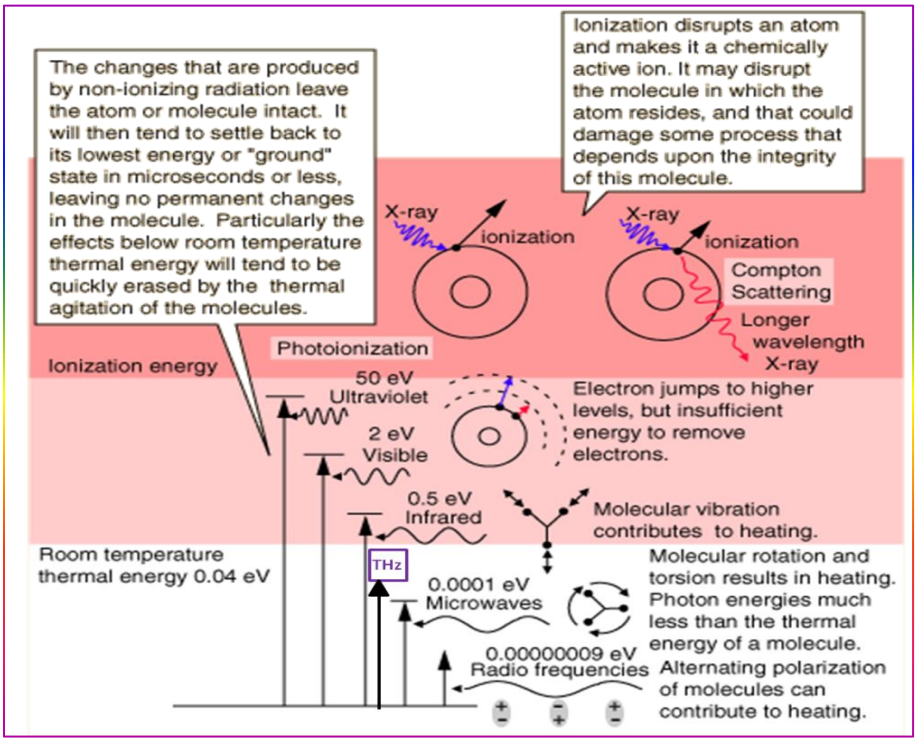

Figure 1.5: Interaction of mater with electromagnetic radiation [73].

The absorption spectrum of a molecule is determined by all the allowed transitions between pair of energy levels and whether the molecule exhibits a sufficiently strong electric or magnetic dipole moment (permanent or otherwise) to interact with the radiation field. Electronic, vibrational and rotational energy levels are superimposed in Fig. 1.6. V is vibrational quantum number; J is the rotational quantum number.

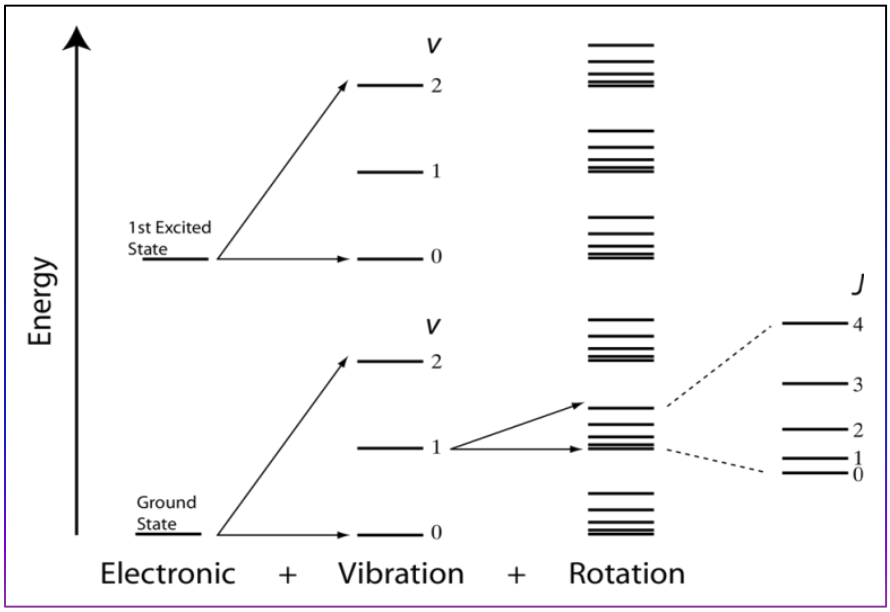

Figure 1.6: Absorption spectra of molecules.

1.3.2. UV-Visible absorption mechanism HEMs byproducts

Due to strong coupling between the high vibrational levels of X^2A_1 ground state $^2B_2$ or $^2B_1$, the optically stored energy entirely contributes to the sample heating regardless of whether the excited level belongs to the $^2B_2$ or $^2B_1$ state [51]. Therefore, the dependence of the PA signal on the absorbed energy will not change in the entire visible range. NO_2 is excited to the $^2B_1$ state due to absorption of 532 nm, and its excitation energy is lost to PA signal generation by Vibrational-Transitional (V-T) and Vibrational-Vibrational (V-V) relaxations of NO_2 in collisions with nitrogen or air molecules as shown in Fig. 1.7.

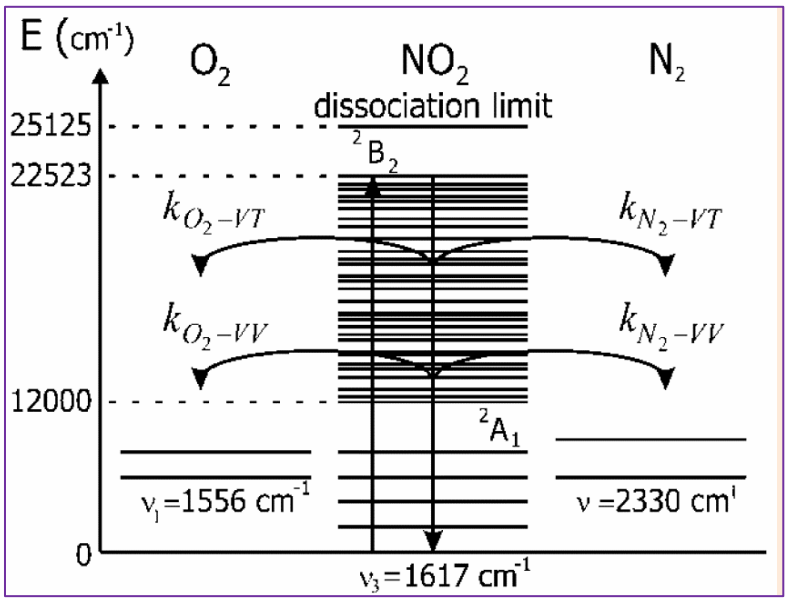

Figure 1.7: The relaxation of NO_2 to N_2 and O_2 via V-T and V-V transitions [52].

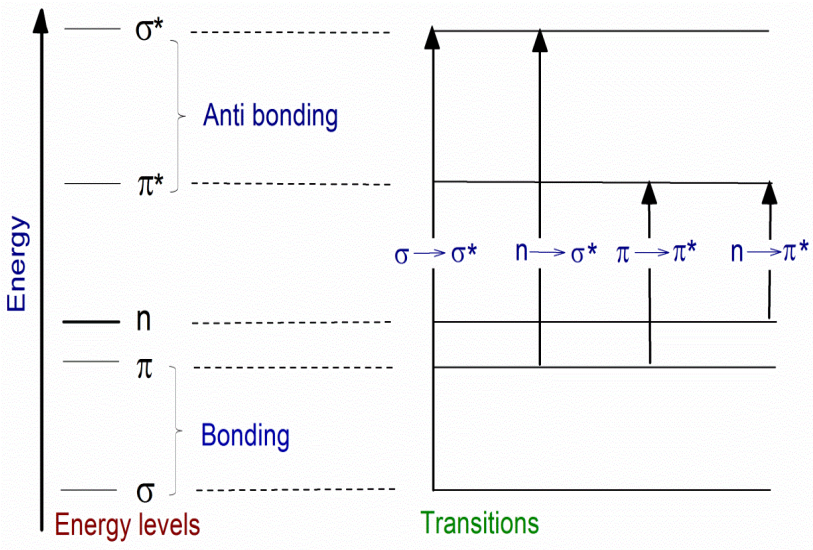

Figure 1.8: The Electron transitions in ultraviolet/visible spectroscopy.

However, in the case of 266 nm wavelength the absorptions mechanism allowed the π→π*, n→σ* and n→ π* transitions. Valence electrons can be found in one of three types of electron orbital: single (σ) bonding orbitals; double or triple bonds (π bonding orbitals) and nonbonding orbitals (lone pair electrons). Sigma bonding orbitals tend to be lower in energy than π bonding orbitals, which in turn are lower in energy than non-bonding orbitals.

When electromagnetic radiation of the exact frequency is absorbed, a transition occurs from one of these orbitals to an empty orbital, usually an anti-bonding orbital, σ* or π*. The exact energy difference between the orbitals depends on the atoms present and the nature of the bonding system. Most of the transitions from bonding orbitals are of too high frequency (too short a wavelength) to measure easily, so most of the absorptions observed involve only π→π*, n→σ* and n→π* transitions. Here, the HEMs vapor follows the photodissociation process and converts into their byproducts due to n→π* transitions [53-57]. The electron transition in ultraviolet/visible spectroscopy is shown in Fig. 1.8.

1.3.3. Terahertz absorption mechanism

Terahertz waves are the best frequencies for gas phase vibrational-rotational spectroscopy. Electronic absorption spectroscopy involves photons of UV-visible light. When electrons in a molecular bond absorb a photon, they get excited and jump to a higher energy level. Rotational spectroscopy detects rotations of atomic nuclei or entire molecules. The rotations typically manifest themselves at sub millimeter wavelengths or terahertz frequencies. Even slight difference in the mass of an atom's nucleus alters its rotation enough to shift their terahertz spectrum. So, this type of spectrometry can be distinguished even between two different isotopes of the same element. The weight might differ by a single neutron. The possible relative positions of transitions in the

absorption spectrum of a molecule in a vibrational-rotational transitions due to THz radiation is shown in Fig. 1.9.

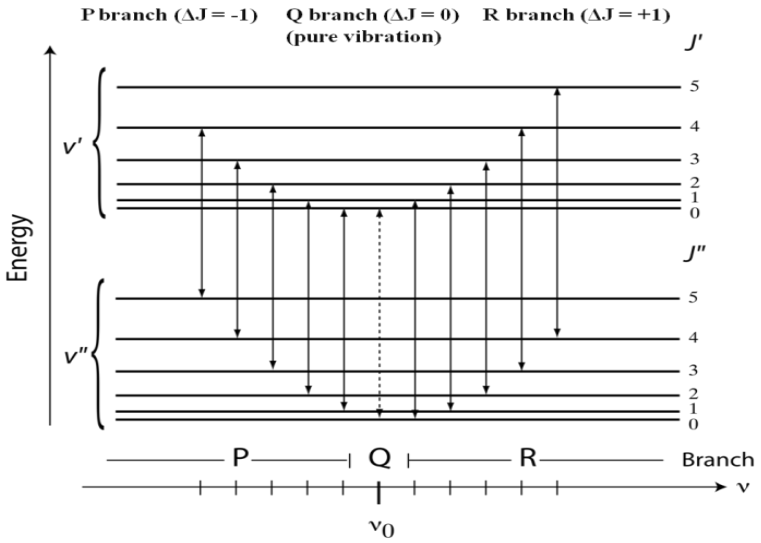

Figure 1.9: Vibrational-rotational transitions in THz domain.

It is well known that in the thermal decomposition of energetic material, it release several gaseous fragments. It is clear that UV 266 nm wavelength absorbed by total molecule vapor, and visible 532 nm wavelength absorbed NO_2 molecules. But, it is difficult to assign the contribution of PA signal generated by THz radiation from HEMs mixture, because all these byproducts has several rotational lines in the THz domain. Therefore, initially, we have recorded the time resolved PA spectra of one of the major byproducts of HEMs i.e. N_2O with broad band THz pulses as well as using 0.5 and 1.5 THz bands. In addition, attention is focused on nitromethane (NM) is a volatile organic compound, which is explosive in nature and available in liquid form at room temperature. It is widely used as a laboratory solvent, synthetic reagent and fuel. The results are compared with another laboratory solvent methanol, which has several rotational lines in THz domain.

1.4. Terahertz radiation

Terahertz radiation refers to electromagnetic waves propagating at frequencies in the terahertz range. It is also termed as submillimeter radiation, terahertz waves, terahertz light, T-rays, T-light, T-lux and THz. The term typically applies to electromagnetic radiation with frequencies between the high-frequency edge of the microwave band, 100 gigahertz (1×10^{11} Hz), and the long-wavelength edge of far-infrared light, 10000 GHz (10×10^{12} Hz or 10 THz). In wavelengths, this range corresponds to 0.1 mm (or 100 μm) infrared to 3.0 mm microwave. The THz band bestraddle the region where electromagnetic physics are well described by its wave-like (microwave) and its particle-like (infrared) characteristics. THz radiation is also known as submillimeter radiation,

terahertz waves, tremendously high frequency, consists of electromagnetic waves within the band of frequencies from 0.1 to 10 THz (1 THz= 10^{12} Hz). Fig. 1.10 shows the complete range of THz radiation in the electromagnetic spectrum regarding frequency, wave number, wavelengths, photon energy and temperature.

THz band has various unique features when compared to other bands of electromagnetic spectrum. It can interact strongly with polar materials, thereby penetrating through non-polar and non-metallic materials. It has high reflection from metallic surfaces due to high electrical conductivity of metals. In particular, the use of pulsed THz radiation generated and detected with ultrashort pulsed lasers opened the first practical and powerful applications of THz waves in spectroscopy and imaging [74,75]. In THz based spectroscopy, these frequencies are the access to vibrational-rotational translations lines of in gas/liquid/solids materials. Therefore, the recorded time-resolved absorption spectra of materials in THz domain can be treated as a characteristic spectrum of corresponding molecules.

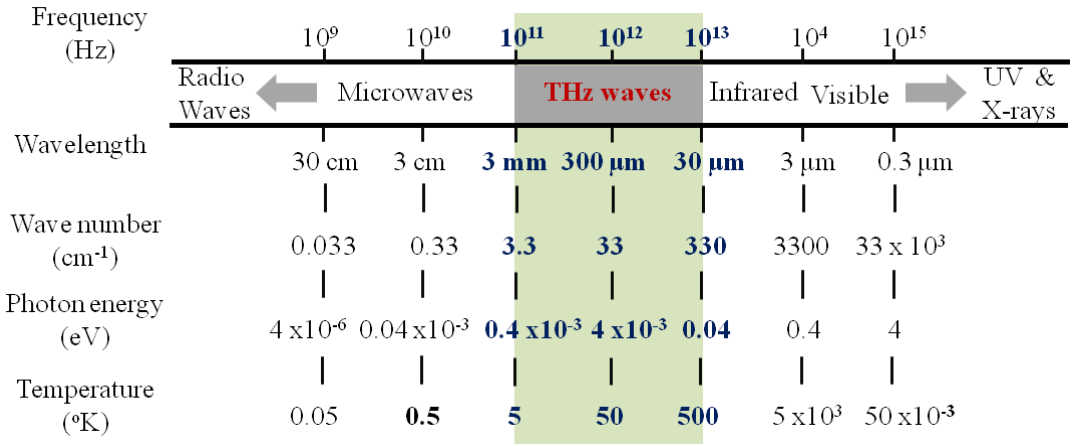

Figure 1.10: Terahertz band in the electromagnetic spectrum [Adopted from [76]].

1.4.1. Terahertz generation and detection mechanisms

THz radiation can be generated from different sources using various mechanisms [77-84]. Among them, ultrafast optical excitation of nonlinear crystals (having second order susceptibilities i.e. $\chi^{(2)}$) is one of the prominent technique used for THz generation. The optical rectification mechanism is responsible for THz emission from nonlinear crystals. We have employed the optical rectification technique for generation of pulsed THz waves using DAST and $ZnGeP_2$ nonlinear crystals and measured the power of terahertz pulses using pyroelectric detector. Table 1.3 shows the brief descriptions of the schemes used for the generation and detection of THz radiation [85]. Advantages and disadvantages of different NLO methods for generation of THz radiation is shown in Table 1.4.

Table 1.3: Overview of different electronic and optoelectronic THz sources and detectors [85].

	Generation	Detection
Electronic	• Microwave multiplier chain • Backward-wave oscillator • Gunn diode • Resonant tunnel diode	• Schottky diode • Backward wave • Rectifying transistor (Tera-FET) **Thermal** • Bolometer, Golay cell, pyroelectric, thermopile
Laser	• Quantum cascade laser • P-type Germanium laser • Molecule gas laser • Free electron laser (Large facility)	
Optical • Femtosecond pulse • Incoherent multi mode • Two color continuous wave	• Photoconductive switch Antenna/photomixer • Optical rectification • Surface emitter • Photo-induced plasma (Amplifier laser)	• Photoconductive switch Antenna/photomixer • Electro-optic sampling • Biased air detection

Table 1.4: Advantages and disadvantages of different NLO methods.

Generation by	Advantages	Disadvantages
Optical Rectification	- easy alignment - waveform synthesis - broadband THz spectrum - high time resolution	- fs laser needed - limited output power - difficult phase matching - broadband line widths
Difference Frequency Generation	- ns laser needed - narrow line widths - cw possible	- difficult alignment -two lasers needed
Parametric Oscillation	- fast tuning possible	- limited output power

1.4.1.1. Optical Rectification

Optical rectification is one of the second-order nonlinear processes. Dc polarization with a duration in the sub-picoseconds emits when a nonlinear material is illuminated and subjected to intense laser pulses. The duration of this dc polarization is in the order of when a nonlinear material is illuminated with ultra short pulses. The THz generation from nonlinear crystal using optical rectification is shown in Fig. 1.11. The dc polarization created by laser field in nonlinear optical crystals in optical rectification process is given by [86,87]

$$P(\omega) = \varepsilon_o \, \chi^{(2)}(\omega = \omega_1 - \omega_2) E^*_{\omega_1} E_{\omega_2} \qquad (1.1)$$

Where, $\chi^{(2)}$ is the second order nonlinear susceptibility, ω is the frequency of generated electromagnetic radiation. The electric field related to THz emission from nonlinear crystal is given as

$$E_{THz}(t,\omega)\ \alpha\ \frac{\partial^2 P(t;\omega)}{\partial t^2}\ \ \alpha\ \omega_x I(\omega_x) \qquad (1.2)$$

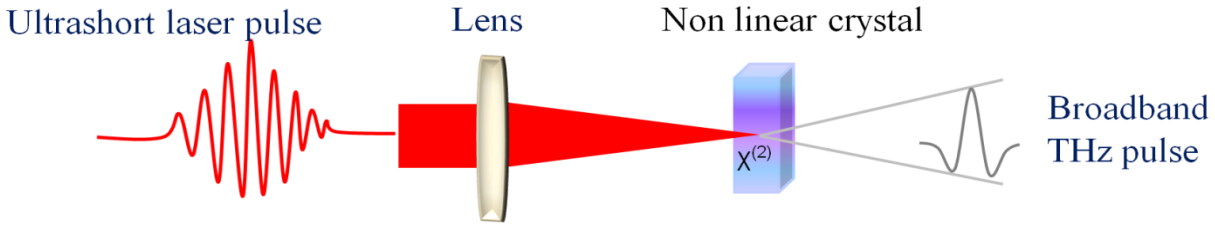

Figure 1.11: Mechanism Optical rectification.

Where ω_x is the central frequency, $I(\omega_x)$ is the bandwidth of the incident laser pulse. It is observed that the bandwidth of generated THz radiation is proportional to central frequency and bandwidth of the incident laser pulse. This shows that a higher bandwidth pulse leads to generation of broadband THz pulses. In optical rectification process, the THz generation depends on nonlinear properties of material. Therefore, the nonlinear crystals, which have higher values of second order nonlinear susceptibilities, generate broadband terahertz pulses. The nonlinear crystals are widely used for THz generation due to the simplicity in alignment and ability to sustain at high laser powers. The amplitude and bandwidth of emitted THz pulses using OR depend on properties of incident laser pulse and nonlinear materials, crystal orientation, thickness, damage threshold, THz and optical absorption of the material.

1.4.1.2. THz applications

THz radiation has several applications in various fields due to its unique characteristics associated with fundamental process such as transparent to dielectric materials, high reflection from metal surfaces, high absorption in water vapor, rotational transitions of molecules, large-amplitude vibrational motions of organic compounds, lattice vibrations in solids, intraband transitions in semiconductors, and energy gaps in super- conductor. Moreover, it is non-ionizing and non-invasive in nature as compared to X-rays. The chemical substances, explosive materials, organic and biological molecules, etc. have their characteristic spectra at terahertz frequencies. THz applications exploit these unique characteristics of material responses to THz radiation. Therefore, THz spectroscopy is one of the promising technique in identification and characterization of explosives and other materials such as drugs and bio-agents etc [88-91].

Condensed matter is largely grouped into three categeries: water, metal, and dielectric based on the optical properties at THz frequencies. Water is a polar liquid, which is highly absorptive in the THz region. Metals are highly reflective at THz frequencies due to its high electrical conductivity.

Nonpolar and nonmetallic materials, i.e., dielectrics such as paper, plastic, clothes, wood, and ceramics that are usually opaque at optical wavelengths, are transparent to THz radiation.

In addition, THz radiations are useful for many imaging applications. Since common packaging materials are dielectric, THz imaging is applied to nondestructive testing to inspect sealed packages. In THz region water has high absorption; due to this, hydrated substances are easily differentiated from dried ones. Metal objects can also be easily identified due to their high reflectivity and complete opacity. The same concept is applied to security applications. THz imaging is used to identify weapons, explosives, and illegal drugs concealed underneath typical wrapping and packaging materials.

1.5. TG-DTA technique

Thermo gravimetric analysis (TG) is a method of thermal analysis where the changes in physical and chemical properties of materials are deliberate as a function of increasing temperature with constant heating rate [92]. In addition to that it measures changes in weight in relation to changes in temperature. The measured weight loss curve gives information on: (a) changes in sample composition, (b) thermal stability, and (c) kinetic parameters for chemical reactions in the sample.

Table 1.5: Process and advantages of TG-DTA technique.

<table>
<tr><th colspan="2">TG: Phenomena causing mass changes</th><th colspan="2">DTA: Phenomena causing changes in heat /temperature</th></tr>
<tr><th>Physical</th><th>Chemical</th><th>Physical</th><th>Chemical</th></tr>
<tr><td>o Gas adsorption
o Gas desorption
o Phase transitions
• Vaporization
• Sublimation</td><td>o Decomposition
o Break down reactions
o Gas reactions
o Chemisorptions (adsorption by means of chemical instead of physical forces)</td><td rowspan="2">o Adsorption (exothermic)
o Desorption (endothermic)
o A change in crystal Structure (endo)-or exothermic)
o Crystallization (exothermic)
o Melting (endothermic)
o Vaporization (endothermic)
o Sublimation (endothermic)</td><td rowspan="2">o Oxidation (exothermic)
o Reduction (endothermic)
o Break down reactions (endo – or exothermic)
o Chemisorptions (exothermic)
o Solid state reactions (endo - or exothermic)</td></tr>
<tr><td colspan="2">TG: Applications
o Characterization of
▪ Thermal stability
▪ Material purity
▪ Determination of humidity
o Examination of
▪ Corrosion studies (e.g. oxidation or reactions with reactive gases)
▪ Gasification processes
▪ Kinetic processes</td></tr>
</table>

Differential thermal analysis (DTA) is a thermo analytic technique; in which the material under study and an inert reference are made to undergo identical thermal cycles, while recording any temperature difference between sample and reference [93]. The differential temperature is then

plotted against time/temperature (DTA curve or thermogram). Changes in the sample, either exothermic or endothermic, can be detected relative to the inert reference. Thus, a DTA curve provides data on the transformations that have occurred, such as glass transitions, crystallization, melting, decomposition and sublimation. The area under a DTA peak is the enthalpy change and is not affected by the heat capacity of the sample. In our case, we have focused to find out the melting and decomposition temperature of the HEMs and nature of reaction i.e. exothermic (exo) or endothermic (endo). The overall advantages of TG-DTA technique for characterizing the physical and chemical properties of materials are given in Table 1.5.

1.6. Overview of thesis

The overview of the thesis is presented in below flow chart (Fig. 1.12), the detail discussion of each chapter included below.

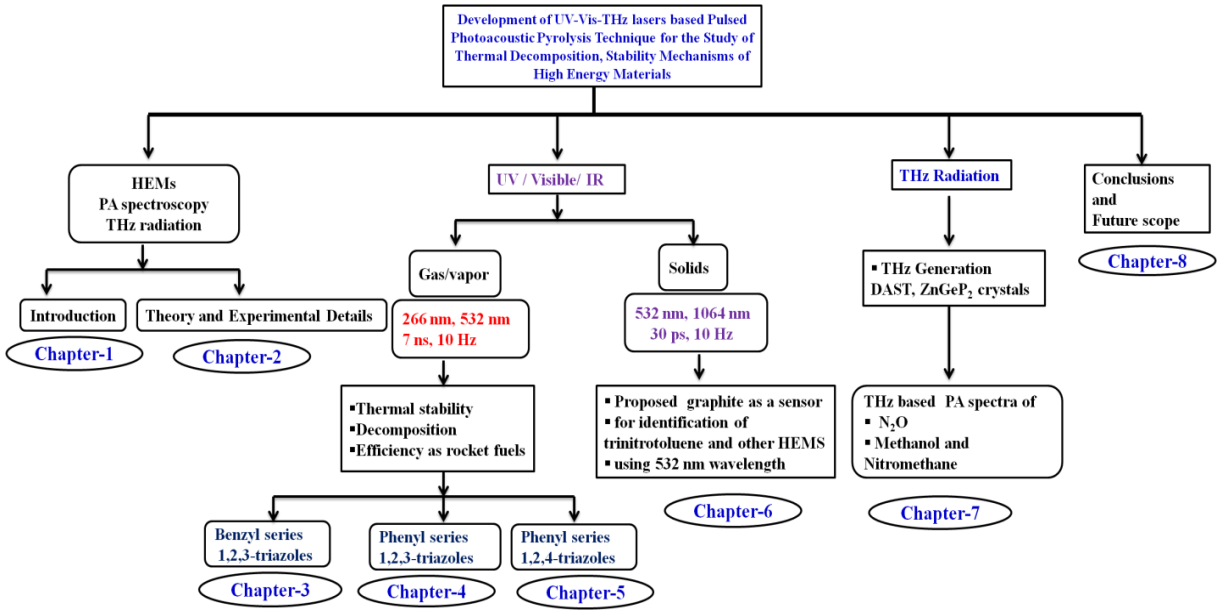

Figure 1.12: Overview of thesis.

Chapter 1 (Introduction)

This chapter comprises the general classification of HEMs/explosives and several laser-based detection techniques, along with the current state of knowledge in this field. Other sub-sections in the chapters also deals with the general introduction of photoacoustic spectroscopy, generation and detection techniques of THz radiation.

Chapter 2 (Theory and experimental details)

This chapter describes the basic principle of pulsed PA spectroscopy, the selection/design of PA cell to record the thermal PA spectra and experimental setup used for the study of thermal stability of energetic materials in the vapor phase. It also includes solid photoacoustic cell design and experimental layout. The instrumental details of TG-DTA, FTIR, Raman, GC-MS are also provided.

In addition, we discussed basics of the nonlinear frequency process, phase matching, group velocity mismatch, effective and coherence lengths of the crystals, etc. The information of the second section is used for the generation mechanisms of THz radiation using nonlinear crystals such as DAST and $ZnGeP_2$.

Chapter 3 (Benzyl-series 1,2,3-triazoles: Study of thermal decomposition, stability, and acoustic fingerprint spectra)

This chapter deals with the basic information about the chemical and physical properties of benzyl series 1,2,3-triazoles named as 1-(2,4-dinitrobenzyl)-1H-1,2,3-triazole (S_1), 1-(3,5-dinitrobenzyl)-1H-1,2,3-triazole (S_2), 1-(2-methoxy-3,5-dinitrobenzyl)-1H-1,2,3-triazole (S_3), 1-(4-methoxy-3,5-dinitrobenzyl)-1H-1,2,3-triazole (S_4), 1-(2,4-dinitrobenzyl)-4-nitro-1H-1,2,3-triazole (S_6). An overview of different types of benchmark explosives and up to date studies carried out by various groups are also provided. We introduced the pulsed laser photoacoustic pyrolysis technique to study thermal decomposition, stability and acoustic fingerprints of selected nitro rich benzyl-series 1,2,3-triazoles (labeled as S_1, S_2, S_3, S_4, S_6) using visible 532 nm and UV 266 nm wavelengths obtained from Q-switched Nd: YAG laser of 7 ns pulse duration and repetition rate of 10 Hz. The thermal stability and decomposition mechanisms of these compounds are also verified using thermo gravimetric-differential thermal analysis (TG-DTA) technique. In addition, the thermal stability of the compounds was also explained on the basis of the effect of data acquisition time, incident laser energy and thermal quality factor 'Q' of the PA cavity. The study is also carried out to find the efficiency order of these triazole derivatives as rocket fuel.

Chapter 4 (Phenyl-series 1, 2, 3-triazoles: Study of thermal decomposition, stability, acoustic fingerprint spectra and absorption cross section)

This chapter describes the general properties, thermal stability, acoustic fingerprint spectra of phenyl series 1,2,3-triazoles such as 1-(2-methoxy,-3,5-dinitrophenyl)-1H-1,2,3-triazole (S_5), 1-(3-methoxy, 2, 6 dinitrophenyl) 1, 2, 3 triazole (S_{10}), 1-(4-nitrophenyl)-1H-1,2,3-triazole (S_8) and bis series compound: 2,6-bis ((4-(nitromethyl)-1H-1,2,3-triazol-1-yl)methyl) pyridine (S_9) using nanoseconds laser pulses of 532 nm and 266 nm wavelengths. We also reported that recording of thermal PA spectra of phenyl series triazoles requires higher incident laser energies as compared the benzyl series 1,2,3- triazoles. This shows that phenyl series triazoles release a low quantity of gaseous in their decomposition than the benzyl series. This clearly shows that phenyl series triazoles are more thermally stable than the benzyl series 1,2,3- triazoles. Also, the molecular density and absorption cross sections of S_8 and S_9 are ascertained based on released NO_2 molecules using 532 nm wavelength. However, the study also shows that position of $-NO_2$ groups decides the thermal stability of isomers S_5 and S_{10}. The Gas chromatic–mass spectra of S_5 and S_{10} are also incorporated.

Chapter 5 (Phenyl-series 1,2,4-triazoles: Bond breaking mechanism and thermal stability)

This chapter describes the effect of bond lengths of major chemical substituents on thermal stability of nitro rich 1,2,4-triazoles named 1-(4-Methyl-3,5-dinitrophenyl)-1H-1,2,4-triazole (*P*-**Me**-DNPT),1-(4-Methoxy-3,5-dinitrophenyl)-1H-1,2,4-triazole (*P*-**OMe**-DNPT), 2,6-Dinitro-4-(1H-1,2,4-triazol-1-yl) aniline (*P*-**NH_2**-DNPT) between 30 and 350 ^oC range using pulsed photoacoustic pyrolysis technique. Thermal stability and photoacoustic fingerprint spectra of these compounds are evaluated in terms of thermally released NO_2 molecules and total molecule vapor by employing 7 ns pulse duration and 10 Hz repetition rate pulses of second and fourth harmonic wavelengths i.e. 532 nm and 266 nm respectively. The thermo gravimetric-differential thermal analysis (TG-DTA) data along with PA results highlights the multistep decomposition mechanism of phenyl series triazoles. These studies also help us to distinguish the characteristic behavior of propellants and explosives of reported molecules as a rocket fuel.

Chapter 6 (Identification of trinitrotoluene and other HEMs in graphite mixture)

This chapter deals with the time-resolved PA spectra of different types of solid carbon blacks obtained from wood charcoal, graphite powder and diesel soot using 532 nm wavelength pulses of duration 30 ps at a repetition rate of 10 Hz. The results of the photoacoustic and Raman spectroscopy allow us to evaluate the potential use of graphite powder for the identification of trinitrotoluene (TNT) explosive using visible 532 nm wavelength. Also, we have recorded the PA spectra of explosives such as nitrogen-rich imidazole, 1, 2, 4-triazole and tetrazole-based solid compounds mixtures in graphite matrix using 532 nm /1064 nm wavelengths pulse duration 30 ps and repetition rate 10 Hz. At these wavelengths, the HEMs do not have any absorption, however, after mixing in graphite mixture, these compounds absorb the incident wavelengths. As a result, strong PA signal is observed compared to pure graphite signal. We have investigated the phonon transfer mechanism to identify TNT and other HEMs molecules using picoseconds laser pulses. These results are further explained with the help of double resonant Raman spectroscopy.

Chapter 7 (THz generation and detection its applications in PA spectroscopy)

This chapter describes the THz radiation generation using optical rectification process in an indigenously grown organic salt 4-N, N-dimethylamino-4'-N'-methyl-stilbazoliumtoyslate (DAST) and imported crystal zinc germanium phosphide ($ZnGeP_2$). The optical parametric amplifier pulses tunable between 0.8-1.6 μm and 1.15-1.6 μm range, having pulse duration 60 femtosecond and repletion rate 1 kHz were employed to generate THz. The maximum conversion efficiency (η) of generated THz is 0.0161% which is obtained at pump wavelength 1.3 μm. In addition, we have

selected two rotational lines i.e. J= 19, 58 of pure N_2O gas by using 0.5 and 1.5 THz bandpass filters for recording the time-resolved photoacoustic spectra at 1 atm pressure. The THz radiation generated from $ZnGeP_2$ crystal is further utilized to record the PA spectra of nitromethane and methanol vapor at 0.5 and 1.5 THz bands.

Chapter 8: (Conclusions and Future Scope)

This chapter summarizes the work of previously mentioned chapters and provides the future scope of the work. Our new investigations on thermal decomposition mechanisms of explosives, role of graphite as a TNT sensor and THz based photoacoustic spectroscopy have opened several new channels for future research. By judiciously selecting, the tunable laser in Mid-IR range will helps us to identify different types of gaseous species produced during thermal decomposition.

References:

1. David S Moore, Sen. Image **8**, 9(2007).
2. A. Jai Prakash and H. Robert, *Organic Chemistry of Explosives* (Wiley, 2006).
3. J. Akhavan, *Chemistry of Explosives* (The Royal Society of Chemistry, 2004).
4. R. Meyer, J. Köhler, and A. Homburg, *Explosives* (Wiley-VCH, Weinheim, 2007).
5. A. Bailey and S. G. Murray., *Explosives, Propellants and Pyrotechnics* (London, 2000).
6. S. Fordham, *High Explosives and Propellants* (2013).
7. J. Akhavan, *The Chemistry of Explosives* (The Royal Society of Chemistry, 2011).
8. T. M. Klapotke, *Chemistry of High Energy Materials* (2011).
9. J.P. Agrawal, *High Energy Materials* (Wiley, 2010).
10. *Committee on the Review of Existing and Potential Stand-off Explosives Techniques, National Research Council, Washington* (2004).
11. C. P. Letters, Chem. Phys. Lett. **149**, 123 (1988).
12. S. M. Angel, L. F. Katz, D. D. Archibald, and D. E. Honigs, Appl. Spectrosc. **43**, 367 (1989).
13. D. B. Chase and B. A. Parkinson, Appl. Spectrosc. **42**, 1186 (1988).
14. M. Fleischmann, P. J. Hendra, and A. J. McQuillan, Chem. Phys. Lett. **26**, 163 (1974).
15. F. Yehya and A. K. Chaudhary, Sensors Actuators B. Chem. **178**, 324 (2013).
16. A. K. Chaudhary, G. C. Bhar, and S. Das, J. Appl. Spectrosc. **73**, 123 (2006).
17. F. Yehya, A. K. Chaudhary, D. Srinivas, and K. Muralidharan, Appl. Phys. B **121**, 193 (2015).
18. R. Turcotte, M. Vachon, Q. S. M. Kwok, R. Wang, and D. E. G. Jones, Thermochim. Acta **433**, 105 (2005).
19. D. E. G. Jones, P. D. Lightfoot, R. C. Fouchard, Q. Kwok, A. M. Turcotte, and W. Ridley, Thermochim. Acta **384**, 57 (2002).
20. M. F. Foltz, C. L. Coon, F. Garcia, and A. L. Nichols III, Propellants, Explos. Pyrotech. **19**, 133 (1994).
21. G. Singh, S. P. Felix, and P. Soni, Thermochim. Acta **426**, 131 (2005).
22. A. Strachan, E. M. Kober, A. C. T. van Duin, J. Oxgaard, and W. a Goddard, J. Chem. Phys. **122**, 54502:1 (2005).
23. H. S. Jadhav, M. B. Talawar, R. Sivabalan, D. D. Dhavale, S. N. Asthana, and V. N. Krishnamurthy, J. Hazard. Mater. **143**, 192 (2007).
24. Y. Zhang, D. A. Parrish, and J. M. Shreeve, J. Mater. Chem. A **1**, 585 (2013).
25. N. Fischer, D. Fischer, T. M. Klapötke, D. G. Piercey, and J. Stierstorfer, J. Mater. Chem. **22**, 20418 (2012).
26. T. M. Klapötke and C. M. Sabaté, Chem. Mater. **20**, 3629 (2008).
27. P. Zhang, S. J. Klippenstein, L. B. Harding, H. Sun, and C. K. Law, RSC Adv. **4**, 62951 (2014).
28. T. M. Klapo, P. Mayer, A. Schulz, and J. J. Weigand, J. Am. Chem. Soc. **127**, 2032 (2005).
29. X. Liu, Q. Yang, Z. Su, S. Chen, G. Xie, Q. Wei, and S. Gao, RSC Adv. **4**, 16087 (2014).
30. A. S. Kumar, V. D. Ghule, S. Subrahmanyam, and A. K. Sahoo, Chemistry **19**, 509 (2013).
31. A. S. Kumar, N. Kommu, V. D. Ghule, and A. K. Sahoo, J. Mater. Chem. A **2**, 7917 (2014).

32. D. Chakraborty, R. P. Muller, S. Dasgupta, and Wi. A. Goddard, J. Phys. Chem. A **105**, 1302 (2001).

33. G. A. West, J. J. Barrett, D. R. Siebert, and K. V. Reddy, Rev. Sci. Instrum. **54**, 797 (1983).

34. D. W. Ball, Spectroscopy **21**, 14 (2006).

35. A. Rosencwaig, Opt. Commun. **7**, 305 (1973).

36. P. Repond and M. W. Sigrist, Appl. Opt. **35**, 4065 (1996).

37. Y. Pinchasov-Grinblat and Z. Dubinsky, Artif. Photosynth. 257 (2012).

38. a Petzold and R. Niessner, Appl. Phys. Lett. **66**, 3 ST (1995).

39. W. Markus, Photoacoust. Spectrosc. , Appl. 1800 (1997).

40. M. W. Sigrist, A. Bohren, T. Lerber, M. Nägele, and A. Romann, Anal. Chem. **17**, 511 (2001).

41. J. B. Kinney and R.H. staley, Ann.Rev. Mater. Sci. **12**, 295 (1982).

42. C. S. Sunandana, Phys. Status Solidi A **105**, 11 (1988).

43. A. Thöny and M. W. Sigrist, Infrared Phys. Technol. **36**, 585 (1995).

44. W. M. Sigrist, *In Air Monitoring by Spectroscopic Techniques* (John Wiley & Sons, Inc., New York, 1994).

45. A. Miklós, P. Hess, and Z. Bozóki, Rev. Sci. Instrum. **72**, 1937 (2001).

46. V. Slezak, G. Santiago, and A. L. Peuriot, Opt. Lasers Eng. **40**, 33 (2003).

47. F. J. M. Harren, G. Cotti, J. Oomens, and S. L. Hekkert, Encycl. Anal. Chem. 2203 (2000).

48. S. Schäfer, M. Mashni, J. Sneider, and A. Mikl, Appl. Phys. B **66**, 511 (1998).

49. F. Yehya and A. K. Chaudhary, Spectrochim. Acta. A. Mol. Biomol. Spectrosc. **115**, 544 (2013).

50. F. Yehya and A. K. Chaudhary, Opt. Commun. **312**, 16 (2014).

51. G. D. Gillispie and A. U. Khan, J. Chem. Phys. **65**, 1624 (1976).

52. J. Kalkman and H. W. Van Kesteren, Appl. Phys. B Lasers Opt. **90**, 197 (2008).

53. Y. Q. Guo, a Bhattacharya, and E. R. Bernstein, J. Phys. Chem. A **113**, 85 (2009).

54. J. F. Arenas, J. C. Otero, D. Peláez, and J. Soto, J. Chem. Phys. **119**, 7814 (2003).

55. S. Zabarnick, J. W. Fleming, and a. P. Baronavski, J. Chem. Phys. **85**, 3395 (1986).

56. L. J. Butler, D. Krajnovich, Y. T. Lee, G. S. Ondrey, and R. Bersohn, J. Chem. Phys. **79**, 1708 (1983).

57. K. S. Rao, A. K. Chaudhary, F. Yehya, and A. S. Kumar, Spectrochim. Acta Part A Mol. Biomol. Spectrosc. **147**, 316 (2015).

58. E. D. Palik and K. N. Rao, J. Chem. Phys. **25**, 1174 (1956).

59. D. M. Mittleman, R. H. Jacobsen, R. Neelamani, R. G. Baraniuk, and M. C. Nuss, Appl. Phys. B-Lasers Opt. **67**, 379 (1998).

60. A. G. Bell, Am. J. Sci. **118**, 305 (1880).

61. J. Tyndall, Proc. Roy. Soc. **31**, 307 (1881).

62. W. C. Röntgen, Ann. Phys. **248**, 155 (1881).

63. M. L. Veingerov, Dokl. Akad. Nauk. USSR **19**, 687 (1938).

64. A. Miklós, S. Schäfer, and P. Hess, *Photoacoustic Spectroscopy , Theory* (1999).

65. E. L. Kerr and J. G. Atwood, Appl. Opt. **7**, 915 (1968).

66. L. B. Kreuzer, J. Appl. Phys. **42**, 2934 (1971).

67. C. K. N. Patel, **8**, 145 (1975).

68. C. . K. . N. Patel and A. C. Tam, Rev. Mod. Phys. **53**, 517 (1981).

69. A. Rosencwaig, J. Appl. Phys. **49**, 2905 (1978).

70. C. Brand, A. Winkler, P. Hess, A. Miklos, Z. Bozoki, and J. Sneider, Appl. Opt. **34**, 3257 (1995).

71. D. V Bageshwar, A. S. Pawar, V. V Khanvilkar, and V. J. Kadam, Eurasian J. Anal. Chem. **5**, 187 (2010).

72. F. Yehya and A. K. Chaudhary, Appl. Phys. B **110**, 15 (2012).

73. Http://hyperphysics.phy-astr.gsu.edu/hbase/mod3.html.

74. D. Grischkowsky, S. Keiding, M. van Exter, and C. Fattinger, J. Opt. Soc. Am. B **7**, 2006 (1990).

75. B. B. Hu and M. C. Nuss, Opt. Lett. **20**, 1716 (1995).

76. T. Nagatsuna, Electron. Express **8**, 1127 (2011).

77. P. R. Smith, D. H. Auston, and M. C. Nuss, IEEE J. Quantum Electron. **24**, 255 (1988).

78. A. Rice, Y. Jin, X. F. Ma, X. C. Zhang, D. Bliss, J. Larkin, and M. Alexander, Appl. Phys. Lett. **64**, 1324 (1994).

79. X. C. Zhang and D. H. Auston, J. Appl. Phys. **71**, 326 (1992).

80. G. H. Welsh, N. T. Hunt, and K. Wynne, Phys. Rev. Lett. **98**, 3 (2007).

81. P. C. M. Planken, M. C. Nuss, I. Brener, K. W. Goossen, M. S. C. Luo, S. L. Chuang, and L. Pfeiffer, Phys. Rev. Lett. **69**, 3800 (1992).

82. M. C. Beard, G. M. Turner, and C. A. Schmuttenmaer, J. Phys. Chem. A **106**, 878 (2002).

83. J. Shen, X. Fan, Z. Chen, M. F. Decamp, H. Zhang, and J. Q. Xiao, Appl. Phys. Lett. **101**, 072401 (2012).

84. D. J. Cook and R. M. Hochstrasser, Opt. Lett. **25**, 1210 (2000).

85. W. Zouaghi, M. D. Thomson, K. Rabia, R. Hahn, V. Blank, and H. G. Roskos, Eur. J. Phys. **34**, S179 (2013).

86. K. Sakai, *Terahertz Optoelectronics* (2005).

87. K. Radhanpura, All-Optical Terahertz Generation from Semiconductors: Materials and Mechanisms, 2012.

88. Y. C. Shen, T. Lo, P. F. Taday, B. E. Cole, W. R. Tribe, and M. C. Kemp, Appl. Phys. Lett. **86**, 1 (2005).

89. D. F. Plusquellic, K. Siegrist, E. J. Heilweil, and O. Esenturk, ChemPhysChem **8**, 2412 (2007).

90. Y. C. Shen, Int. J. Pharm. **417**, 48 (2011).

91. P. F. Taday, I. V. Bradley, D. D. Arnone, and M. Pepper, J. Pharm. Sci. **92**, 831 (2003).

92. A. W. Coats and J. P. Redfern, Analyst **88**, 906 (1963).

93. J. Pask, *Differential Thermal Analysis - Methods and Techniques* (1953).

Chapter 2

Theory and experimental details

Abstract

In this chapter incorporated the details of photoacoustic spectroscopy theory, the experimental setups used for the study of thermal stability and identification of solid energetic materials. In addition provided the brief summary on some nonlinear frequency processes i.e. various phase matching conditions for uniaxial and biaxial crystals, equations for group velocity mismatch, effective and coherence lengths of the crystals. The technical information for instruments and laser systems are also included.

2.1. Process of photoacoustic technique

The Photoacoustic effect is based on the sample heating produced by optical absorption. Once an absorbing molecule is excited by a laser beam to a higher energy level, it eventually falls down to its initial energy level through several processes as follow [1, 2];

(a) Radiation (stimulated or spontaneous emission of a photon),

(b) Chemical reactions such as a bond rearrangement-photochemistry,

(c) Non-radiative deactivation, which consist in energy transfer towards surrounding molecules through collisions.

The latter process is responsible for the increase in the kinetic energy of the molecules, which causes local heating, and subsequently a thermal expansion in the medium. If the intensity of the light radiation is modulated at a given frequency, the induced periodical thermal expansion gives rise to a sound wave at the same frequency. This process is known as photoacoustic effect. However, there are two type of excitation process in PA technique. The first process is modulated excitation mechanism, where the intensity of radiation sources fluctuates periodically in the form of a square or a sine wave by a mechanical chopper. In this process, the PA signal is enhanced due to acoustic resonance. The second process is pulsed excitation mechanism, where laser pulses of nanosecond/picoseconds duration is used for the generation of the PA signal. The repetition rates are in the range of a few Hz (in our case 10 Hz), which provides a short illumination time followed by a much longer dark period. This leads to a fast thermal expansion of the sample medium resulting in a short shock pulse. The fast Fourier transform (FFT) used for conversion of time domain signal into the frequency domain results in a wide spectrum of acoustic frequencies occupied according to the dimensions of the PA cavity. However, the CW laser beam modulated in the form of a sine wave excites one single acoustic frequency, whereas short laser pulses are broadband acoustic sources.

2.1.1. Design of PA resonant cavity (PA cell) for gas/vapor samples

The laser source, microphone, acoustic cell, preamplifier, oscilloscope and personal computer are essential parts of the PA sensor. It helps us to develop an efficient system for the study of thermal stability and decomposition mechanisms of HEMs. The pulsed PA pyrolysis technique requires following information before performing the experiment:

Selection of a laser source: some knowledge of decomposition molecules and their absorption wavelengths which can be found from HITRAN database [3-6]. Initially it can be noted that the melting and decomposition temperatures and weight loss of the compounds from TG-DTA technique. This profile enables selection of suitable wavelengths. The gas molecules have certain

wavelength range only for a strong absorption. Therefore, select those laser wavelengths to find out the particular absorption properties of gas components in terms of PA signal.

Selection of a microphone: Microphone should have high responsivity broad frequency range, low power requirement, and suitable dimension, which enabled it to be housed in the cylindrical cavity.

Designing aspects of acoustic cell: A well-designed PA cell also works as an amplifier and allows to excite all types of cavity modes with respect to the incident laser beam also possess high quality factor.

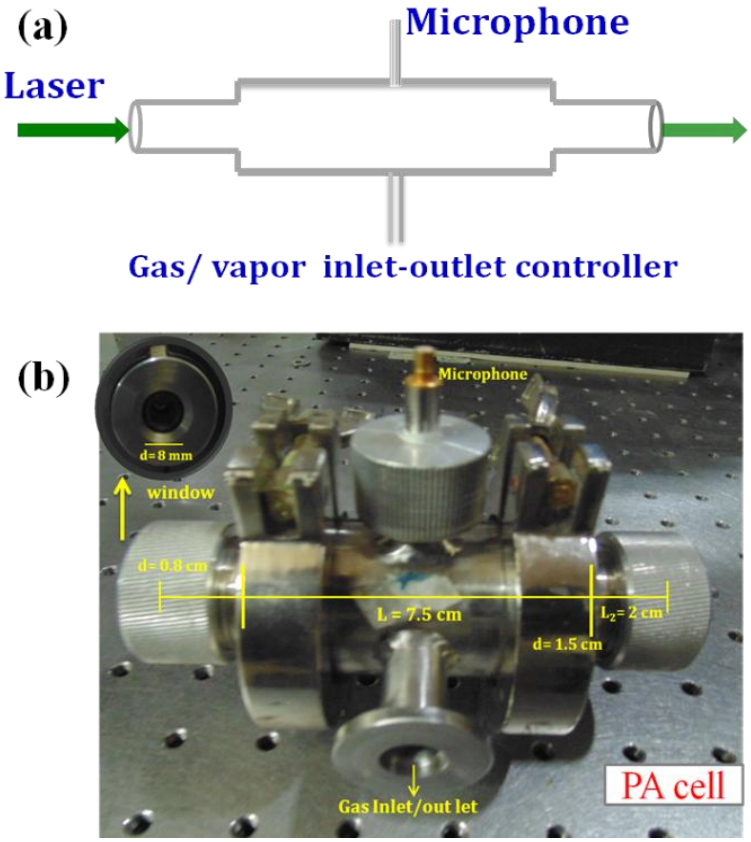

Figure 2.1: Designed PA cell of length: 7.5 cm, radius: 0.75 cm.

The thermal PA spectra of reported energetic compounds were recorded using laboratory designed acoustic filter type resonance PA cell of length (L) = 7.5 cm, radius (R) = 0.75 cm (as shown Fig. 2.1) [7]. The resonant cell, with higher Q-value works as an amplifier, lowers the concentration of gas, enables the system for a trace level detection. In a cylindrical PA resonance cell, the three types of eigenmodes are excited i.e. longitudinal, azimuthal and radial modes. The noise generated at the cell windows due to light source can be controlled by buffer volume known as acoustic filters. In the designed PA cell, these have a length of 2 cm and a diameter of 0.8 cm. These filters suppress the noise from outside the sample. Now the main cavity works as a resonator and it is acoustically isolated [8]. In the case of a longitudinal resonator, the buffer volume should have a $\lambda/4$ length, where λ is the wavelength of the sound wave.

2.1.2. Calculated eigenmodes of the PA cavity

In PA technique, the PA cells serve as a container for the gas sample and the microphone device, which is used, for detection of generated PA signals [2]. According to the mode of operation, the PA cells are divided into two categories. The first category belongs to the non-resonant cell where the geometrical cavity is not matched with the acoustic wavelength as a result standing wave patterns cannot be formed and excited frequency does not match with any of the eigenmodes. The second category deals with the resonant cell where the modulation frequency of the source matches with one of the eigenmodes of the cavity. As a result, the quality factor of the cell becomes high and the amplitude of the excited resonance mode is amplified. Therefore, the resonance cells are made by fitting the PA cavity dimensions according to the desired acoustic modes. The resonance type of PA cell based on the cylindrical geometry offers an intrinsic symmetry, easy overlapping of different types of excited resonant modes excited by laser beam. In addition, it possess high sensitivity, high quality factor and selection of suitable place to house a microphone to collect the best acoustic modes of the cavity. Therefore, the cylindrical cavities are widely used in the field of photoacoustic spectroscopy [2,9]. The inhomogeneous wave equation of the sound pressure in the lossless cylindrical resonator is well explained by different groups [1,2,9-14]

$$\frac{d^2P(r,t)}{dt^2} - c^2\nabla^2P(r,t) = (\gamma - 1)\frac{dH(r,t)}{dt} \quad (2.1)$$

Where, c, γ and H are the sound velocity, the adiabatic coefficient of the gas and the heat density deposited in the gas by light absorption, respectively. Because, the sound velocity, which is proportional to the gradient of P(r), vanishes at the cell wall, the P(r) must satisfy the boundary conditions of the vanishing gradient of p(r) normal to the wall [11]. The solution of equation (2.1) is given by:

$$P(r,t) = C_0(t) + \sum_{n=0}^{\infty} C_n(t)P_n(r) \quad (2.2)$$

Where $C_0(t)$, $C_n(t)$ are the eigen mode amplitude of corresponding sound wave, $C_n(t)$ is given by the Fourier series as :

$$C_n(t) = \sum_{n,m}^{n} A_{n,m}\, e^{imw_o t} \quad (2.3)$$

The dimensionless eigenmodes distribution of cylindrical resonator is the solution of the homogeneous wave equation and given by:

$$P_n(r,t) = P_n(r)e^{iw_n t} \quad (2.4)$$

Where W_n is the resonance frequency of the cavity resonator, $P_n(r)$ is:

$$P_n(r) = P_{mnq}(r,\emptyset,z) = J_m(K_r r)\cos(K_z z)\left\{\begin{matrix}\cos(m\emptyset)\\ \sin(m\emptyset)\end{matrix}\right\} \quad (2.5)$$

Where the amplitude (A_n) of modulated beam is:

$$A_n = \frac{iw_0(\gamma-1)f_n}{w_n^2 - w_0^2 + \left(iw_o\frac{w_n}{Q}\right)} \quad (2.6)$$

and amplitude (A_n) of the pulsed laser is:

$$A_n = \frac{(\gamma-1)\, L\, f_n\, P_n\, (r_m)\alpha\, E}{V} \quad (2.7)$$

Where f_n is the overlap integral which describes the effect of overlapping between the pressure distribution of the n^{th} acoustic resonance frequency and the propagating laser beam divided by the normalized value of the n^{th} eigen mode as:

$$f_n = \frac{\int H(r)P_n(r)dv}{\int Pn^2(r)dv} \quad (2.8)$$

The generated acoustic resonant modes inside the cylindrical cells can also be expressed as:

$$F_{mnq} = \frac{c}{2}\left(\left(\frac{\propto_{mn}}{R}\right)^2 + \left(\frac{q}{l}\right)^2\right)^{\frac{1}{2}} \quad (2.9)$$

Where c is the sound velocity, a_{mn} is the nth zero of the derivative of the m^{th} Bessel function at $r = R$ divided by π, where R and l represent the radius and the length of the cylinder, respectively. The normal modes are separated into longitudinal (q), radial (n) and azimuthal (m) modes. For pure longitudinal modes (i.e. q≠0, m=0, n=0), the resonance frequencies can be calculated from equation (2.9) is

$$F_{00q} = \frac{c}{2}\left(\frac{q}{l}\right) \quad (2.10)$$

The eigenmode function as described in equation (2.5) is:

$$P_n(r) = P_{00q}(z) = \cos(K_z z) \quad (2.11)$$

In the radial mode and azimuthal modes the indices q = 0 and the resonance frequencies is calculated by using

$$F_{mn0} = \frac{c}{2}\left(\frac{\propto_{mn}}{R}\right) \quad (2.12)$$

It is observed that the PA spectra of HEMs recorded using UV-Visible radiations occupy frequency between 0-50 kHz range. The excited acoustic frequencies of the given PA cell of length (L) =7.5 cm, radius (R) = 0.75 cm**.** are listed in Table 2.1. The linear response of the detector microphone lies in between 0-60 kHz frequency range. In PA spectra of compounds, the mixtures of the eigenmodes (i.e. acoustic frequencies) are strongly excited than the individual cavity modes. For this PA cell, the sixth and twelfth longitudinal modes are overlapped with first radial and azimuthal modes respectively. These modes are clearly observed and which are predominant in nature in PA spectra of HEMs compounds recorded at fourth (266 nm) and second (532 nm) harmonic wavelengths of nanoseconds laser pulses [15].

Table 2.1: Calculated frequencies of PA cell (L=7.5 cm, R = 0.75 cm)

Longitudinal (q) Modes f (kHz)	1	2	3	4	5	6	7	8	9	10	11
	2.28	4.57	6.86	9.14	11.43	13.72	16.00	18.29	20.58	22.86	25.15
(q) f (kHz)	12	13	14	15	16	17	18	19	20	21	22
	27.44	29.72	32.01	34.30	36.58	38.87	41.16	43.44	45.73	48.02	50.30

Radial (n) modes f (kHz)	1	2	3	*Azimuthal(m)modes f (kHz)*	1	2
	13.4	22.2	30.5		27.89	38.8

2.1.3. PA experimental setup

The thermal PA spectra of 1,2,3-triazoles and 1,2,4-triazoles reported in chapter-3,4 and 5 were recorded using a PA cell made of stainless steel with internal diameter of 1.5 cm and length of 7.5 cm.

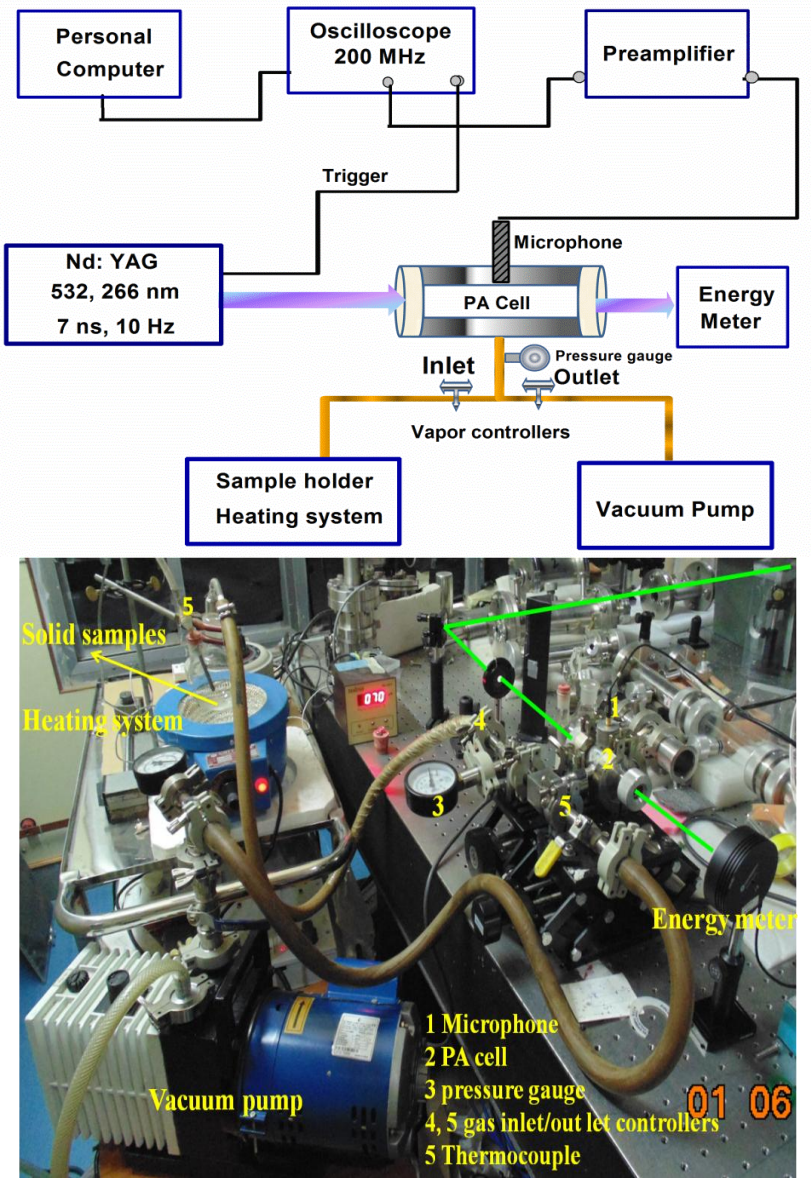

Figure 2.2: Experimental setup.

Fig. 2.2 (a) shows the experimental design used in laboratory and Fig. 2.2(b) is the image of the actual set up. A Q-switched Nd: YAG laser (Model Spit, Germany) of second and fourth harmonic wavelengths i.e. 532 nm, 266 nm, respectively of pulse duration 7 ns and repetition rate 10 Hz were used to excite the vapor of the compounds in a cylindrical PA cavity. The laser beam diameter is adjusted to 6 mm using aperture and allowed to pass through the centre of the PA cavity. The generated PA signal was detected by a pre-polarized microphone of responsivity 50 mV/Pa (BSWA, China) and 0-60 kHz frequency range, which was housed in the centre of a PA cell. The output signal of the microphone was fed to the preamplifier coupled to a 200 MHz oscilloscope (Tektronix, U.S.A.). The analysis was carried out using data acquisition program, which was developed using LabView software. The solid compound of small quantity (~ 1 mg) is kept in a specially designed heating system, which facilitates the controlled pyrolysis between 30 and 350 ^{o}C range. The entire system was evacuated up to 10^{-2} Torr using a rotating vacuum pump. The released vapor of the solid energetic material at required temperature was introduced into the PA cell for recording of PA spectrum at desired incident laser energy and data acquisition time. The input/output energies of exciting laser pulses were measured with power meter (EPM2000, Coherent).

2.2. PA spectroscopy of solids

2.2.1. Theory on time-domain PA spectroscopy of solids

Most conventional photoacoustic spectroscopy of solids employs a periodically modulated light source. The theory of photoacoustic effect in solids is well explained using R-G theory [16]. The availability of high-intensity pulsed laser sources of short pulse duration make possible the study of time response of a photoacoustic system in which the solid is excited by a single optical pulse. In photoacoustic spectroscopy of solids, the sample to be studied is placed inside a closed cell containing a gas, such as air, and a sensitive microphone. The sample is then irradiated with required CW/pulsed excitation laser wavelengths; due to absorption, it emits periodic heat flow to the surrounding gas molecules. The analog signal from the microphone is fed to a pre amplifier, whose output is recorded as a function of the incident laser wavelength at required energy and data acquisition time. Mandelis et al. reported the time-domain photoacoustic spectroscopy of solids [17]. The photoacoustic cell excited by a light pulse of short duration leads to the following physical process such as optical, acoustic, and thermal. The geometry of the PA cell can treated as one-dimensional approximation corresponding to the configuration as shown in Fig. 2.3. A solid of thickness l (cm) having an optical absorption coefficient, β (cm^{-1}) is supported on an optically transparent backing. The cell, of length L (cm), contains an optically transparent gas and the light pulse enters the cell through a non-absorbing window. Both the backing and the window are taken

to be thick so that their exterior boundaries are not important. The sample is excited by a light pulse in the form of a Heaviside function of duration τ_p (sec) and an irradiance of I_o(W cm^{-1}).

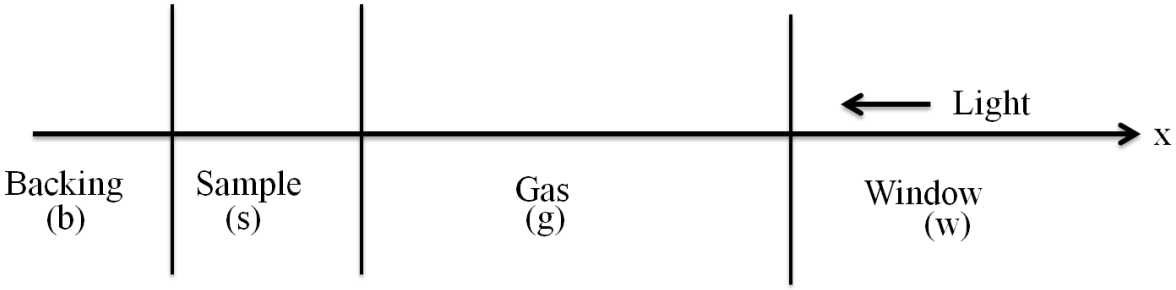

Figure 2.3: Schematic layout of one –dimensional cell geometry [17].

The nonradiative de-excitation processes following light absorption in the solid are taken to be instantaneous. The pressure in the cell (the PA signal) is assumed to be uniform throughout the cell and exhibits no delays due to the finite velocity of sound.

The thermal diffusion equations for each of the regions of the cell can be written, with only that for the solid containing a distributed heat source for the duration of the pulse. For the solid

$$\frac{\partial^2}{\partial x^2} T_s(x,t) - \frac{1}{\alpha_s}\frac{\partial}{\partial t} T_s(x,t) = 0, \qquad \text{for all } t$$

Where for

$$= \frac{-\eta\beta I_o}{K_s}\exp(\beta x), \qquad 0 < t \le \tau_p, \quad -l \le x \le 0$$

$$= 0. \qquad t > \tau_p, \qquad -l \le x \le 0 \tag{2.13}$$

Where $T_s(x,t)$ is the temperature of the solid, η is the efficiency of the nonradiative processes, K_s is the thermal conductivity, and $\alpha_s = K_s/\varrho_s C_s$, is the thermal diffusivity. C_s, and ϱ_s are the specific heat and density of the solid, respectively.

Three similar equations, but with no source term, hold for the other regions of the cell. These have the form

$$\frac{\partial^2}{\partial x^2} T_s(x,t) - \frac{1}{\alpha_s}\frac{\partial}{\partial t} T_s(x,t) = 0, \qquad \text{for all } t$$

Where for

$$\begin{aligned} &x \le -l, && i = b \quad \text{(backing)} \\ &0 \le x \le L, && i = g \quad \text{(gas)} \\ &x \ge L, && i = w \quad \text{(window)} \end{aligned} \tag{2.14}$$

Since only temperature changes due to the light pulse are of interest, equations (2.14) are subject to the initial condition: $T_s(x,0) = 0$ and to the condition of temperature and heat flux continuity at the boundaries between the regions for all times. The time-domain equations (2.14) are solved in Laplace space s by taking their Laplace transforms.

In order to obtain the expression for the photoacoustic response of a cell excited by a light pulse, the time development of the temperature profile in the gas must be converted to an average pressure in the cell. This average pressure is detected by the microphone. Under typical experimental conditions the gas in the cell may be treated as an ideal gas and from the equation of state:

$$p(x,t) = R\,\varrho(x,t)T(x,t), \qquad (2.15)$$

where $\varrho(x,t)$ is the density of the gas in the one-dimensional enclosure and R is the gas constant. The average pressure in the chamber can be computed by taking the spatial average of $p(x,t)$.

2.2.2. Experimental setup for solids

Fig. 2.4 shows the photoacoustic experimental layout for solid samples reported in chapter 6. The samples were placed in an aluminum cubic shaped (5*5*5 cm^3) cell. The PA spectra of wood black, graphite, diesel soot, TNT, including several energetic materials in graphite matrix were recorded using Q-switched Nd: YAG laser (PL-2250 Ekspla, Lithuania) of wavelength 532 nm and 1064 nm wavelengths, 30 ps duration, 10 Hz repetition rate.

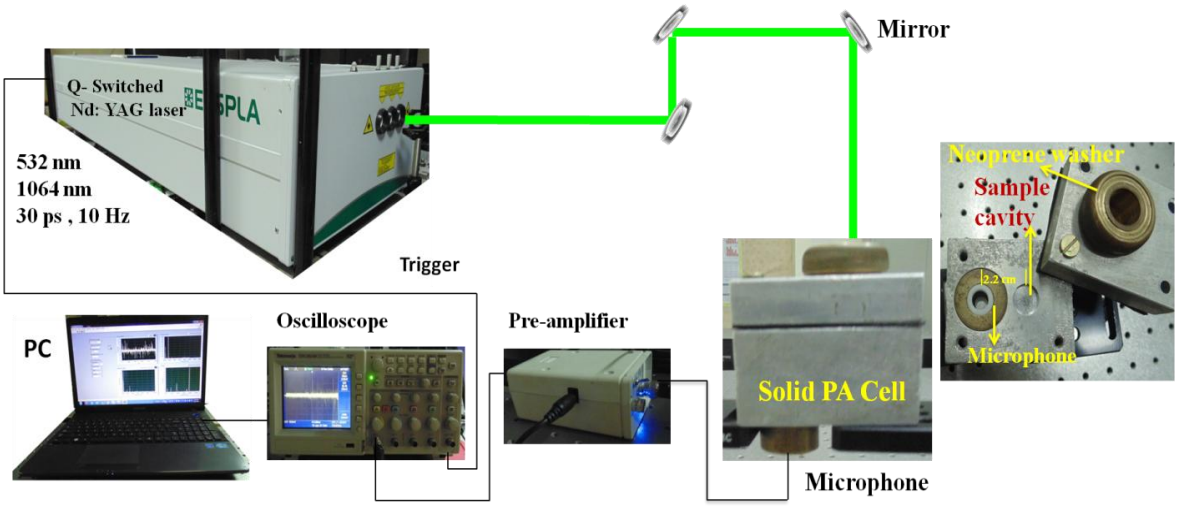

Figure 2.4: Solid PA cell experimental set up.

The generated PA signal recorded using a pre-polarized microphone (BSW, China), which was housed in a Teflon jacket and placed at a distance of 1.0 cm from the sample cavity. Carbon black samples were adjusted in the form of a circular disk of uniform thickness. The distance between the centres of the sample to the microphone head was 2.2 cm. An aluminium plate along with neoprene washer was used to cover the cavity. The plate has one-inch diameter glass window for irradiating the sample kept in the cavity. The pre-amplified PA signal fed to the digital storage oscilloscope (Tektronix, 200 MHz) to record the time domain signal. The output of oscilloscope was connected to the personal computer for recording the fast Fourier transform spectra using indigenously

developed data acquisition program in the LabView software. Weights of the samples were measured using digital balance (Sartorius BSA224S –CW).

2.3. Instruments

2.3.1. TG-DTA Instrument

Thermo gravimetric-differential thermal analysis (TG-DTA) was carried out using TA instrument (Model No. Q600DT). The solid compound was introduced into an alumina crucible and heated between ~30-500 °C range in nitrogen atmosphere (flow rate of 100 cm^3 / min) which works as the purge and protective gas. An empty alumina crucible was used as reference. Non-isothermal TGA runs were conducted between ~30-500 °C range at nitrogen atmosphere with purge rate of 10 °C/min. The thermo gravimetric analysis provides the weight loss in the compounds, where as DTA/ DSC provides the rate of heat flow as a function of temperature. Heat flow curve provide the information about melting, decomposition temperatures of the energetic materials. The compounds follow endothermic at their melting temperature and either exothermic or endothermic at decomposition temperature.

2.3.2. FTIR Instrument

Infrared spectra of reported HEMs compounds were recorded using Perkin-Elmer IR spectrometer in between 400-4000 cm^{-1} range in form of KBr pellets. The working principle of an FT-IR spectrometer is infrared light emitted from a source is directed into an interferometer**,** which modulates the light. After the interferometer, the light passes through the sample and is then focused onto the detector. The signal measured by the detector is called the interferogram, which is obtained from equation (2.13). The FTIR spectrometer operates on a different principle called Fourier transform.

The mathematical expression of Fourier transform can be expressed as

$$F(\omega) = \int_{-\infty}^{+\infty} f(x) e^{i\omega x}\, dx \qquad (2.16)$$

And the inverse Fourier transform is

$$f(x) = \frac{1}{2\pi} \int_{-\infty}^{+\infty} F(\omega) e^{-i\omega x}\, d\omega \qquad (2.17)$$

Where, ω is angular frequency and x is the optical path difference. F(ω) is the spectrum and f(x) is called the interferogram. The total internal energy of a molecule in a first approximation it can be resolved into the sum of rotational, vibrational and electronic energy levels [18]. Infrared spectroscopy is the study of interactions between matter and electromagnetic fields in the IR region.

In this spectral region, the electromagnetic waves mainly couple with the molecular vibrations. An infrared spectrum represents the fingerprint of a sample with absorption peaks, which correspond to the frequencies of vibrations between the bonds of the atoms making up the material. Because each different material is a unique combination of atoms, no two compounds produce exactly same infrared spectrum. Therefore, infrared spectroscopy can result in a positive identification (qualitative analysis) of every different kind of material. In addition, the size of the peaks in the spectrum is a direct indication of the quantity of material present [19].

Some of the major advantages of FTIR over the dispersive technique include: speed sensitivity mechanical simplicity, internally calibrated. These advantages, along with several others, make measurements made by FTIR extremely accurate and reproducible. Thus, it is a very reliable technique for the positive identification of virtually any sample. The sensitivity benefits enable identification of even the smallest of contaminants. This makes FTIR an invaluable tool for quality control or quality assurance applications whether it is batch-to-batch comparisons to quality standards or analysis of an unknown contaminant. In addition, the sensitivity and accuracy of FTIR detectors, along with a wide variety of software algorithms, have dramatically increased the practical use of infrared for quantitative analysis. Thus, the Fourier Transform Infrared (FTIR) technique has brought significant practical advantages to infrared spectroscopy.

2.3.3. Raman Instrument

The Raman spectroscopy measures the vibrational motions of a molecule like the infrared spectroscopy. It is the physical method of observing the vibrations; however, it is different from infrared spectroscopy. This spectroscopy measures the light scattering while infrared spectroscopy is based on absorption of photons. Raman spectra of carbon materials i.e. wood black, graphite powder, diesel soot and energetic compounds such as trinitrotoluene and other HEMs were recorded using λ = 532 nm (model: Witech focus innovations 300 system software, with central wavelength 600 nm). When monochromatic radiation is incident upon a sample then this light will interact with the sample in some fashion. It may be reflected, absorbed or scattered in some manner [20-22]. Raman spectroscopy comprises the family of spectral measurements made on molecular media based on inelastic scattering of monochromatic radiation [23-24]. During this process, energy is exchanged between the photon and the molecule such that the scattered photon is of higher or lower energy than the incident photon. The difference in energy is due to change in the rotational and vibrational energy of the molecule and provides information about the energy levels. The diagram of the Rayleigh and Raman scattering process are shown in Fig. 2.5.

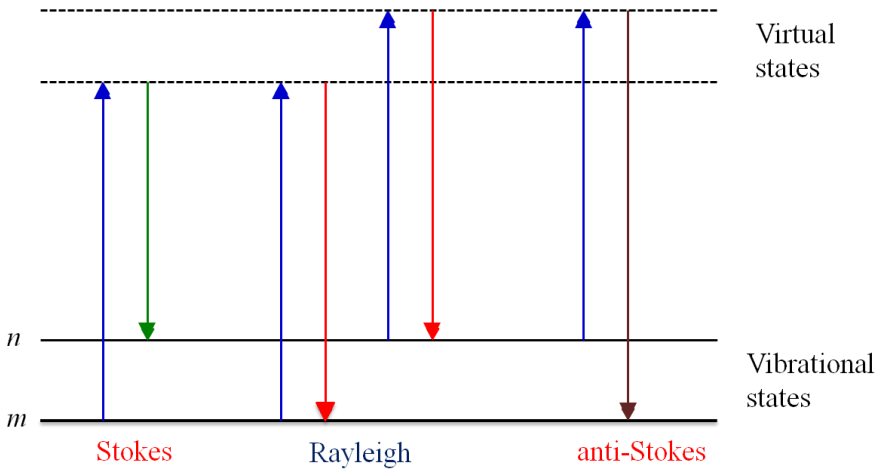

Figure 2.5: diagram of the Rayleigh and Raman Scattering process.

2.3.4. GC-MS instrument

The Gas-chromatic (GC) separates the compounds from each other, while the mass spectrometer helps to identify them based on their fragmentation pattern. Gas Chromatography (GC) is a commonly used analytic technique in many research and industrial laboratories for quality control as well as identification and quantization of compounds in a mixture. GC is also a frequently used technique in many environmental and forensic laboratories because it allows for the detection of very small quantities. Many GC instruments are coupled with a mass spectrometer, which is a very good combination. A broad variety of samples can be analyzed as long as the compounds are sufficiently thermally stable and reasonably volatile. A mobile and a stationary phase are required for this technique. The mobile phase (carrier gas) is comprised of an inert gas i.e., helium, argon, or nitrogen. The stationary phase consists of a packed column in which the packing or solid support itself acts as a stationary phase, or is coated with the liquid stationary phase. Most analytical gas chromatographs use capillary columns, where as the stationary phase coats the walls of a small-diameter tube directly. The separation of compounds is based on the different strengths of interaction of the compounds with the stationary phase. The stronger the interaction, the longer the compound interacts with the stationary phase, and more retention time it takes to migrate through the column. Mass spectrometry is a powerful analytical technique used to quantify known materials, to identify unknown compounds within a sample, and to elucidate the structure and chemical properties of different molecules. The complete process involves the conversion of the sample into gaseous ions, with or without fragmentation, which are then characterized by their mass to charge ratios (m/z) and relative abundances. This technique studies the effect of ionizing energy on molecules. It depends upon chemical reactions in the gas phase in which sample molecules are consumed during the formation of ionic and neutral species. The compounds reported in chapter-4

i.e. S_5 and S_{10} dissolved in chloroform ($CHCl_3$) to record the Gas Chromatography (Agilent7890a) – Mass spectra (AccuTOF GCV): 0.4 μL solution of the compound was injected after making a saturated solution. The temperature of injector, ion source and transfer line were maintained at 250, 200 and 260 °C, respectively.

2.4. Lasers technical details

2.4.1. Q-Switched Nd: YAG nanoseconds laser

The thermal stability and decomposition mechanism of HEMs were studied using a ns pulsed laser 'SpitLight 1200 Nd: YAG Laser System with Seeder' from InnoLas GmbH. A Q-switched Nd:YAG system produced infrared laser pulses of fundamental frequency at 1064 nm wavelength. The second (532 nm), third (354 nm) and fourth (266 nm) harmonics are produced by using nonlinear optical crystals such as KD*P or KTP in harmonic generating assemblies. The Nd: YAG laser rod was pumped by Xenon-filled flash lamps. The ns pulses were produced using Q-switching mechanism, achieved by a pockels cell and a polarizer in the oscillator cavity. The pulses were further amplified in preamplifier and main amplifier sections of the laser. The maximum energy of the laser pulses was ~1300 @ mJ 1.064 μm at the repetition rate of 10 Hz. The harmonic generating assemblies containing KDP crystals were used to produce the SHG at 532 nm wavelength

2.4.2. Q-Switched Nd: YAG picoseconds laser

The time resolved photoacoustic spectra of TNT and other HEMs compounds were recorded using high energy picoseconds Q-Switched Nd:YAG Laser (EKSPLA PL2250) of fundamental (1064 nm) and second harmonic (532 nm) wavelengths of duration 30 ps and 10 Hz repetition rate. It has two amplifiers, one is diode pumped regenerative amplifier other one is flash lamp pumped power amplifier producing upto 100 mJ per pulse at 1064 nm, 30 ps pulse duration and excellent pulse duration stability upto 50 Hz repetition rate.

2.4.3. Femtosecond laser system

Micra: The fs oscillator (Coherent, MICRA 10, Ti: Sapphire laser oscillator system) capable of producing mode-locked fs pulses with bandwidth adjustable from 30 nm to over 100 nm at a repetition rate 76 MHz. The laser operated at a center wavelength of 800 nm and was tunable from 750 nm to 950 nm [6]. The ~15 fs (FWHM) pulses (spectral bandwidth of 55-60 nm, FWHM) with typical energy of ~1 nJ from oscillator was used as a seed for the amplifier pulses from an oscillator.
Regenerative Amplifier: The amplifier (Legend-HE, Coherent) is capable of producing amplified fs pulses with an average energy ~2.5 mJ at 1 kHz repetition rate. The fs amplifier is based on

chirped pulse amplification process. First the pulses were stretched in time (up to ~200 ps) and send to the regenerative amplification stage, where another Ti: Sapphire present in the cavity (pumped by high power Nd: YLF laser with a 1 kHz repetition rate) amplifies them. The pulses go through several round trips (~16) in the cavity to gain the energy. After gaining energy, they are ejected out of the cavity and pass through the compression region. At this stage, the pulse was compressed to ~40 fs duration [7].

TOPAS-C: is a two-stage parametric amplifier of white-light continuum. Its basic configuration comprises of several subunits: pump beam delivery and splitting optics (PO), white-light continuum generator (WLG), a pre-amplifier or first amplification stage (PA1), a signal beam expander-collimator (SE) and a power amplifier or second amplification stage (PA2). These subunits are arranged in a single compact unit. The device employs computer controlled translation and rotation stages that allow for a fast and precise optimization of positions of certain optics when tuning the output wavelength of TOPAS-C. Nonlinear crystals used in TOPAS-C for generation of IR tunable pulses (~ 60 fs duration) as well as crystals for second harmonics or sum frequency generation are fabricated of beta-barium borate (BBO) or lithium triborate (LBO). These crystals are known to be hygroscopic. Crystals used in TOPAS-C have protective coatings.

2.5. Nonlinear frequency mixing processes

Some of the nonlinear frequency mixing optical processes are classified according to generation mechanism of wavelengths such as [25,26]

(1) Second Harmonic Generation (SHG), generation of visible green light with a doubled frequency, two photons are destroyed creating a single photon at two times the frequency,

(2) Sum Frequency Generation (SFG), generation of UV light with a frequency that is the sum of two other pump and signal frequencies

(3) Difference Frequency Generation (DFG), generation of infrared light (idler) with a frequency that is the difference between two other frequencies (i.e. pump and signal).

(4) Optical Parametric Oscillation (OPO) is used for generation of a signal and idler waves in visible and Mid-IR range.

(5) Optical Rectification (OR) generation of quasi-static electric fields which lies in the THz domain.

Second harmonic generation is a special case of SFG, while OPO and OR process are special cases of DFG. The stronger and wide band terahertz radiation can be generated through DFG and OR process. In case of DFG two closer wavelengths of pump and signal are phase matched in suitable nonlinear medium to generated the idler (which is in THz domain). However, in case of OR only

single beam of ultrafast duration is enough to generate the broadband THz radiation. DFG process is limited to some of the crystals only (ex: $ZnGeP_2$, ZnTe, $LiNbO_3$), because limitation of availability of dispersion relations (sellmeir equations) in the terahertz domain to calculate the phase matching angles. We have theoretically predicted the generation of THz radiation from $ZnGeP_2$ using DFG process by calculating phase matching angle, group velocity mismatch, and effective length of crystals depend upon pulse duration. The geometry and energy level diagrams of NL process are described in Fig. 2.6.

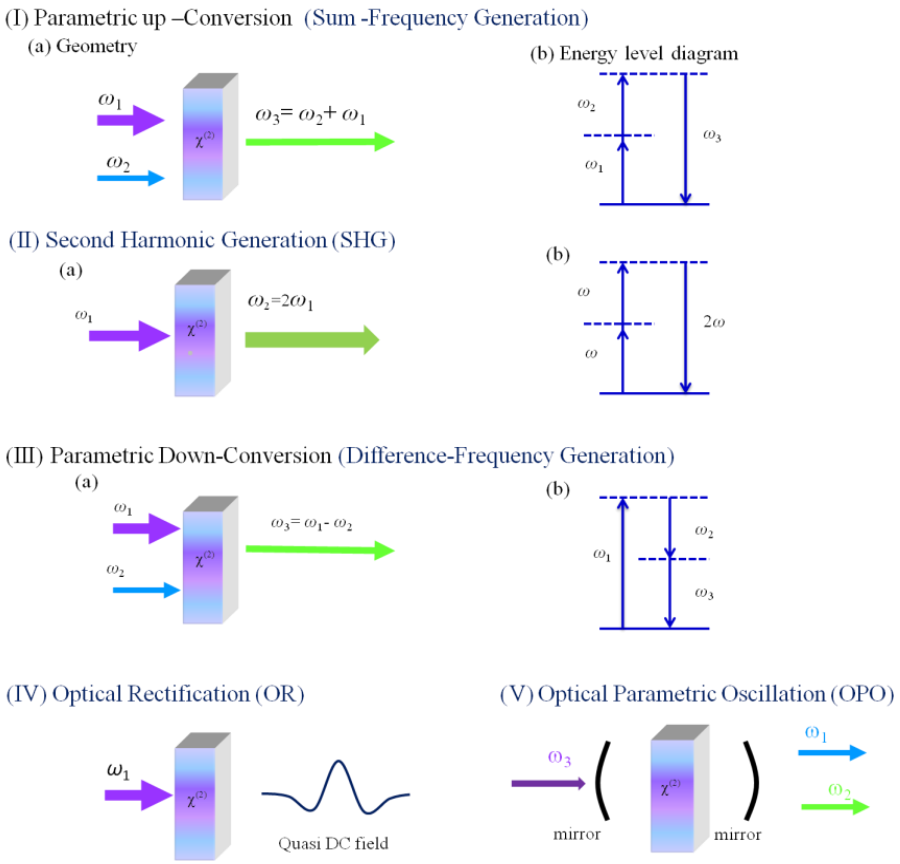

Figure 2.6: Geometry and energy level diagram describing NLO process.

2.5.1. Phase matching conditions for uniaxial crystal and biaxial crystals

Light polarized in the plane containing wave propagation vector *k* and the optic axis is called the extraordinary polarization and experiences a refractive index $n_e(\theta)$ that depends on the angle θ (called phase matching angle) between the optic axis and *k* according to the relation

$$\frac{1}{n_e(\theta)^2} = \frac{cos^2(\theta)}{n_o^2} + \frac{sin^2(\theta)}{n_e^2}. \qquad (2.18)$$

Eq'n (2.18) is used to obtain the proper cut of NLO crystals for all types of phase matching conditions like type I , type IIA, type IIB in different nonlinear wave mixing process listed in Table 2.2 for uniaxial crystals. However, in case of biaxial crystal extraordinary refractive index in along with the principle plane XY, YZ and XZ are defined by

$$n^{e}_{xy}(\lambda_c)=\left(\frac{\cos^2\phi}{n_y^2(\lambda_c)}+\frac{\sin^2\phi}{n_x^2(\lambda_c)}\right)^{-1/2}$$
$$n^{e}_{yz}(\lambda_b)=\left(\frac{\cos^2\theta}{n_y^2(\lambda_b)}+\frac{\sin^2\theta}{n_z^2(\lambda_b)}\right)^{-1/2}$$
$$n^{e}_{xz}(\lambda_c)=\left(\frac{\cos^2\theta}{n_x^2(\lambda_c)}+\frac{\sin^2\theta}{n_z^2(\lambda_c)}\right)^{-1/2} \quad (2.19)$$

Table 2.2 shows the schemes and phase matching conditions for positive and negative uniaxial crystals, while Table 2.3 indicates for biaxial crystals in three different principle planes.

Table 2.2: Phase matching conditions for uniaxial crystals.

Nonlinear process	Scheme	PM condition uniaxial crystals	
		negative	positive
SHG	Type-I	$k_2^e(\theta)=2k_1^o$	$k_2^o=2k_1^e(\theta)$
	Type-II	$k_2^e(\theta)=k_1^e(\theta)+k_1^o$	$k_2^o=k_1^e(\theta)+k_1^o$
SFG	Type-I	$k_3^e(\theta)=k_2^o+k_1^o$	$k_3^o=k_1^e+k_2^e(\theta)$
	Type-II	$k_3^e(\theta)=k_2^e(\theta)+k_1^o$	$k_3^o=k_1^o+k_2^e(\theta)$
DFG	Type-I	$k_3^o=k_2^e(\theta)-k_1^o$	$k_3^e(\theta)=k_2^o-k_1^e(\theta)$
	Type-IIA	$k_3^e(\theta)=k_2^e(\theta)+k_1^o$	$k_3^o=k_2^o-k_1^e(\theta)$
	Type-IIB	$k_3^o=k_2^e(\theta)-k_1^e(\theta)$	$k_3^e(\theta)=k_2^o-k_1^o$
OR	Type-I	$k_3^o=k_2^e(\theta)-k_1^e(\theta)$ $(if\ k_1=k_2)$	$k_3^e(\theta)=k_2^o-k_1^o$ $(if\ k_1=k_2)$

Table 2.3: Phase matching conditions for biaxial crystals.

Principle plane	Type of PM SFG/SHG pump+signal→idler	Type of PM DFG pump-signal→idler	PM condition For SFG /SHG for $n_x<n_y<n_z$
XY θ=90° ‖ to -ve uniaxial	Type I: o+o→e	Type I: e-o→o	$\eta_z(\lambda_b)+\eta_z(\lambda_a)\le\eta_y(\lambda_c)$ $\eta_z(\lambda_b)+\eta_z(\lambda_a)\ge\eta_x(\lambda_c)$
	Type II: o + e →e	Type II: e-o →e	$\eta_z(\lambda_b)+\eta_y(\lambda_a)\le\eta_y(\lambda_c)$ $\eta_z(\lambda_b)+\eta_x(\lambda_a)\ge\eta_x(\lambda_c)$
	Type III: e+ o→e	Type III: e-e→o	$\eta_y(\lambda_b)+\eta_z(\lambda_a)\le\eta_y(\lambda_c)$ $\eta_x(\lambda_b)+\eta_z(\lambda_a)\ge\eta_x(\lambda_c)$
YZ φ=90° ‖ to (+ve) uniaxial	Type I: e+e→o	Type I: o-e→e	$\eta_y(\lambda_b)+\eta_y(\lambda_a)\le\eta_x(\lambda_c)$ $\eta_z(\lambda_b)+\eta_z(\lambda_a)\ge\eta_x(\lambda_c)$
	Type II: e+o→o	Type II: o-e→o	$\eta_y(\lambda_b)+\eta_x(\lambda_a)\le\eta_x(\lambda_c)$ $\eta_z(\lambda_b)+\eta_x(\lambda_a)\ge\eta_x(\lambda_c)$
	Type III o+e→o	Type III o-o→e	$\eta_x(\lambda_b)+\eta_y(\lambda_a)\le\eta_x(\lambda_c)$ $\eta_x(\lambda_b)+\eta_z(\lambda_a)\ge\eta_x(\lambda_c)$
XZ φ=0° θ<Vz (-ve)	Type I :o+o→e	Type I: e-o→o	$\eta_y(\lambda_b)+\eta_y(\lambda_a)\ge\eta_x(\lambda_c)$
	Type II :o+e→e	Type II: e-o →e	$\eta_y(\lambda_b)+\eta_x(\lambda_a)\ge\eta_x(\lambda_c)$
	Type III: e+o→e	Type III: e-e→o	$\eta_x(\lambda_b)+\eta_y(\lambda_a)\ge\eta_x(\lambda_c)$
θ>Vz (+ve)	Type I :e+e→o	Type I: o-e→e	$\eta_z(\lambda_b)+\eta_z(\lambda_a)\ge\eta_y(\lambda_c)$
	Type II: e+o→o	Type II: o-e→o	$\eta_z(\lambda_b)+\eta_y(\lambda_a)\ge\eta_y(\lambda_c)$
	Type III: o+e→o	Type III o-o→e	$\eta_y(\lambda_b)+\eta_z(\lambda_a)\ge\eta_y(\lambda_c)$

Here, η is the ratio of refractive index to the corresponding wavelength of laser pulses i.e. $\eta = n/\lambda$.

2.5.2. Group velocity

Group velocity depends upon the refractive index (n) of medium, and it is defined by

$$v_g = \frac{c}{n\left(1 - \frac{\lambda}{n}\frac{dn}{d\lambda}\right)} \tag{2.20}$$

Where, λ is the wavelength of laser pulses, and n is the refractive index of crystal. c is velocity of light, the denominator of Eq'n (2.20) is nothing but the group refractive index (n_g).

2.5.3. Group velocity mismatch

Group velocity mismatch (GVM) between the generated and pump pulses is given by

$$GVM \equiv \frac{1}{v_g(\lambda_{i,s})} - \frac{1}{v_g(\lambda_p)}. \tag{2.21}$$

Where, λ_p, λ_s, and λ_i are wavelengths of pump, signal, and idler pulses.

2.5.4. Group velocity dispersion and phase delay

The propagation vector (k) can be expanded using Taylor series in the spectral domain up to second order

$$k(\omega) = k(\omega_o) + k'(\omega_o)(\omega - \omega_o) + \frac{1}{2}k''(\omega_o)(\omega - \omega_o). \tag{2.22}$$

Detuning frequency $\Omega = \omega - \omega_o.$ (2.23)

Inverse of the group velocity $1/v_g = k'(\omega_o).$ (2.24)

Group velocity $\beta = k''(\omega_o) = \frac{\partial^2 k}{\partial \omega^2}.$ (2.25)

Phase delay $D = \beta L \Omega.$ (2.26)

L is the length of the crystal

2.5.5. Effective length of the crystal (L_{eff})

Assuming that a very short pulse enters the crystal, the length of the generated pulse, τ will be determined by the difference in light-travel times through the crystal [27]:

$$\tau = L_{eff} \Delta v_g \tag{2.27}$$

τ is the temporal width of the fundamental pulse, Δv_g is the group velocity mismatch, L_{eff} is the effective interaction length. Group velocity mismatch between required pulses can be calculated using Eq'n (2.21).

2.5.6. Walk off length (l_w)

In the optical rectification process the walk off length crystal is defined by

$$l_w = \frac{c\,\tau}{(n_{opt} - n_{THz})}. \qquad (2.28)$$

Where τ is the pulse duration of pump pulse, n_{opt}, n_{THz} are the refractive indices of optical and generated THz pulses respectively.

2.5.7. Coherence length (l_c)

The coherence length for the crystal between optical and THz pulses are given by

$$l_c = \frac{\pi c}{w_{THz}(ng_{opt} - n_{THz})} \qquad \text{or}$$

$$l_c = \frac{\lambda_{THz}}{2\,(ng_{opt} - n_{THz})} \qquad (2.29)$$

Where w_{THz}, is angular frequency THz pulses, ng_{opt} is the group index of pump pulses. The stronger THz wave can be generated if coherence length of the crystal is greater than the length of the crystal (L).

2.6. Conclusions

The theory of photoacoustic spectroscopy and the experimental setups used for the study of thermal stability and decomposition of energetic materials have been presented. The type phase matching conditions for uniaxial and biaxial crystals are provided. The formulae for group velocity mismatch, effective length, coherence length of the crystals are also presented. For the selection of suitable thickness of the crystals to generate the other radiations either second harmonic signal, THz radiation using different nonlinear process, we have to know that sellmeir equations, phase matching type, group velocity mismatch, effective length and coherence lengths. The generation of other wavelengths using sum frequency generation and difference frequency, we can consider the effective length of crystal, which also depends upon pulse duration of pump wavelengths. While in the case of optical rectification process, the coherence length of crystal must be taken in to account, which depends upon angular frequency of generated THz pulses.

References

1. A. Rosencwaig, *Photo Acoustic and Photo Acoustic Spectroscopy* (John Wiley and Sons, New York, 1980).

2. W. M. Sigrist, *In Air Monitoring by Spectroscopic Techniques* (John Wiley & Sons, Inc., New York, 1994).

3. A. Strachan, E. M. Kober, A. C. T. van Duin, J. Oxgaard, and W. A Goddard, J. Chem. Phys. **122**, 54502:1 (2005).

4. J. P. Agrawal, *High Energy Materials: Propellants, Explosives and Pyrotechnics.* (Weinheim: Wiley-VCH., 2010).

5. R. Turcotte, M. Vachon, Q. S. M. Kwok, R. Wang, and D. E. G. Jones, Thermochim. Acta **433**, 105 (2005).

6. HITRAN 2014 Database,online Http//www.hitran.com/.

7. F. Yehya, J. Mod. Phys. **02**, 200 (2011).

8. P. M. Pellegrino, R. G. Polcawich, and S. L. Firebaugh, in *Proc. SPIE* (2004), pp. 42–53.

9. A. Miklós, P. Hess, and Z. Bozóki, Rev. Sci. Instrum. **72**, 1937 (2001).

10. A. . Tam, *Ultra Sensitive Laser Spectroscopy* (Academic Press, New York, 1983).

11. A. Miklós and A. Lörincz, Appl. Phys. B Photophysics Laser Chem. **48**, 213 (1989).

12. A. Thöny and M. W. Sigrist, Infrared Phys. Technol. **36**, 585 (1995).

13. A. Petzold and R. Niessner, Appl. Phys. Lett. **66**, 3 ST (1995).

14. Z. Bozoki, Ar. Mohacsi, G. Szabo, Z. Bor, M. Erdelyi, W. Chen, and F. K. Tittel, Appl. Spectrosc. **56**, 715 (2002).

15. K. S. Rao, A. K. Chaudhary, and F. Yehya, Appl. Phys. B **121**, 375 (2015).

16. A. Rosencwaig, J. Appl. Phys. **47**, 64 (1976).

17. A. Mandelis and B. S. H. Royce, J. Appl. Phys. **50**, (1979).

18. W. D. Perkins, J. Chem. Educ. **63**, A5 (1986).

19. M. A. Ganzoury, N. K. Allam, T. Nicolet, and C. All, Renew. Sustain. Energy Rev. **50**, 1 (2015).

20. A. Smekal, Naturwissenschaften, **11**, 873 (1923).

21. A. H. Compton, Phys. Rev. **21**, 483 (1923).

22. Landsberg and L. Mandelstam, Naturwissenschaften **16**, 557 (1928).

23. C. V Raman and K. S. Krishnan, Nature **121**, 377 (1928).

24. C. V Raman and K. S. Krishnan, Proc. R. Soc. London A Math. Phys. Eng. Sci. **122**, 23 (1929).

25. R. W. Boyd, *Nonlinear Optics, Second Edition* (2002).

26. R. L. Sutherland, D. G. Mclean, and S. Kirkpatrick, *Handbook of Nonlinear Optics*.

27. K. Hussain and P. Kumbhakar, Brazilian J. Phys. **36**, 1281 (2006).

Chapter 3

Benzyl-series 1H-1,2,3-triazoles: Study of thermal decomposition, stability and acoustic fingerprint spectra

Abstract

In this chapter, the study of thermal decomposition, stability and acoustic fingerprints of nitro rich benzyl-series 1H-1,2,3-triazoles is discussed using visible 532 nm and UV 266 nm wavelengths obtained from Q-switched Nd: YAG laser of 7 ns pulse duration and repetition rate of 10 Hz. The thermal stability and decomposition mechanism of these compounds is also verified using thermo gravimetric-differential thermal analysis (TG-DTA) technique. In addition, the thermal stability of the compounds is explained using effect of data acquisition time, incident laser energy and thermal quality factor 'Q' of the PA cell. Further, study is carried out for finding the efficiency of these triazole derivatives as rocket fuels.

A part of the work presented in this chapter has appeared in the following publications:

[1] **K. S. Rao**, F. Yehya, A. K. Chaudhary, A. S. Kumar, and A. K. Sahoo, *J. Anal. Appl. Pyrolysis*, 2014, **109**, 132–139.

[2] **K. S. Rao**, A. K. Chaudhary, F. Yehya, and A. S. Kumar, *Spectrochim. Acta Part A Mol. Biomol. Spectrosc.*, 2015, **147**, 316–323.

[3] **K. S. Rao** and A. K. Chaudhary, *Thermochim. Acta*, 2015, **614**, 149–156.

[4] **K. S. Rao**, A. K. Chaudhary, and F. Yehya, *Appl. Phys. B*, 2015, **121**, 375–384.

3.1. Introduction

The present global trend is to develop some new eco-friendly long chain nitrogen or oxygen rich high energy materials which should possess high detonation performance and heat of formation in combination with good thermal and shock stability. These compounds can be used as efficient rocket fuels and gun propellants [1-5]. Therefore, the study of thermal stability, decomposition and testing the efficiency of rocket fuels becomes important to understand the molecular dynamics of these compounds under different temperatures. Recent advances in spectroscopy techniques such as CW, pulsed laser based interferometer techniques, supersonic jet coupled with time of flight mass spectrometer and ultrafast spectroscopy has opened a new channel for understanding the molecular dynamics of HEMs [6-9]. Some groups studied the thermal decomposition and stability mechanism of HEMs using TG-DSC/DTA coupled with Fourier transform infrared spectroscopy (FTIR) or Gas chromatography–mass spectrometry (GC-MS). They demonstrated that volatile decomposition starts above the melting point [10-16]. All the techniques mentioned above revealed that NO_2 molecule is one of the principal volatile byproduct gasses released by HEMs during the process of thermal decomposition, and it was treated as a thermal marker. We have studied the thermal stability and decomposition mechanisms of HEMs in terms of released quantity of gaseous molecules using pulsed photoacoustic technique by employing visible 532 nm and UV 266 nm wavelengths as an excitation source [17,18]. These laser pulses are second and fourth harmonic wavelengths obtained from Q-switched Nd: YAG laser system of 7 ns duration, 10 Hz repetition rate.

The photoacoustic pyrolysis technique offers main advantages such as high sensitivity, selectivity, compact setup and fast time-response, and is widely recognized for its excellent performance in trace gas detection from ppb to ppt level [19-24]. The NO_2 molecules have strong absorption in visible 532 nm wavelength and is excited to $^2B_2$ state, which is responsible for V-T and V-V relaxations [22,25,26]. Besides, series of some other intermediate byproduct gasses such as N_2O, NO, H_2O, CO, CO_2, H_2 etc. are simultaneously released from HEMs [27,28]. Many of these gaseous molecules have strong absorption in UV 266 nm range [29]. The released vapor of HEMs subsequently follows the process of photodissociation due to $\pi^* \leftarrow n$ electronic transition inside the PA cell when it is excited by UV 266 nm wavelength [30,31]. The nitrogen and oxygen or nitro rich energetic molecules have C-NO_2 or N-NO_2 bonds according to structure of HEMs. These molecules follow the root of cleavage of C-NO_2, N-NO_2 bonds from ring structure inside the heating chamber during the pyrolysis (pyro analysis) process [32,33]. In the next step, released vapor is allowed into the PA cell and it is excited by suitable laser wavelength. The PA spectra were recorded at required temperature and pressure of vapor also selected the suitable incident laser energy and data acquisition time. The Thermal stability, decomposition mechanism and efficiency of compounds as rocket fuel was studied for the

compounds like 1-(2,4-dinitrobenzyl)-1H-1,2,3-triazole (S_1), 1-(3,5-dinitrobenzyl)-1H-1,2,3-triazole (S_2), 1-(2-methoxy-3,5-dinitrobenzyl)-1H-1,2,3-triazole (S_3), 1-(4-methoxy-3,5-dinitrobenzyl)-1H-1,2,3-triazole (S_4), 1-(2,4-dinitrobenzyl)-4-nitro-1H-1,2,3-triazole (S_6). These compounds are synthesized by A. S. Kumar et al [3]. The study reveals that thermal stability of these compounds depends on the positions of principal functional groups (mainly position of -NO_2) present in the compounds. The structures, chemical formula, density (ρ), velocity of detonation (VOD), detonation pressure (DP) and heat of formation (ΔH_f) is shown in Table 3.1. The positions of principle functional groups are clearly observed in the structure of the compounds.

Table 3.1: Crystal structure, formula and energetic properties of the compounds.

Sample	Structure	Formula	ρ gm/cm^3	VOD km/s	DP GPa	ΔH_f kJ/mol
S_1	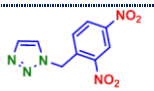	$C_9H_7N_5O_4$	1.53	6.26	15.73	381.9
S_2	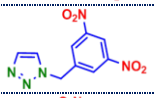	$C_9H_7N_5O_4$	1.53	6.27	15.77	364.8
S_3	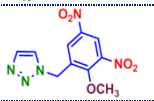	$C_{10}H_9N_5O_5$	1.53	5.90	14.08	197.4
S_4	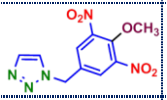	$C_{10}H_9N_5O_5$	1.54	5.92	14.08	232.6
S_6	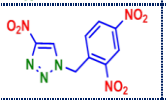	$C_9H_6N_6O_6$	1.64	6.99	20.7	390.3

Compounds S_1 and S_2 are isomers, whereas S_6 is improvised version of S_1 having additional NO_2 group present at triazole moiety. Similarly, S_3 and S_4 are isomers, where the position of methoxy group is different. A. S. Kumar et al. calculated the velocity of detonation and detonation pressure of the samples using Kamlet-Jacobs empirical equations [3]. The detonation performance depends on the crystal density. Of these materials S_6 has high crystal density i.e. 1.64 gm/cm^3 and possesses high performance which is 6.99 km/s. However, PA results compared with TG-DTA technique shows that S_6 is more thermally stable compound. The experimental set up carried out in the laboratory is shown in Fig. 2.2. The PA cell of length (L) =7.5 cm, radius (R) = 0.75 cm is used to record the thermal PA spectra.

3.2. FTIR spectra of S_1, S_2, S_3, S_4 and S_6.

Fig. 3.1(a-e) shows the FTIR spectra of S_1, S_2, S_3, S_4 and S_6 recorded in the form of KBr pellets. It confirms the presence of different functional groups. The strongest absorption peaks of C-O-C, -NO_2, –N=N$^+$=N$^-$, -OCH_3 and C-H are observed between 1300-1000 cm^{-1}, 1550-1300 cm^{-1}, 2400-2000 cm^{-1} and 2850-2810 cm^{-1}, range respectively. The line bond structures of compounds shows in the inset of Fig. 3.1.

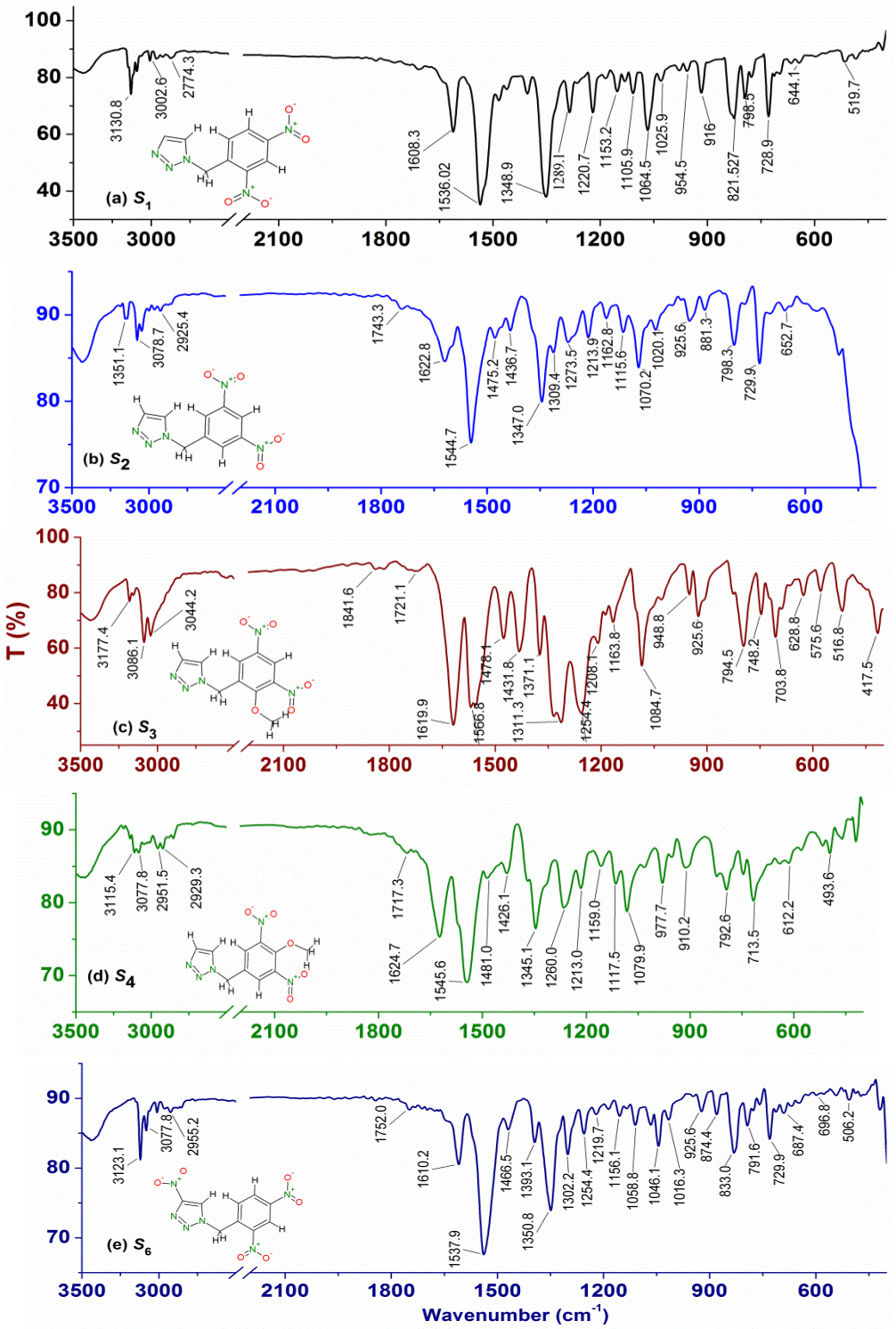

Figure 3.1: FTIR spectra of S_1, S_2, S_3, S_4 and S_6.

3.3. 532 nm based thermal PA spectra of compounds

Fig. 3.2(a-e) and 3.2(f-j) show the thermal PA spectra of S_1, S_2, S_3, S_4 and S_6, recorded at 532 nm and 266 nm wavelengths, respectively. The 532 nm based PA spectra recorded at the input laser energy; E_{in}=5.25 mJ and vapor pressure of 600 Torr. The data acquisition time for recording the PA spectrum for S_1 was selected to be 2.5 ms, which covers up to 50 kHz of acoustic frequency range. In the case of other triazole compounds, the 532 nm based PA spectrum is restricted up to 25 kHz frequency range only. Therefore, it was decided to select data acquisition time of 5 ms to record the thermal PA spectra of other compounds, which also enhance the lifetime of the

microphone sensor. In the case of lower data acquisition time, the frequency conversion time is more. Consequently, the sensor (microphone) is exposed to high temperature for a longer duration off which causes damage to the diaphragm, whereas, in the case of UV 266 nm wavelength the PA spectra occupies the frequency range of 0-50 kHz. The used incident laser energy and data acquisition time for recording of PA spectra of compounds are listed in Table 3.2 for both excitation wavelengths. In this case, lower time scales are suitable for recording the PA spectra. However, we have selected t = 1 ms for recording the PA spectra because the incident laser energy was comparatively low for 266 nm to achieve the higher amplitude of PA signal. In both cases, the temperature based PA spectra are recorded between 30-350 °C range and the highest intensity of PA signal was achieved at either compound melting or decomposition temperatures.

Table 3.2: Incident laser energies and data acquisition time.

Samples	532 nm		266 nm	
	E_{in} (mJ)	t (ms)	E_{in} (mJ)	t (ms)
S_1	5.25	2.5	0.5	1
S_2	5.25	5	0.05	1
S_3	5.25	5	0.5	1
S_4	5.25	5	0.56	5
S_6	5.25	5	0.08	0.25

3.3.1. Thermal PA spectra of S_1

Fig. 3.2(a) shows the thermal PA spectra of S_1 recorded at 532 nm wavelength. It clearly shows that there is not much significant change in the strength (intensity) of PA signal as a function of temperature. However, there is a small change at 145 °C and 225 °C, which are the melting and decomposition temperatures of S_1, respectively. The PA signal curves show that between 30-225 °C, there is a very small percentile change in the quantity of released NO_2. However, there is some significant change is observed in the intensity of acoustic modes due to the release of extra NO_2 gas between 225-350 °C range. In the thermal PA spectra of S_1 the predominant acoustic mode present at 8.95 kHz. Elevation of this mode might be due to the release of free NO_2 gas molecules at a different temperature. However, there are some small peaks of PA spectra are also located at 3.1, 12.7 and 15.4 kHz frequency range for 532 nm wavelength. Finally, the PA signal curves of S_1 confirmed that it is thermally stable in the temperature range of 30-225 °C.

Fig. 3.2(f) depicts the thermal PA spectra of S_1 at 266 nm wavelength. The PA signal has the highest intensity at melting temperature 150 °C (T_m=145 °C) it is attributed to the higher concentration of released vapor at this temperature. However, the decomposition temperature of S_1 is 215 °C but there is no significant change in the PA signal. It means that S_1 does not release any other gas, which has strong absorption in 266 nm range.

3.3.2. Thermal PA spectra of S_2

Fig. 3.2(b) depicts the 532 nm based thermal PA spectra of S_2 recorded between 50-310 °C range. The intensity of the PA signal for different acoustic modes varies as a function of temperature. In this case, the predominant acoustic mode is located at 8.89 kHz and few other modes are present at 3.1, 12.7, and 15.3 kHz. The strength of PA signal varies from 5.71-15.3 mV, between 50-310 °C range. The PA spectra of S_2 have a maximum intensity at 130 °C (T_m) and 310 °C (T_d), and shows that it continuously releases more quantity of NO_2 between 50-130 °C range. However, there is a stiff fall in the PA signal between 130-220 °C and again shows enhancement between 220-310 °C range. The intensity of 8.89 kHz mode at T_m and T_d varies from 12.12 mV to 15.3 mV only.

Fig. 3.2(g) depicts the thermal PA spectra of S_2 recorded between 60 and 330 °C range using 266 nm at 0.05 mJ laser energy. The intensity of PA signal shows saturation behavior between 60 and 312 °C range. The PA signal shows highest intensity at 330 °C, which indicates that at higher temperature, this compound releases molecular vapor if high concentration.

3.3.3. Thermal PA spectra of S_3

Fig. 3.2(c) indicates 532 nm based thermal PA spectra of S_3 recorded in the temperature range of 30-270 °C. The acoustic mode present at 8.88 kHz is one of the predominant modes of S_3. However, the behavior of PA signal, in case of S_3 is very different from other samples. First, it does not have any melting temperature consequently; the sample underwent a phase transition from solid to vapor at 215 °C, which is also the decomposition temperature. The intensity of PA signal is constant at ~6.0 mV up to 160 °C. After that a sharp rise is observed and it reaches up to 12.12 mV at 215 °C. However, beyond 270 °C range i.e. there was no change in the temperature for more than 15 minutes time. Even though the sample was heated continuously, after that vapor was allowed to enter the PA cell. Then a drastic increase in the strength of PA signal was observed, which reaches to maximum value i.e. 275.0 mV along with the presence of some new and strong acoustic modes as shown in the inset of Fig. 3.2(c). The pair of peaks of new acoustic modes is located at 3.08, 3.96, 5.74, 6.38, 9.6, 10.2, 12.92, 14.6, 16.22, 18.42, and 23.4 kHz frequency domain. This phenomenon indicates that S_3 has critical decomposition temperature, which lies beyond 270 °C. The presence of new strong peaks of comparatively lower frequencies as compared to the peaks and shifts in the frequency of acoustic modes towards lower range confirms the formation of new gaseous products [34]. Fig. 3.2(h) shows the PA spectra of S_3 for 266 nm carried out in the span of 70-350 °C. At 209 and 300 °C, higher PA signals are obtained which is similar to the 532 nm based PA spectra, it has highest PA signal at 300 °C. It is 91 °C more than the decomposition temperature. The strength of the PA signal is high due to free release of a high quantity of NO_2 along with other byproduct gases.

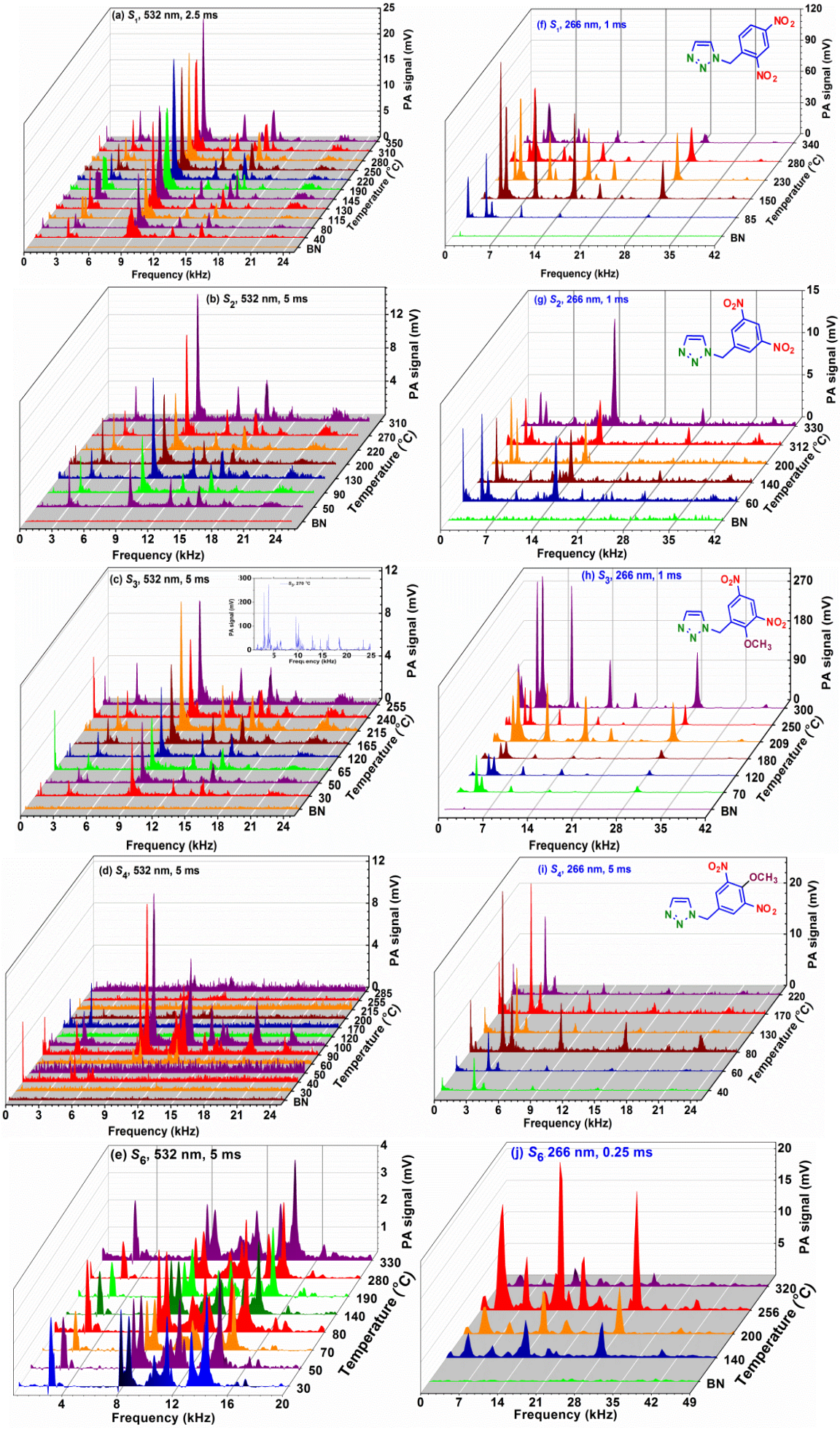

Figure 3.2: Thermal PA spectra of S_1, S_2, S_3, S_4, and S_6 for (a-e) 532 nm and (f-j) 266 nm.

3.3.4. Thermal PA spectra of S_4

Fig. 3.2(d) shows the 532 nm based PA spectra of S_4 recorded between 30-310 °C range. The strength of the PA signal varies between 0.45-14.5 mV range. The PA spectra has a high intensity at 90 °C (T_m) and 100 °C, respectively, rather than decomposition temperature (T_d: 170 °C); at remaining temperatures the strength of PA signal has very small value. The maximum intensity of acoustic mode at T_d was 4.0 mV, which is located at 12.8 kHz. The predominant acoustic mode for S_4 is located at 9.5 kHz at T_m, whereas it is shifted to 12.8 kHz at T_d. The predominant order of acoustic modes varies due to the change in the concentration of released gaseous molecules as a function of vapor temperature.

Fig. 3.2(i) depicts the thermal PA spectra of sample S_4 using UV 266 nm between 40 and 220 °C range. The PA spectra has highest PA signal peak at T_m (80 °C) and T_d (170 °C), respectively. The maximum intensity of PA signal is observed for S_4 at its melting temperature for 532 nm and 266 nm wavelengths. It clearly indicates that S_4 is thermally stable during the entire pyrolysis process.

3.3.5. Thermal PA spectra of S_6

Fig. 3.2(e,j) shows the thermal PA spectra of S_6 produced by excitation wavelength 532 nm and 266 nm, respectively. The acoustic modes in PA spectra of 532 nm forms a cluster between 8-16 kHz frequency range, which is endorsed to NO_2 fragments, released at different temperatures. Moreover, the strength of the PA signal at different temperatures appears to be quite similar with an equal shift in the frequency of acoustic modes. Therefore, it confirms that the generated acoustic signal using 532 nm is contributed by NO_2 only. In addition, other gaseous fragments released during the process of thermal decomposition induce a change in the vapor density of the PA cell. As a result, there is a shift in frequency of the acoustic modes. However, when the compound vapor is irradiated with 266 nm, a strong PA signal was perceived with variable intensity, but there is no shift in the frequency of acoustic modes with respect to temperature. During pyrolysis, the majority of the gaseous products released by S_6 have strong absorption at 266 nm. Therefore, it is considered that the total gas mixture is responsible for the generation of the resultant PA signal.

The predominant order of acoustic modes varies for 532 nm based excited modes, whereas it does not change in 266 nm case on temperature, as shown in Fig. 3.2(e) and Fig. 3.2(j), respectively. This clearly indicates the PA signal generated due to the contribution of NO_2 molecules and total molecule vapor for the excitation 532 nm and 266 nm, respectively. Fig. 3.2(j) shows the PA spectra at 256 °C has high intensity and a maximum number of acoustic modes. Because 256 °C is the T_d of S_6, due to the release of a lot of gaseous molecules as well as these molecules, have strongly absorbed 266 nm.

3.4. Comparative fingerprint spectra

Fig. 3.3 (a-e) and 3.3(f-j) show comparative fingerprint spectra of S_1, S_2, S_3, S_4 and S_6 at t = 1 ms for 532 nm and 266 nm, respectively. The provided spectra in Fig. 3.3 are where the compounds possess highest strength of the PA signal in the region of 30-350 °C. Inset figures show the corresponding time domain signal of the molecules. It is observed that the time domain signal of S_1 is saturated as shown in inset of Fig. 3.3(a). However, its intensity is less than S_2, S_3 and S_4, even the time domain signals of these compounds does not show saturation behavior. The 532 nm based PA spectra occupy the 0-25 kHz range while it is extended to 0-40 kHz range for 266 nm.

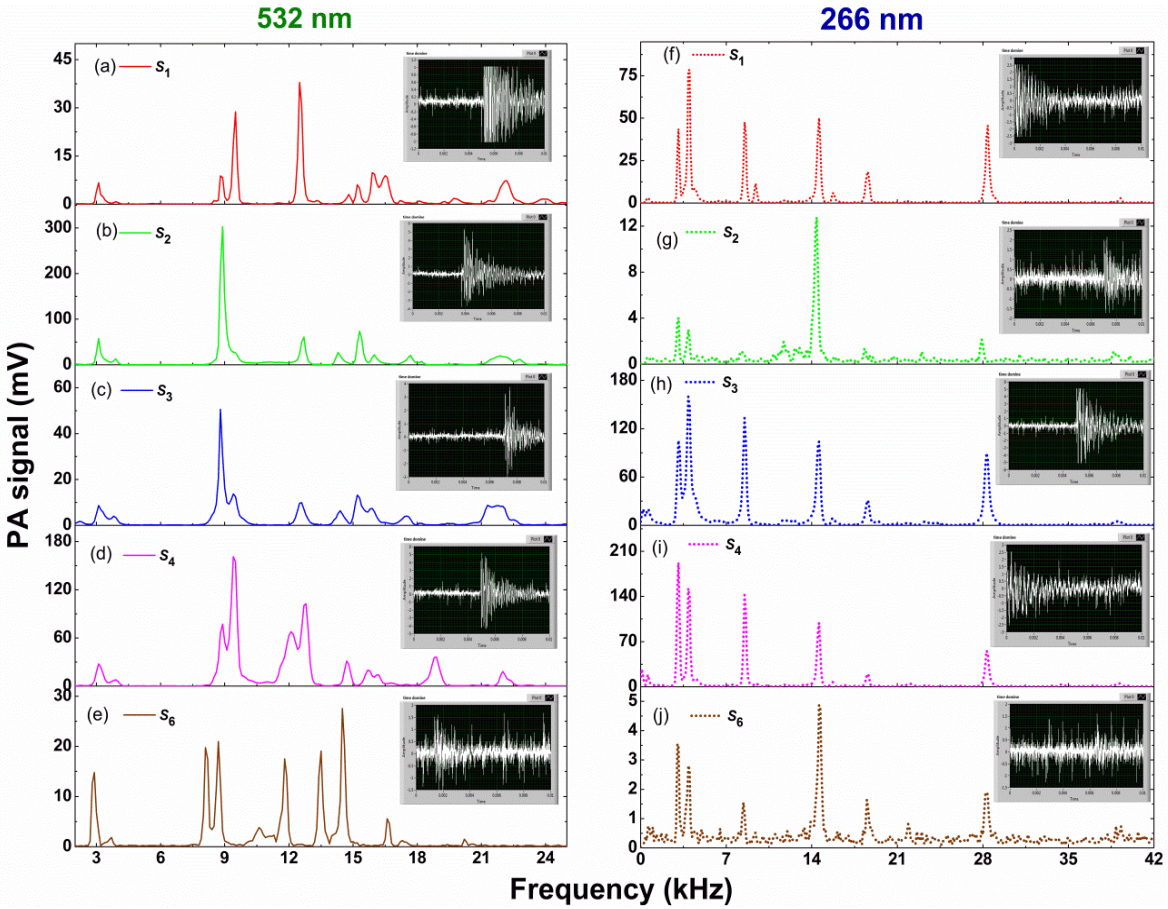

Figure 3.3: Comparative fingerprint spectra of S_1, S_2, S_3, S_4 and S_6 at t = 1 ms, (a-e) 532 nm (f-j) 266 nm.

Table 3.3 shows the excited acoustic modes of the compounds. The highest intensities for S_1, S_2, S_3, S_4, S_6 are obtained at 12.5, 8.9, 8.8, 9.4 and 8.7 kHz, their corresponding intensities are 37.9, 302.8, 50.5, 161.2 and 20.9 mV, respectively. The strength of PA signals from lower to higher order follows $S_6<S_1<S_3<S_4<S_2$. For 266 nm based PA spectra; the acoustic mode frequencies and their corresponding order of predominant modes for each compound are identical between 30 and 350 °C temperature range. The only difference is the variation in the strength of their corresponding PA signal. Moreover, the concentration or density of HEMs vapor mixture varies from sample to sample as a function of temperature, resulting considerable change in the intensity of the PA signal. However, the shift in frequencies of acoustic modes and excitation of different modes are clearly seen in 532 nm based PA spectra. It is observed that

very low incident laser energy is sufficient to generate a significant amount of PA signal at UV 266 nm wavelength. The full width at half maxima of excited acoustic modes for 266 nm is lower than the 532 nm. This is only possible when the total vapor is responsible for the generation of the acoustic signal.

Table 3.3: Excited acoustic modes and corresponding intensities at t = 1 ms (Bold font represent a predominant acoustic mode of the PA cavity).

532 nm	**Acoustic modes in kHz, PA signal (mV)**
S_1	kHz : 3.1 8.8 9.5 **12.5** 14.8 15.2 15.9 16.5 19.8 22.2 23.5 mV : 6.7 8.8 28.7 37.9 3.0 6.1 9.5 8.9 1.73 7.3 1.62
S_2	kHz : 3.1 3.9 **8.9** 12.7 14.3 15.3 16 17.7 21.8 mV : 57.4 12.9 302.8 60.8 26.8 73.3 21.6 20.4 19.0
S_3	kHz : 3.1 **8.8** 9.4 12.6 15.2 15.9 17.5 21.3 mV : 8.6 50.5 13.7 9.8 13.2 7.4 4.1 8.7
S_4	kHz : 3.1 3.9 8.9 **9.4** 12.1 12.8 14.7 15.7 16.2 18.9 22.0 mV : 27.7 7.9 77.3 161.2 67.6 102.6 31.3 20.1 14.0 36.2 18.1
S_6	kHz : 2.9 8.1 **8.7** 10.6 11.8 13.5 14.5 16.6 17.3 20.2 mV : 14.8 19.7 20.9 3.8 17.5 19.1 27.5 5.6 1.23 1.5
266 nm	**Acoustic modes in kHz, PA signal (mV)**
S_1	kHz : 3.1 **4** 8.5 9.4 14.6 15.8 18.6 28.4 mV : 43.5 78.4 47.5 11.5 50.1 5.9 18.4 45.6
S_2	kHz : 3.1 3.9 8.2 11.9 **14.4** 18.3 23.0 27.9 31.0 mV : 4.1 3.0 1.1 1.2 12.7 1.3 1.1 2.2 0.9
S_3	kHz : 3.1 **3.9** 8.5 14.6 15.7 18.6 21.9 28.3 39.1 mV : 105.3 159.4 133.2 103.8 9.3 30.9 4.9 8.9 5.8
S_4	kHz : **3.1** 3.9 8.5 14.6 15.7 18.6 22.0 28.3 34.4 39.1 mV : 192.3 152.3 142.3 99.2 7.5 20.4 5.6 55.8 3.3 5.1
S_6	kHz : 3 3.9 8.4 **14.6** 18.5 21.9 28.3 mV : 3.5 2.8 1.5 4.8 1.6 0.8 1.9

3.5. PA: TG–DTA analysis

Fig. 3.4 show the behavior of acoustic modes for excitation wavelengths 532 nm and 266 nm, and TG-DTA curves with respect to temperature for S_1, S_2, S_3, S_4 and S_6 respectively. Initial weight (I_w) the compounds S_1: 2.235 mg, S_2: 3.643 mg, S_3: 3.391 mg, S_4: 3.912 mg and S_6: 2.379 mg were used to record TG-DTA curves. The heat flow curve of TG-DTA technique provides the T_m and T_d of the compounds, which are incorporated in Table 3.4. The reported benzyl series 1,2,3-triazole derivatives were decomposed in the range of 140-320 °C.

Table 3.4: Comparison of between TG-DTA and PA acoustic results

Sample	TG-DTA		Maximum intensity of PA signal obtained at T (°C), in case of	
	T_m (°C)	T_d (°C)	532 nm	266 nm
S_1	145.0	256.52	145, 225	145
S_2	131.12	312.12	130, 310	200, 330
S_3	209.23		215	209
S_4	90.13	170.0	90,170	80,170
S_6	195.45	256.52	70,200	256

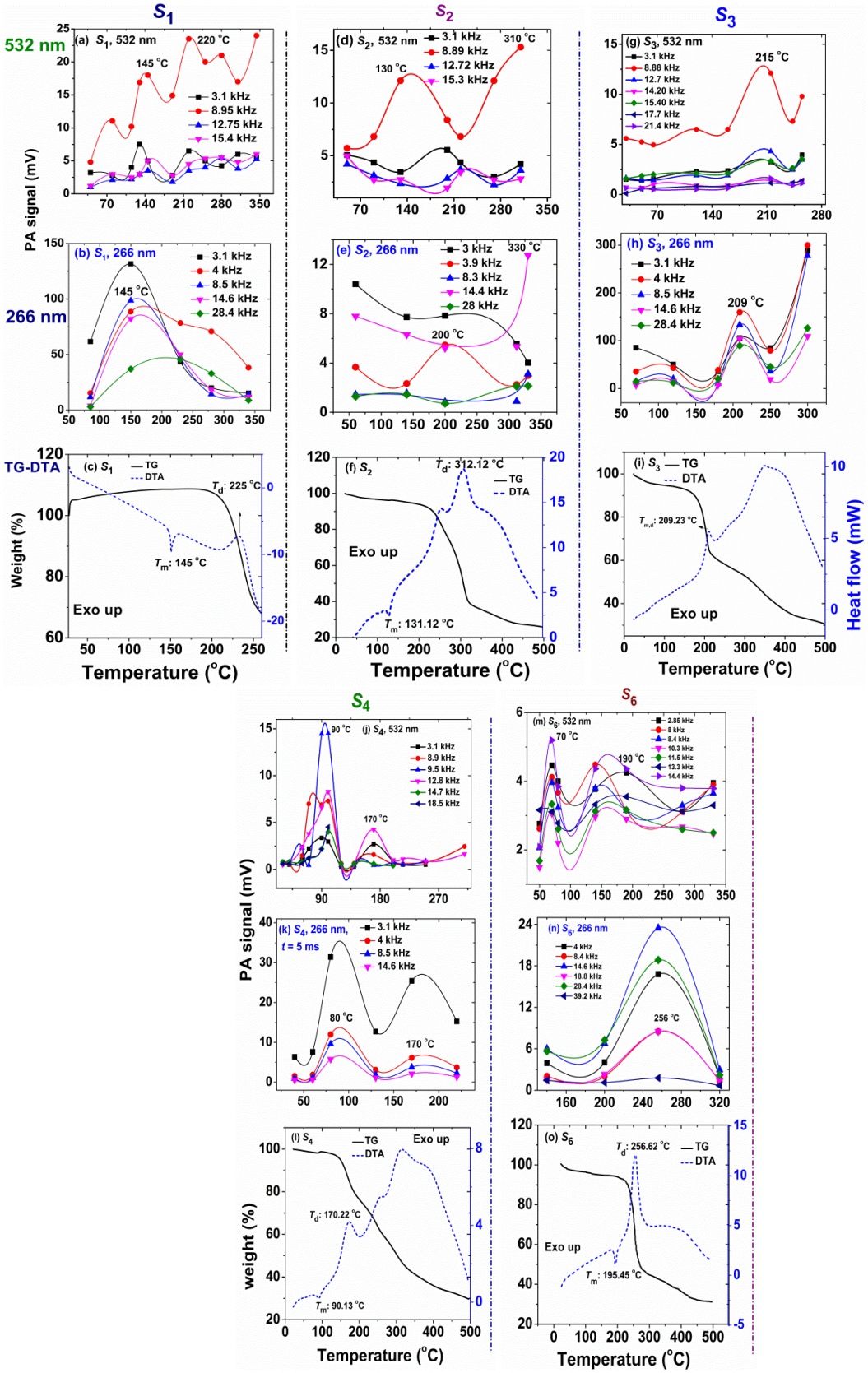

Figure 3.4: Behavior of acoustic modes vs temperature for 532, 266 nm wavelengths and TG-DTA curves for S_1, S_2, S_3, S_4 and S_5.

The compound S_1 has T_m and T_d at 145 °C and 225 °C. The weight loss curve of TG-DTA data as shown in Fig. 3.4(c) clearly indicates that S_1 is thermally stable up to 200 °C, and shows the residual mass percentage 32.88 %. Moreover, the heat flow curve linearly decayed. However, in the case of 532 nm as shown in Fig. 3.4(a), the predominant acoustic mode present at 8.9 kHz

frequency shows periodic variation with respect to temperature. It was observed that S_1 releases less amount of NO_2 at each temperature starting from 60 °C onwards. The periodic variation in the strengths of PA signal demonstrates the rearrangement of molecular groups present in the sample that ultimately control the free release of NO_2 molecules. Whereas, as shown in Fig. 3.4(b) for 266 nm, the strength of PA signal has the highest value at 150 °C (T_m=145 °C) which indicates that the density of released vapor is high at this temperature. After crossing this temperature, the tendency of PA signal curves shows a decrease even at 215 °C which indicates that the concentration of other gaseous molecules are low, and have strong absorption in 266 nm range. Whereas, 532 nm based PA signal curves show periodic increment in their intensities. It means that S_1 released systematically by NO_2 molecules than other molecules.

In case of S_2 for 532 nm, the mode 8.89 kHz has maximum peaks at 130 °C and 310 °C, as shown in Fig. 3.4(d). While, Fig. 3.4(e) shows the highest PA signal obtained at 330 °C for 266 nm. The weight loss curve shows that the compound does not lose much of its weight up to 220 °C, and there was a drastic change in the weight loss (~52 %) between 220-325 °C range. After that, it shows exponential decay behavior and gives 25.92 % of residual weight at 500 °C.

Fig. 3.4(g), 3.4(h) shows for S_3 the maximum intensity peak at 215 °C and 209 °C, respectively; this is the decomposition temperature. In Fig. 3.4 (i) the first kinks of heat flow curve located at 209.23 °C represent the T_d. It shows that S_3 was decomposed without melting. While, weight loss curve clearly demonstrates that the sample lost its weight linearly with respect to a small change in the temperature, which continues up to 170 °C. The sample lost its weight drastically between 170-220 °C range. Thereafter, it showed linear decay between 220-450 °C range and becomes saturated beyond 450 °C, which provides residual mass percentage ~ 30.79%.

Similarly, in case of S_4, 9.5 kHz mode has maximum intensity peaks located at 90, 100 °C, while 12.8 kHz has a maximum peak at 170 °C as shown in Fig. 3.4(j). Whereas Fig. 3.4(k) shows two highest PA signal peaks at T_m (80 °C) and T_d (170 °C). It clearly indicates that S_4 is thermally stable during the process of pyrolysis. The heat flow curve of S_4 as shown in Fig. 3.4(l), other than T_m and T_d it has some exothermic kinks located at 275 and 325 °C that represents the multiple decomposition points. Also, weight loss curve of S_4 loses only 4% of weight up to 140 °C, and beyond this temperature, it is rapidly lost, which finally provides the residual weight percentage ~29.68%.

Due to large variation in the melting (< 91 °C) and decomposition (> 170 °C) temperatures, the compound S_4 can be useful as melt-castable explosive. Fig. 3.4(m) shows for S_6 the excited acoustic modes for 532 nm at different frequencies, which have their initial peak at 80 °C. The PA predominant mode present at 14.6 kHz has two peaks at 80 °C and 140 °C and their corresponding intensities are 5.3, 4.3 mV respectively. These two peaks reveal the information regarding the systematic release of NO_2 from S_6 during decomposition. However, in the region of 200-350 °C, there is no considerable change in the strength of PA signal of acoustic modes

located at 10.3, 11.8 and 13.3 kHz. This clearly indicates that S_6 does not release a more quantity of NO_2 molecules even at T_m and T_d. Therefore, it can be treated as a thermally stable compound up to 350 °C. However, in case of 266 nm for S_6 as shown in Fig. 3.4(n), the highest PA signal strength is obtained at 256 °C (i.e. T_d). Moreover, the strength of the PA signal is almost identical for 140, 200 and 320 °C. It reveals that the density of the released gaseous molecules with respect to temperature remains constant and confirms that S_6 is thermally stable. The weight loss curve shown in Fig. 3.4(o) indicates that the S_6 is thermally stable up to 225 °C. However, there is a rapid change in the percentile of weight and it became 91 to 48 % in the range of 225-274 °C. Measured weight of the residual amount of the compound obtained at 500 °C is 0.7415 mg, which is around 31.17 % of the initial weight.

3.6. Evaluation of stability and efficiency of S_1, S_2, S_3, S_4 and S_6 as rocket fuel

The thermal stability of the compounds and their efficiency as rocket fuels were evaluated based on, ratio of residual weights to the maximum PA signal, positions of principal functional groups, thermal quality factor, data acquisition time and incident laser energy.

3.6.1. Evaluation based on ratio of residual weight to maximum PA signal

The area of each sector of the pie chart of Fig. 3.5(a, b) shows the stability percentage of S_1, S_2, S_3, S_4 and S_6. The stability of these compounds is defined by the ratio of their residual weight (R_w) obtained from weight loss curve and corresponding maximum PA signals obtained at 532 nm, t = 1 ms and 5 ms, respectively. The I_w, R_w and highest strength of PA signals for the compounds are comprised in Table 3.5. The stability criteria in terms of area percentage of each sector in pie charts show the order as S_6>S_1>S_3>S_4>S_2. The intensity order of PA signals also follows the similar order, without considering the residual weights. The stability order of these compounds with 266 nm wavelength follows the similar order as reported using 532 nm. This is explained in detail in the following thermal quality factor section.

Table 3.5: Initial, residual weights and obtained the higher strength of PA signals (at 532 nm) of the samples.

Samples	TG-DTA		PA signal (mV)	
	I_w (mg)	R_w (%)	t = 1 ms	t = 5 ms
S_1	2.235	32.88	37.5	6.5
S_2	3.643	25.92	300	15.3
S_3	3.391	30.99	70	12.15
S_4	3.912	29.68	160	14.52
S_6	2.379	31.17	27.5	4.5

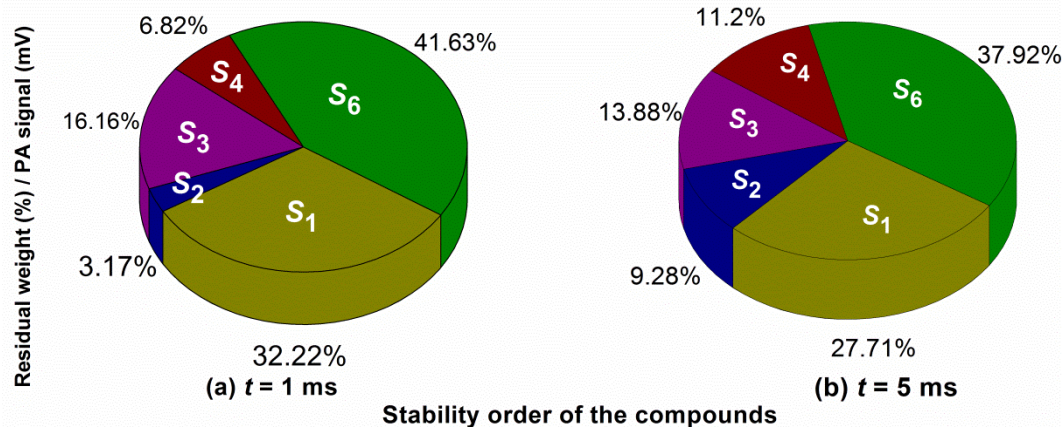

Figure 3.5: Stability order of the compounds at (a) t = 1 ms (b) t = 5 ms for 532 nm.

The stability of these molecules further compared based on the positions of functional groups (-OCH_3 and -NO_2) on the ring structure. For example, it is monitored that S_1 is more stable than S_2, S_3 and S_4. The -NO_2 groups are located at 2- and 3-positions on the benzyl ring whilst, the triazole moiety was inserted at the 1-position of the benzyl ring in the structure of S_1. The structural bonding shows that 1-position of triazole and 2-position -NO_2 are strongly attached to the benzyl ring. However, another -NO_2 which is located at 4-position of a benzyl ring is weakly bonded. As a result, S_1 releases small quantity of -NO_2 at the time of heating which may be attributed to 4-position -NO_2. Next, S_2 is less thermally stable as compared to S_1, S_3 and S_4 owing to their -NO_2 groups which are attached to 3-and 5-position on the benzyl ring and both are equally one position away from the triazole ring. Therefore, while heating, the energy contribution comes from both positions of -NO_2 groups. Consequently, total released amount of NO_2 is much higher than the remaining samples. Similarly, the molecules S_3 and S_4 have similar kind of structure except the position of a methoxy group, which is located at 2- and 4-positions, respectively. However, the positions of -NO_2 groups are same and located at 3- and 5-positions of the benzyl ring. Based on our thermal analysis S_3 appears to be more thermally stable than S_4. In the case of S_4, the -OCH_3 group is present in 4-position of the benzyl ring and equally away from the neighboring -NO_2 groups. While, in the case of S_3, although one -NO_2 group is adjacent to a -OCH_3 group, the another one is located at 5-position which is far away from the methoxy group and liable to release free -NO_2 at the time of heating.

S_6 is the improvised version of S_1 (S_2 is isomer to S_1) that has an additional NO_2 group. As a result, the T_m of S_6 is 50 °C higher than S_1 and S_2. The T_m of S_1, S_2 and S_6 are observed at 145.0, 131.12 and 195.46 °C, respectively. However, the T_d of S_6 lies between S_1 and S_2 i.e. at 256.62 °C. The ratio of the residual mass to the PA signal for S_6, S_1 and S_2 at E_{in} = 5.25 mJ and t = 5 ms are estimated to be 5.88, 5.05 and 1.69 % / mV, respectively. Therefore, from above values, S_6 has a higher ratio that confirms it to be more thermally stable than S_1 and S_2. From the study of PA technique combined with TG-DTA analysis, the efficiency of these compounds as rocket fuels are estimated to be in the order of S_2>S_4>S_3>S_1>S_6.

3.6.2. Evaluation based on Thermal quality factor

The quality factor 'Q' is defined as the ratio of the energy stored in PA cavity to the energy lost by the gas molecules per cycle. The mathematical expression for quality factor is given by

$$Q = \frac{\omega}{\Delta\omega}. \quad (3.1)$$

Where, ω and $\Delta\omega$ are the central frequency and full width at half maximum (FWHM) of the excited acoustic modes.

Fig. 3.6(a-e) and 3.6(f-j) shows the Lorentz fits of one of the sharp, intense peak and for different temperatures with 532 nm and 266 nm, respectively. The approximate central frequency of the acoustic mode is shown on X-axis of the respective figures. Fig. 3.6(a-e) clearly shows that the central frequency of the acoustic modes vary with respect to the temperature while it is a constant in the case of Fig. 3.6(f-j). This is due to the selection of excitation wavelength and is associated with the change in concentration of released NO_2 and other byproducts.

The quality factor 'Q' is directly proportional to ω of the acoustic mode. Therefore, high-frequency acoustic modes of PA spectra give a higher quality factor. In addition, higher data acquisition time leads to high quality factor because the gap between the two adjacent data points of PA spectra is lower (i.e. provides low $\Delta\omega$). From Eq. 3.1 it is clear that lower $\Delta\omega$ value provides high-quality factor. Therefore, for evaluation of quality factor of PA cavity it is necessary to select the fixed data acquisition time and considered the common approximate acoustic mode at different temperatures. Here, t = 5 ms, is fixed in case of 532 nm PA spectra while t = 1 ms used for 266 nm PA spectra except for S_6. We have selected t = 0.5 ms for S_6 to record the thermal PA spectra. Because the resolution of PA spectra is weak at higher data acquisition time, which is due to thermal stability of S_6, and concentration of released molecules are low. The obtained quality factors of the compounds at reported excited modes in the domain of 30-350 °C are comprised in Table 3.6. The highest Q values are obtained either at T_m, T_d or after T_d of the compound. Table 3.6 show in case of 266 nm wavelength the highest quality factors are achieved at compounds melting temperature. However, in the case of 532 nm highest quality factors are obtained at either of T_m, T_d and after crossing the T_d, because the generation of acoustic signal solely depends on NO_2 molecules.

Fig. 3.6(a-e) shows the profile of Lorentz fits of data points of acoustic modes for 532 nm and also highlight the stability criteria of these compounds regarding their FWHM. For example, the value of FWHM for S_1, S_2, S_3, S_4 and S_6 at their respective melting temperature are 308, 183, 203, 202 and 229 Hz, respectively. Therefore, one can easily infer that samples, which have a broader profile, are more thermally stable. For example, the stability profile of compounds are given by $S_6 > S_1 > S_3 > S_4 > S_2$. Hence, S_6 can be treated as more stable in nature, and releases less

amount of NO_2 and is less efficient as a fuel. However, S_2 is comparatively less stable, which releases more amount of NO_2 and is treated as a more efficient rocket fuel.

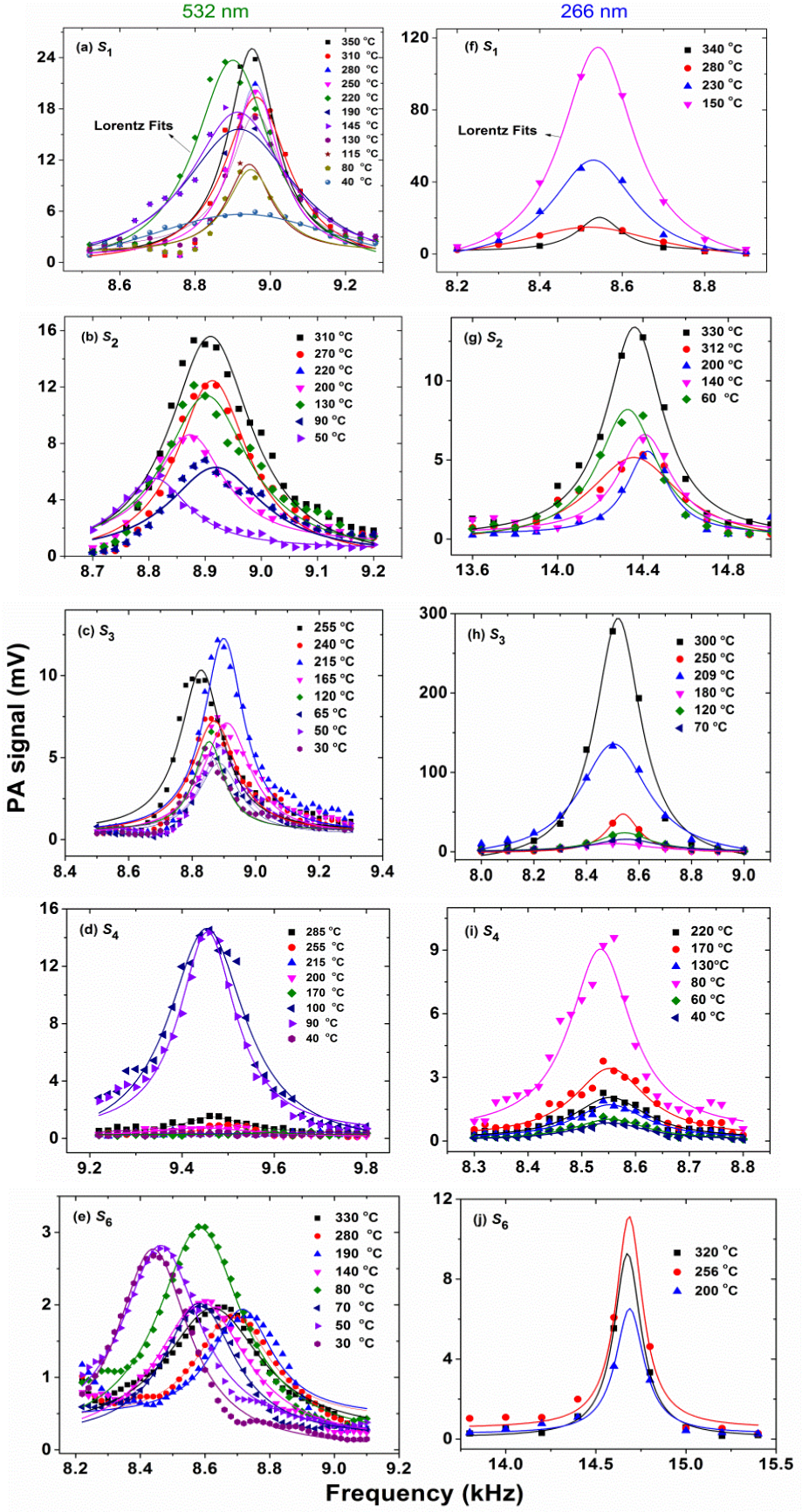

Figure 3.6: Lorentz fit of sharp intense modes at (a - e) 532 nm (f - j) 266 nm for S_1, S_2, S_3, S_4 and S_6, respectively.

Table 3.6: Quality factors of the compounds.

Samples	532 nm	266 nm
S_1	T: 40 80 115 130 145 190 220 250 280 310 350 Q: 12 57 62 53 29 24 36 58 60 43 57	150 230 280 340 66 20 34 39
S_2	T: 50 90 130 200 220 270 310 Q: 59 44 48 59 44 58 50	60 140 200 312 330 43 27 60 47 42
S_3	T: 30 50 65 120 165 215 240 255 Q: 64 61 56 78 49 58 53 55	70 120 180 209 250 300 28 35 24 26 59 40
S_4	T: 40 90 100 170 200 215 255 285 Q: 25 59 55 30 33 24 25 24	40 60 80 130 170 220 52 52 61 52 52 52
S_6	T: 30 50 70 80 140 190 280 330 Q: 31 29 32 22 27 38 33 24	200 256 320 76 82 80

Similarly, Fig. 3.6(f-j) shows the Lorentz fits of data points for 266 nm at t = 1 ms for other compounds while 0.5 ms for S_6. The number of data points for 266 nm is less than 532 nm spectra. Because 532 nm spectra are recorded at higher time scale i.e. at t = 5 ms. The gap between two data points for t = 0.5, 1, 2.5 and 5 ms are 200, 100, 40 and 20 Hz, respectively. The quality factor of S_3 is higher than S_1. It is clearly observed that S_2 has high-quality factor values as compared to S_4. The incident laser energy, which is used for S_1 and S_3 is comparatively higher than S_2, S_4, and S_6. Therefore, it is assumed that S_1 and S_3 show high Q-value as compared to the Q-values of S_2 and S_4. However, it is observed that high Q- values obtained in the case of S_2 and S_4, which implies that S_4 and S_2 are less stable as compared to that of S_1 and S_3. The quality factor for S_6 at 532 nm is comparatively lower than other compounds, while 266 nm values are high, which is due to lower data acquisition time. However, all individual compounds show lower, and constant quality factors as a function of temperature that reveal the thermal stability of the compounds. The stability order of the compounds ascertained by Q-value is of the order of S_6>S_1>S_3>S_4>S_2.

3.6.3. Evaluation based on Data acquisition time

Fig. 3.7(a, b) exhibits a normalized intensity of one of the predominant acoustic modes for the compounds as a function of data acquisition time for 532 nm and 266 nm wavelengths respectively. The excited acoustic modes of the compounds decayed exponentially on data acquisition time. The stability criteria of the compounds can be explained regarding decay time obtained from the first order exponential decay equation i.e.

$$y = y_o + A_1\, e^{\frac{x}{t_1}} \qquad (3.2)$$

Where, y_o, A_1, t_1 (exponetial decay time of acoustic mode with respect to data acquisition time) are the fitting constants which are comprised in the Table 3.7.

The stability of the compounds can also be explained in terms of the constant values i.e. t_1 and A_1 obtained by exponential fit. The values of decay time of the compound follow the order for 532 nm is S_6<S_1<S_3<S_4<S_2, while for 266 nm it is S_6<S_1<S_4<S_3<S_2. Almost in both cases the values of decay times follow a similar order. The highest decay time and lower A_1 values can be

achieved at wherever the response of PA signal is high. This is possible only when the compound releases higher concentration of gaseous molecules. Therefore, that particular compound can be treated as a low thermally stable and highly resourceful as a rocket fuel. Whereas thermally stable compounds have higher values of A_1 and lower decay times. The non-radiative decay time of sample does not vary as a function of t and E_{in}, but these parameters are responsible for the difference in the amplitude of time domain PA signal. As a result, there is a change in the intensity of acoustic modes. Therefore, exponential decay behavior of acoustic modes with respect to the data acquisition time reveals the stability order of the compounds.

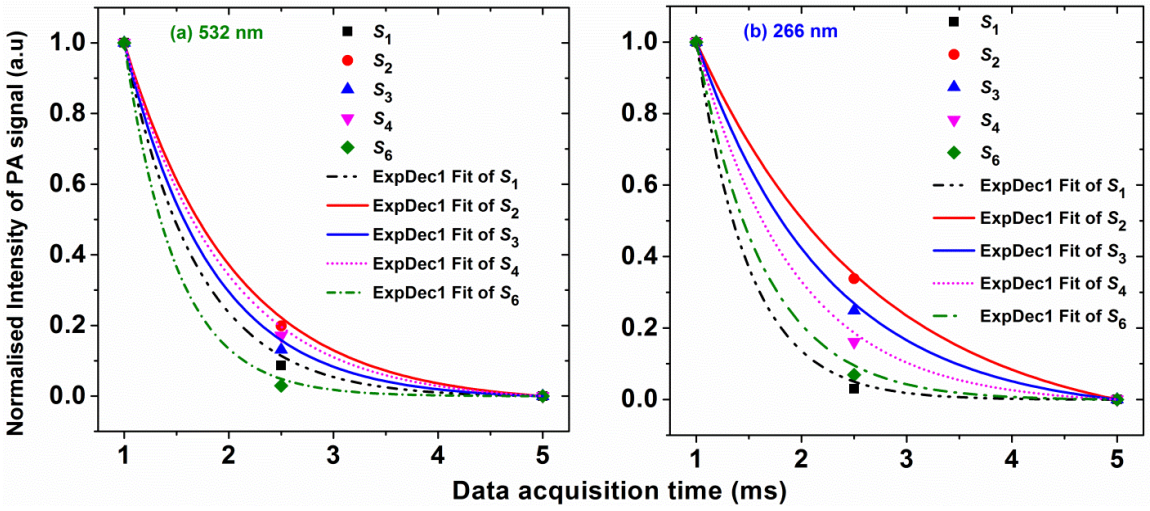

Figure 3.7: Decay behavior of acoustic modes of compounds w.r.to data acquisition time (a) 532 nm (b) 266 nm.

Table 3.7: Fitting constants of y_o, A_1 and t_1.

Samples	532 nm			266 nm		
	y_o	A_1	t_1	y_o	A_1	t_1
S_1	-0.032	4.202	0.698	-0.0003	7.338	0.501
S_2	-0.022	2.651	1.049	-0.1035	1.993	1.690
S_3	-0.082	3.351	0.832	-0.0410	2.336	1.237
S_4	-0.015	2.887	0.956	-0.0133	2.989	0.924
S_6	-0.0003	7.461	0.497	-0.0019	4.750	0.642

3.6.4. Evaluation based on Incident laser energy

The incident laser energy based study at 532 nm for different excited acoustic modes of S_1, S_2, S_3, S_4 and S_6 are carried out at 145, 310, 215, 90 and 190 °C respectively. The selection of these temperatures is based on their either T_m or T_d. The strength of PA signal for S_6 is comparatively lower than the other compounds due to its high thermal stability. Therefore, the behavior of acoustic modes for this compound is shown in the inset of Fig. 3.8. The intensity of acoustic modes for S_2, S_3, S_4 and S_6 possess cubic polynomial growth, whereas S_1 shows linear growth. The compounds S_1, S_3 and S_4, show linearity up to 8.13 mJ laser energy while S_2 shows linearity up to 5.6 mJ only. After that, these compounds show exponential growth with higher incident laser power. However, none of these compounds shows saturation. It confirms that freely

released NO_2 molecules produced by these samples are responsible for higher PA signals. The predominant order of acoustic modes varies with respect to incident laser energy, but the central frequency is unaltered. For S_1 and S_3, at initial energy i.e. 3.82 mJ the intensities are 6.6 mV (at t = 1 ms) and 5.12 mV (t = 5 ms) respectively. However, S_1 has the almost similar intensity to S_3. In spite PA signal of S_1 is recorded at lower data acquisition time. This indicates that S_1 is more stable than S_3. From Fig. 3.8, the intensity of the PA signals obtained as a function of incident laser energy follows $S_2>S_4>S_3>S_1>S_6$. This clearly supports the order of the compounds as rocket fuel.

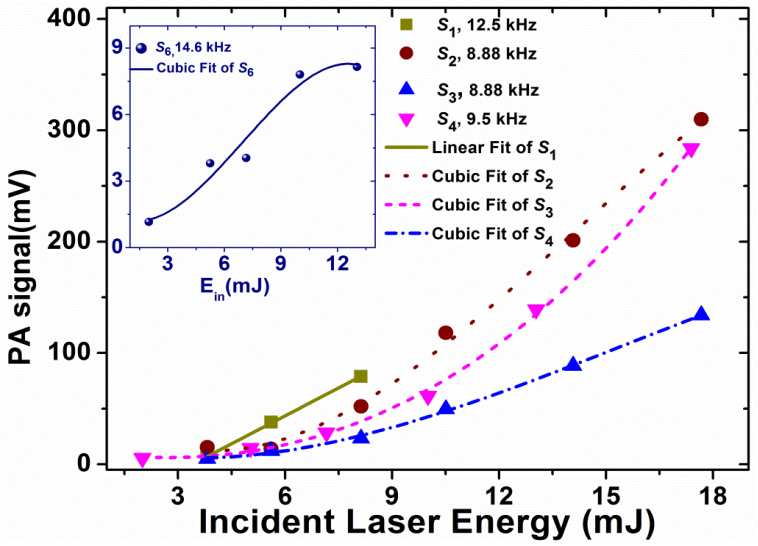

Figure 3.8: PA signal vs incident laser energy at 532 nm wavelength.

3.7. Conclusions

The thermal PA spectra of benzyl series 1H-1,2,3-triazoles were successfully recorded using visible 532 nm and UV 266 nm wavelengths. The results of PA spectra are compared with TG-DTA technique to understand the thermal stability of HEMs. The PA fingerprint spectra of the compound were shown in terms of excited acoustic modes and their corresponding strength of PA signal, which solely depends on the released quantity of gas molecules during pyrolysis between 30-350 °C range. The stability mechanism, and efficiency as a rocket fuel of the compounds have been ascertained based on the studies of PA and TG-DTA techniques, data acquisition time, incident laser energies and thermal quality factor 'Q' of the PA cavity irrespective of the incident laser pulses. The PA and TG-DTA analysis show that stability of the compounds follows the order of $S_6>S_1>S_3>S_4>S_2$. The efficiency of these compounds as a rocket fuel was follow the order of $S_2>S_4>S_3>S_1<S_6$ for efficient rocket fuels. Finally, concluding that the study of energetic materials using pulsed photoacoustic pyrolysis technique with UV 266 nm and visible 532 nm laser wavelengths reveal their thermal stability, decomposition, and efficiency as a rocket fuel.

References:

1. R. S. Damse and A. K. Sikder, J. Hazard. Mater. **166**, 967 (2009).

2. H. S. Jadhav, M. B. Talawar, R. Sivabalan, D. D. Dhavale, S. N. Asthana, and V. N. Krishnamurthy, J. Hazard. Mater. **143**, 192 (2007).

3. A. S. Kumar, V. D. Ghule, S. Subrahmanyam, and A. K. Sahoo, Chemistry **19**, 509 (2013).

4. V. D. Ghule, D. Srinivas, S. Radhakrishnan, P. M. Jadhav, and S. P. Tewari, Struct. Chem. **23**, 749 (2012).

5. N. Kommu, V. D. Ghule, A. S. Kumar, and A. K. Sahoo, Chem. Asian J. **9**, 166 (2014).

6. R. W. Conner and D. D. Dlott, J. Phys. Chem. C **116**, 14737 (2012).

7. J. K. Cooper, C. D. Grant, and J. Z. Zhang, J. Phys. Chem. A **117**, 6043 (2013).

8. F. Muhlberger, Anal. Chem. **73**, 3590 (2001).

9. M. R. Saraji-Bozorgzad, T. Streibel, E. Kaisersberger, T. Denner, and R. Zimmermann, J. Therm. Anal. Calorim. **105**, 691 (2011).

10. R. Turcotte, M. Vachon, Q. S. M. Kwok, R. Wang, and D. E. G. Jones, Thermochim. Acta **433**, 105 (2005).

11. D. E. G. Jones, P. D. Lightfoot, R. C. Fouchard, Q. Kwok, A. M. Turcotte, and W. Ridley, Thermochim. Acta **384**, 57 (2002).

12. M. F. Foltz, C. L. Coon, F. Garcia, and A. L. Nichols III, Propellants, Explos. Pyrotech. **19**, 133 (1994).

13. G. Singh, S. P. Felix, and P. Soni, Thermochim. Acta **426**, 131 (2005).

14. A. Strachan, E. M. Kober, A. C. T. van Duin, J. Oxgaard, and W. A Goddard, J. Chem. Phys. **122**, 54502:1 (2005).

15. D. Chakraborty, R. P. Muller, S. Dasgupta, and Wi. a. Goddard, J. Phys. Chem. A **105**, 1302 (2001).

16. F. Yehya and A. K. Chaudhary, Sensors Actuators B. Chem. **178**, 324 (2013).

17. K. S. Rao, F. Yehya, A. K. Chaudhary, A. S. Kumar, and A. K. Sahoo, J. Anal. Appl. Pyrolysis **109**, 132 (2014).

18. K. S. Rao, A. K. Chaudhary, F. Yehya, and A. S. Kumar, Spectrochim. Acta Part A Mol. Biomol. Spectrosc. **147**, 316 (2015).

19. E. L. Kerr and J. G. Atwood, Appl. Opt. **7**, 915 (1968).

20. L. B. Kreuzer, J. Appl. Phys. **42**, 2934 (1971).

21. L. Jaeglé, C. R. Webster, R. D. May, D. W. Fahey, E. L. Woodbridge, E. R. Keim, R. S. Gao, M. H. Proffitt, R. M. Stimpfle, R. J. Salawitch, S. C. Wofsy, and L. Pfister, Geophys. Res. Lett. **21**, 2555 (1994).

22. M. A. Gondal and M. A. Dastageer, J. Environ. Sci. Health. A. Tox. Hazard. Subst. Environ. Eng. **45**, 1406 (2010).

23. Z. Bozoki, A. Mohacsi, G. Szabo, Z. Bor, M. Erdelyi, W. Chen, and F. K. Tittel, Appl. Spectrosc. **56**, 715 (2002).

24. J. Kalkman and H. W. Van Kesteren, Appl. Phys. B Lasers Opt. **90**, 197 (2008).

25. A. Karbach and P. Hess, J. Chem. Phys. **84**, 2945 (1986).

26. F. Yehya and A. K. Chaudhary, Appl. Phys. B **106**, 953 (2011).

27. J. Akhavan, *Chemistry of Explosives* (The Royal Society of Chemistry, 2004).

28. A. Jai Prakash and H. Robert, *Organic Chemistry of Explosives* (Wiley, 2006).

29. HITRAN 2014 Database,online Http//www.hitran.com/

30. Y. Q. Guo, A Bhattacharya, and E. R. Bernstein, J. Phys. Chem. A **113**, 85 (2009).

31. X. Yue, J. Sun, Q. Wei, H. Yin, and K. Han, Chinese J. Chem. Phys. **20**, 401 (2007).

32. G.B. Manelis, *Thermal Decomposition and Combustion of Explosives and Propellants* (Taylor & Francis, 2003).

33. C. Wu, Proc. Elev. Symp. (1998).

34. F. Yehya and a. K. Chaudhary, Opt. Commun. **312**, 16 (2014).

----------Intentionally left Blank Page----------

Chapter 4

Phenyl-series 1, 2, 3-triazoles: Study of thermal decomposition, stability and absorption cross section

Abstract

In this chapter, the thermal stability, decomposition and acoustic fingerprint spectra for some of the phenyl series 1,2,3-triazoles labeled as S_5, S_{10}, S_8 and bis-series compound S_9 using 532 nm and 266 nm wavelengths have been examined. The study shows that phenyl series triazoles are more thermally stable compared to 1,2,3 benzyl series triazoles. Therefore, phenyl series releases low quantity of gaseous molecules. Therefore, higher incident energy is required for recording the PA spectra as compared to 1,2,3 benzyl series triazoles. Also, ascertained molecular density and absorption cross sections of S_8 and S_9 using 532 nm wavelength. The study also shows that the position of -NO_2 groups decides the thermal stability of isomers (i.e. S_5 and S_{10}).

A part of the work presented in this chapter has appeared in the following publication:

[1] A. K. Chaudhary, **K. S. Rao**, and A. Sudheer Kumar, *Appl. Opt.*, 2016, **55**, 817–824.

[2] **K. S. Rao** and A. K. Chaudhary, *Thermochim. Acta.* 2015, **614**, 149–156.

[3] **K. S. Rao** and A. K. Chaudhary, *Thermochim. Acta.* 2016, **638**,17-24.

4.1. Introduction

Synthesis of new triazole-based energetic materials are one of the focused areas of current research, these materials are widely used for both military and civilian applications due to their thermal stability, high performance [1-5]. The aromatic triazole moiety enhances the thermal stability of a molecule and reduces its sensitivity. Furthermore, the nitro (-NO_2) group significantly contributes towards improving the detonation performance of a molecule. Therefore, the synthesis of novel molecular entities containing the triazole moiety, -NO_2 group attracted to many research groups for their potential use as rocket fuels, gun propellants and civil explosives [6-11]. Several research groups demonstrated various theoretical and experimental techniques to study the thermal decomposition, stability and performance of different types of energetic materials [12-17]. The present study has been focused on the use of the pulsed photoacoustic technique to examine the decomposition, stability, and efficiency of several newly synthesized HEMs using UV-visible radiations as an excitation source [18-21].

The reported compounds such as 1-(2-methoxy,-3,5-dinitrophenyl)-1H-1,2,3-triazole (S_5), 1-(3-methoxy, 2, 6 dinitrophenyl) 1H-1, 2, 3 triazole (S_{10}), 1-(4-nitrophenyl)-1H-1,2,3-triazole (S_8) and 2,6-bis ((4-(nitromethyl)-1H-1,2,3-triazol-1-yl)methyl) pyridine (S_9) were synthesized by Sudheer Kumar et al [22]. Among these, S_5, S_{10}, S_8 are phenyl-series derivatives while S_9 is bis-series compound. However, S_5 and S_{10} are isomers that have same molecular formulae ($C_9H_7N_5O_5$) with different structures i.e. the positions of major functional groups -NO_2 and -OCH_3 are different. The compound S_8 has one -NO_2 group attached at the *para* position of the phenyl ring whereas in the case of S_9; two -NO_2 groups are present at end positions of heterocyclic -CH_2 groups. The structure of the compounds as shown in Table 4.1 clearly shows the positions of major functional groups.

Our study reveals the significant information about release of NO_2 and other of gaseous molecules in multiple steps. It also shows that the phenyl and bis-series triazoles release less quantity of NO_2 compared to the benzyl series. Therefore, higher incident laser energy is required to record thermal PA spectra, which directly indicates that the phenyl series 1H-1,2,3-triazoles are more thermally stable than benzyl series 1H-1,2,3-triazoles. In addition, using Beer's Lamberts law, we have quantified the NO_2 molecules released due to thermal decomposition of S_8 and S_9 in terms of number density and absorption cross sections at different vapor pressures. Study is also carried out to understand the effect of the vapor pressure of released NO_2 at decomposition temperature. The experimental results shows that NO_2 released from S_8 and S_9 have similar transmission, absorption cross section, and number density. It once again confirms that radiative and nonradiative techniques are complimentary to each other.

Table 4.1: Structure, formula and energetic properties of compounds.

Sample	Structure	Formula	ρ gm/cm³	VOD km/s	DP GPa	ΔH_f kJ/mol
S_5	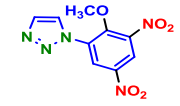	$C_9H_7N_5O_5$	1.57	6.34	16.41	253.5
S_{10}	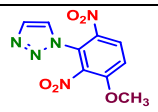	$C_9H_7N_5O_5$	1.58	6.40	16.82	263.1
S_8	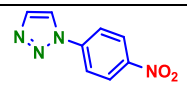	$C_8H_6N_4O_2$	1.48	5.13	10.33	383.2
S_9	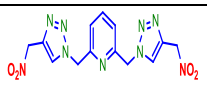	$C_{13}H_{13}N_9O_4$	1.49	5.75	13.05	585.7

4.2. FTIR spectra of compounds

Fig 4.1 shows the IR spectra of compounds confirming the presence of principal functional groups. The inset figures shows the line bond structure of the reported 1,2,3-phenyl and bis-series compounds.

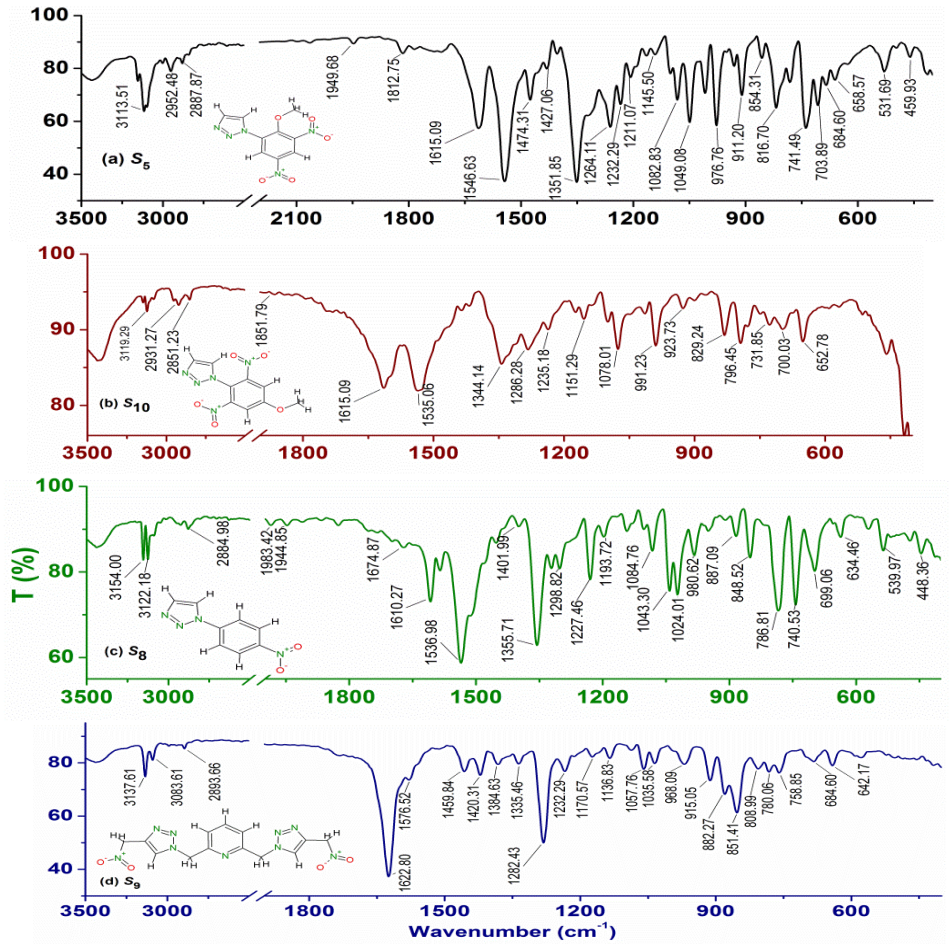

Figure 4.1: FTIR spectra of the compounds (a) S_5 (b) S_{10} (c) S_8 and (d) S_9.

4.3. Study of thermal stability and absorption cross-section of S_8 and S_9 using 532 nm

4.3.1. Temperature based PA spectra S_8 and S_9

The temperature and pressure based PA spectra of compounds were recorded at incident laser energy 7.0 mJ and data acquisition time 0.5 ms. The effect of incident laser energy was studied between 7.0-16.7 mJ range [19]. It reveals that phenyl series 1,2,3-triazoles are more thermally stable than benzyl series 1,2,3-triazoles. Therefore, higher incident laser energy and lower data acquisition times were used to record the PA spectra of phenyl series 1,2,3-triazoles. The initial quantity of S_8: 3.279 mg and S_9: 3.637 mg were used to carry out the TG-DTA analysis.

Fig. 4.2 (a, d) shows the thermal PA spectra for S_8 and S_9. The intensity of acoustic modes in PA spectra illustrates the concentration of thermally released NO_2 gas molecules as a function of vapor temperature. Higher concentration of NO_2 is observed at their melting and decomposition temperatures. The PA cell has multiple eigenmodes; some of these modes are resonant with the acoustic modes produced by the NO_2 molecules due to non-radiative decay. It is observed that 9.0 and 12.6 kHz modes have higher intensities for S_8 and S_9. The excited acoustic modes for thermal PA spectra of S_8 and S_9 recorded at 95 °C and 225 °C are shown in Table 4.2, which have ± 400 Hz deviation on their central frequency.

Table 4.2: Excited acoustic modes *f* (kHz) and corresponding strength of PA signal *I* (mV).

S_8,	*f*:	3.0	3.6	8.2	9.0	11.8	16.2	20.2	23.6	30.6	39.4	
T=95 °C	*I*:	1.43	0.23	1.17	5.54	2.54	1.18	2.98	0.64	0.41	0.5	
S_9,	*f*:	3.0	8.6	12.6	15.0	18.2	22.0	28.6	33.6	37.8	42.6	46.0	50.8
T=225 °C	*I*:	5.19	2.65	10.7	1.58	2.82	6.21	8.1	3.35	2.40	1.22	1.57	1.49

Fig. 4.2(b) shows the behavior of acoustic modes with respect to temperature for S_8. The intensity of acoustic modes shows two strong peaks at 95 and 260 °C, these temperatures are near to the T_m and T_d of S_8, whereas all excited acoustic modes shows similar behavior except variation in their amplitude. In addition there is another set of peaks appeared at 260 °C and 350 °C. However, overall strength of the PA signal of all acoustic modes except the mode at 11.8 kHz remains constant between 95-350 °C range, which confirms that S_8 is thermally stable also confirming the process of thermal decomposition completed in multiple steps. First batch of NO_2 is released at 95 °C, and then later batch releases in two steps at 260 °C and 350 °C. The weight loss curve shown in Fig. 4.2 (c) exhibits that S_8 is thermally stable up to 190 °C. S_8 decomposed from 96 to 1.62 % of initial weight between 190-260 °C range and totally decomposed between 260-500 °C range. In Fig. 4.2(d) the acoustic mode located at 3.0 kHz show linear growth between 70-310 °C range, but

remaining all other modes show similar behavior with respect to temperature. S_9 releases high quantity of NO_2 and other gaseous byproducts after crossing the decomposition temperature. As a result, the PA spectra occupy 0-50 kHz range and have at least two acoustic modes in each 10 kHz range. The acoustic mode present at 12.6 kHz shows saturation behavior between 225-320 °C range. Fig. 4.2 (f) shows the TG-DTA curves S_9, which confirms the process of decomposition start at 100 °C. However, actual process of decomposition starts due to dissociation at 120 °C and reaches to maximum at 150 °C.

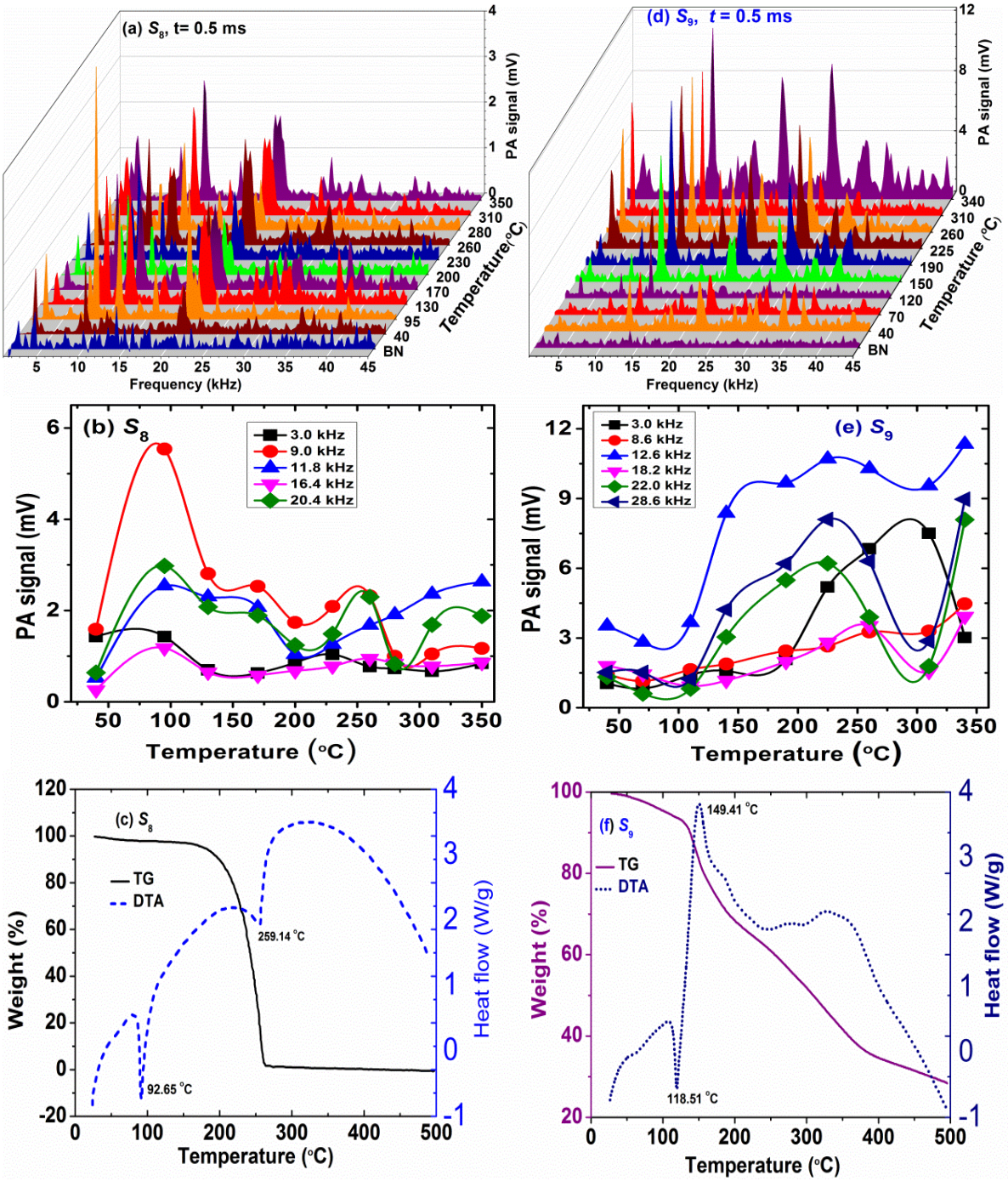

Figure 4.2: Thermal PA spectra, intensities of acoustic modes, TG-DTA curves of S_8 and S_9.

The heat flow curve of S_9 shows that it has T_m and T_d at 118.51 °C and 149.41 °C, respectively. The weight loss curve shows that S_9 decomposes in multiple steps between 100-500 °C range. The thermal zones occupy between the range of 100-250 °C, 250-380 °C, and 380-500 °C. Fig. 4.2(e) shows that S_9 decomposed rapidly between the melting and decomposition temperatures region i.e. 100-250 °C. As a result, the strength of PA signals starts rising between 100-250 °C range. The residual amount of S_9 at 500 °C is obtained around 30 % from original quantity of the compound. Therefore, overall combined results obtained from PA and TG-DTA techniques confirm the thermal stability of S_8 and S_9, which follows the multiple step thermal decomposition.

4.3.2. Pressure based PA spectra of S_8 and S_9

Fig. 4.3(a,b) shows the pressure based PA spectra of S_8 and S_9, respectively. However, the compounds have different structures, but excited acoustic modes occupy almost similar frequencies between 0-25 kHz ranges. The excited acoustic modes for S_8 are located at 2.8, 8.4, 11.4,1 3.8, 15.8, 20.2, 24.4, 26.4, 28.2, 29.8, 32 and 33.4 kHz, while for S_9 are present at 3, 8.6, 11.4, 13.6, 15.6, 18, 19.8, 23, 26, 29.2, 32.2, 45.6 and 52 kHz, at P = 500 Torr.

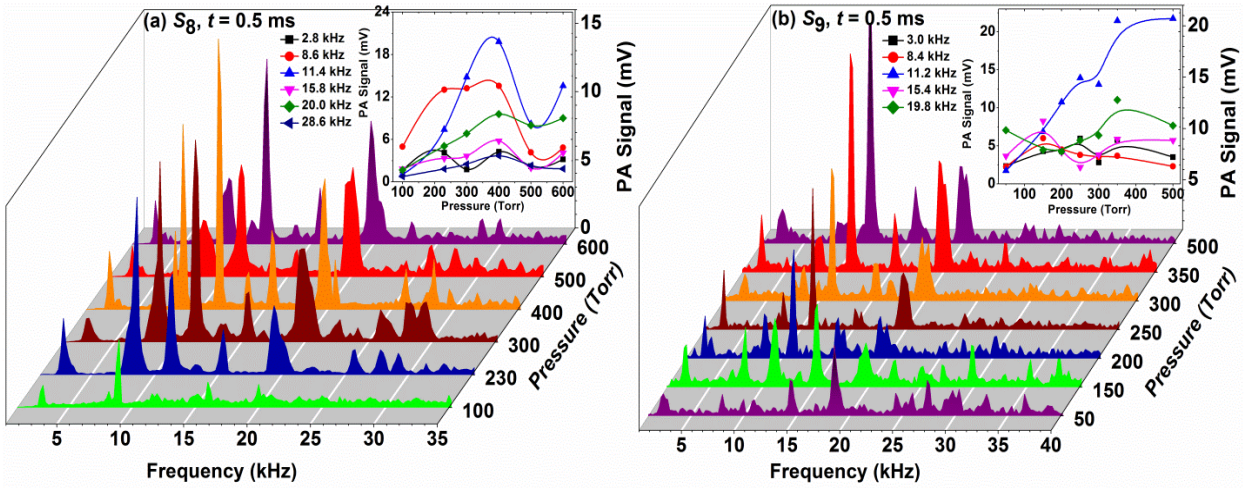

Figure 4.3: Pressure based PA spectra of compounds (a) S_8, (b) S_9.

The compounds S_8 and S_9 are heated up to 200 °C and 150 °C, respectively, at different pressures the released vapor was allowed to enter the PA cell. The variations in the pressure control the concentration of NO_2 and other gaseous molecules at given temperature. Therefore, the strength of PA signal for pressure based PA spectra is higher than the thermal PA spectra of compounds at their melting and decomposition temperatures. The pressure based PA spectra show that the major acoustic modes have identical frequencies; while these were different in the case of thermal PA spectra. The significance of higher order acoustic modes i.e. 25-40 kHz frequency range is present in the temperature based PA spectra of S_9. But, in pressure based PA spectra of S_8 and S_9 for vapor

pressure below 200 Torr possess the acoustic modes between 25-40 kHz range. Whereas, for higher pressures above 250 Torr this frequency range modes disappeared due to the variations in the concentration of NO_2 at higher-pressure range. It indicates that at higher pressures lower order acoustic modes are excited. The insets of Fig. 4.3(a, b) show the behavior of major acoustic modes with respect to vapor pressure. In PA spectra of S_8 and S_9 highest PA response is obtained at 11.4 kHz. It is observed that for both compounds all other excited acoustic modes shows saturation behavior as a function of vapor pressure. It is known that the higher incident laser energy, as well as high vapor pressure saturates the PA signal [23].

4.3.3. Number density and absorption cross section of S_8 and S_9 vapor

The number density (n) and the absorption cross section (σ) of S_8 and S_9 are recorded at 200 °C and 150 °C at different vapor pressure.

Number density (n): The number density at a given temperature and pressure can be easily calculated using the ideal gas law [24,25]

$$n = \frac{P}{(K_B T)P_o} \tag{4.3}$$

Where, P_o (760 Torr) is the atmospheric pressure, T is the temperature of the vapor, K_B is the Boltzmann gas constant 1.38×10^{-23} J/K. Here, the constant $1/K_BT$ is known as Loschmidt number [26]. The values of Loschmidt number at 200 °C (473 K) and 150 °C (423 K) are 1.53×10^{20} cm^{-3} and 1.71×10^{20} cm^{-3} respectively.

***Absorption cross section* (σ):** we have calculated the absorption cross section (σ) of S_8 and S_9, which is a function of transmission (τ) can be determined using Beer-Lambert's law

$$\sigma = \frac{1}{N}\ln(\tau) \tag{4.4}$$

Where $N = n\times L$ is the column density, L is the length of the PA cell, τ is the transmission of the incident laser energy measured at different vapor pressures. Laser energy is measured with energy meter (EPM2000, Coherent).

Fig. 4.4(a) depicts the number density in cm^{-3} and absorption cross section in kilo barn on different pressure. It is clear that the number density is high for lower temperatures at constant pressure. The absorption cross section of vapor decreases with increasing the pressure at constant temperature. However, absorption cross section is directly proportional to the temperature of vapor. Therefore, σ values for S_8 (at 200 °C) are higher than that of S_9 (at 150 °C). The absorption cross section values of S_8 and S_9 lies between 0.5 to 6 kb range for 50-600 Torr pressure range.

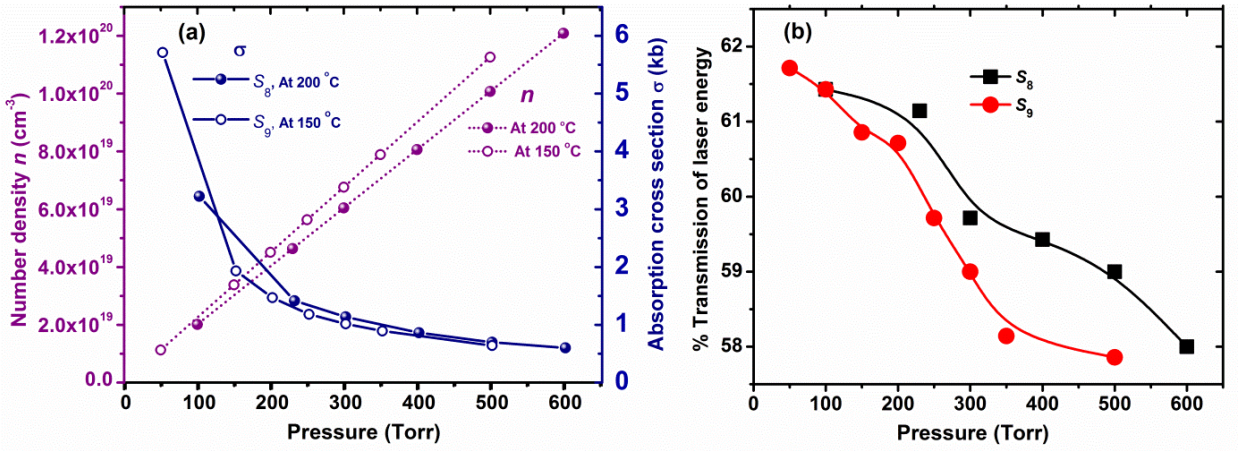

Figure 4.4: (a) Number density and absorption cross section of S_8 and S_9 (b) percentile transmission of laser energy.

Fig. 4.4(b) shows the percentile transmission of incident laser energy for different vapor pressure of S_8 and S_9. The percentile transmission of S_9 is lower than S_8, which clearly indicates that S_9 vapor absorbed more laser energy than S_8 vapor. As a result, S_9 has strong PA signal than S_8. The study of S_8 and S_9 with different vapor temperature, pressure, number density and absorption cross section using 532 nm reveals that S_9 is a more efficient energetic material than S_8. It is ascertained based on the thermally released NO_2 molecules from the compounds during the controlled pyrolysis between 40-350 °C range.

4.4. Study of thermal stability and PA spectra isomers using 532 nm

4.4.1. Thermal PA spectra of S_5 and S_{10}

Fig. 4.5(a) shows the thermal PA spectra of S_5 recorded between 40-350 °C temperature range, at E_{in} = 5.25 mJ and t = 5 ms. The excited acoustic modes are located at 3.04, 3.2, 8.7, 9.2, 11.4, 12.6, 14.4, 15.5, 16, 18.4, and 21.2 kHz, respectively. The strongest mode is present at 8.7 kHz. The acoustic modes of thermal PA spectra have ± 100 Hz variation in their central frequency. The PA spectra clearly show the presence of three sets of paired acoustic peaks between 8-16 kHz frequency range and intensity of acoustic modes at different temperatures is almost similar. This confirms that freely released NO_2 contributes to the generated acoustic signal. However, the presence of other gaseous fragments leads to a change in the central frequency of acoustic modes. The propagation of acoustic signal is affected due to the changes in the released concentration of gaseous molecules.

Fig. 4.5(b) shows the thermal PA spectra of S_{10} using 532 nm wavelength, recorded at t=1 ms, and E_{in}=14.98 mJ between 30 - 340 °C range. PA spectra recorded between 170 - 310 °C range shows frequency shift towards right-hand side to the central frequency of acoustic modes. The predominant acoustic mode of the thermal PA spectrum is present at 3 kHz between 30 - 220 °C

range. However, a shift in the position of 4 kHz mode is observed between 270 - 340 °C range, which is attributed to change in the density of the gaseous mixture and part of the thermal decomposition process. The excited PA modes at 170 °C are present at 3, 8.3, 11.2, 12, 14.4, 15.5, 16.9, and 17.9 kHz and their corresponding strengths are 4.18, 0.56, 0.92, 1, 1.31, 2.17, 0.62 and 1.1 mV. However, at 310 °C, the excited PA modes show some shift in the frequency of their actual position. The new positions occupy at 3.9, 8.2, 9.2, 11.3, 12.5, 14.6, 15.5, and 28.1 kHz and their corresponding strengths are 21.58, 1.24, 2.89, 1.03, 1.18, 0.86, 1.14, and 2.96 mV. An additional PA peak observed at 28.1 kHz between 270 - 310 °C range. The PA spectrum recorded at 170 °C has a predominant acoustic mode at 3 kHz along with some other strong peaks located between 11 - 18 kHz range.

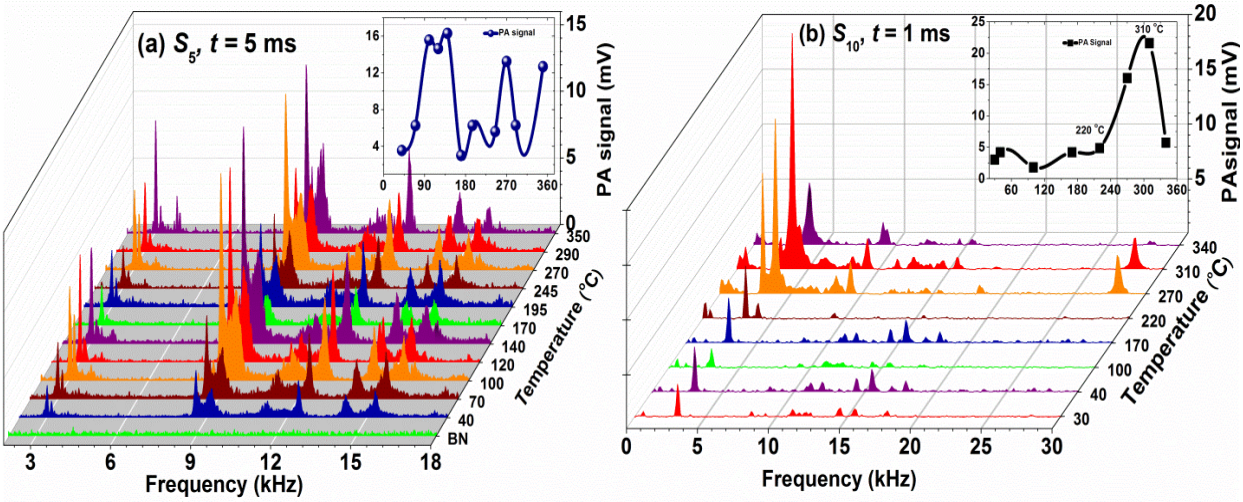

Figure 4.5: thermal PA spectra of (a) S_5 (b) S_{10}.

The shift in frequencies of the PA signal is observed due to the change in the density of gas mixture released from S_{10} at different temperatures. The behavior of thermal PA signal of S_{10} is similar to the benzyl series compound S_3 (1-(2-methoxy-3,5-dinitrobenzyl)-1H-1,2,3-triazole). The minimum incident laser energy i.e. E_{in}=14.98 mJ is required to record the PA signal of S_{10} while for S_3, it was only 3.25 mJ. The strength of PA signal of S_{10} is comparatively lower than the S_3 even at higher incident laser energies. This is attributed to the structure of the compound. In the case of S_3, the triazole and phenyl rings are connected through $–CH_2$ group, while in the case of S_{10} these rings are directly connected to each other. Moreover, these two samples have common $–OCH_3$ functional group in their structures. But for S_3 the $-NO_2$ occupies the 3- and 5- position in the phenyl ring, while, for S_{10} it is located at 2- and 6- positions and equally away from the triazole functional group. Therefore, during the process of thermal decomposition S_{10} releases less quantity of NO_2 and other gaseous mixture. Therefore, it concludes that phenyl series triazole derivatives require high incident laser energy to record the PA signal as compared to the benzyl series. The lower quantity of gaseous

molecules released from phenyl series triazole derivatives indicates that these are thermally more stable than the benzyl series derivatives.

4.4.2. Effect of position of NO_2 groups on thermal stability of isomers S_5 and S_{10}

The phenyl series 1,2,3-triazole compounds such as 1-(2-methoxy,-3,5-dinitrophenyl)-1H-1,2,3-triazole (S_5), 1-(3-methoxy-2,6-dinitrophenyl)-1H-1,2,3-triazole (S_{10}) (shown in inset of Fig. 4.6(a,b)) are isomers, i.e. which have same molecular formulae, but -NO_2 and –OCH_3 groups are positioned at different places on phenyl ring. Therefore, these molecules have different melting and decomposition temperatures. The melting and decomposition temperatures of S_{10} are present at 168.91 and 315.35 °C respectively. Whereas S_5 has, two decomposition temperatures present at 151.10 and 315.35 °C. Here, we have shown the thermal stability and decomposition mechanisms of these compounds depends on positions principal functional groups present in the phenyl rings of 1,2,3-triazoles [27]. The study has been carried out as a function of incident laser energy for understanding the released quantity of gaseous molecules during decomposition process of S_5 and S_{10}.

Fig. 4.6(a) shows the PA spectra of S_5 recorded at 150 °C, t = 5 ms between 3.25-17.5 mJ, range. The acoustic modes at 8.6 and 9.1 kHz possess clear-cut separation with an increase in the incident laser energy i.e. the amplitude of modes increases. However, the acoustic modes present at 12.6 and 14.4 kHz have active profiles without any split. The central frequency of the acoustic modes remains unaltered, but there is a significant change in the order of predominant modes with respect to the incident laser energy. In the case of S_{10}, 14.78 mJ energy was used to record the thermal PA spectra. However, for S_5 5.25 mJ energy is sufficient to record the PA signal. The PA spectra of S_{10} recorded at T_m i.e. at 170 °C and t = 5 ms between 14.78-32.1 mJ, range, which is shown in Fig. 4.6(b). In the case of PA spectra of S_{10}, at E_{in} = 14.78, t = 5 ms, some higher order excited acoustic modes are absent. The acoustic modes show the highest intensity at E_{in} = 32.1 mJ, t = 5 ms. However, Fig. 4.6(a) demonstrates that the lower incident laser energy was sufficient to generate high PA signal from S_5. The strength of PA signal of S_5 is greater than S_{10} even at small incident laser energy. This is due to the location of two nitro groups, which are two positions away from the triazole moiety in the case of S_5. While, for S_{10} they are one position away from triazole moiety. Besides, the methoxy group for S_5 is present at 2nd-position from the phenyl ring, which lies in the middle of the nitro group and triazole moiety, while for S_{10} it is present at 3rd-position of the phenyl ring and completely away from -NO_2 groups to triazole moiety. Therefore, the supplied heat energy initially ceases NO_2 from the phenyl ring, which is followed by the methoxy group, and triazole moiety, respectively. While for S_{10} the NO_2 groups have strong bonding with phenyl ring than triazole moiety.

Consequently, a little quantity of NO_2 is released from the compound during the process of decomposition. However, S_5 releases more quantity of NO_2 molecules than $S_{10.}$ Therefore, at low incident laser energy i.e. 5.25 mJ as well as t = 5 ms is sufficient to record high PA signal from S_5. The present study reveals the efficiency of the isomers (i.e. S_5 and S_{10}) as a rocket fuel (S_5 is efficient rocket fuel than S_{10}). This is ascertained based on the quantity of released NO_2 concerning strength of the PA signal. Therefore, the photoacoustic pyro analysis is treated as one of the potential analytical techniques to study the performance of newly synthesized energetic materials as a rocket fuel.

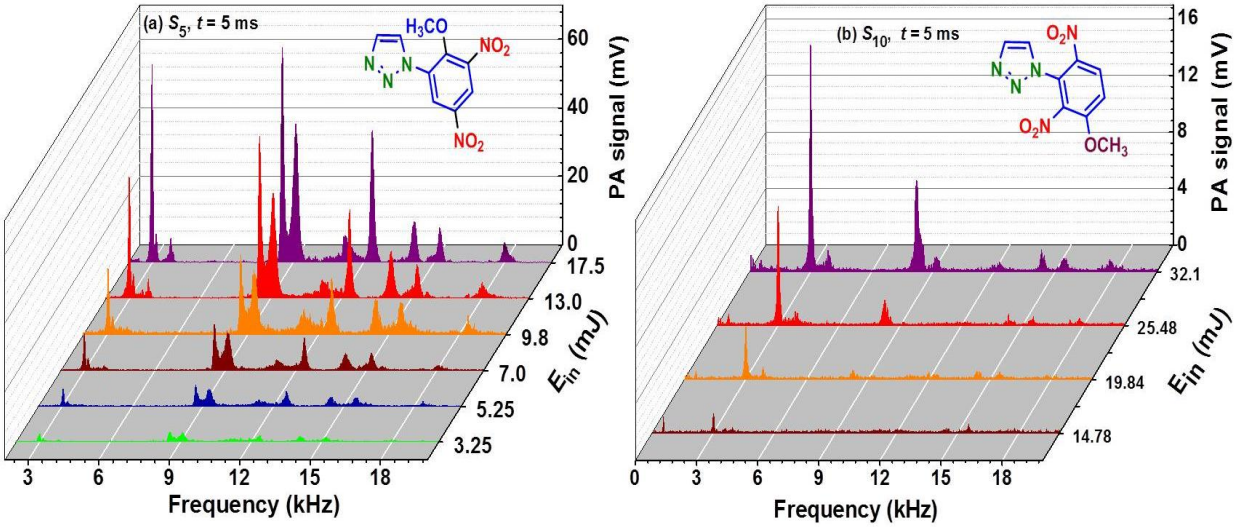

Figure 4.6: PA spectra of compound vs incident laser energy for (a) S_5 (b) S_{10} at t = 5 ms.

4.4.3. GC-MS spectra of S_5 and S_{10}

The Gas chromatography-Mass spectroscopy (GC-MS) is a well-known analytical technique, which is used for solids, liquids and gases. It works on the principle of column separation for which the solid sample is required to be dissolved in a particular solvent. The solid sample heated more than 200 °C introduced to oven along with injector (N_2 or He). Each gas/component has it own retention time. Therefore, based on retention times and column condition we can identify the individual concentrations of released byproducts. The gas chromatic and mass spectra of S_5 and S_{10} are shown in Fig. 4.7 (a,b) and Fig. 4.8 (a,b). GC instrument provided the initial retention time starts above 3.12 min, and MS instrument starts its mass to charge ratio (m/z) value at 40. The retention times of some of the gas components are listed in Table 4.2 [28]. GC spectra show the retention time of some gaseous components such as CO (14.5 min), NO (18.5 min), but not NO_2 peak because it is a volatile component its retention time below 3 min. The NO_2 molecules converted into NO at atmospheric pressure; because of it the significance of NO_2 also not able to quantify with GC instrument. MS spectra confirm that all these molecules occupy their position below 50

(m/z value), whereas for N_2O and CO_2 (m/z= 44) [29]. The m/z values provided in Table 4.2 shows the significance of NO_2, NO, and N_2O have one common m/z value at 30 but the employed instrument begins its value at 40. These spectra were recorded at the temperatures of the injector, ion source and transfer line maintained at 250, 200 and 260 °C respectively.

Table 4.3: Retention times and m/z ratio of some gases [28,29].

Gas	R_t (min)	Gas	m/z
H_2	3.0	H_2O	16 17 18 19 20
N_2	9.5	NO_2	14 16 30 46
O_2	11.3	N_2	10 15 16 28 29 30 31 44 45
CO	14.5	CO	12 16 28 29
NO	18.8	NO	14 15 16 30 31 32
CH_4	25.5	HCN	12 13 14 15 26 27 28 29
CO_2	35.0	CO_2	12 16 22 28 29 44 45 46
N_2O	38.4	CH_2O	12 13 14 15 28 29 30

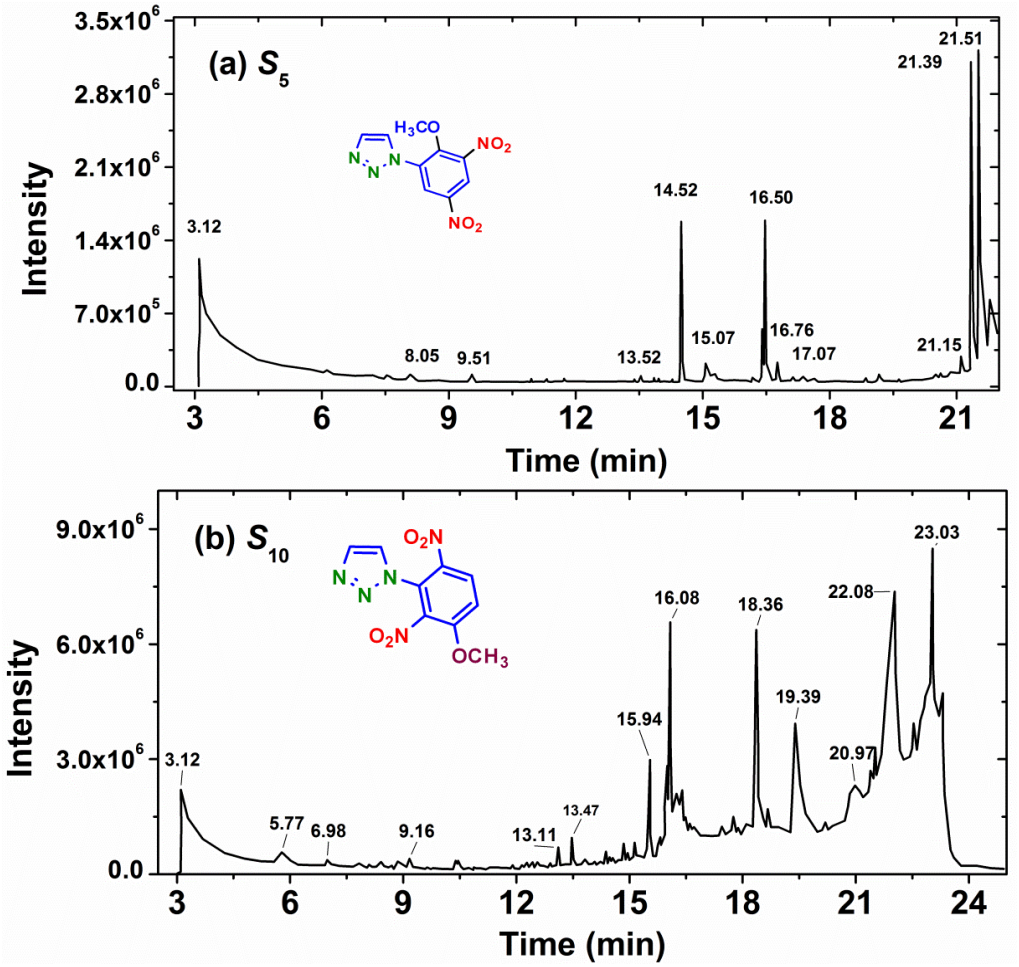

Figure 4.7: Gas chromatic spectra of (a) S_5 (b) S_{10}.

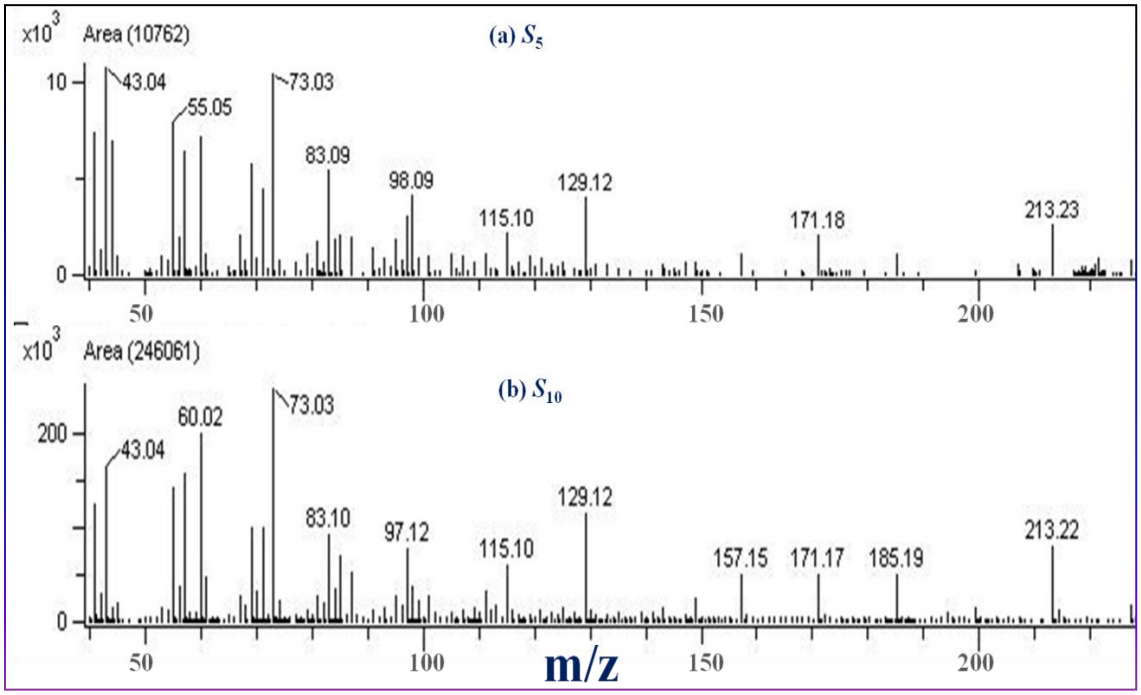

Figure 4.8: Mass spectra of (a) S_5 (b) S_{10}.

The PA pyrolysis technique is a simple non-destructive in nature, which does not require sample preparation, and need a very small quantity of solid samples. It provides significant information about NO_2 before the melting point. Here, laser excitation wavelength is selected according to the absorption characteristics of released gas (in our 532 nm for NO_2) from the solid material. In addition, it does not require any purge gas. The PA signal is produced due to non-radiative transition which is detected by a pre-polarized microphone. This is treated as one of the most sensitive detection technique and has low-level detection limit of the order of ppb. The GC-MS technique requires minimum vapor pressure of the order of 10 Torr, whereas PA technique needs vapor pressure ≤ 1 Torr. Furthermore, the controlled pyrolysis of the compound helps us to monitor the release of NO_2 gas at different temperatures. Apart from NO_2 other gaseous components can also be identified by the selection of tunable laser wavelengths. Therefore, it confirms that pulsed photoacoustic technique has superiority over the well-known GC-MS technique.

Unlike GC-MS, the present form of PA technique is not able to monitor the individual concentrations of byproduct gas molecules released from HEMs during the thermal decomposition process. However, we can monitor the release of NO_2 below the melting temperature to study the thermal stability of energetic materials by selection 532 nm wavelength. The significance of other byproducts can be identified in terms of shift in acoustic mode frequency. The concentration of these gaseous fragments changes the density of vapor, as a function of temperature, which affects on the propagation of generated acoustic signal.

4.5. Study of thermal stability of S_5, S_{10}, S_8 and S_9 using 266 nm

4.5.1. Thermal PA spectra S_5, S_{10}, S_8, and S_9

Fig. 4.9(a-d) shows the thermal PA spectra of S_5, S_{10}, S_8 and S_9 recorded at E_{in}=10 μJ, t =0.5 ms. Inset of figures shows the molecular structures. In the thermal PA spectra of S_5, lower order acoustic modes have higher intensities than the higher order modes. The predominant order of acoustic modes follows the descending order in the acoustic spectra of S_5. The mode present at 3.8 kHz is identified as a predominant mode of the PA cavity, which remains unchanged even for higher temperature range. Similarly, it is also one of the higher intensity acoustic modes in the thermal PA spectra of S_{10}, while other acoustic modes have comparatively lower intensities as compared to 3.8 kHz mode. This indicates that the released quantity of gaseous mixture leads to excite the first order longitudinal mode of the cavity than the other modes. The maximum strength of PA signal for S_5 and S_{10} at 350 °C is 40 mV and 12 mV respectively.

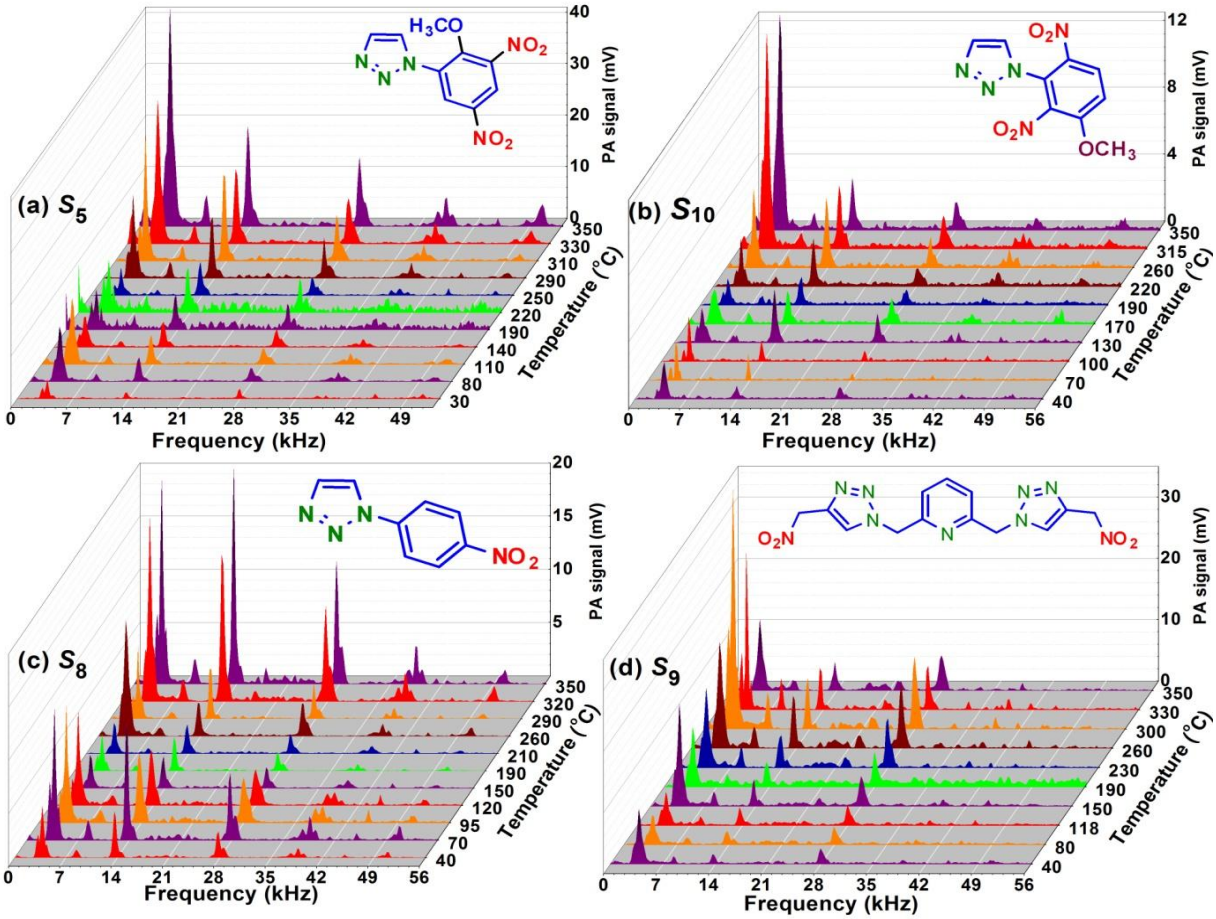

Figure 4.9: Thermal PA spectra of (a) S_5 (b) S_{10} (c) S_8 and (d) S_9 at t =0.5 ms.

Similarly, in the case of thermal PA spectra of S_8 the excited acoustic modes at 3.8 and 13.8 kHz are predominant in nature along with another mode present at 27.8 kHz. The predominant order of

acoustic modes is changing with respect to vapor temperature due to variations in the quantity of released vapor. Consequently, in the thermal PA spectra of S_9 the mode present at 3.8 is the first predominant mode while 28.2 kHz is the second dominant one. However, 13.8 kHz is also exciting simultaneously along with 28.2 kHz mode. This compound has additional small intensity acoustic modes compared to other compounds. The highest strength of PA signal is obtained at higher temperature region i.e. 300 °C for S_9, and at 350 °C for other compounds.

4.5.2. Comparative fingerprint spectra of compounds

Fig. 4.10(a-d) shows the PA spectra of S_5, S_{10}, S_8 and S_9, recorded at T = 350 °C, E_{in}=10 μJ, and t = 1 ms. Insets of Fig. 4.10 shows the corresponding time domain PA signals. All the compounds possess similar principal acoustic modes with a small variation in their central frequencies. These modes are approximately located at 3.8, 8.5, 13.6, 28 and 38.6 kHz. The intensities of excited acoustic modes and their predominant order vary from compound to compound and depend on their decomposition process. The entire HEMs vapor and its byproduct gases have strong absorption at 266 nm [30]. Therefore, the PA spectra recorded at different temperatures possess similar acoustic frequencies with variation in their intensity due to released quantity of gaseous molecules. Thus, the PA spectra are treated as fingerprint spectra of compounds for a particular PA cell. The excited acoustic modes and their corresponding intensities are listed in Table 4.4. The acoustic mode at 3.8 kHz in PA spectra at 0.5 ms is splitting into three modes at 3.1, 3.8 and 4.2 kHz, in 1.0 and 2.5 ms PA spectra due to the low separation between two data points (Δω =40, 100 and 200 Hz for t = 2.5, 1.0 and 0.5 ms, respectively).

It is known that only NO_2 molecules have strong absorption at 532 nm and presence of other gas lead to shifting in the frequency of acoustic modes [31]. Even S_8 has one NO_2 group, and its strength of PA signal lies between than S_5 and S_{10}. However, S_{10} has a lower intensity than S_8 even though it has two -NO_2 groups, because it is more thermally stable compound. The melting temperatures of S_8 (92.50 °C) and S_{10} (168.91 °C) also show that S_{10} is more thermally stable than S_8. The PA spectra of S_5 and S_{10} are identical except their intensity of acoustic modes because these are isomers. As a result, these compounds release similar type of gaseous byproducts in different concentrations leads to change in the intensity of acoustic modes.

Table 4.4: Excited acoustic modes of the PA cavity in kHz.

***S*5**	3.1	3.8	4.3	8.4	13.6	18.2	20.7	27.7	28.4	37.6	38.5	39.5	45.0	50.0	
***S*10**	3.1	3.9	4.3	8.6	13.8	17.2	21.0	28.2	28.9	35.2	36.3	39.1	40.2	44.9	
***S*8**	3.1	3.8	4.3	8.3	13.6	17.0	19.2	20.7	27.6	28.3	37.5	38.5	39.2	41.3	45.0
***S*9**	3.1	3.8	4.3	8.5	13.7	17.2	22.5	24.8	27.9	33.3	35.3	36.8	38.7	41.6	45.0

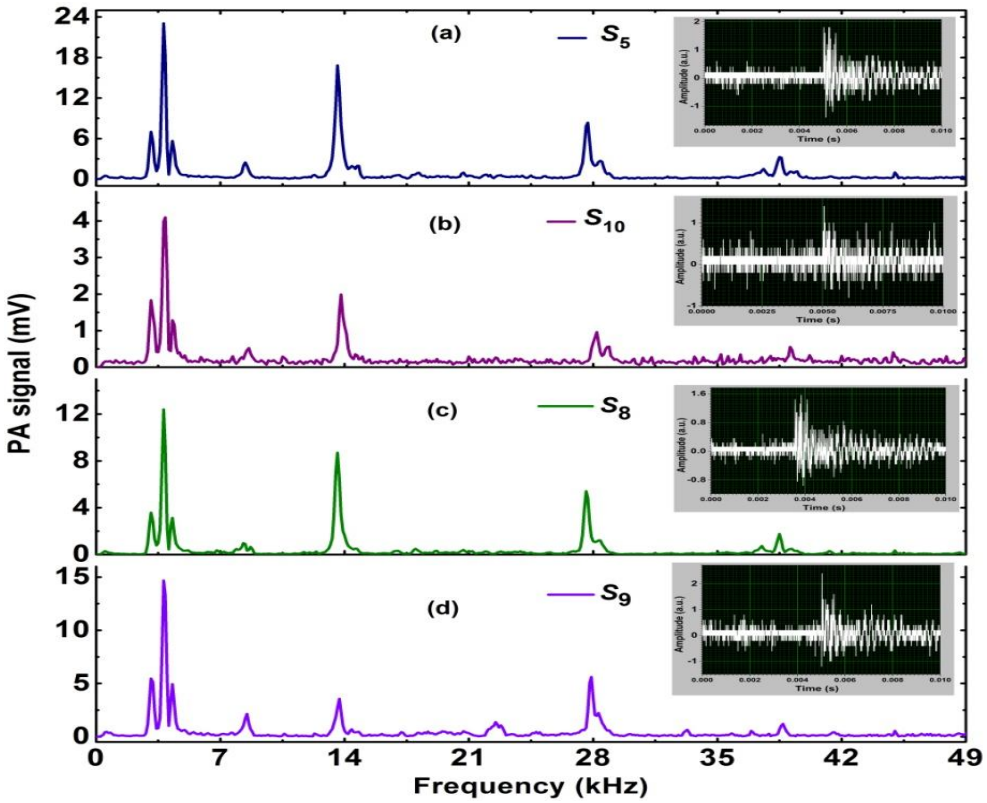

Figure 4.10: PA fingerprint spectra of (a) S_5 (b) S_{10} (c) S_8 and (d) S_9 at T= 350 °C, t = 1 ms.

4.5.3. Thermal stability and decomposition criteria

Fig. 4.11(a, c, e and g) shows the behavior of three major acoustic modes and Fig. 4.11(b, d, f and h) exhibits the TG-DTA curves of S_5, S_{10}, S_8 and S_9, with respect to temperature. The compounds S_{10}, S_8 and S_9 have melting and decomposition temperatures at 168.91, 92.50, 118.51 °C, and 231.51, 259.14 and 149.41 °C respectively. S_5 decomposed without melting it has two decomposition points at 151.10 and 315.35 °C. The PA signal curves for S_5 shows two peaks at 110 and 220 °C between the 30-350 °C range. The intensity of PA signal increases after crossing the temperature 250 °C and reaches its maximum value at 350 °C. The weight loss curve of S_5 shows that decomposition initiates at 140 °C. However, the corresponding compounds show initial PA signal peaks at 70, 100, 190 and 118 °C, respectively. The PA signal curves for acoustic modes show that S_5, S_{10}, S_8 and S_9 are thermally stable upto 250, 260, 270 and 280 °C, respectively. The compounds losess weight gradually as a function of temperature and decomposes rapidly at 270, 170, 200 and 118 °C, respectively. It was demonstrated that the NO_2 molecules releases before the melting temperature [18] and follow multiple thermal zones during the process of thermal decomposition. We also inferred that $\pi^* \leftarrow n$ transition is a strongest electronic transition in NO_2. Therefore, it governs the growth of PA signal and plays leading role to show the decomposition mechanism.

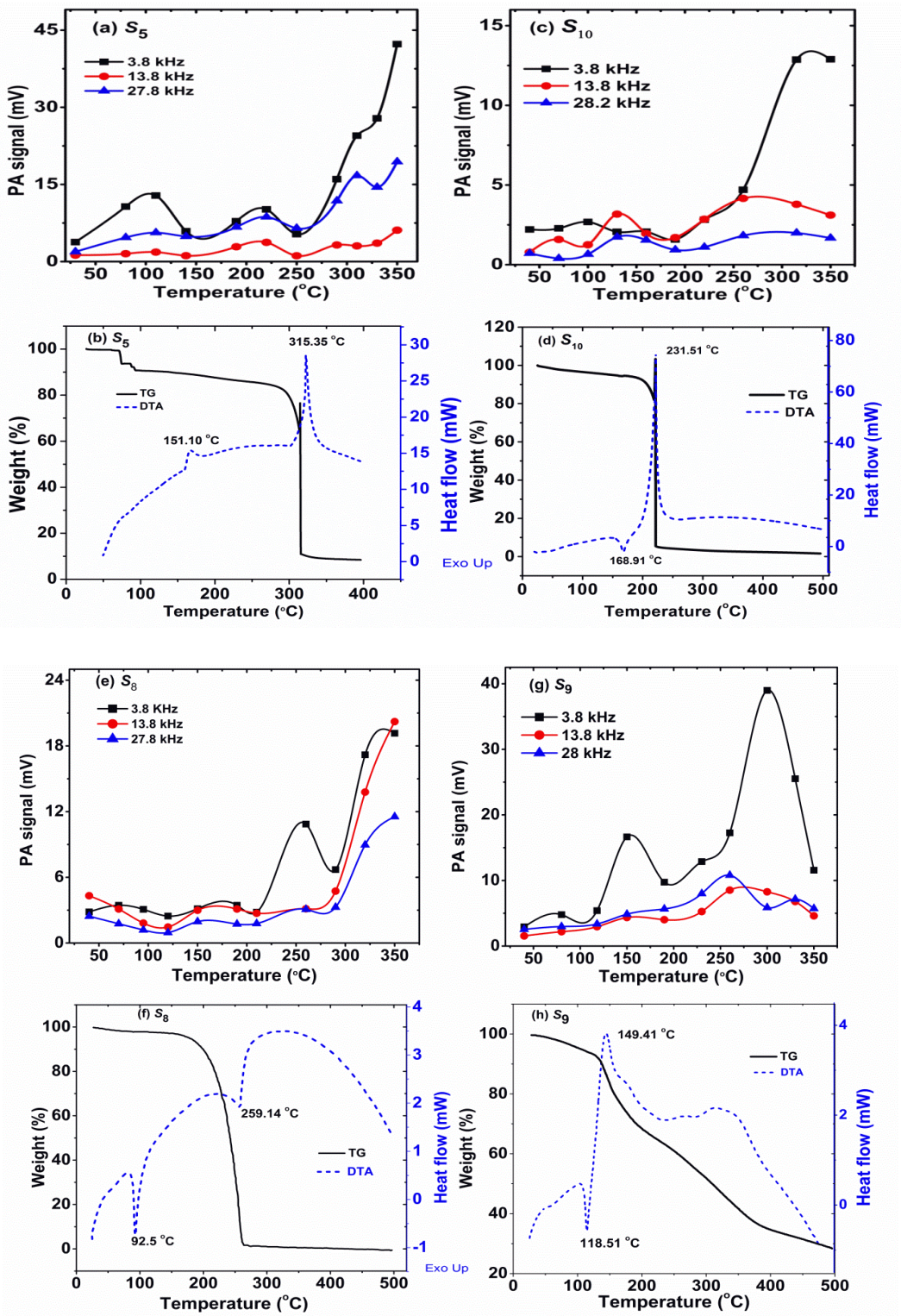

Figure 4.11: (a, c, e, g) Behavior of acoustic modes, and (b, d, f , h) TG-DTA curves with respect to temperature, for S_5, S_{10} , S_8 and S_9 respectively.

Fig. 4.11(c) shows the S_{10} has initial PA signal peak at 140 °C and the strength of the PA signal increases between 200-350 °C range. However, as shown in Fig. 4.11(e, g), for S_8 and S_9 the predominant mode at 3.8 kHz has peaked at their decomposition temperatures i.e. 260 and 150 °C, respectively. All these compounds show maximum intensities of PA signal at decomposition

temperature and increased more after crossing it. The peaks of PA spectra at given temperature confirms the process of decomposition occurs in multiple steps. The curves of PA signal, weight loss obtained from PA spectroscopy and TG-DTA confirm the thermal stability of the compounds. The stability order of these energetic materials are found to be S_{10}> S_8>S_9>S_5. This is ascertained based on the highest strength of PA signal obtained from these compounds. The released quantity of gaseous molecules depends on the density and occupied positions of $–NO_2$ groups in the structure of the compounds.

4.5.4. Effect of incident laser energy

Fig. 4.12 exhibits the PA spectra of compounds with respect to incident laser energy recorded at 350 °C, t = 0.5 ms. Insets in Fig. 4.12 show the behavior of two principal acoustic modes. The minimum incident laser energy order of 10 μJ, which is sufficient to record the PA spectra using 266 nm wavelengths, and the central frequency of the predominant acoustic modes does not vary with respect to incident laser energy. However, higher energy leads to affect the other excited cavity modes. This is due to strong absorption of HEMs vapor at 266 nm wavelength region.

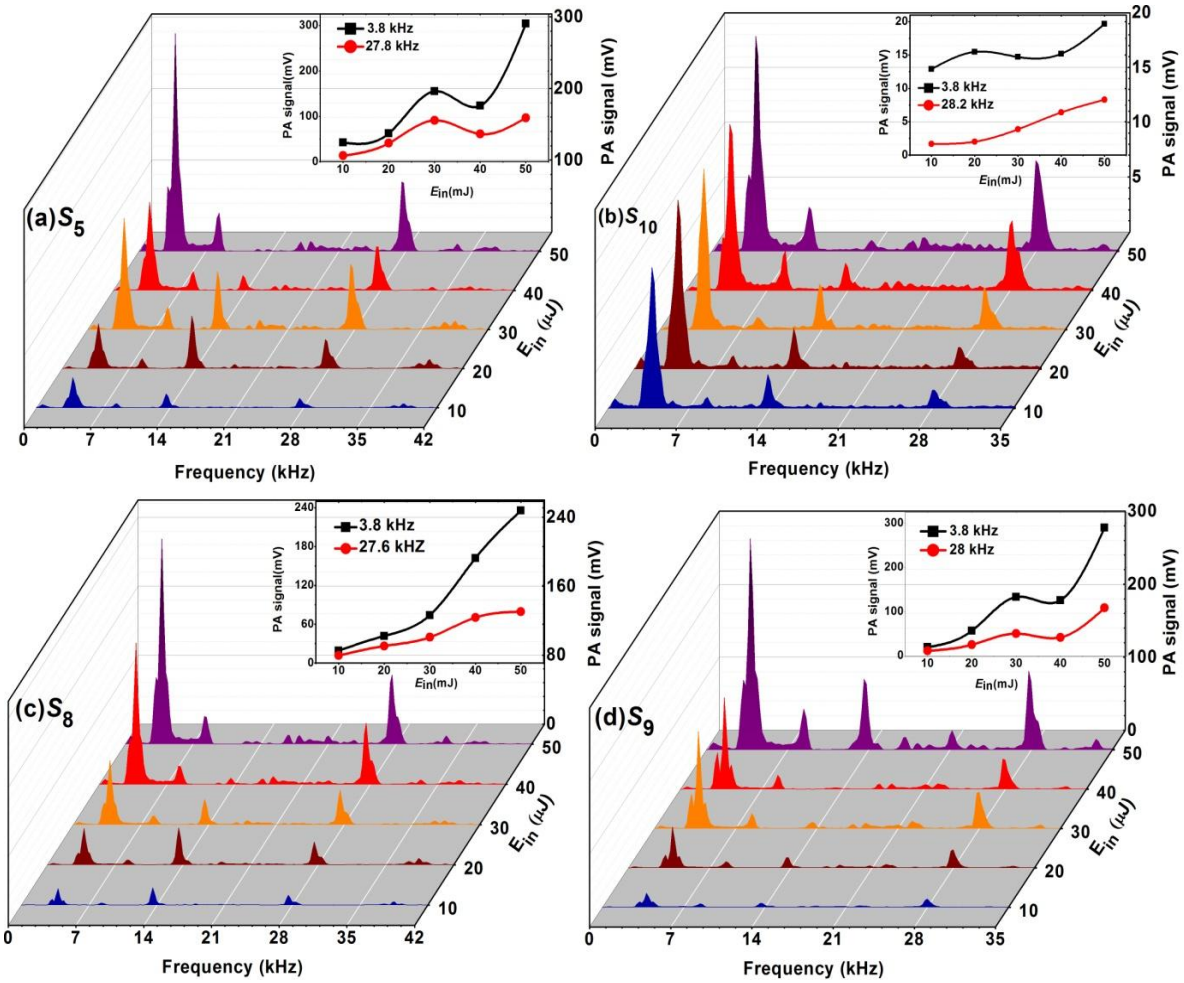

Figure 4.12: PA spectra and behavior of acoustic modes with incident laser energy for (a) S_5 (b) S_{10} (c) S_8 and (d) S_9.

The strength of PA signal for S_{10} is lower than other compounds with respect to incident laser energy, which shows that it is more stable. All excited acoustic modes are present in PA spectra of lower incident laser energies. The PA spectra get saturated after crossing the 30 μJ energy. Therefore, for the recording of the PA spectra of newly synthesized energetic compounds require low laser energy at 266 nm. Because the PA signal saturated with the higher incident laser energy. In case of S_5, S_{10} and S_8 at 50 μJ energy the excited acoustic mode 13.8 kHz disappeared. This indicates that the absorbed radiation accumulated at the first longitudinal and azimuthal modes. Higher incident laser energy utilized in case of S_9 to excite the first longitudinal (3.8 kHz), radial (13.8 kHz), and azimuthal modes (27.8 kHz).

4.5.5. Effect of data acquisition time

Fig. 4.13 (a-d) shows the decay behavior of acoustic mode present at 3.8 kHz with respect to data acquisition time at different incident laser energies for S_5, S_{10}, S_8 and S_9. The acoustic modes show exponential decay behavior, each having different decay times.

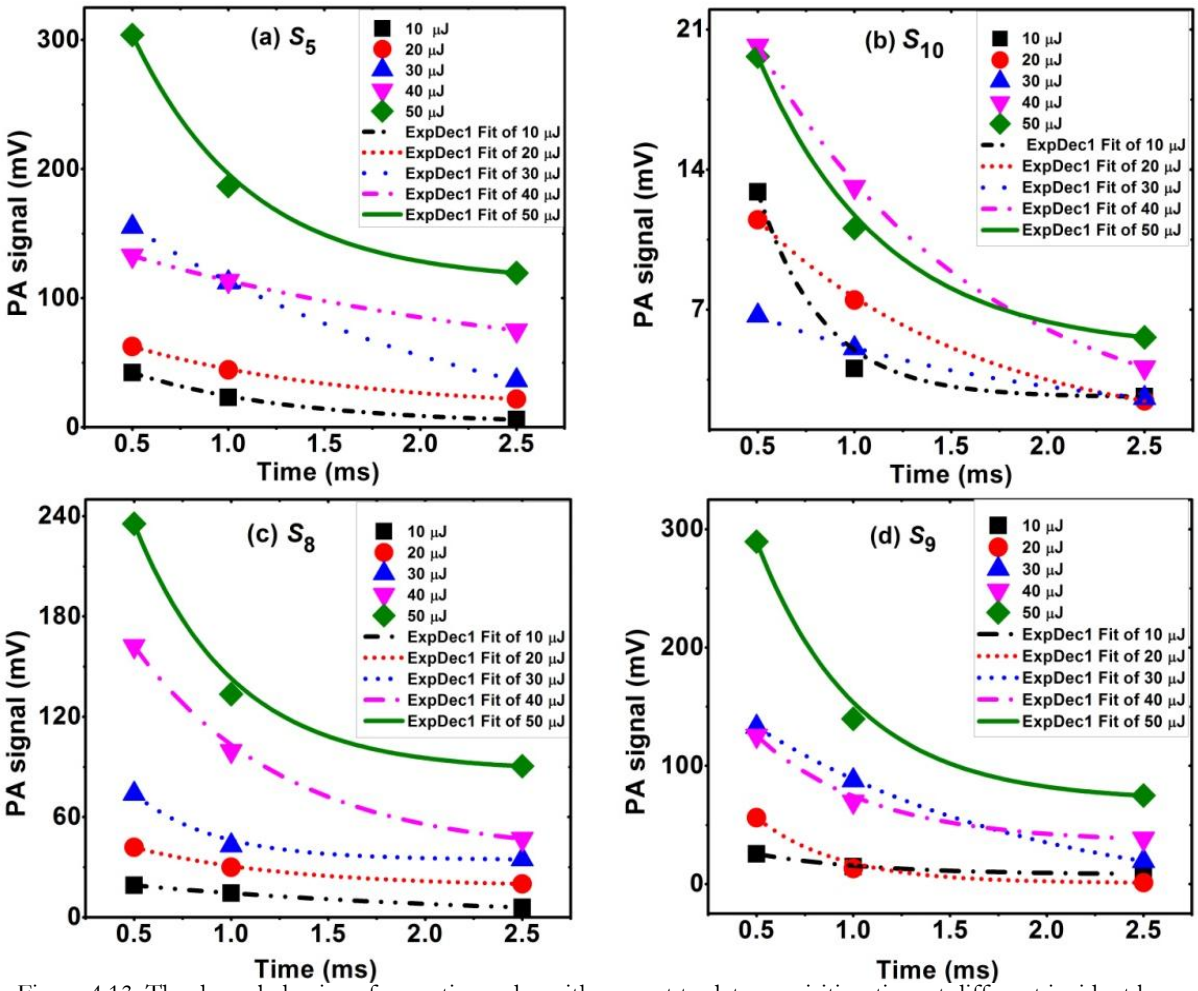

Figure 4.13: The decay behavior of acoustic modes with respect to data acquisition time at different incident laser energies for (a) S_5 (b) S_{10} (c) S_8 and (d) S_9.

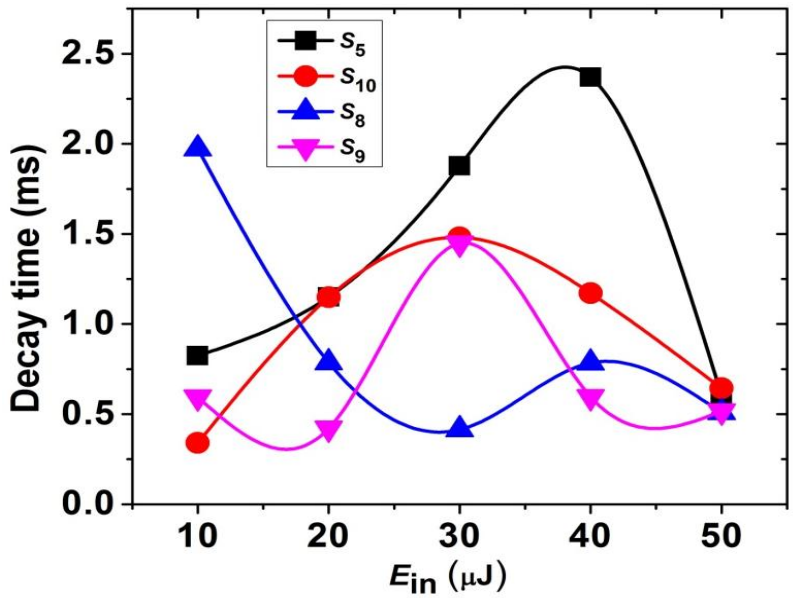

Figure 4.14: Exponential decay times for compounds with incident laser energies.

Fig. 4.14 shows the corresponding decay times of the compounds for 3.8 kHz mode. At 10 mJ, the compound S_8 has higher decay time i.e. 1.97 ms. The acoustic mode has higher decay time when the relative difference between the intensities of this mode is lower as function of data acquisition time. This is possible only at concentration of absorbed gas molecules are high in quantity inside the PA cell. The acoustic modes have higher decay times, which turned to linear decay considering that these are the predominant modes. The decay times of the compound varies as a function of incident laser energy. The decay time curves of S_5 and S_{10} shows approximately identical decay behavior with different values. The decay times at 50 μJ have almost identical values, but there is considerable change in their values at lower energy i.e. 10 μJ. This reveals the fact that the response of PA signal is identical at higher incident laser energy. Therefore, the minimum energy associated with excitation wavelength is suitable for recording the signature of the newly synthesized molecules.

4.5.6. Thermal quality factor

The quality factor "Q" is defined in terms of ratio of accumulated energy to the energy loss over one cycle. Physically, it is given by the ratio of central frequency (ω) to the full width at half maxima ($\Delta\omega_c$) of the corresponding acoustic mode.

$$Q = \frac{\omega}{\Delta\omega_c} \tag{4.4}$$

Fig. 4.15 shows the Lorentz fit of acoustic modes located at ~13.8 kHz for S_5, S_{10}, S_8, and S_9 at different temperatures. It is observed that central frequency of acoustic modes does not show any variation while full width at half maxima (FWHM) of modes varies as a function of temperature. This clearly reveals that the difference in the concentration of released quantity of gaseous

byproducts. The intensities of 3.8 kHz mode for S_8, is higher than S_9 because in the case of S_8 is a second predominant mode while for S_9 it is the third mode. This is due to modulations in acoustic pressure wave caused by different concentrations of released gaseous molecules. However, the energetic materials possess similar excitation modes due to absorption of 266 nm by all released gaseous fragments irrespective of their quantity in the total vapor mixture.

Fig. 4.16 (a-d) shows the obtained quality factors for S_5, S_{10}, S_8, and S_9. The highest Q values i.e. 36, 32, 40, and 42 obtained for S_5, S_{10}, S_8, and S_9 at temperatures 290, 70, 290, and 330 °C, respectively. If the higher quantity of absorbed gas molecules present in the PA cavity, then the cavity work as a high sensitive resonator and enhance the quality factor. The compounds can release higher number of gas molecules at melting, decomposition or after crossing the decomposition temperatures. However, in the present case average constant quality factor i.e. 24 is obtained as a function of temperature. The lower and constant values of quality factors with respect to vapor temperature indicate that the compounds release less quantity of gaseous fragments. This directly shows that the reported compounds are thermally stable in nature.

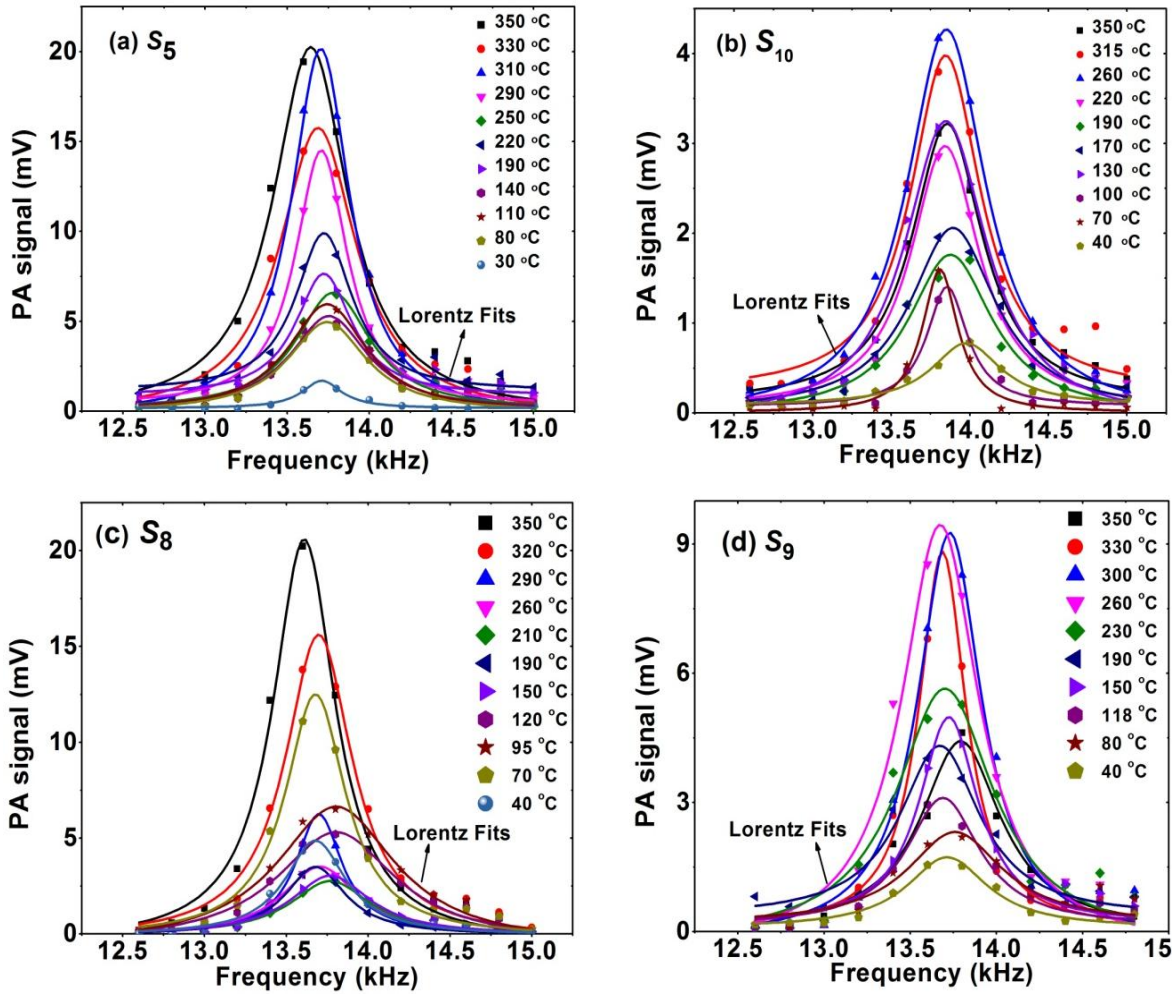

Figure 4.15: Lorentz fits of ~13.8 kHz mode of (a) S_5, (b) S_{10}, (c) S_8, and (d) S_9 at different temperatures.

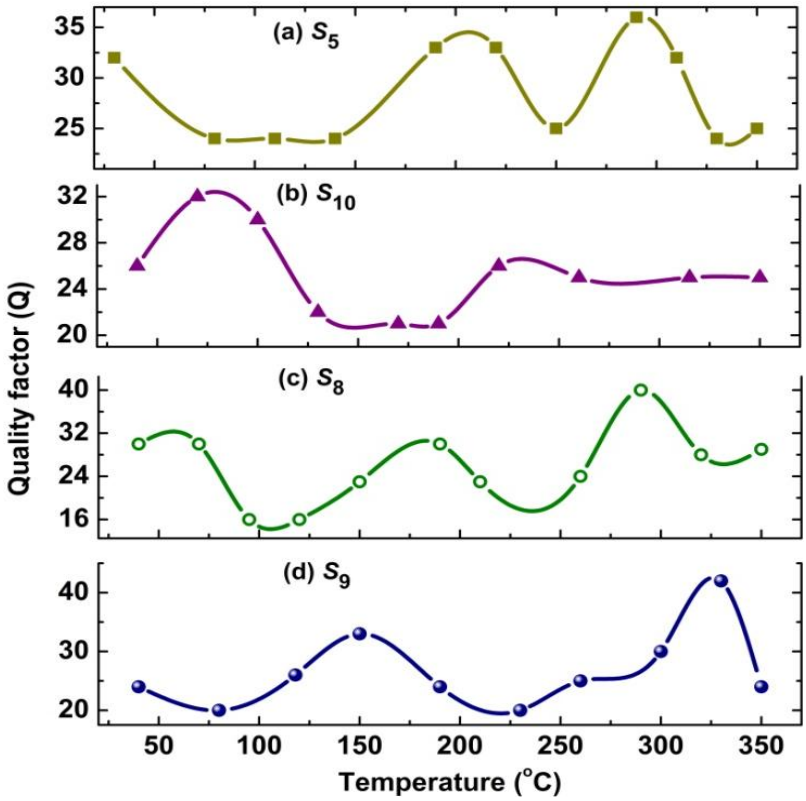

Figure 4.16: Quality factors for compounds at 13.8 kHz.

4.6. Conclusions

We have successfully recorded temperature and pressure based time-resolved PA spectra of S_8 and S_9 using 532 nm wavelength. The number density, absorption cross section of S_8 and S_9 are calculated using gas law and Beer Lambert's law. This shows that the molecules released from S_9 have high number density than S_8. It is observed that for the recording of PA spectra of 1,2,3 phenyl series triazoles requires high incident laser energies as compared the benzyl series 1,2,3-triazoles. It shows that phenyl series triazoles are more thermally stable as compared to the benzyl series. The thermal stability of S_5, S_{10}, S_8, S_9 was cross-verified with UV 266 nm wavelength and recorded the PA fingerprint spectra. The advantages and limitations of pulsed photoacoustic pyrolysis technique compared with the GC-MS technique were presented.

References

1. Q.-H. Lin, Y.-C. Li, Y.-Y. Li, Z. Wang, W. Liu, C. Qi, and S.-P. Pang, J. Mater. Chem. **22**, 666 (2012).
2. A. A. Dippold, D. Izsok, T. M. Klapotke, and C. Pfloger, Chem. - A Eur. J. **22**, 1768 (2016).
3. V. D. Ghule, R. Sarangapani, P. M. Jadhav, and S. P. Tewari, J. Mol. Model. **17**, 1507 (2011).
4. W. Dehaen and V. A. Bakulev, *Chemistry of 1,2,3-Triazoles* (Springer, 2012).
5. A. Jai Prakash and H. Robert, *Organic Chemistry of Explosives* (Wiley, 2006).
6. A. S. Kumar, N. Kommu, V. D. Ghule, and A. K. Sahoo, J. Mater. Chem. A **2**, 7917 (2014).
7. N. Kommu, V. D. Ghule, A. S. Kumar, and A. K. Sahoo, Chem. - An Asian J. **9**, 166 (2014).
8. Q. Wu, W. Zhu, and H. Xiao, RSC Adv. **4**, 53000 (2014).
9. Y. Zhang, D. A. Parrish, and J. M. Shreeve, J. Mater. Chem. A **1**, 585 (2013).
10. R. S. Damse and A. K. Sikder, J. Hazard. Mater. **166**, 967 (2009).
11. A. K. Sikder and N. Sikder, J. Hazard. Mater. **112**, 1 (2004).
12. A. Strachan, E. M. Kober, A. C. T. van Duin, J. Oxgaard, and W. A Goddard, J. Chem. Phys. **122**, 54502:1 (2005).
13. V. D. Ghule, J. Phys. Chem. A **116**, 9391 (2012).
14. X. Jin, B. Hu, H. Jia, Z. Liu, and C. Lu, Quim. Nova **37**, 74 (2014).
15. Y. Li, W. Liu, and S. Pang, Molecules **17**, 5040 (2012).
16. P. G. Laye and D. C. Nelson, Thermochim. Acta 153, 221 (1989).
17. R. Turcotte, M. Vachon, Q. S. M. Kwok, R. Wang, and D. E. G. Jones, Thermochim. Acta **433**, 105 (2005).
18. F. Yehya and A. K. Chaudhary, Sensors Actuators B. Chem. **178**, 324 (2013).
19. A. K. Chaudhary, K. S. Rao, and A. Sudheer Kumar, Appl. Opt. **55**, 817 (2016).
20. K. S. Rao, A. K. Chaudhary, N. Kommu, and A. K. Sahoo, RSC Adv. **6**, 4053 (2016).
21. K. S. Rao, A. K. Chaudhary, F. Yehya, and A. S. Kumar, Spectrochim. Acta Part A Mol. Biomol. Spectrosc. **147**, 316 (2015).
22. A. S. Kumar, V. D. Ghule, S. Subrahmanyam, and A. K. Sahoo, Chemistry **19**, 509 (2013).
23. F. Yehya and A. K. Chaudhary, Opt. Commun. **312**, 16 (2014).
24. A. K. Chaudhary, G. C. Bhar, and P. Kumbhakar, J. Quant. Spectrosc. Radiat. Transf. **98**, 157 (2006).
25. W. Demtroder, *Laser Spectroscopy, Basic Concepts and Instruments*, 2nd ed. (Springer, Berlin, 1996).
26. A. Asfaw, T. B. Bacha, and D. D. Venable, J. Quant. Spectrosc. Radiat. Transf. **74**, 655 (2002).
27. K. S. Rao and A. K. Chaudhary, Thermochim. Acta **614**, 149 (2015).
28. A. Lamb, K. A. Larson, and E. L. Tollefson, J. Air Pollut. Control Assoc. **23**, 200 (1973).
29. *NIST Chemsitry WebBook (Http://webbook.nist.gov/chemistry))*.
30. HITRAN 2014 Database,online Http//www.hitran.com/.
31. K. S. Rao, A. K. Chaudhary, and F. Yehya, Appl. Phys. B **121**, 375 (2015).

Chapter 5

Phenyl-series 1,2,4-triazoles: Study of bond breaking mechanism and thermal stability

Abstract

In continuation of our studies reported in chapter 3 and 4, we have described in this chapter the effect of bond lengths of major chemical substituents on thermal stability of nitro rich 1H-1,2,4-triazoles between 30-350 °C range. Thermal stability and PA fingerprint spectra of these compounds are evaluated in terms of thermally released NO_2 molecules and total molecule vapor by employing second and fourth harmonic wavelengths i.e. visible 532 nm and UV 266 nm of a 7 ns pulse duration and 10 Hz repetition rate. These samples were also subjected to TG-DTA technique for recording their melting and decomposition temperatures. Thermo gravimetric-differential thermal analysis (TG-DTA) data along with PA results highlight the multistep decomposition mechanism of the reported compounds. The study also helps us to identify the characteristic behavior of propellants and explosives of the reported molecules which are used as a rocket fuel.

A part of the work presented in this chapter has appeared in the following publications:

[1] **K. S. Rao**, A. K. Chaudhary, N. Kommu, and A. K. Sahoo, *RSC Adv.*, 2016, **6**, 4053–4062.

[2] **K. S. Rao** A. K. Chaudhary, *RSC Adv.*, 2016, **6**, 47646–47654.

5.1. Introduction

Nitro rich triazole derivatives which possess high heat of formation, detonation velocities, pressure, shock sensitivity, and good thermal stability due to the presence of aromatic ring are treated as HEMs [1-3]. The synthesis and characterisation of these materials have attracted many researchers to evaluate their potential in military applications such as rocket fuel, gun propellants and explosives [4-10]. The study of thermal stability and decomposition mechanisms of premier HEMs can be studied using different analytical techniques [11-20]. The thermal decomposition mechanism and stability criteria of different types of energetic 1H-1,2,4-triazoles performed various theoretical and experimental studies [21-27]. Zhang Rui-Zhou *et al.* reported the theoretical studies on a series of 1,2,4-triazoles derivatives as potential high energy density compounds [28]. Tagomori *et al.* examined the thermal decomposition mechanism of 1H-1,2,4-triazole (1Htri) and its derivatives having different substituent such as -NO_2, -NH_2, -CH_3, -OCH_3 and -COOH using sealed-cell differential scanning calorimetry (SC-DSC) [29].

The high nitrogen content of 1,2,3- and 1,2,4-triazoles contributes to high positive heat of formation [30-38]. The heat of formation of the 1,2,3-triazole is higher (272 kJ/mol) than 1,2,4-triazole (191 kJ/mol)[39,40,41]. Therefore, 1,2,3-triazole-based compounds are energetically superior than 1,2,4-triazole derivatives. This is also verified using pulsed photoacoustic technique in terms of released quantity of gaseous molecules. However, the reported 1H-1,2,4-triazoles such as 1-(4-Methyl-3,5-dinitrophenyl)-1H-1,2,4-triazole (*P*-Me-DNPT), 1-(4-Methoxy-3,5-dinitrophenyl)-1H-1,2,4-triazole (*P*-OMe-DNPT), 2,6-Dinitro-4-(1H-1,2,4-triazol-1-yl) aniline (*P*-NH_2-DNPT) have identical structures except the presence of one chemical substituent such as -CH_3, -OCH_3, and -NH_2 at the *para* position of the phenyl ring. In chapters 3 and 4, we have discussed about thermal stability and decomposition mechanisms of different isomers of benzyl and phenyl series of 1H-1,2,3-triazoles. In the present chapter, the role of the major chemical substituent based on their bond lengths have been investigated in the decomposition mechanism and stability of the reported energetic materials under controlled pyrolysis between 30-350 ^{o}C range using pulsed photoacoustic pyrolysis technique. Our main aim is to propose that the pulsed photoacoustic technique is one of the emerging tools to study the thermal stability and decomposition mechanisms of various types of HEMs. In this chapter, we have chosen the compounds of nitro rich 1H-1,2,4-triazoles, which have identical structures but a different chemical substituent at *para* position in the phenyl ring. The strength of the PA signal is directly related to the released gaseous molecules from solid sample, which is available in small quantity (~1 mg) during the pyrolysis process. The strength and frequency of the PA signal is based on the selection of proper excitation wavelength and dimensions of the PA cell.

It is well known that the vapor of HEMs and their byproducts have strong absorption in 266 nm wavelength range and also involved in photodissociation process due to π*←n transitions [42-44]. The HEMs release several types of byproduct gases, such as NO_2, NO, CO_2, CO, HCN, and H_2O .etc during the process of thermal decomposition. Consequently, when 266 nm selected as an excitation wavelength, the study of thermal decomposition is shifted to NO and total compounds vapor. The laser-based excitation is responsible for the reduction of activation barriers for decomposition reactions [42,45,46]. Kimmel .et al suggested the dynamics and steady roots of thermal decomposition mechanism of HEMs with NO_2 and NO as byproducts [47]. The NO_2 molecules photodissociated to NO in presence of ultraviolet (UV) radiations [48-53]. It is also known that NO_2 is one of the principal byproduct gas obtained during the decomposition of HEMs [13,54-56]. There might be possibility that NO_2 molecules follow the root of photodissociation with excitation of UV 266 nm wavelength and converted into NO by following root,

$$NO_2 + h\nu \rightarrow NO + O \qquad (5.1)$$

Kommu et al. reported the synthesis of these nitro rich 1,2,4-triazoles derivatives such as *P*-Me-DNPT, *P*-OMe-DNPT and *P*-NH_2-DNPT [57]. The structures along with the chemical formulas, ρ,VOD, DP and ΔH_f of these compounds are shown in the Table 5.1.

Table 5.1: structure and energetic properties of 1,2,4-triazoles.

Sample	Structure	Formula	ρ gm/cm³	VOD km/s	DP GPa	ΔH_f kJ/mol
***P*-Me-DNPT**	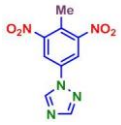	$C_9H_7N_5O_4$	1.62	6.40	17.01	268.25
***P*-OMe-DNPT**		$C_9H_7N_5O_5$	1.64	6.68	18.68	167.38
***P*-NH_2-DNPT**		$C_8H_6N_6O_4$	1.66	6.66	18.74	235.85

The reported energetic 1H-1,2,4-triazoles can be used as explosives and as propellants. Explosives generate supersonic reaction waves, which propagate with the speed of several km/s inside the matter. The corresponding process is known as detonation. Similarly, propellants generate subsonic reaction waves, which propagate with the speed of several km/s accompanied with hot gasses. The corresponding process is known as deflagration [58]. It is observed that for these compounds higher incident laser energy and lower data acquisition time are required to record the thermal PA spectra as compared to benzyl series 1,2,3-triazoles confirming these are thermally more stable [59].

5.2. IR spectra of compounds

Fig. 5.1(a-c) shows the IR spectra of *P*-Me-DNPT, *P*-OMe-DNPT, and *P*-NH_2-DNPT, respectively. Inset tables and structures of Fig. 5.1 show the positions of principal functional groups and line bond structures of the compounds. The absorption peaks of the amino group are present at 3419.18, 3254.79 and 1649.32 cm^{-1}. The strongest absorption peaks of C-O-C, -NO_2, -N=N^+=N^-, -OCH_3 and C-H are observed between 1300-1000 cm^{-1}, 1550-1300 cm^{-1}, 2400-2000 cm^{-1} and 2850-2810 cm^{-1}, range respectively. Therefore, given FTIR spectra confirm the presence of different functional groups in the reported compounds.

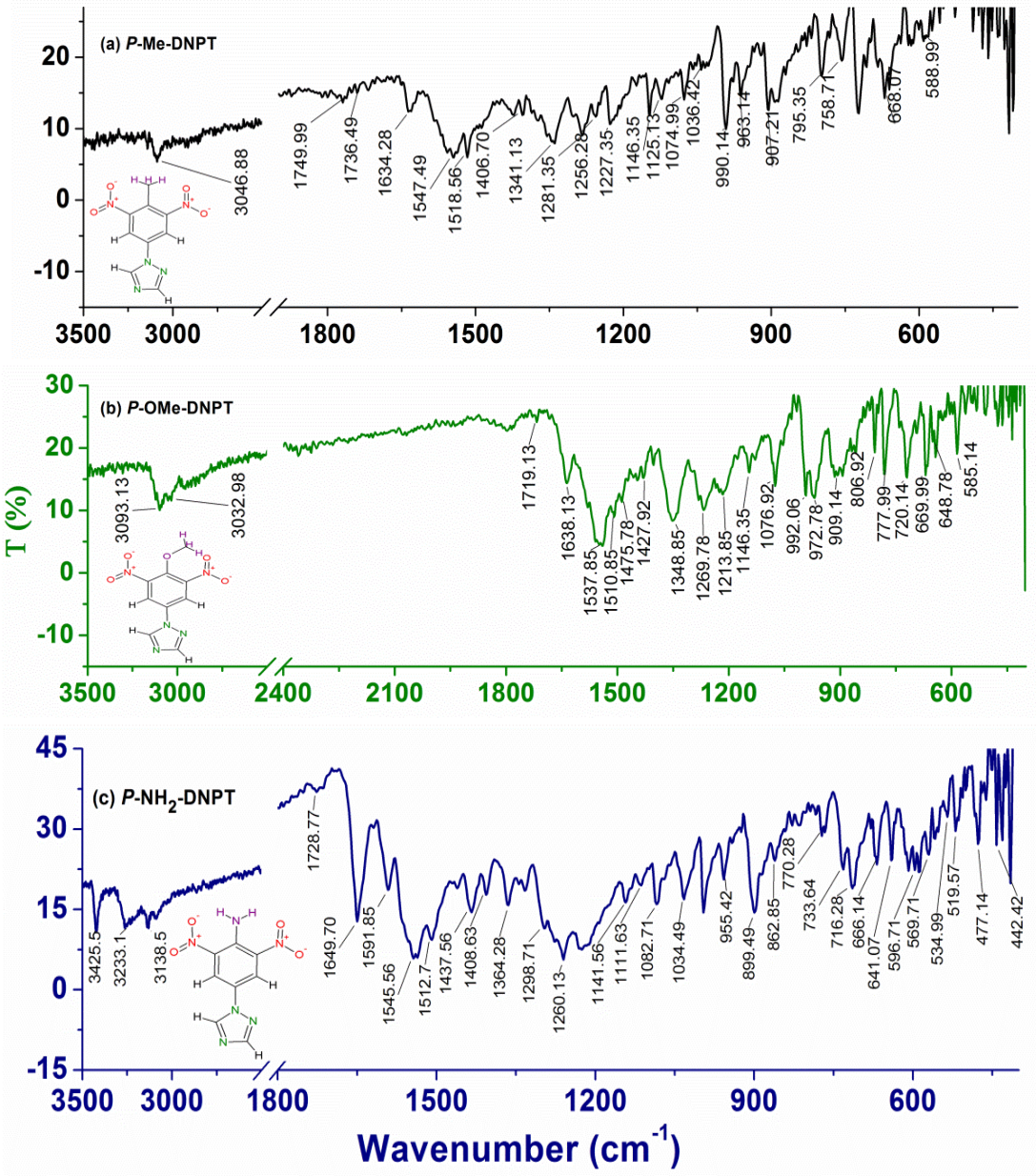

Figure 5.1: IR spectra of solid compounds.

5.3. 532 nm based study of 1,2,4-triazoles

5.3.1. Thermal PA spectra

Fig. 5.2(a-c) shows the thermal PA spectra recorded at E_{in} = 8.63 mJ, t = 0.5 ms for *P*-Me-DNPT, *P*-OMe-DNPT and *P*-NH_2-DNPT, repectively. The background noise signal of the system is of the order of 0.05 mV. Fig. 5.2(a) shows that *P*-Me-DNPT does not provide any PA signal up to 60 °C. The first PA signal is observed at 90 °C, which is treated as the initial point of thermal decomposition. The PA spectra also show some sharp, intense acoustic modes located at 12.4 and 36.4 kHz. Some other excited acoustic modes appear in cluster form and occupy the frequency range between 16 and 35 kHz. The excited acoustic modes of the PA cavity at T_d = 250 °C are present at 3.2, 8.4, 12.4, 18.0, 20.8, 22, 23.2, 27.4, 32.2, 36.4, 42.2 and 44.2 kHz. Amongst 12.4 kHz is one of the predominant acoustic modes of the cavity and has the intensity of the order of 54.11 mV. The acoustic modes of PA spectra of the compound have ± 200 Hz variation with respect to their central frequency as a function of temperature.

Fig. 5.2(b) shows the thermal PA spectra of *P*-OMe-DNPT. Though its melting temperature (T_m) is 97.92 °C, the process of dissociation initiates at 30 °C. Therefore, once again it is confirmed that NO_2 molecules are released much before the melting temperature of the HEMs [55,60]. The majority of acoustic modes exhibit a pair of peaks behavior and have broad profiles due to the change in the density of released vapor. The sharp, intense peaks are located at 3.8 and 13.8 kHz between 30-350 °C range. However, the other higher intensity acoustic modes are present at 17.2, 22.0 and 35.8 kHz. It is observed that almost all acoustic modes of PA spectra are excited simultaneously and possess identical intensities. Since the PA spectra of the compound is generated due to absorption of incident laser radiation by NO_2 and the presence of other gaseous fragments leads to the change in the density of the cell medium which affects the velocity of acoustic pressure waves. As a result, the profile of acoustic modes shows broadening effect along with a shift in the frequency with respect to the central frequency. The predominant order of excited acoustic modes gradually changes their position with respect to vapor temperature.

The thermal PA spectrum of *P*-NH_2-DNPT at 130 °C as shown in Fig. 5.2(c) possess two weak and one strong modes located at 4.0, 13.8 and 27.4 kHz respectively. The PA spectra have strong and sharp acoustic peaks, this is the indication of presence of more quantity of NO_2 molecules. The maximum PA signal is obtained at 315 °C and the excited acoustic modes are located at 4.0,12.4,13.8,27.4,37.6,38.6 and 39.11 kHz. During the experiment, thermally released reddish brown colored vapor was observed in the heating flask, which clearly indicates that the vapor contains a high amount of NO_2 as compared to other gaseous molecules.

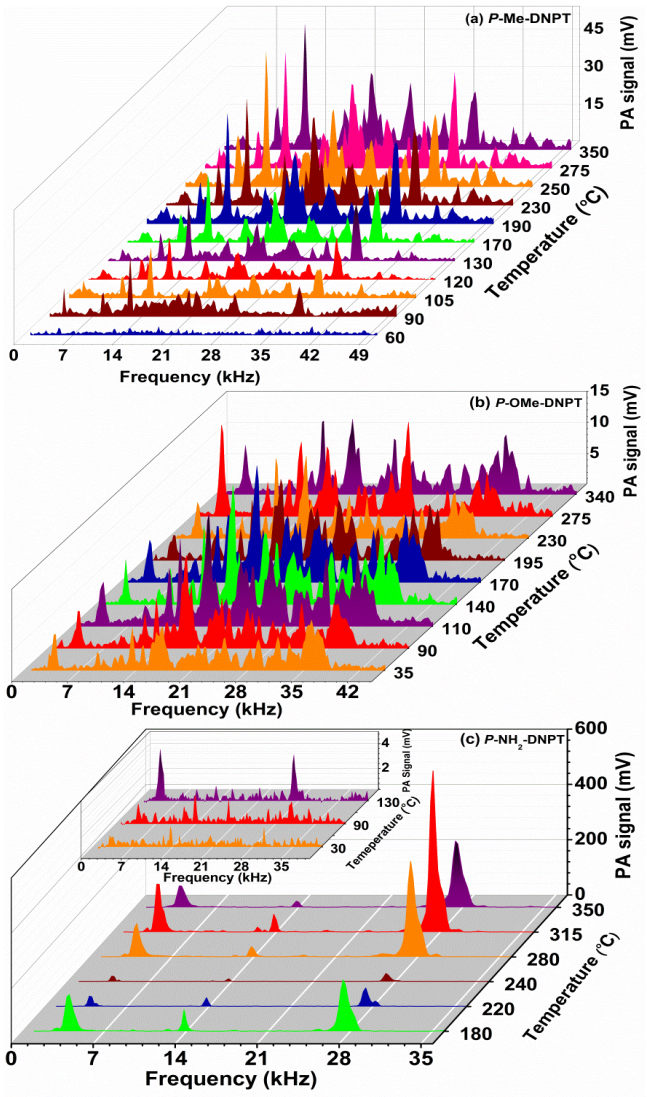

Figure 5.2: 532 nm based thermal PA spectra of (a) *P*-Me-DNPT, (b)*P*-OMe-DNPT and (c) *P*-NH_2-DNPT.

Fig. 5.3(a-c) shows the 532 nm based PA spectra recorded at 250, 170 and 280 °C at t = 1 ms for *P*-Me-DNPT, *P*-OMe-DNPT, and *P*-NH_2-DNPT. Inset figures show the corresponding time domain signals. The PA spectra in Fig. 5.3(d) shows the total number of 24 calculated eigenmodes which comprises 19-longitudinal (q), 3-radial (n) and 2-azimuthal (m) modes of the PA cavity, which occupies the frequency between 0-45 kHz. The first q, n and m modes frequencies are located at 2.28, 13.4 and 27.89 kHz. The calculated frequencies of sixth and twelfth longitudinal modes are almost equal to the first radial mode (i.e., at 13.8 kHz) and azimuthal mode (i.e. 27.4 kHz) respectively. Therefore, it is inferred that these common eigenmodes are the strongest excited acoustic modes of PA spectra. These modes are clearly observed in PA spectra of *P*-NH_2-DNPT. The PA cavity have maximum numbers of even order of longitudinal modes. The order of acoustically excited modes varies from sample to sample which is attributed to the change in the density of released gaseous molecules. In case of PA spectra of *P*-Me-DNPT and *P*-OMe-DNPT, the acoustic modes are well separated and have sharp peaks between 0-15 kHz frequency range. Whereas, low-

intensity acoustic modes appeared in a pair between 15-45 kHz range. It confirms that the higher order modes are forming clusters due to percentile change of NO_2 as well as other gaseous molecules present in the vapor. PA spectra of *P*-NH_2-DNPT has two kinks at 4.4 and 28.3 kHz. The PA spectra of *P*-NH_2-DNPT depicts well separated sharp peaks as compared to the other two compounds and confirms that *P*-NH_2-DNPT releases more quantity of NO_2 as compared to other byproduct gasses. While, the kinks of acoustic modes show the presence of other gaseous molecules released in less quantity.

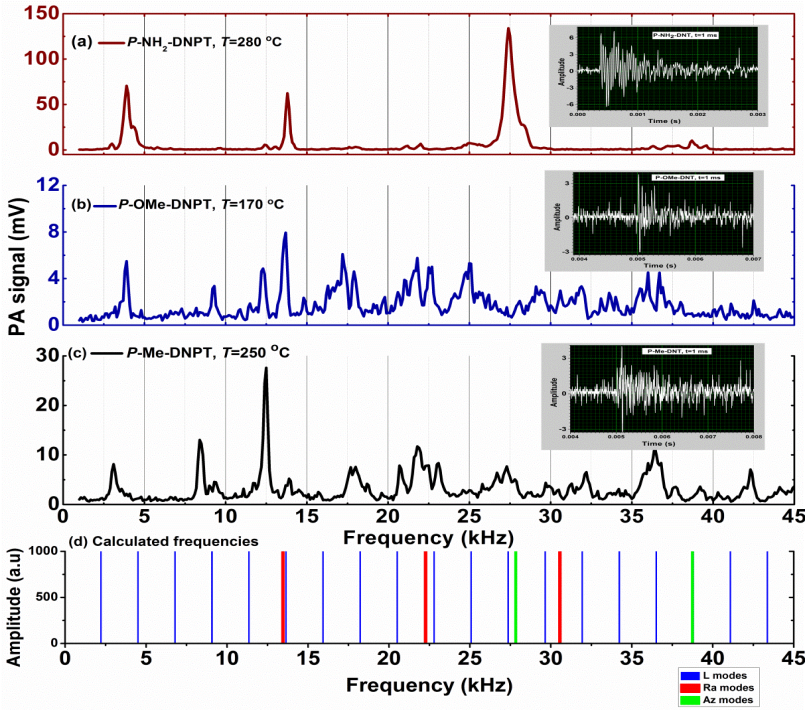

Figure 5.3: PA fingerprint spectra at t =1 ms of (a) *P*-NH_2-DNPT (b) *P*-OMe-DNPT (c) *P*-Me-DNPT, and (d) calculated longitudinal, radial and azimuthal modes of PA cavity.

In the chapter 3, we have already shown the thermal stability and acoustic fingerprints of S_1, S_2, S_3, S_4 and S_6. The effect of methoxy group on PA spectra of S_3 and S_4 was observed in the form of a pair of peaks. However, additional acoustic peaks are absent in the PA spectra of S_1 and S_2. The compound *P*-OMe-DNPT has -OCH_3 group similar to other methoxy group compounds. The fragments released due to –OCH_3 affect the concentration of NO_2 as well as density of total vapor resulting a pair of acoustic peaks is obtained in PA spectra. Due to the pair of peaks, the intensity of acoustic modes for *P*-OMe-DNPT is comparatively lower than the remaining two compounds. The thermally released other gasses such as oxygen (O) or CO from methoxy group, might react with freely released NO_2 molecules and lead to conversion of NO_2 into NO along with formation of other gasses such as O_2 and CO_2 etc. using following chemical roots [61,62]

$$NO_2 + O \rightarrow NO + O_2 \quad (5.1)$$

$$NO_2 + CO \rightarrow NO + CO_2 \quad (5.2)$$

In case of 266 nm due to strong absorption of total molecule vapor the intensity order of PA signals follows the density order: *P*-NH_2-DNPT > *P*-OMe-DNPT >*P*-Me-DNPT, which indicates that higher density molecules release a high quantity of gaseous byproducts.

5.3.2. Thermal stability

Fig. 5.4(a), 5.4(c) and 5.4(e) show the behavior of acoustic modes with respect to temperature while Fig. 5.4(b), 5.4(d) and 5.4(f) show TG-DTA curves of *P*-Me-DNPT, *P*-OMe-DNPT, and *P*-NH_2-DNPT, respectively. In the case of *P*-Me-DNPT, the first predominant acoustic mode located at 12.4 kHz has highest PA signal at T_d i.e. 250 °C. The compound starts releasing NO_2 at 90 °C and this temperature region is treated as the first thermal zone for the release of NO_2. However, fixed intensity of acoustic modes shows the stability of compound between 90-170 °C range. The acoustic modes located at 8.5 and 22 kHz are stable between 190-350 °C range. The heat flow curve of *P*-Me-DNPT as shown in Fig. 5.4(b) indicates that it has T_m and T_d at 129.80 and 259.89 °C. The weight loss curve shows that it is thermally stable up to 150 °C and after crossing this temperature, it lost about 95 % of weight at 233.48 °C.

The heat of decomposition (ΔH) depends on the overall decomposition and type of by-products formed. The ring breakdown reactions in the process of thermal decomposition are either exothermic or endothermic in nature. The endothermic peak represents the solid–solid phase transition points, which is due to release of condensed water. Fig. 5.4(b) shows the heat flow curve of *P*-Me-DNPT at decomposition temperature (259 °C) with an endothermic peak, whereas the weight loss curve indicates that almost 95 % weight is lost between 150-260 °C range. This shows that the molecule starts decomposing at 259 °C, by releasing different types of gaseous byproducts along with condensed water (which is due to lack of high nitrogen content). Consequently, it shows an endothermic peak for *P*-Me-DNPT [33].

Fig. 5.4(c) shows the behavior of acoustic modes for *P*-OMe-DNPT with respect to temperature. The acoustic mode present at 17.2 kHz is one of the strongest PA mode between 90 and 195 °C temperature range. Similarly, modes present at 13.6 kHz show highest PA peak at 140 and 230 °C, while mode at 17.2 kHz has a higher peak at 140 and 275 °C.

Fig. 5.4(d) shows the TG-DTA curves of *P*-OMe-DNPT. It has T_m at 97.92 °C and T_d at 274.43 °C. The heat flow curve shows that a broad peak present at 165 °C between 150-180 °C range, which is also considered as the decomposition point and is correlated to the strong PA signal due to the release of more quantity of NO_2. The compound gradually loses its weight between 25-275 °C range. The rate of decomposition gets accelerated after crossing 275 °C. It is also reflected in the strength of the PA signal of acoustic modes present at 4.0, 22.0 and 35.8 kHz which show stable behavior up to 275 °C.

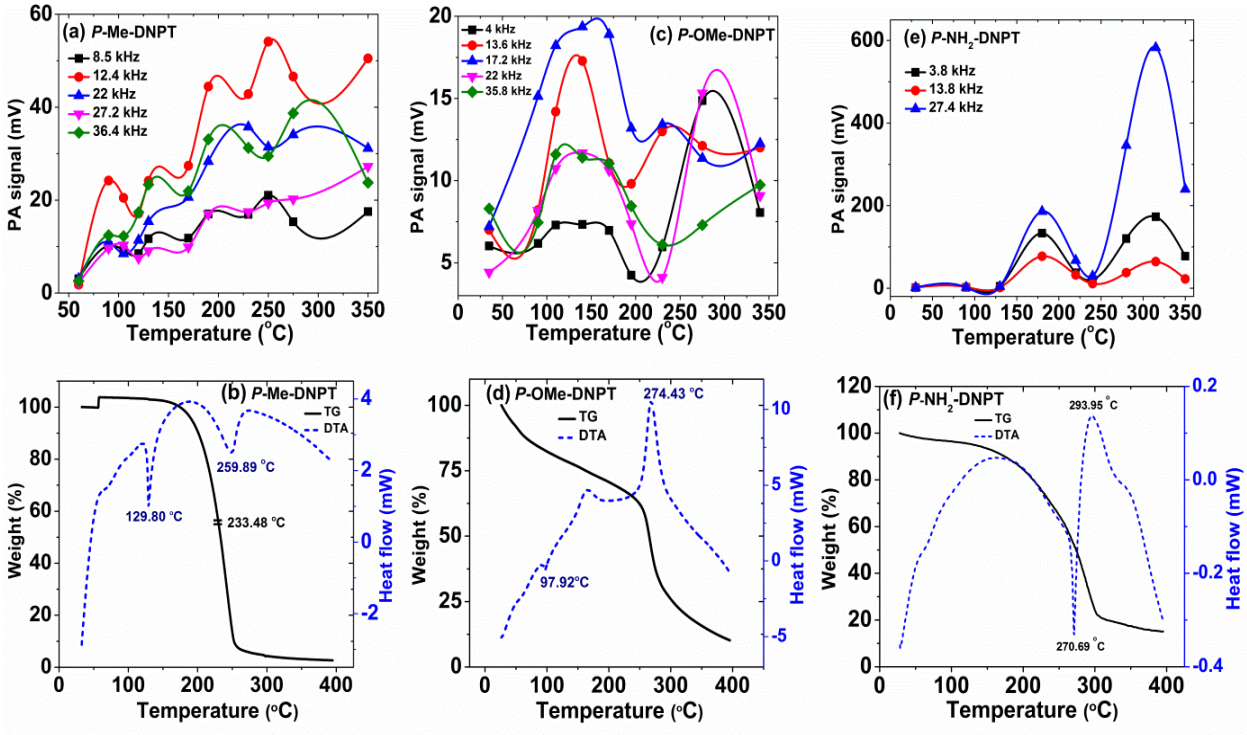

Figure 5.4: Shows the behavior of acoustic modes and TG-DTA curves *P*-Me-DNPT, *P*-OMe-DNPT, and *P*-NH_2-DNPT respectively.

Fig 5.4(e) shows the behavior of three predominant modes present at 3.8, 13.8 and 27.4 kHz. They show similar excitation behavior and the intensities of PA spectra have two major peaks at 180 and 315 °C. The PA signal curves indicating that *P*-NH_2-DNPT is thermally stable up to 130 °C. The heat flow curve in Fig. 5.4(f) exhibits that the process of melting initiates at 180 °C and decomposed with an endothermic peak at 270 °C, further possess exothermic nature at 293 °C. The weight loss curve shows that compound is thermally stable up to 150 °C after this it loses around 70 % of its total weight between 150-300 °C range. But, the signature peak of PA signal appears at 130 °C, after that it shows rapid growth up to 180 °C. The PA signal shows two additional peaks at 315 °C and 280 °C. The results obtained from PA technique for the 1H-1,2,4-triazoles have excellent agreement with the TG-DTA analysis i.e. at the T_m and T_d of the compounds achieved the highest PA signals. *P*-NH_2-DNPT has an additional N (due to -NH_2) which increases the density of compound (1.66 g/cm^3) as compared to other compounds and leads to releases of more quantity of NO_2 than other gaseous molecules. Therefore, the synthesis of nitrogen (N) rich green energetic materials can be treated as potential rocket fuel [2,3]. The compounds *P*-OMe-DNPT and *P*-NH_2-DNPT are oxygen and nitrogen-rich compounds. As a result, at decomposition temperature, the ring-breaking reaction appears in the form of exothermic peaks (due to oxidation of nitrogen) as shown in Fig. 5.4(d) and 5.4(f). *P*-OMe-DNPT shows two exothermic peaks at 150 °C and 274.43 °C. The first exothermic peak is due to breaking of principal functional groups attached to the ring while the second one is due to aromatic ring breaking and indicates the completion of total decomposition process.

5.3.3. Bond breaking mechanism and scaling the efficiency as a rocket fuel

The sequence of bond breaking mechanism of major functional groups from solid compounds during the pyrolysis process is explained based on their bond lengths. It is accertained that, the functional group which has higher bond length from the phenyl ring carbon is released initially, than other groups. The bond length of some principal functional groups are listed in Table 5.2, which are calculated by optimizing the structure in Gaussian 03 using B3PW91 functional with 6-31G(d,p) basis set [57].

Table 5.2: Bond lengths of compounds and PA signal at t = 0.5 ms.

Functional groups	*P*-Me-DNPT	*P*-OMe-DNPT	*P*-NH_2-DNPT
C_{phenyl} - $N_{triazole}$	1.407 Å	1.412 Å	1.410 Å
C_{phenyl} – *para* group	1.503 Å ($C-CH_3$)	1.345 Å ($C-OCH_3$)	1.330 Å ($C-NH_2$)
$-C-NO_2$	1.474 Å	1.476 Å	1.450 Å
Strength of PA signal	54.11 mV	19.36 mV	582.99 mV

In the case of *P*-Me-DNPT, the methyl group is present at the *para* position of phenyl ring with sigma bond which has a bond length of the order of 1.503 Å. In addition, two NO_2 groups are sigma bonded at 3,5 (*meta*)-positions of the phenyl ring and has a length of 1.474 Å. Since the bond length of the *para* position methyl group is higher than that of nitro group, the supplied heat energy during pyrolysis was first used to cease the methyl group followed by the nitro group and then triazole group. Consequently less quantity of NO_2 molecules is released. While, for *P*-NH_2-DNPT the bond lengths between the *para* position amino group to phenyl ring and *meta* nitro groups to phenyl ring are 1.330 Å and 1.450 Å. The supplied heat energy at initial level is utilized to cease the $–NO_2$ groups from the phenyl ring rather than an $–NH_2$ group, because the NO_2 group attached to the phenyl ring with higher bondlength than $–NH_2$ group. Consequently, high yield of NO_2 molecules are released which leads to the generation of the strongest PA signal of the order of 582.99 mV.

In case of *P*-OMe-DNPT, the bond length between *para* methoxy group to phenyl ring is 1.345 Å, and nitro group to phenyl ring is 1.476 Å. Therefore, in decomposition process NO_2 molecules released initially and followed by $–OCH_3$ group and its fragments. $-OCH_3$ group is can be defragmented into O, CO, H_2, H_2O etc. It appears that the concentration of either of these fragments is equally high along with NO_2 in the gas mixture which has no absorption in 532 nm range. Therefore, the acoustic modes possess a pair of peaks and have low strength PA signal for *P*-OMe-DNPT, even though, *P*-OMe-DNPT initially releases a high quantity of NO_2 along with other gaseous molecules. The strength of the PA signal is only monitored in terms of NO_2 concentration. Whereas, the presence of other gas molecules leads to broadening of the profile of acoustic modes

along with the shift from the actual central frequency and calculated values of modes. It is well known that the double bonded molecules have higher bond strengths. Therefore, the rupture of single bond (C-N) molecules requires lower energy than the double bond (N=N) molecules. Here, the process of decomposition of reported 1,2,4-triazoles is completed in two steps. In the first step, the triazole moiety is separated from the phenyl ring, and the final step follows with concerted ring breaking. The aromatic ring like triazole moiety requires high energy than the aliphatic groups such as $-CH_3$, $-OCH_3$ and $-NH_2$ for separation from the ring. The entire molecules along with their principal functional groups are decomposed easily at high temperature. The expected order of ceased functional groups from the ring during the process of decomposition with respect to the supplied heat energy is listed in Table. 5.3. The decomposition mechanism might be more complex, and it may involve bond rearrangements and isomerizations before fragmentation or decomposition. However, the order of ceased functional groups from compounds can be confirmed on the basis of PA spectra in terms of their excited acoustic modes and intensity.

Table 5.3: The expected order of ceased functional groups.

Compound	Ceased order
P-Me-DNPT	$-CH_3$, $-NO_2$, -triazole
P-OMe-DNPT	$-NO_2$, -triazole, $-OCH_3$
P-NH_2-DNPT	$-NO_2$, -triazole, $-NH_2$

The initial weights (I_w) of *P*-Me-DNPT, *P*-OMe-DNPT and *P*-NH_2-DNPT used for TG-DTA analyis are 1.589 mg, 1.002 mg and 3.254 mg, respectively. The estimated percentile of residual quantity for corresponding compounds from weight loss curve at 400 ^oC are 3%, 10% and 15% respectively. The highest PA signal obtained for this successive compounds at t = 0.5 ms are given by 54.11, 19.36 and 582.99 mV. While, for t = 1 ms, these are 30.08, 9.7 and 36.12 mV, respectively. Even though the initial weight of *P*-OMe-DNPT is less, it shows comparatively high residual weight and lower strength of the PA signal than the other two compounds. Hence, on the basis of the residual weight from TGA curve and the strength of the PA signal, the efficiency of these compounds as a rocket fuel follows the sequence: *P*-NH_2-DNPT > *P*-Me-DNPT > *P*-OMe-DNPT. The similar order is applicable for explosive properties of these compounds. The efficiency of these compounds as a rocket fuel is ascertained on the basis of released quantity of NO_2 molecules in terms of the strength of PA signal. Because, NO_2 is identified as freely released gas during the pyrolysis of HEMs, which is treated as a thermal marker [55,60,63].

5.4. 266 nm based study of 1,2,4-triazoles

5.4.1. Thermal PA spectra

Fig. 5.5(a-c) shows 266 nm based thermal PA spectra of *P*-Me-DNPT, *P*-OMe-DNPT and *P*-NH_2-DNPT, respectively. The PA spectra were recorded between 40-350 °C range, at E_{in} = 10 µJ and t = 0.5 ms. In the case of 266 nm, very low incident laser energy of the order of 10 µJ is sufficient to generate the strong PA signal. This is because HEMs vapor and its dissociation fragments such NO_2, NO, CO, CO_2, HCN, and H_2O etc. have strong absorption. The PA spectra of these compounds have similar excited acoustic modes located at 3.8, 8.4, 13.8, 27.8 and 38.8 kHz with small variation in the central frequency of acoustic modes. Whereas, it remain's unchanged for particular compound as a function of temperature. This indicates that compounds release similar type of gaseous mixture during their decomposition between 40-350 °C range. The central frequencies of acoustic modes have shifted to ± 200 Hz from one to another compound.

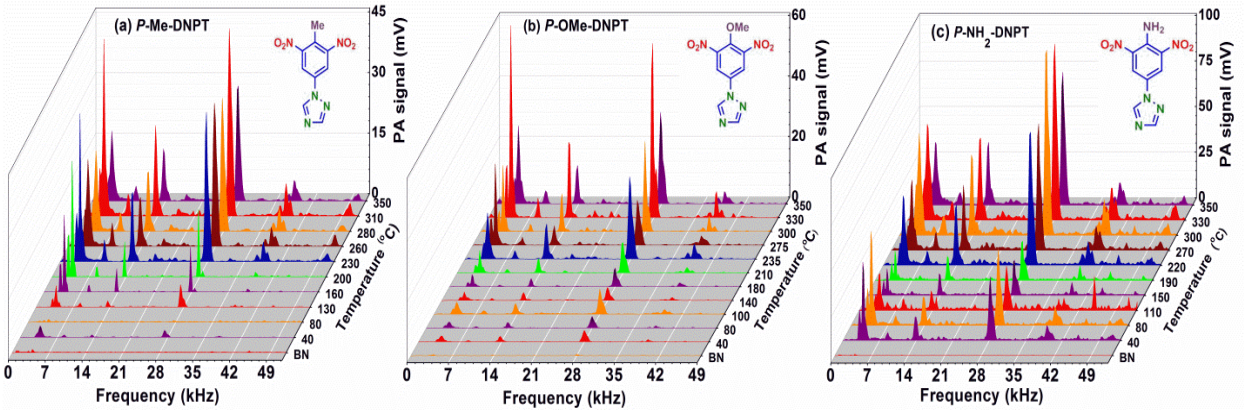

Figure 5.5: Temperature based PA spectra of (a) *P*-Me-DNPT, (b) *P*-OMe-DNPT and (c) *P*-NH_2-DNPT.

In the thermal PA spectra of *P*-Me-DNPT as shown Fig. 5.5(a), first PA signal obtained at 130 °C and the modes become more intense with further increase in temperature. Fig. 5.5(b) shows that *P*-OMe-DNPT has almost constant PA signal between 40-180 °C range. However, Fig. 5.5(c) indicates that *P*-NH_2-DNPT has a strong signal at 40 °C, and then after the intensity is decreased up to 190 °C. The maximum strength of PA signal is obtained at 310 °C for *P*-Me-DNPT, 330 °C for *P*-OMe-DNPT and 300 °C for *P*-NH_2-DNPT. These temperatures are near to the actual decomposition temperatures 260, 275 and 270 °C. The maximum strength of PA signals obtained for the studied compounds follows the order: *P*-NH_2-DNPT > *P*-OMe-DNPT > *P*-Me-DNPT. Due to the presence of -NH_2 group, *P*-NH_2-DNPT has higher density, which leads to release the high quantity of gaseous mixture, as a result provided the higher strength of PA signal as compared to the other compounds. The N-NO_2 and C-NO_2 bonds are the weakest bonds in the energetic ring, and the rupture of these bonds is the initial step in the decomposition [64-66]. The chemical substituent like -NH_2,-OCH_3 are increase the

density of compounds than -CH_3 and initially lead to the release NO_2 molecules which is followed by other gaseous byproducts. The results obtained from PA technique reveal that higher concentrations of gaseous molecules are released from *P*-NH_2-DNPT and *P*-OMe-DNPT as compared to *P*-Me-DNPT. Therefore, nitrogen (N), oxygen (O), and nitro (NO_2) rich triazole derivatives are potentially interesting energetic materials because of high density, energy. These materials can be used as solid propellants and explosives [67].

5.4.2. Evaluation of thermal stability and efficiency as a rocket fuel

Fig. 5.6(a-c) shows the behavior of excited acoustic modes with respect to temperature. Fig. 5.6 (a) shows that *P*-Me-DNPT released a similar concentration of gaseous fragments between the temperature 40-130 °C with further increase in vapor temperature, the acoustic modes show growth in their intensity and has two peaks at 230, 310 °C. All the acoustic modes show similar behavior with variation in their predominant order with respect to temperature. The significance of PA signal observed at initial temperatures due to strong absorption of 266 nm by entire molecule vapor.

Fig. 5.6(b) depicts that *P*-OMe-DNPT releases a nearly similar quantity of gaseous molecules between 40-210 °C, range. However, the PA signal curves have slightly high intensity near the melting temperature i.e. 100 °C (97.92 °C). The intensity of acoustic modes is high at the temperatures 235 and 330 °C. For *P*-NH_2-DNPT, as shown in Fig. 5.7(c), The intensity of acoustic modes at 8.4, 18.8 and 38.8 kHz does not show any variation between 40-190 °C, range. The intensity of predominant modes present at 3.8 kHz and 28.2 kHz are high at the initial temperature. However, all the acoustic modes possess maximum intensity at 220 and 300 °C. The constant PA signals obtained as a function of temperature confirms the thermal stability of compounds.

In addition, the efficiency of these compounds as a rocket fuel is found to be of the order of *P*-NH_2-DNPT > *P*-Me-DNPT > *P*-OMe-DNPT. This evaluation is based on the strength of PA signal obtained from PA spectra and residual weight measured from the weight loss (TGA) curve. The energetic properties, I_w and R_w obtained from TG-DTA data and maximum intensity of PA signal of the compounds are comprised in Table 5.4.

Table 5.4: The values of ρ, D, P, I_w, R_w and intensity of PA signal.

Compound	ρ (g/cm³)	D (km/s)	P (GPa)	TG-DTA		PAS (mV)
				I_w (mg)	R_w (%)	t = 0.5 ms
P-Me-DNPT	1.62	6.40	17.01	1.589	3	46.42
P-OMe-DNPT	1.64	6.68	18.68	1.002	10	63.55
P-NH_2-DNPT	1.66	6.66	18.74	3.254	15	101.42

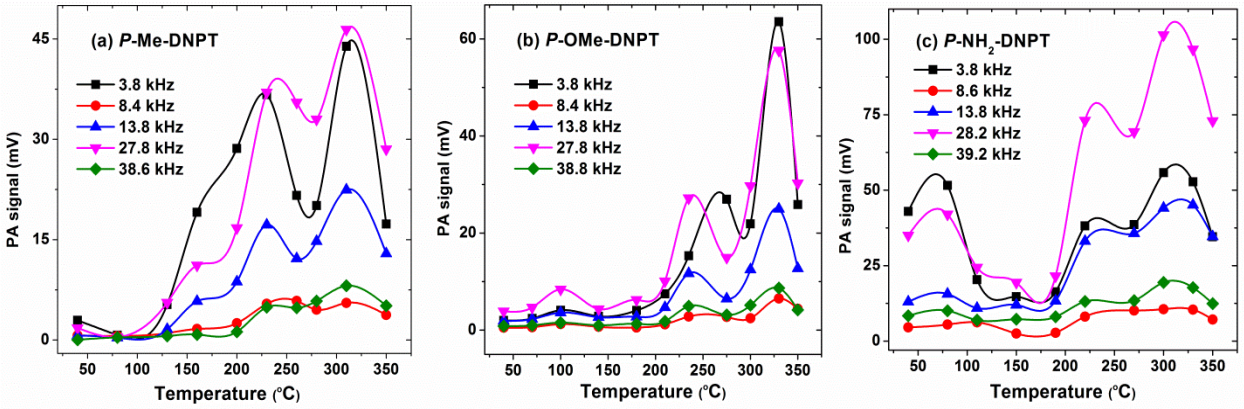

Figure 5.6: PA signal of acoustic modes vs temperature (a) *P*-Me-DNPT (b) *P*-OMe-DNPT and (c) *P*-NH_2-DNPT.

P-OMe-DNPT is less efficient as a rocket fuel compared to that of *P*-Me-DNPT even though it released high quantity of gaseous molecules and having high detonation pressure and velocity of detonation. Because, it shows more residual weight is 10 % for the initial weight of 1.002 mg, whereas residual weight for *P*-Me-DNPT is 3% of initial weight of 1.589 mg. *P*-OMe-DNPT has the highest residual weight even for a small quantity of initial weight, which indicates that it is less efficient for rocket fuel.The controlled PA pyrolysis process carried out for all the solid samples using a small quantity i.e. ~1.0 mg. *P*-NH_2-DNPT has highest density 1.66 g cm^{-3}, detonation pressure 18.74 GPa. Therefore, it releases a high concentration of gaseous byproducts. Consequently, the strength of PA signal is higher as compared to other compounds and indicates that it is much efficient material as a rocket fuel. The velocity of detonation for these compounds has been shown in Table 5.4 is 6.66, 6.40, 6.68 km/s, respectively. *P*-OMe-DNPT has high detonation velocity it might be due to presence of additional O atom. High density play vital role in the performance of an energetic material because the detonation pressure is proportional to the square of its density [68].

In earlier section-5.3.2, the thermal stability of these compounds was evaluated based on the released quantity of NO_2, which depends on bond lengths of deposited chemical substituent. In the present case the thermal stability of the compound is evaluated on the basis of released quantity of total vapor. The results obtained from both the laser pulses confirms that PA technique is one of the emerging spectroscopic analytical technique to examine the thermal stability and decomposition mechanism of newly synthesized energetic materials and to scale their efficiency as a rocket fuel. The burning temperature of rocket fuels is more than 400 °C. Here, the compounds are directly burnt with oxidizers as a result the compounds release the end products of C-H-N-O [69]. Moreover, in the present experiment recording of PA signal above 400 °C is restricted due to the diaphragm of the microphone because it can get damage at higher temperature region. Therefore, the thermal stability and efficiency of HEMs as a rocket fuel evaluated up to 400 °C.

5.4.3. Comparative study on PA fingerprints

Fig. 5.7(a-c) shows the maximum intensity PA spectra of 1,2,4-triazoles. The inset figure shows the time signals recorded at incident laser energy of E_{in} = 10 μJ and data acquisition time of t = 1 ms. The excited acoustic modes and corresponding intensities are comprised in Table 5.5. The structures of these compounds are similar except their major chemical substituent present at *para* position of the phenyl ring. These compounds release similar type of gaseous mixture with different concentrations. As a result, the compounds possess similar cavity modes with a small shift in the frequency, and they have different intensities. The intensity of acoustic modes is high for *P*-NH_2-DNPT and it has additional modes compared to other samples. The additional acoustic modes in the PA spectra represents that the material is decomposed totally and released various types of byproducts.

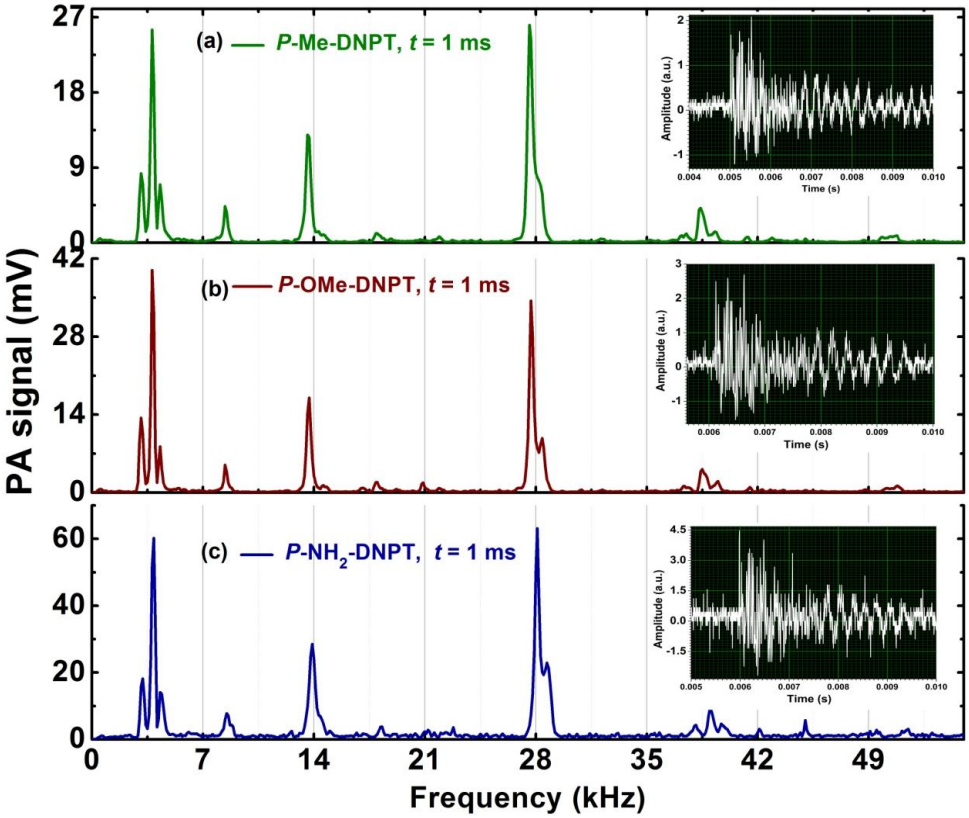

Figure 5.7: PA fingerprint spectra of (a) *P*-Me-DNPT (b) *P*-OMe-DNPT and (c) *P*-NH_2-DNPT at T_d and t = 1 ms.

Table 5.5: Excited acoustic modes f (kHz) and their intensities I (mV).

P-Me-DNPT	*f*:	3.1	3.8	4.3	8.4	13.6	18	27.6	37.5	38.4	39.3					
	I:	8.3	25.5	6.9	4.4	12.9	1.1	26.1	1.1	4.2	1.3					
P-OMe-DNPT	*f*:	3.1	3.8	4.3	8.4	13.7	18	20.9	27.7	28.4	38.5	39.5				
	I:	7.9	23.6	4.9	2.9	10.1	1.1	1.0	20.4	5.8	2.5	1.2				
P-NH_2-DNPT	*f*:	3.2	3.9	4.3	8.5	13.9	18.3	21.2	22.8	28.1	28.7	38.1	39.0	39.7	42.1	45.0	51.5
	I:	18.2	60.3	14.1	7.8	28.5	3.8	2.8	3.6	63.2	22.9	4.3	9.5	4.7	3.1	5.7	3.1

It is clearly observed in Table 5.5, that the excited acoustic modes have small shift in their central frequencies from one sample to another sample. The predominant modes in PA spectra of all compounds are occupied at 3.8, 13.8 and 27.8 kHz. The 532 nm based PA spectra of compounds completely differ from the 266 nm based PA spectra. In both cases, the PA spectra were recorded using same PA cell of internal radius 0.75 cm and length of 7.5 cm. This supports that the absorption mechanism of gas molecules is different from UV-visible wavelengths. As a result, the propagation of generated acoustic pressure waves were different.

5.5. Conclusions

The thermal PA spectra have been successfully recorded for the newly synthesized 1,2,4-triazoles. The bond breaking mechanism during thermal decomposition process ascertained based on bond lengths of principal functional groups. The thermal stability explained based on the strength of PA signal obtained from UV-visible wavelengths and TG-DTA analysis. The efficiency of these compounds as a rocket fuel was investigated and found to be in the given order *P*-NH_2-DNPT > *P*-Me-DNPT > *P*-OMe-DNPT.

References

1. Q. Wu, W. Zhu, and H. Xiao, RSC Adv. **4**, 53000 (2014).
2. D. Srinivas, V. D. Ghule, and K. Muralidharan, RSC Adv. **4**, 7041 (2014).
3. A. S. Kumar, V. D. Ghule, S. Subrahmanyam, and A. K. Sahoo, Chemistry **19**, 509 (2013).
4. Y. Zhang, D. A. Parrish, and J. M. Shreeve, J. Mater. Chem. A **1**, 585 (2013).
5. N. Fischer, D. Fischer, T. M. Klapötke, D. G. Piercey, and J. Stierstorfer, J. Mater. Chem. **22**, 20418 (2012).
6. T. M. Klapötke and C. M. Sabaté, Chem. Mater. **20**, 3629 (2008).
7. H. S. Jadhav, M. B. Talawar, R. Sivabalan, D. D. Dhavale, S. N. Asthana, and V. N. Krishnamurthy, J. Hazard. Mater. **143**, 192 (2007).
8. P. Zhang, S. J. Klippenstein, L. B. Harding, H. Sun, and C. K. Law, RSC Adv. **4**, 62951 (2014).
9. T. M. Klapo, P. Mayer, A. Schulz, and J. J. Weigand, J. Am. Chem. Soc. **127**, 2032 (2005).
10. X. Liu, Q. Yang, Z. Su, S. Chen, G. Xie, Q. Wei, and S. Gao, RSC Adv. **4**, 16087 (2014).
11. V. Kraft, W. Weber, M. Grutzke, M. Winter, and S. Nowak, RSC Adv. **5**, 80150 (2015).
12. J. Cheng, R. Zhang, Z. Liu, L. Li, F. Zhao, and S. Xu, RSC Adv. **5**, 50278 (2015).
13. R. Turcotte, M. Vachon, Q. S. M. Kwok, R. Wang, and D. E. G. Jones, Thermochim. Acta **433**, 105 (2005).
14. M. F. Foltz, C. L. Coon, F. Garcia, and A. L. Nichols III, Propellants, Explos. Pyrotech. **19**, 133 (1994).
15. D. E. G. Jones, P. D. Lightfoot, R. C. Fouchard, Q. Kwok, A. M. Turcotte, and W. Ridley, Thermochim. Acta **384**, 57 (2002).
16. S. Mousavi and K. Esmaeilpour, Cent. Eur. J. Energ. Mater. **10**, 455 (2013).
17. X.-R. Li and H. Koseki, J. Loss Prev. Process Ind. **18**, 460 (2005).
18. P. G. Laye and D. C. Nelson, Thermochim. Acta **153**, 221 (1989).
19. J. S. Caygill, F. Davis, and S. P. J. Higson, Talanta **88**, 14 (2012).
20. J. Hildenbrand, J. Herbst, J. Wöllenstein, and A. Lambrecht, Proc SPIE **7222**, 72220B (2009).
21. V. L. Korolev, T. V. Petukhova, T. S. Pivina, A. A. Porollo, A. B. Sheremetev, K. Y. Suponitskii, and V. P. Ivshinb, Russ. Chem. Bull. Int. Ed. **55**, 1388 (2006).
22. I. V Tselinskii, V. V Tolstyakov, S. M. Putis, and S. F. Mel, Russ. Chem. Bull. Int. Ed. **58**, 2356 (2009).
23. R. Tsyshevsky and M. Kuklja, Molecules **18**, 8500 (2013).
24. D. R. Godhani, A. A. Jogel, A. M. Sanghani, and J. P. Mehta, J. Chem. Pharm. Res **6**, 1034 (2014).
25. R. S. Stepanov, L. A. Kruglyakova, O. A. Golubtsova, and A. M. Astakhov, Chem. Heterocycl. Compd. **39**, 604 (2003).
26. A. A. Dippold and T. M. Klapötke, Chemistry **18**, 16742 (2012).
27. N. Sasidharan, B. Hariharanath, and a. G. Rajendran, Thermochim. Acta **520**, 139 (2011).
28. Z. Rui-Zhou, L. Xiao-Hong, and Z. Xian-Zhou, J. Chem. Sci. **124**, 995 (2012).
29. S. Tagomori, Y. Kuwahara, H. Masamoto, M. Shigematsu, and K. Wasana, 4th Int. Conf. Biol. Environ. Chem. IPCBEE **58**, (2013).
30. T. M. Klapotke, D. G. Piercey, and J. Stierstorfer, Eur. J. Inorg. Chem. 1509 (2013).
31. C. Ye, G. L. Gard, R. W. Winter, R. G. Syvret, B. Twamley, J. M. Shreeve, and M. Shreeve, Org. Lett. **9**, 3841 (2007).
32. Y. C. Li, C. Qi, S. H. Li, H. J. Zhang, C. H. Sun, Y. Z. Yu, and S. P. Pang, J. Am. Chem. Soc. **132**, 12172 (2010).
33. A. S. Kumar, N. Kommu, V. D. Ghule, and A. K. Sahoo, J. Mater. Chem. A **2**, 7917 (2014).
34. S. Garg and J. M. Shreeve, J. Mater. Chem. **21**, 4787 (2011).
35. A. A. Dippold, D. Izs??k, and T. M. Klap??tke, Chem. - A Eur. J. **19**, 12042 (2013).
36. G.-H. Tao, B. Twamley, and J. M. Shreeve, J. Mater. Chem. **19**, 5850 (2009).
37. V. Thottempudi, H. Gao, and J. M. Shreeve, J. Am. Chem. Soc. 6464 (2011).
38. D. Srinivas, V. D. Ghule, and K. Muralidharan, RSC Adv. **4**, 7041 (2014).

39. M. Crawford, K. Karaghiosoff, T. M. Klapo, and F. A. Martin, Inorg. Chem. **48**, 1731 (2009).
40. C. Darwich, T. M. Klapotke, and C. M. Sabate, Chem. - A Eur. J. **14**, 5756 (2008).
41. J.-T. Wu, J.-G. Zhang, X. Yin, Z.-Y. Cheng, and C.-X. Xu, New J. Chem. **39**, 5265 (2015).
42. Y. Q. Guo, a Bhattacharya, and E. R. Bernstein, J. Phys. Chem. A **113**, 85 (2009).
43. HITRAN 2014 Database,online Http//www.hitran.com/.
44. K. S. Rao, A. K. Chaudhary, F. Yehya, and A. S. Kumar, Spectrochim. Acta Part A Mol. Biomol. Spectrosc. **147**, 316 (2015).
45. M. S. Park, K.-H. Jung, H. P. Upadhyaya, and H.-R. Volpp, Chem. Phys. **270**, 133 (2001).
46. A. Strachan, E. M. Kober, A. C. T. van Duin, J. Oxgaard, and W. a Goddard, J. Chem. Phys. **122**, 54502:1 (2005).
47. A. V. Kimmel, P. V. Sushko, A. L. Shluger, and M. M. Kuklja, J. Chem. Phys. **126**, 234711:1 (2007).
48. T. B. Ryerson, E. J. Williams, and F. C. Fehsenfeld, J. Geophys. Res. **105**, 26447 (2000).
49. Y. Sadanaga, Y. Fukumori, T. Kobashi, M. Nagata, and N. Takenaka, Anal. Chem. **82**, 9234 (2010).
50. I. During, W. Bachlin, M. Ketzel, A. Baum, U. Friedrich, and S. Wurzler, Meteorol. Zeitschrift **20**, 67 (2011).
51. I. Barnes and K. J. Rudziński, NATO Sci. Peace Secur. Ser. C Environ. Secur. **120**, 15 (2013).
52. E. J. Dunlea, S. C. Herndon, D. D. Nelson, R. M. Volkamer, F. San Martini, P. M. Sheehy, M. S. Zahniser, J. H. Shorter, J. C. Wormhoudt, B. K. Lamb, E. J. Allwine, J. S. Gaffney, N. a. Marley, M. Grutter, C. Marquez, S. Blanco, B. Cardenas, a. Retama, C. R. Ramos Villegas, C. E. Kolb, L. T. Molina, and M. J. Molina, Atmos. Chem. Phys. **7**, 2691 (2007).
53. C. T. Dinh, S. Hoogland, and E. H. Sargent, Ind. Eng. Chem. Res. **54**, 12750 (2015).
54. A. Strachan, E. M. Kober, A. C. T. van Duin, J. Oxgaard, and W. A. Goddard, J. Chem. Phys. **122**, 54502:1 (2005).
55. F. Yehya and A. K. Chaudhary, Sensors Actuators B. Chem. **178**, 324 (2013).
56. F. Yehya and A. K. Chaudhary, Appl. Phys. B 22 (2012).
57. N. Kommu, V. D. Ghule, A. S. Kumar, and A. K. Sahoo, Chem. Asian J. **9**, 166 (2014).
58. J. A. Conkling, *Propellants*, Second Edi (Scientific American, 1996).
59. K. S. Rao and A. K. Chaudhary, Thermochim. Acta **614**, 149 (2015).
60. F. Yehya and A. K. Chaudhary, Appl. Phys. B **110**, 15 (2012).
61. P. J. Crutzen and M. Oppenheimer, Clim. Change **89**, 143 (2008).
62. A. Burcat and A. Lifshitz, J. Phys. Chem. **74**, 263 (1970).
63. K. S. Rao, F. Yehya, A. K. Chaudhary, A. S. Kumar, and A. K. Sahoo, J. Anal. Appl. Pyrolysis **109**, 132 (2014).
64. Q. Zhao, S. Zhang, and Q. S. Li, Chem. Phys. Lett. **407**, 105 (2005).
65. J. S. Murray and P. Politzer, in *Chem. Phys. Energ. Mater. SE - 8*, edited by S. Bulusu (Springer Netherlands, 1990), pp. 157–173.
66. S. Zhang and T. N. Truong, J. Phys. Chem. A **104**, 7304 (2000).
67. J. S. Boyer, *Nitrozoles* ((Deerfield Beach: VCH Publishers), 1986).
68. T. Fendt, N. Fischer, T. M. Klapötke, and J. Stierstorfer, Inorg. Chem. **50**, 1447 (2011).
69. A. Jai Prakash and H. Robert, *Organic Chemistry of Explosives* (Wiley, 2006).

Intentional left blank page

Chapter 6

Identification of solid HEMs in graphite mixture

Abstract

This chapter describes the time resolved PA spectra of different types of solid carbon blacks obtained from wood charcoal; graphite powder and diesel soot using 532 nm wavelength pulses of duration 30 ps at a repetition rate of 10 Hz. The results of the photoacoustic and Raman spectroscopy allow us to evaluate the potential use of graphite powder as a sensor for the identification of trinitrotoluene (TNT) explosive. For the first time a new modality has been developed based on graphite and propose the potential use of visible-IR wavelengths i.e. 532, 1064 nm for identification of solid HEMs.

A part of the work presented in this chapter has appeared in the following publication:

[1] **K. S. Rao**, A. K. Chaudhary, and F. Yehya, *Sensors Actuators B Chem.*, 2016, **231**, 830–836.

6.1. Introduction

In recent years, many optical techniques have been used for the detection of explosives such as CL-20, RDX, TNT, HMX, PETN, ANTA and other high-energy materials (HEMs) in solid, liquid and vapor phase [1-5]. These techniques are mainly based on either absorption or emission of light from the explosive materials. These explosive molecules exhibit strong absorption in deep UV (due to electronic transitions), IR region (due to the presence of both vibration and rotational lines) and THz region due to the presence of pure rotational lines in the ground level [6-8]. Therefore, absorption based technique is often divided into three broad categories such as Deep UV- UV, Mid-IR and THz region. Pushkarsky et al. demonstrated the detection of TNT using laser based photoacoustic (PA) technique [9]. They have explored the continuous-wave high-power quantum cascade laser in external grating cavity geometry. The laser was tunable between 400 nm and 7.3 μm wavelength range. M. Snels et al. have detected the solid explosive TNT in the near infrared spectral range between 1560 and 1680 nm using cw cavity ring down (CRD) spectroscopy [10]. They have used a flash heater to evaporate solid TNT in a CRD absorption cell. A.V. Deshmukh et al. investigated the TNT in water samples collected from nearby military training centre using solid phase micro extraction technique coupled with Fourier Transform Raman Spectroscopy [11]. Noorhayati Idros et al. demonstrated the colorimetric-based detection of TNT explosives using functionalized silica nano particles [12]. Many other groups detected or identified the explosives using different types of techniques [13-18]. However, existing spectroscopic data indicates that explosive molecules do not possess any absorption band in the visible region. Therefore, recording of PA signal using visible light is still a major challenge in explosive detection. The time resolved spectra of carbon blacks such as wood charcoal (WB), graphite powder (GP) and soot obtained from diesel (DS), TNT in graphite matrix were recorded using a solid PA cell employed with Q-switched Nd: YAG laser (532 nm, 30 ps, 10 Hz). This is a non-destructive technique and requires a small quantity of sample [19-21]. Wood charcoal, graphite powder and diesel soot are different from each other with respect to their specific surface area, particle size and structure, conductivity, and color. Carbon blacks are manufactured under controlled conditions for commercial use primarily in the rubber, painting, and printing industries. In contrast, soots are unwanted byproducts from the combustion of carbon-based materials for the generation of energy or heat, or for waste disposal [22,23]. The terms carbon black and soot often have been used interchangeable; although carbon black is physically and chemically distinct from soot. The carbon blacks, soot, other carbon elements are associated with the particulate carbon. Therefore, the samples wood black (WB), graphite (GP) and Diesel soot (DS) are subjected to Raman spectra to carry out the comparative study based on

their disorder (D) and graphite (G) bands. Carbon materials are opaque in optical range, and their Raman spectra originate from a few tens of nanometers of the surface due to inelastic scattering [24]. The skin depth factor $(\lambda_o/4\pi nk)$ indicates that higher wavelengths have a greater penetration depth [25], where, λ_o is the wavelength, *n* stands for refractive index and *k* is wave vector. Therefore, it is possible to relate the phenomena of band shifting in the structure below the surface of materials.

The carbon atoms in graphite arranged in a hexagonal structure where one carbon atom forms covalent bond with three surrounding atoms [26]. It is well known that carbon has a valence of 4 and can make four bonds. Therefore, 3 electrons of carbon forms 3 bonds among themselves, and other free electron floats freely between two layers of carbon plates as shown in Fig. 6.1(a). This free electron is delocalized and mobile, thus it can conduct electricity and give graphite the property of an electric conductor despite being a non-metal. A force is created between these two layers of carbon with the aid of the electrons known as Van Der Waal forces [27,28]. A. C. Ferrari studied the origin of the D and G bands along with second order D peak of the graphene [29].

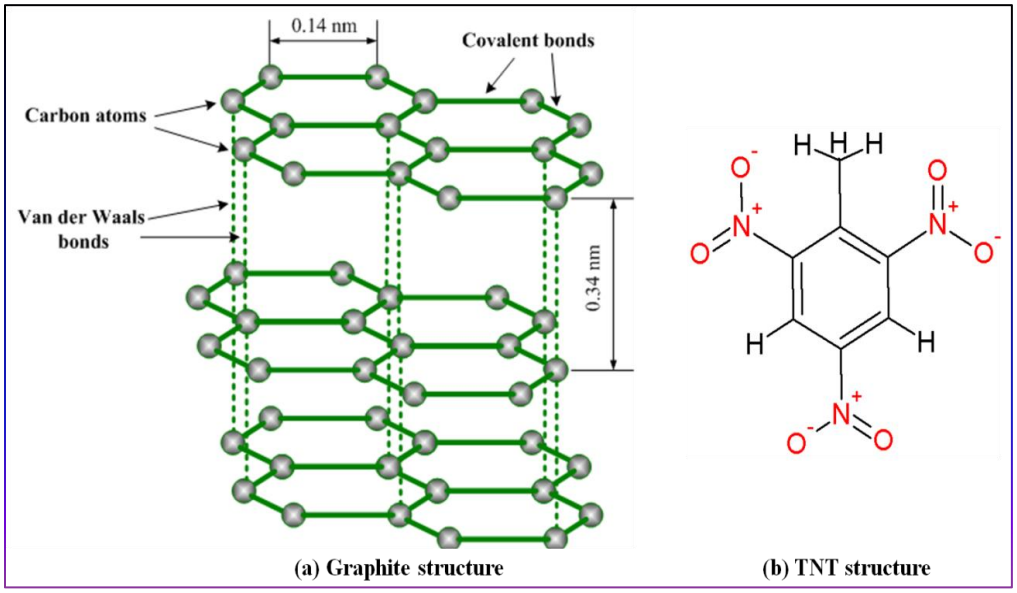

Figure 6.1: Structure of (a) Graphite and (b) TNT.

Graphene is the two-dimensional (2D) building block for carbon allotropes of every other dimensionality. It can be stacked into 3D graphite, rolled into 1D nanotube, or wrapped into 0D fullerenes. The G and 2D Raman peaks change in shape, position and relative intensity with number of graphene layers. This reflects the evolution of the electronic structure and electron–phonon interactions. The broad range of excitation energy of graphite which lies between 1.91 and 2.52 eV i.e. 649 and 488 nm range, showing the first and second order Raman spectra of the graphite [29-33]. Raman spectroscopy is a well-established tool for vibration spectroscopic analysis and employed

for identification and detection of explosives. Xiaofeng Wang et al. analyzed Raman spectra of industrial TNT dissolved in acetone and reported the seven number of major Raman bands [34]. They have used diode pumped Nd: YVO4 solid laser at wavelength 1064 nm as an excitation source. In the present case, we have recorded the solid TNT Raman spectra using λ = 532 nm (model: Witech focus innovations 300 system software, with central wavelength 600 nm). The Raman lines of TNT obtained at 1064 nm from [34] and 532 nm wavelengths (in our case) are listed in Table 6.1.

Table 6.1: TNT Raman lines at 1064 nm and 532 nm wavelengths

Raman lines (cm^{-1})		Description
1064 nm	at 532 nm	
1616.9	1617.95	C=C aromatic stretching vibration
1533.9	1537.26	NO_2 asymmetric stretching vibration
1360.1	1365.14	NO_2 symmetric stretching vibration
1210.5	1214.70	C_6H_2-C vibration
822.9	826.25	nitro-group scissoring mode
792.3	795.27	C-H out-of-plane bend)
326.7	326.16	framework distortion mode

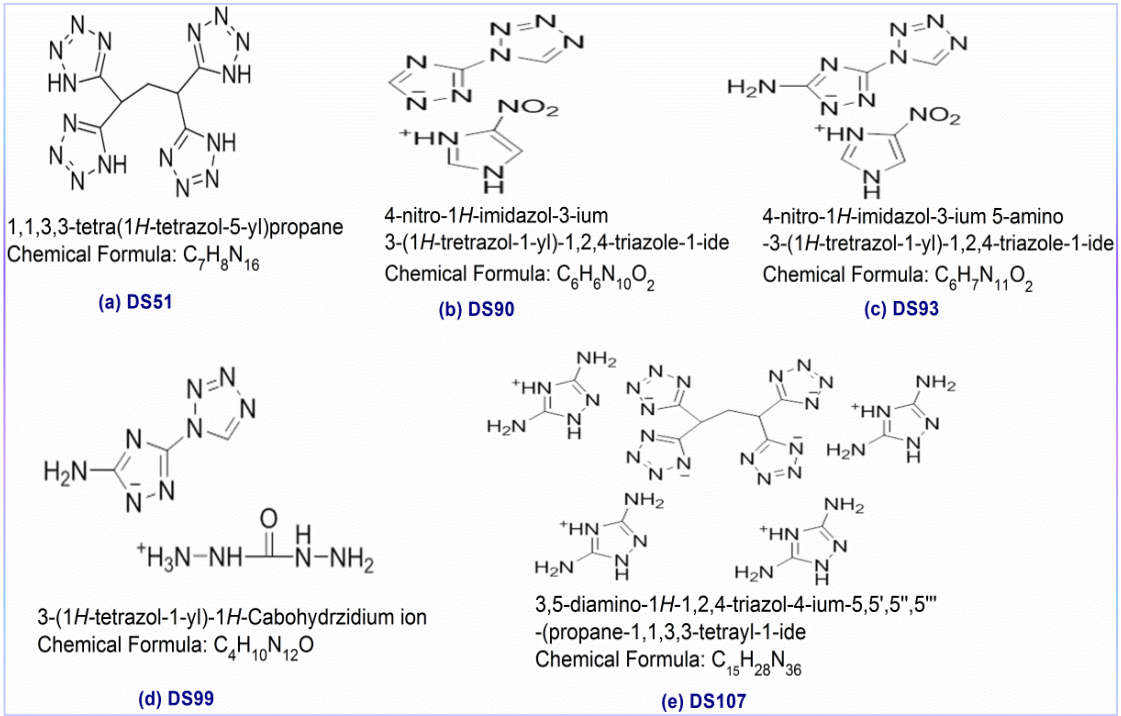

Figure 6.2: Structures of (a) DS51 (b) DS90 (c) DS93 (d) DS99 and (e) DS107.

When laser irradiates the mixture of HEMs in graphite, it provides double resonance Raman lines between them due to the electron-phonon or phonon-phonon interactions. This is possible due to pi-orbitals coupling, which leads to shift in the D and G bands of graphite as well as TNT Raman bands in the mixture. However, other energetic materials reported in this chapter do not show any Raman spectra at 532 nm wavelength. In this case, the Raman spectrum of graphite shows shift and observed that variation in the intensities of D and G bands. This confirms pi-electron coupling between HEMs and graphite. Therefore, our study shows that graphite plays an important role in the recording of photoacoustic fingerprint spectra of TNT and other HEMs such as nitrogen-rich imidazole, 1, 2, 4-triazole and tetrazole-based compounds as shown in Fig. 6.2. The micro structural changes are predicted in terms of shift in Raman lines of graphite and TNT mixture. The physical implications of Raman bands in the identification of explosives can be more efficiently realized when it is combined with pulsed PA spectroscopy technique.

6.2. Selection of graphite as sensor of HEMs in the 532 nm wavelength range

The experimental set up used for this study is shown in Fig. 2.4 (chapter-2). The experiments carried out in four steps: in the first step, the PA spectra of carbon black i.e., WB, GP and soot obtained from diesel recorded at different data acquisition time and incident laser energies. In the second step, the quantity analysis of PA signal of different samples was carries out after calibration and recording the responsivity. In the third step, the Raman spectrum of carbon blacks, diesel soot and HEMs in graphite mixture were recorded. Finally, the PA spectra of solid HEMs mixed with graphite mixture were recorded.

6.2.1. PA spectra of wood black, graphite powder and diesel soot

It was observed that PA spectra of all samples lie between 0-40 kHz range. The acoustic modes between 0-5 kHz possess higher response than the 5-40 kHz range. Moreover, 0-5 kHz is predominant by external noise. However, within 5-40 kHz range the excited acoustic modes show pair of peaks with considerable intensities. Therefore, it is decided to characterize the PA spectra of samples between 5-40 kHz range and presented PA spectra of samples within this range in their respective figures.

Fig 6.3(a-c) shows the PA spectrum of WB, GP and DS samples recorded at data acquisition time (t)=1 ms. The incident laser energy (E_{in})=3.25 mJ is used for WB and GP, while E_{in}=1.0 mJ for DS. Inset figures exhibit the corresponding time domain PA signals. The excited PA modes for WB are located at 13.9, 19.0, 23.9, 29.5 and 31.3 kHz and their corresponding strengths are of the order of 6.91, 12.11, 21.94, 20.10, and 13.91 mV. Out of which the sharp intense peak appears at 23.9 kHz.

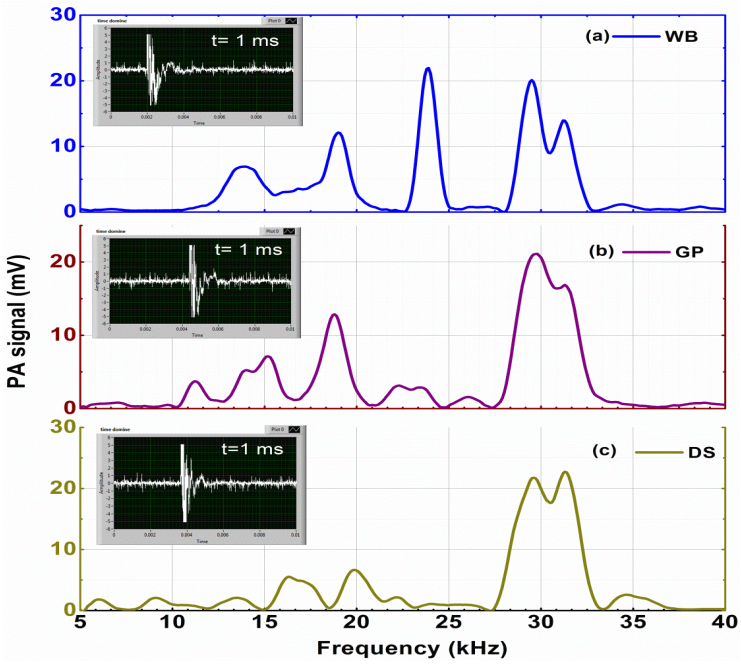

Figure 6.3: PA spectra of (a) WB (b GP and (c) DS.

The excited PA modes for GP are located at 11.2, 14.1 15.1, 18.7, 29.7 and 31.3 kHz having intensities 3.72, 7.12, 7.09, 12.75, 21.09 and 17.17 mV. The PA spectrum of GP has single intense peak at 18.7 kHz along with a pair of signature peaks at 14.1 and 15.1 kHz. The intense acoustic modes for DS are located at 30 and 20 kHz having intensities 22.74 and 7.05 mV. Other excited acoustic modes are present at 6, 9.2, 13.5 16.3, 19.9, 29.6 and 31.3 kHz and having the intensities of order of 1.82, 2.09, 2.08, 5.55, 6.69, 21.75 and 22.74 mV, respectively.

6.2.2. Comparative study of PA spectra of carbon samples

6.2.2.1. Data acquisition time

Fig 6.4(a) depicts the PA signal recorded at E_{in}=3.25 mJ for WB and GP, and E_{in}= 1.0 mJ for DS with respect to different data acquisition time. The excited acoustic modes show exponential decay behavior. The decay time of WB and DS is 0.34 ms, while for GP it is 0.35 ms. GP has faster decay time than the other two samples. Therefore, the excited acoustic modes of GP show moderate PA response as compared to WB and DS.

6.2.2.2. Incident laser energy

Fig. 6.4(b) displays the PA response of carbon samples with respect to incident laser energy. This study highlights the effect of E_{in} on carbon blacks in terms of their time resolved spectra. GP shows little PA response as compared to the WB. However, DS shows the strongest response even when E_{in} is very low, it shows the saturation behavior at 0.7 mJ.

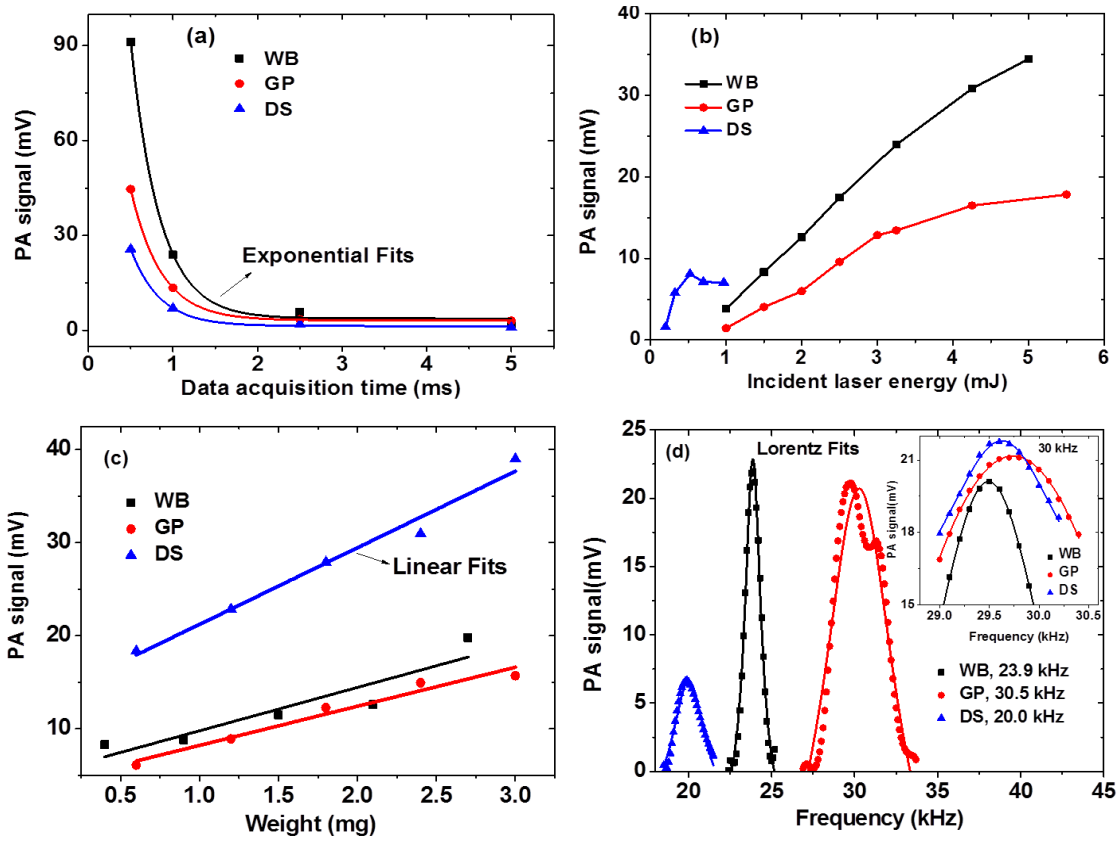

Figure 6.4: PA signals vs (a) *t*, (b) E_{in}, (c) weight of samples, and (d) Lorentz fit of sharp intense modes and 30 kHz mode (inset).

Table 6.2: The responsivity of PA cell with respect to incident laser energy and weight of sample.

Sample	E_{in}: Responsivity (V/J)	Weight: Responsivity (V/g)
WB	7.8	4.65
GP	3.88	4.2
DS	29.0	8.23

The PA responsivity of carbon blacks are measured by means of linear fitting of data points recorded before saturation point. The responsivity of WB, GP and DS is shown in Table 6.2. It is observed that the responsivity of DS is much higher than that of WB and GP. The minimum energy E_{in}= 1.0 mJ is required for the generation of PA signal for WB and GP, while DS needs only 200 μJ to produce a similar spectra. WB and GP are quite stable while DS is more volatile in nature. Therefore, a minimum laser energy is required to excite the DS sample. The full width at half maximum (FWHM) of the excited acoustic modes decrease with further increase in the incident laser energy [35]. The intensity ratio of the first predominant PA mode with respect to the second maximum mode (I_s/I_f) for WB and GP are 0.842 and 0.813, respectively, at E_{in}=3.25 mJ. However,

for DS the ratio of I_s/I_f is 0.29 at E_{in}= 1.0 mJ. The lower values of I_s/I_f provides the significant information about the parallel excitation of acoustic modes of PA cavity with respect to the incident laser wavelength. The I_s/I_f ratio of GP is lower than that of the other two samples, which implies that PA modes for graphite show linear behavior because of its well-defined crystal structure.

6.2.2.3. Weight of sample

Sensitivity/responsivity of the PA system is recorded with respect to different amount of samples. The PA signal increases linearly with sample weight until it becomes equal to the buffer weight. However, after crossing the buffer weight, there is a sharp fall in PA signal. We have recorded the PA signal from a homogeneous mixture of carbon blacks in silica gel matrix. The experiment was repeated several times using different concentrations of the homogeneous mixture of silica gel with each carbon sample. The background noise signal (BS) recorded using pure silica gel. The value of BS is less than 1.0 mV.

Fig 6.4(c) shows the responsivity of PA signal with respect to the weight of sample. As summarized in Table 6.2, the linear fit of the experimental data provided the responsivity of PA cell with respect to weight concentration of the samples. The response of PA signal of three samples is of the order of DS > WB > GP. Higher intercept values indicate that the strength of PA signal is greater at an initial concentration of the sample. Consequently, higher slope values show the high linear response of sample with respect to weight.

6.2.2.4. Quality factor

Quality factor 'Q' is defined in terms of the ratio of accumulated energy to that of energy loss per cycle. It is a ratio of the central frequency (ω) to FWHM (Δω) of the corresponding acoustic mode. Fig 6.4(d) shows the Lorentz fit of the maximum intensity modes of WB, GP and DS, while inset displays the Lorentz fit of 29.5 kHz mode. It provides the information about the central frequency (ω) and FWHM (Δω) which is required for calculating the quality factor. Fig. 6.4(d) clearly shows that WB and DS have sharp intense profile than the GP. At 29.5 kHz mode, the Q values of WB, GP and DS are 16, 5 and 19 respectively. The Q value of GP is less compared to other two samples. The order of the quality factor of carbon blacks is related to their microscopic structure, and it varies from carbon blacks of different sources of origin. Moreover, Q-factor is also related to loss of energy in the cavity for the given sample.

The comparative study is based on t, E_{in}, weight and Q of PA cavity which provides significant information about GP and its application for detection of explosive. It has less responsivity as compared to the WB and DS. If we mix the energetic materials with WB and DS the response of

pure samples is much stronger than the mixtures. However, purity of WB and DS varies from their respective sources and adulteration in diesel, and graphite as additional Raman lines. Therefore, for identification explosives using visible 532 nm wavelengths, GP is found to be the most suitable host medium.

6.2.3. Raman spectra of carbon blacks

Fig 6.5 shows the Raman spectra of carbon blacks. It was observed that GP shows additional Raman lines as compared to the other two samples. For instance, the peak at 2450 cm^{-1} and 2700 cm^{-1} (2D band) is due to double-resonance Raman scattering. WB and DS have similar spectra with a small shift in Raman bands. The strongest Raman peak (G bands) of WB, GP and DS are observed at 1580.82 cm^{-1}, 1585.77 cm^{-1} and 1597.50 cm^{-1}, respectively. The second highest peak (D bands) is found at 1342.62 cm^{-1}, 1361.01 cm^{-1} and 1356.51 cm^{-1}. However, GP shows additional Raman peaks at 2712.26 cm^{-1} and 3242.48 cm^{-1} and represents the 2D and 2G bands. Moreover, it has another line at wave number 2464.5 cm^{-1} (known as the G* band). The ratio of Raman intensities of D, G peaks i.e. I_D/I_G for WB, GP and DS are 0.935, 0.575, and 0.947, respectively. The intensity ratio is also treating as an important parameter to ascertain the quality of carbon blacks. The exciting wavelength of WB and GP for the Raman spectra is 531.91 nm, and for Diesel it is 531.78 nm. The ratios of I_s/I_f (PA) and I_D/I_G (Raman) values of GP are lower than WB.

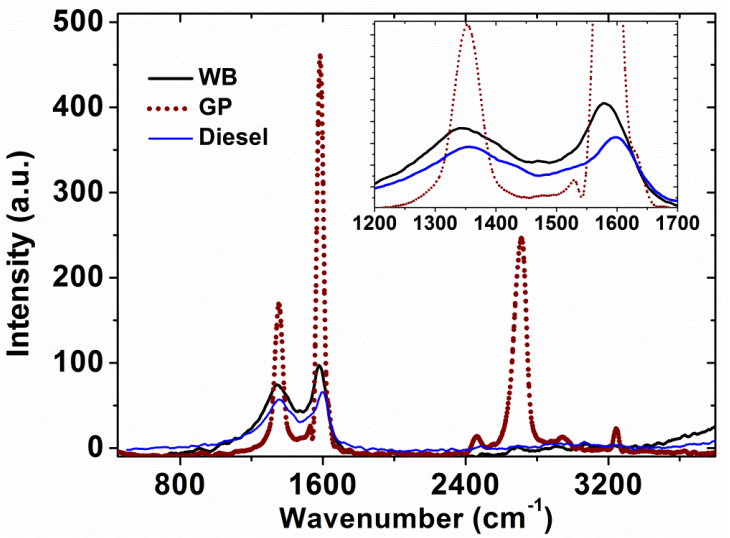

Figure 6.5: Raman spectra of carbon samples.

Raman spectrum of graphite has first order spectrum band at 1585.77 cm^{-1}, and it has a high intensity second order peak at 1361.01 cm^{-1}, which is due to presence of disorder at the focal spot of the laser. The G* and D* bands of graphite leads to across the Fermi energy level and is responsible for the resonant transition from the state '*I*' in the valance band to the state '*a*' in the conduction band. The excited electrons are scattered by phonons of arbitrary wave vector '*q*'. The PA spectrum

that is recorded without focusing the laser beam at wavelength 532 nm/1064 nm is attributed to *'G'* mode of Raman spectra. The intense laser energy enhances the probability of presence of D, D* and G* bands. Due to presence of these bands compared to WB and DS, GP work as a sensor for identification of HEMs.

6.3. Identification of TNT in GP graphite matrix using 532 nm

The PA spectra of TNT mixed with GP in equal ratios are recorded at t = 1 ms. GP shows strong absorption at 532 nm due to its lower band gap. The phonon waves present in D and G bands of graphite transfer their momentum to the D and G bands of TNT, which enhances the process of vibronic level transitions of TNT leads to absorb 532 nm by TNT molecules and help to generate the acoustic signal. The obtained acoustic signal is the resultant of GP and TNT mixture. The PA spectra of pure samples for GP and TNT were also recorded where the maximum background noise signal is 0.45 mV. In case of pure TNT, a small signal is detected after crossing the laser incident energy of 1.5 mJ. The generated acoustic signal of pure TNT is feeble in nature. Even high incident laser energy does not succeed in increasing the strength of the PA signal.

Fig 6.6 shows the normalized offset intensity counts of Raman spectra of GP, TNT and the mixture of GP+TNT samples. TNT has 16 numbers of Raman lines, which lie in the range of 150-3200 cm^{-1}. It has three strong vibronic Raman lines at 1537.26 cm^{-1},1365.15 cm^{-1} and 1617.95 cm^{-1}, confirming the presence of NO_2, CN bond stretching and benzene ring in the molecule of deformation. The strongest Raman line for TNT is present at 1365.15 cm^{-1} that coincides with the D band of graphite. The disorder band (D) of graphite is also responsible for the strong double resonant Raman scattering. It initiates the two-phonon interaction processes [36]. At E_{in}=3.85 mJ, the maximum strength of PA signal of pure graphite is around 9.4 mV while for pure TNT, it is 2.13 mV, whereas for the mixture of TNT and graphite, it is of the order of 64.54 mV (at 32.5 kHz range). It means that graphite can transfer momentum from its phonon waves, which are produced due to double resonance Raman Effect.

Most importantly, we observed that the G-band in GP (~1585.77 cm^{-1}) is downshifted towards ~1581.74 cm^{-1} after interacting with TNT. This downshift is of the order of 4 cm^{-1} and can be explained with the help of electron transfer mechanism between GP and TNT due to an interaction of pi-orbitals. Such an interaction could provide the necessary coupling between GP and TNT resulting in a better PA spectrum as shown in Fig 6.7. In addition, some of the Raman bands of TNT are also downshifted which are listed in Table 6.3, confirming coupling between pi-orbitals of GP and TNT.

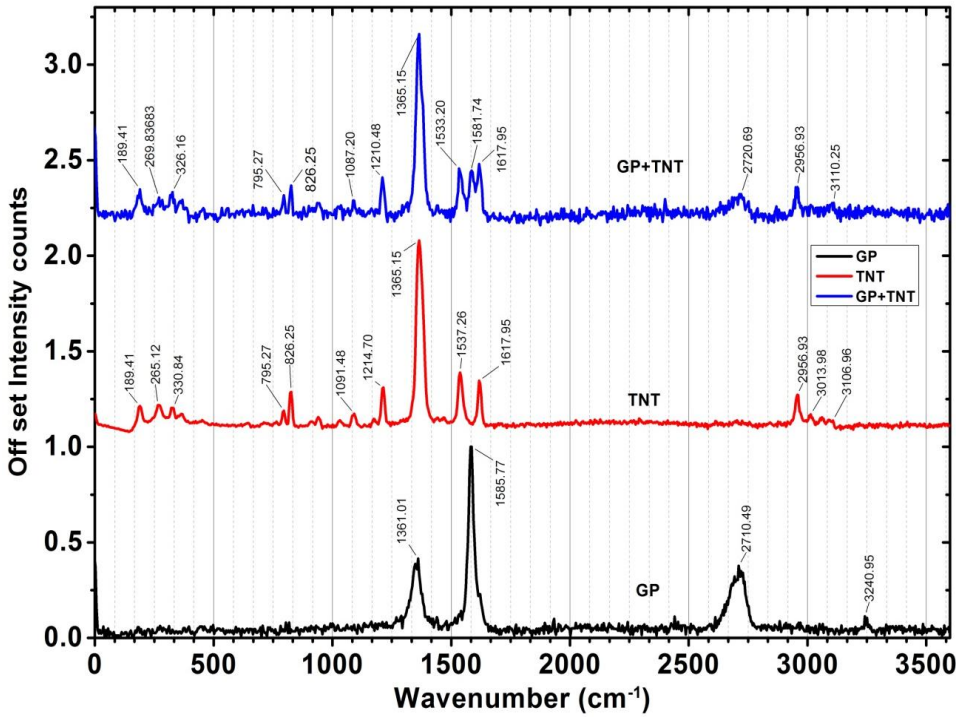

Figure 6.6: Raman spectra of (a) GP+TNT (b) TNT (c) GP.

Table 6.3: Shifted Raman lines of samples.

Raman lines
Actual lines of graphite : 1585.77 2440.60 2710.49 Shifted to (in mixture) : 1581.74 2400.75 2720.69
Actual lines of TNT : 265.12 330.84 1091.48 1214.70 1537.26 3106.96 Shifted to (in mixture): 269.83 326.16 1087.20 1210.48 1533.20 3110.25

Fig. 6.7(a-c) depict the PA spectra of TNT, GP and GP+TNT, respectively at t =1 ms with different incident laser energies. The intensity of PA spectrum for the mixture of TNT+GP is 12.5 times higher than the intensity of PA signal of pure TNT. It is attributed to the small, negligible absorption of TNT at 532 nm. The acoustic mode frequencies (between 5-40 kHz range) and their corresponding strength of PA signals for the pure GP and TNT and the mixture of TNT with GP at t=1 ms, E_{in}=3.85 mJ are given in the Table 6.4. The first six predominant acoustic modes of GP are located at 29.7, 31.3, 18.7, 14.1, 15.1, and 11.2 kHz. While for TNT, these modes are located at 32.2, 30.3, 35.2, 19.9, 21.3 and 6.0 kHz. In case of TNT and GP mixture the predominant modes are located at 34.7, 9.2, 32.4, 20.1, 9.2 and 13.5 kHz. The strength of PA signal of TNT+GP is higher than the pure samples. Further enhancement of the strength of PA signal of TNT mixed with GP was observed with respect to incident laser energy. Therefore, it provides a new nondestructive and dry analytical tool for the detection of explosive molecules. The presence of a pair of peaks in PA

spectra of TNT and graphite between 15-22 kHz and 27-34 kHz ranges also confirms the effect of double resonance where the acoustic signal produced due to phonon waves [29,37].

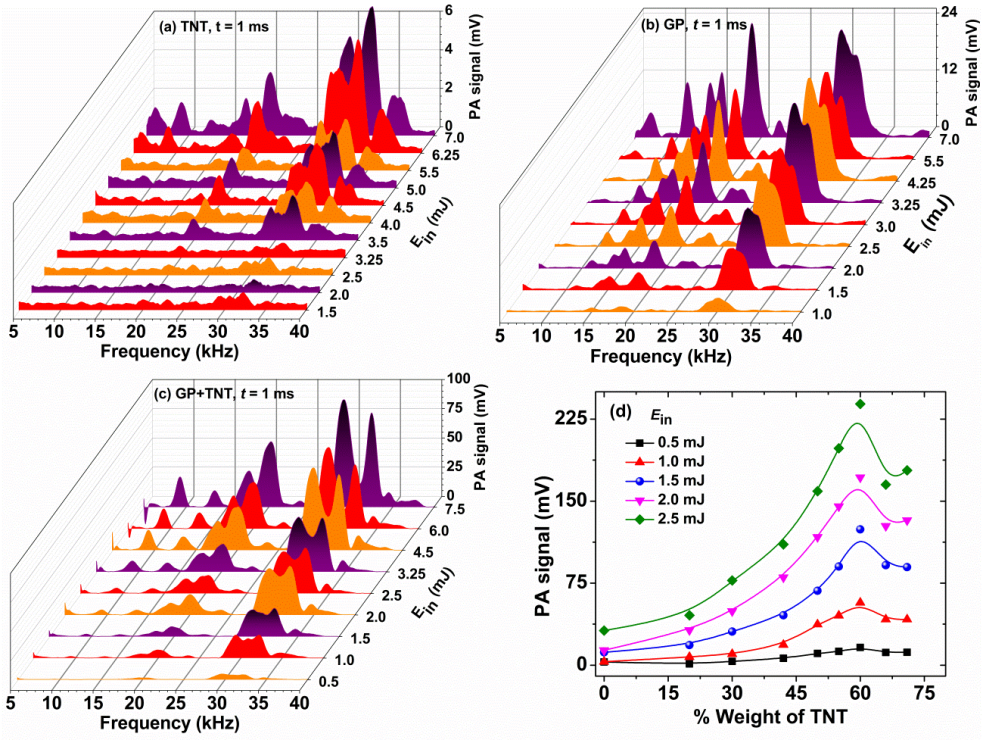

Figure 6.7: PA spectra of (a) TNT (b) GP (c) GP+TNT (d) PA signal vs percentile change in weight of TNT.

Table 6.4: The resonance acoustic modes of PA cell and their strength of PA signals.

Samples	First line: PA modes (kHz), Second line: Intensity (mV)
GP	*f*: 11.2 14.1 15.1 18.7 29.7 31.3 *I*: 3.72 7.12 7.09 12.75 21.09 17.17
TNT	*f*: 6 8.6 13.2 17.4 19.9 21.3 30.3 32.3 35.2 *I*: 0.63 0.58 0.44 0.57 1.26 0.78 1.71 2.13 1.40
TNT with GP	*f*: 9.2 13.5 20.1 23.7 29.2 32.4 34.7 41.0 *I*: 17.07 11.6 37.04 6.7 70.5 64.54 125.3 0.98

Fig 6.7(d) shows the response of PA signal of ~32 kHz mode with respect to the change in percentile (%) weight of TNT in graphite matrix at t = 1 ms for different incident laser energies. The energy varies between 0.5 to 2.5 mJ range. The acoustic modes with E_{in} show similar absorption behavior. Therefore, the response of PA signal was recorded within the 0.5 and 2.5 mJ range. The frequency of excited acoustic mode does not vary, but the corresponding strength of PA signal varies due to incident laser energy. It was also observed that all other excited acoustic modes show similar behavior. Moreover, the PA signal of GP and TNT mixture shows exponential growth of 66 % of TNT, and then it shows downfall with saturation. The graph shown in Fig 6.7(c) confirms that TNT is contributing towards the enhancement of generated PA signal. The initial strength of PA

signal of pure graphite is 11.85 mV at E_{in} = 1.5 mJ while for TNT it is negligibly small and treated to be zero. However, the mixture of GP and TNT has higher response as compared to pure individual samples. This supports our inference of optical phonon wave's momentum transfer between graphite and TNT due to double resonance Raman Effect. If TNT acts as a buffer medium, the strength of PA signal is less, as compared to the signal of pure graphite. Therefore, TNT does not play the role of buffer medium because the strength of PA signal shows rapid growth with respect to change in concentration of TNT in graphite and TNT matrix.

The phenomenon of double resonance Raman Effect can also be explained using bond lengths and band gaps of graphite and TNT. Graphite show SP^2 hybridization with a hexagonal crystal structure and has three σ bonds and one π bond, which is associated with weak Vander wall forces. The values of bond length and band gap of graphite are 1.421°A and -0.04 eV, respectively. Due to low value of the band gap of graphite, it is liable to absorb low energy electromagnetic radiation. Whereas TNT has the band gap of the order of 2.70 eV, this matches with the UV wavelengths (in the case of electronic transitions). The free charge carriers present in graphite molecules easily conduct from valence band to the conduction band due to absorption of incident wavelength. These free charge carriers are responsible for supply of heat energy in form of phonon momentum to TNT molecules. As a result, there is a provision that TNT molecules indirectly absorb the incident radiation, which leads to generation of strong PA signal, which is detected by microphone. The generated PA signal is considered as a resultant of the mixture of TNT and graphite. Therefore, we have experimentally demonstrated the potential use of 532 nm laser pulses for identification of TNT molecules with graphite mixture using the time resolved pulsed photoacoustic technique.

6.3.1. Minimum detectable concentration

We have used 20 % TNT as a minimum quantity in graphite matrix as shown in Fig 6.7(d). The intensity of PA signal at 20 % TNT decreases as compared to pure graphite signal at 0.5 mJ energy. Further, increase in the incident laser energy, the intensity of PA signal shows highest intensities at 20 % TNT. However, at 1.0 mJ the intensity of PA signal increases to 7.5 mV (pure graphite signal is 3.2 mV). Therefore, the selection of low incident laser energy is suitable for measuring the detection sensitivity of the sample. The linear fit of data points ranging between 20-50 % TNT intersects the x-axis at 7 %. Therefore, estimated minimum detectable quantity of TNT in graphite matrix is 7 %. In this study, we proposed the use of pulsed PA technique for identification of the TNT molecules in graphite matrix using 532 nm wavelengths. This is a dry analytical technique compared to all other existing techniques. Most importantly, it is showing the use of visible laser for the detection of TNT.

6.4. Identification TNT in graphite matrix using 1064 nm

Fig. 6.8(a,b) shows the PA spectra of GP and GP+TNT, at t = 1 ms at incident laser energy 2.0 mJ. It is clearly observed that shift in the frequency of acoustic modes for mixture of TNT and graphite from pure graphite. For the mixture of graphite and TNT, the acoustic modes show pair of peaks and broad profile in the domain of 28-35 kHz. The pure graphite has several small intense acoustic modes, whereas in the mixture of TNT and graphite these modes are overlapped each other and amplified almost 10 times. Therefore, it confirms that the graphite and TNT molecules are double resonant to each other with excitation of 1064 nm wavelength.

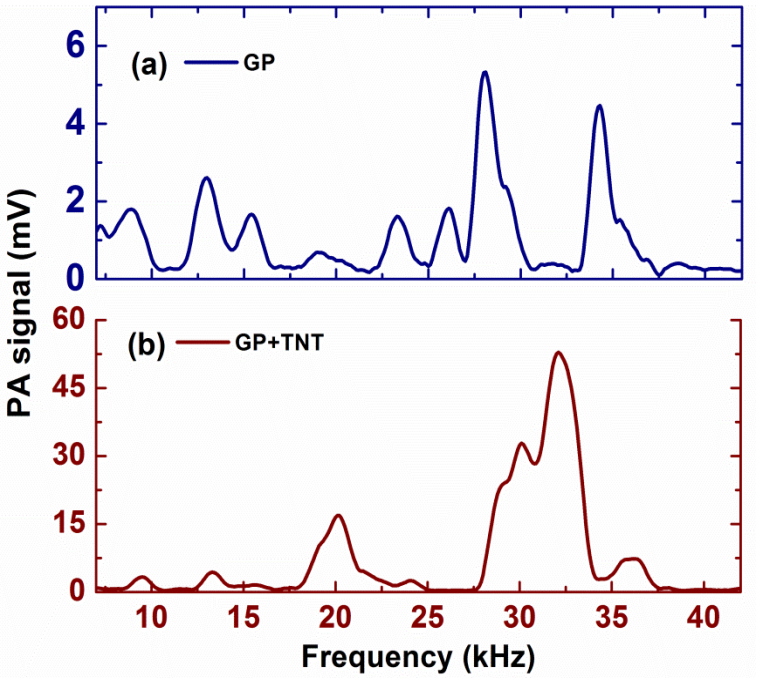

Figure 6.8: PA spectra of (a) GP (b) GP+TNT, at 2.0 mJ, t = 1 ms.

Table 6.5: Excited acoustic modes and their intensities of GP and GP+TNT at 1064 nm.

GP	kHz:	8.9	12.9	15.4	19.0	23.3	26.1	28.1	34.3
	mV:	1.79	2.59	1.66	0.08	1.61	1.81	5.32	4.46
GP+TNT	kHz:	9.6	13.3	20.1	30.1	32	36.1		
	mV:	3.22	4.33	16.86	32.78	52.56	7.28		

Fig. 6.9(a,b) shows the PA spectra of GP and GP+TNT, at t = 1 ms between 0.5-3.0 mJ range. The excited acoustic modes for pure graphite and mixture of TNT with graphite are shown in Table 6.5. The pure solid TNT molecules provide the intensity of PA signal of the order of 1.8 mV, at E_{in}= 3.0 mJ and t = 1 ms. It is clear that pure graphite shows negligible intensity at 0.5 mJ, however, the mixture of TNT and GP shows significant rise in PA signal. The intensity of PA signal for

mixture of TNT and graphite has 10 times higher than the pure graphite signal. This confirms that the pi- electrons of TNT and GP are coupled with excitation of 1064 nm wavelength. As a result, highest strength of PA signal is obtained for mixture of TNT and graphite. It was clearly observed in PA spectra (of samples) the excited acoustic modes of the mixture of TNT and GP shifted from pure GP acoustic modes.

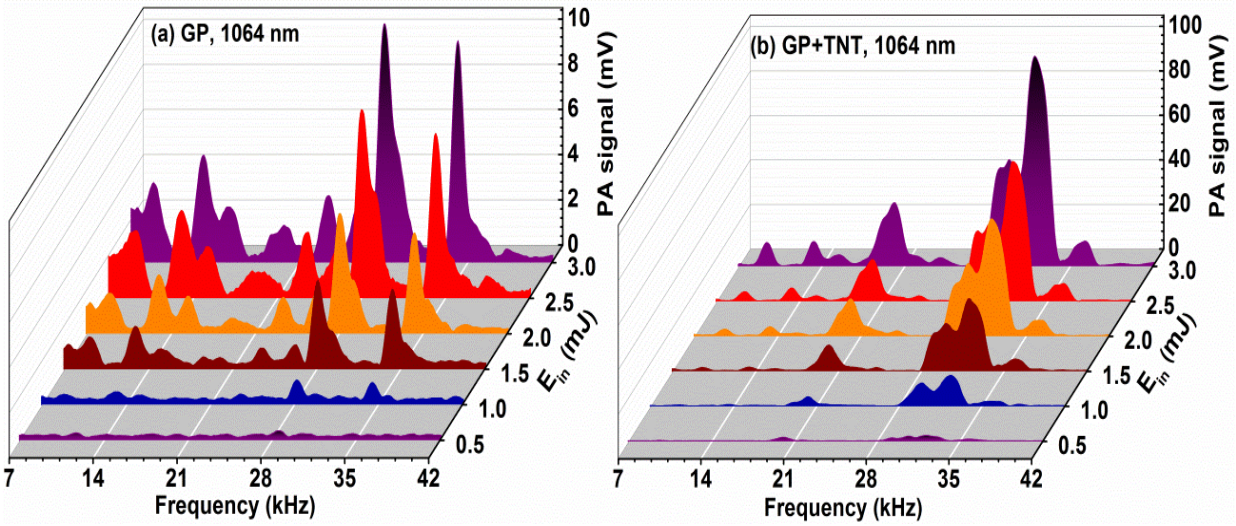

Figure 6.9: PA spectra of (a) GP (b) GP+TNT.

6.5. Identification of solid nitrogen-rich imidazole, 1, 2, 4-triazole and tetrazoles

6.5.1. PA spectra of DS-51, DS-90, DS-93, DS-99, and DS-107 mixed with graphite

Fig. 6.10(a-f) shows the PA spectra of pure GP and DS51, DS90, DS93, DS99, DS10 samples with GP, at E_{in}=1.5 mJ, t=0.5 ms for excitation wavelengths 532 nm and 1064 nm. Many of these compounds mixtures in graphite show higher PA signals at 532 nm than at 1064 nm. Fig. 6.10(a) shows the strongest PA mode at 4 kHz for 532 nm wavelength, but other acoustic modes have higher strengths at 1064 nm. The strength of the PA signal of some predominant acoustic modes present at 4 kHz in case of 532 nm has higher value as when compared to the 1064 nm. Except the strongest cavity mode, i.e. 4 kHz there is a shift in the frequency of remaining other modes from one compound to another. It shows that the absorption mechanism of each mixture varies due to its structure. The excited acoustic modes of DS samples mixtures in graphite and their corresponding intensities summarized in the Table 6.6. It clearly shows the predominant order and central frequency of acoustic modes vary from one sample to another sample in graphite mixture.

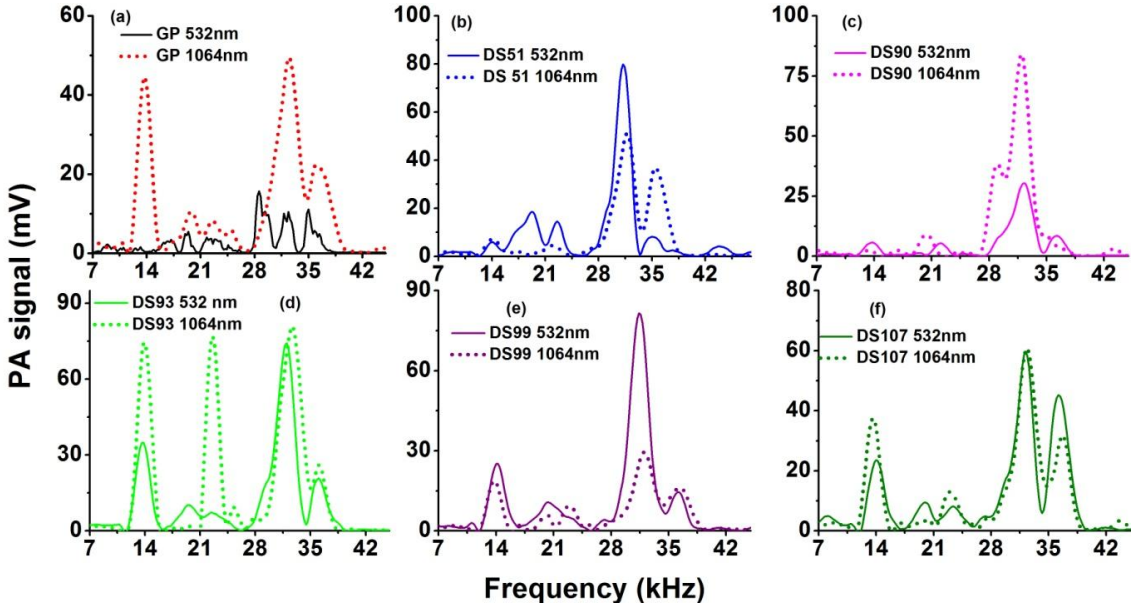

Figure 6.10: PA spectra of DS samples with graphite for 532 and 1064 nm at E_{in}=1.5 mJ. t =0.5 ms

Table 6.6: Excited acoustic modes in kHz (first line), intensities in mV (second line)

Sample	532 nm	1064 nm
GP	19.4 28.6 32.4 35.0 5.5 19.8 10.4 11.0	13.8 19.8 22.6 24.8 32.4 36.2 44.5 10.5 8.3 5.9 49.5 22.3
DS51+GP	19.2 22.6 31.2 35.2 18.5 14.5 79.9 8.0	14.0 22 31.8 35.4 7.2 4.5 51.1 36.9
DS90 +GP	13.8 22.0 32.2 36.2 5.8 5.4 30.4 8.5	20.4 29.0 32.0 9.1 38.4 84.1
DS93+GP	13.8 32.0 36.0 34.9 74.3 20.8	14.0 22.6 25.2 32.6 36.0 74.6 76.9 9.3 80.9 25.96
DS99+GP	14.2 20.4 31.4 36.2 25.2 10.6 81.5 14.6	13.8 20.2 23.2 32 36.4 18.85 6.1 9.49 29.54 16.3
DS107 +GP	14.0 20.0 23.4 32.2 36.2 23.9 9.4 8.2 59.8 45.25	13.6 22.8 32.4 36.6 37.54 12.92 60.91 31.64

6.5.2. Effect of Incident laser energy

Fig. 6.11 shows the PA spectra of GP and DS samples mixed with GP and inset figures shows the behavior of predominant acoustic modes with respect to incident laser energy for excitation wavelengths 532 nm and 1064 nm. The acoustic mode frequency values are similar with respect to increase in the incident laser energy but the corresponding strength of signals and the predominant order varies from sample to sample. The strength of the PA signal of HEMs in graphite mixture shows growth without saturation with respect to incident laser energy. This confirms that the phonon waves of graphite and HEMs compounds are strongly interacting with each other and lead to generation of strong PA signal without saturation.

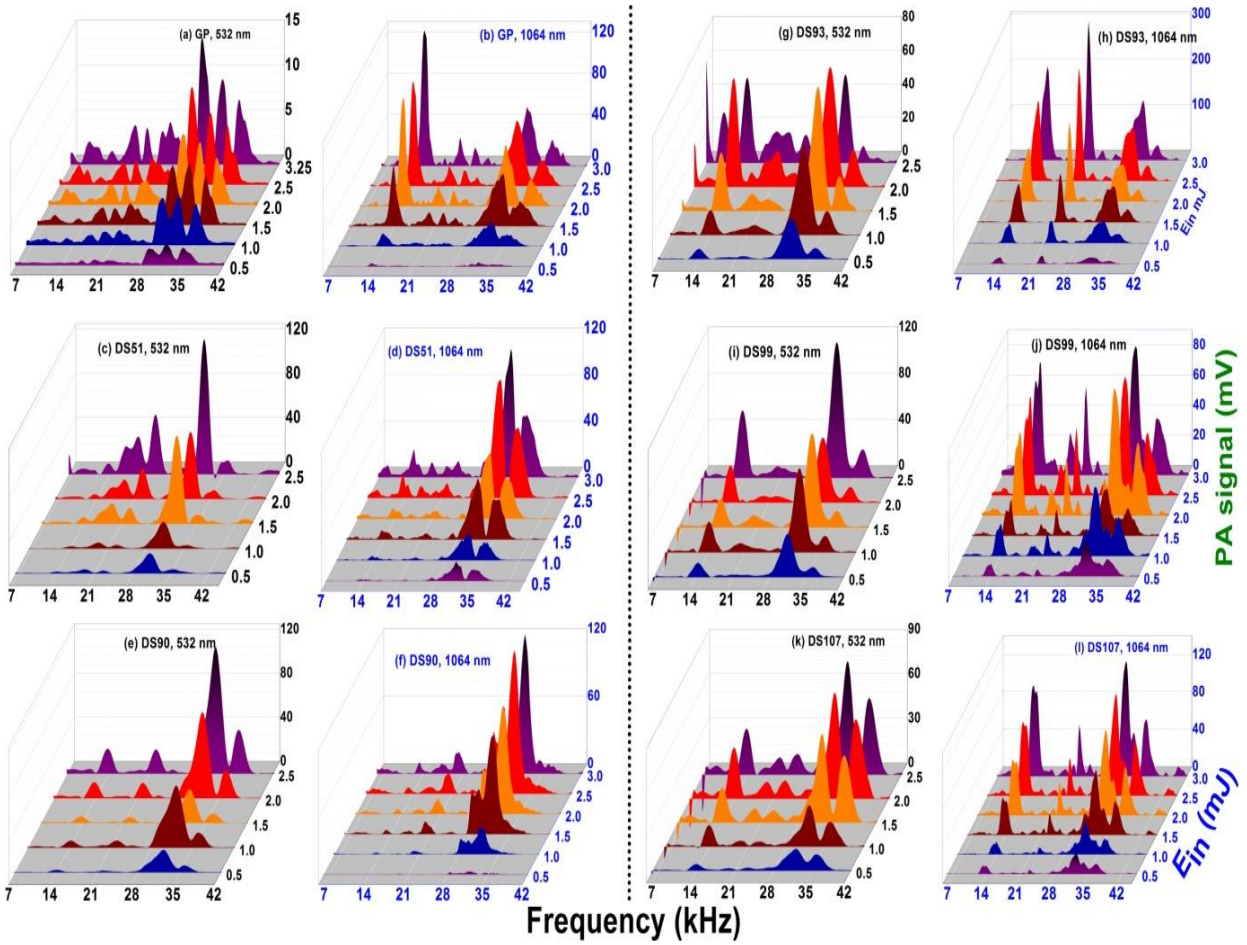

Figure 6.11: PA spectra vs incident laser energy of (a,b)GP,(c,d) DS51, (e, f) DS90, (g,h) DS93, (i,j) DS99 and (k,l) DS107 in graphite matrix at 532 and 1064 nm, respectively.

6.5.3. Non radiative decay time

Fig. 6.12 shows the first derivative time domain signal for samples at incident laser energy 1.5 mJ and t = 0.5 ms for excitation wavelengths 532 nm and 1064 nm. It is clear from Fig. 6.12 the pulse train of PA signals is different from one sample to another. The maximum number of predominant peaks is more than five and its order changes with respect to samples. We have measured the nonradiative decay time (N_t) of samples from its first derivative, because the time domain signal in usual form is complex and it is difficult to find out the exact decay point from the signal. The obtained N_t values are listed in Table 6.7. It is observed that in case of both wavelengths the nonradiative decay times of mixture of HEMs in graphite is higher than the pure graphite. This reveals that the velocities of sound in mixtures are stronger than the pure graphite. The compound mixture of DS90+GP has higher N_t values compared to other compounds. It has 18.8 and 18.4 μs decay times in case of 532 nm and 1064 nm respectively.

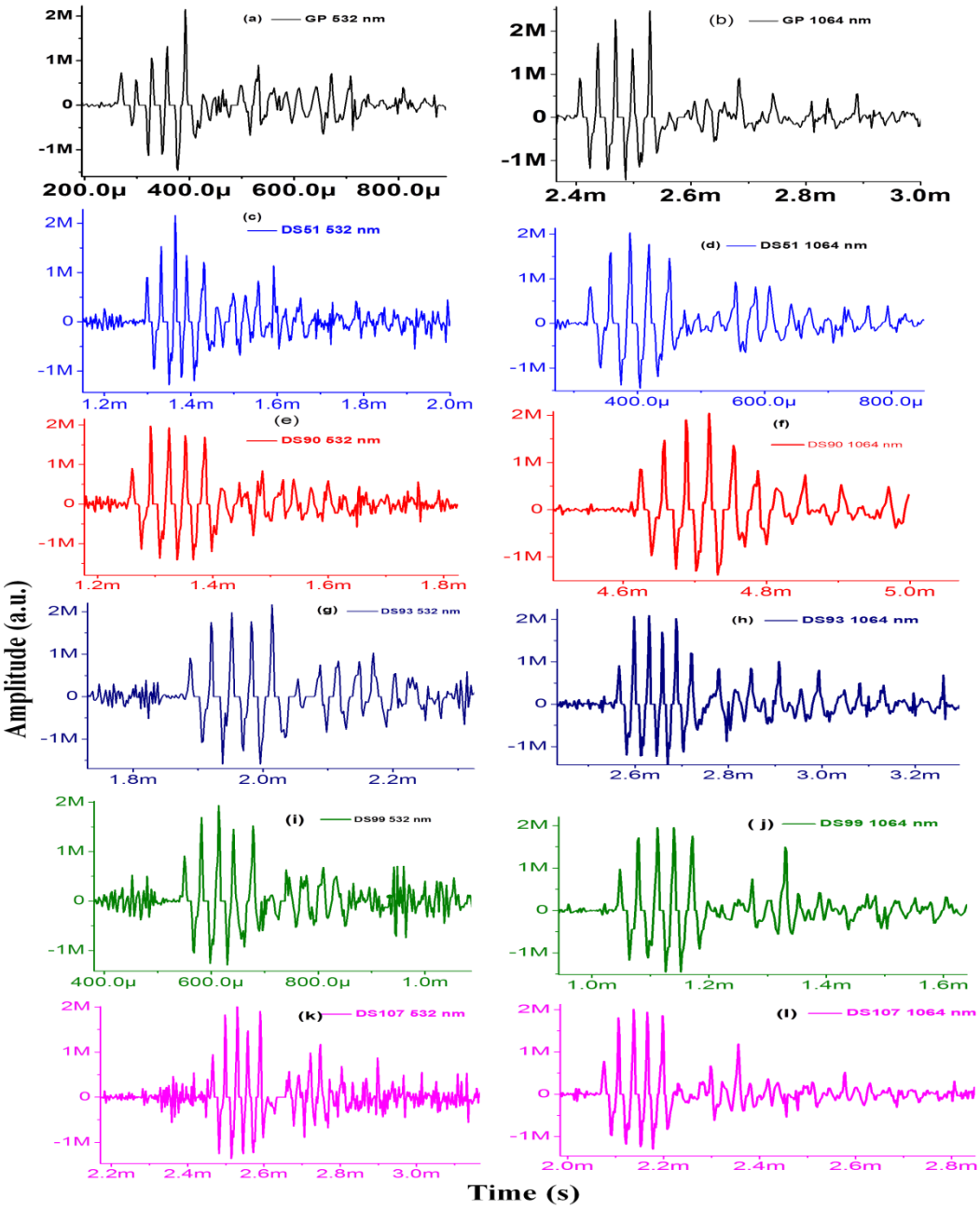

Figure 6.12: First derivative of time domain signal for sample mixtures at E_{in}=1.5 mJ, t =0.5 ms.

Table 6.7: Nonradiative decay times of samples.

Sample	N_t (µs)	
	532 nm	1064 nm
GP	15.4	14.4
DS51+GP	18.6	14.8
DS90 +GP	18.8	18.4
DS93+GP	18.8	17.2
DS99+GP	17.4	15.2
DS107 +GP	15.4	15.0

6.5.4. Raman spectra

Fig. 6.13(a) shows the Raman spectra of DS samples mixed with graphite. The pure DS samples do not show any Raman spectra employing 532 nm wavelength. While these samples mixed with graphite, each molecule spectra shows the Raman spectra of graphite with variations in the intensity of peaks. The ratio of intensities between G and D bands of graphite vary with respect to mixture of DS samples. Fig. 13(b) shows the ratio of I_D and I_G for the mixture of graphite and DS samples. It is clear from figure DS99 ratio is high as compared to the other samples. GP has high I_D/I_G value; showing high variation in the intensity of bands, while in case of mixtures these ratio values are in decreasing order. Thus, it indicates that these samples are interacting with graphite and as a result, these two bands are simultaneously rising with each other. Table 6.8 shows the Raman lines of pure graphite and DS samples mixtures in graphite. It clearly shows that the Raman lines of graphite shifted in the mixture HEMs confirming that the either phonons or pi-orbital electrons are coupled to energetic materials.

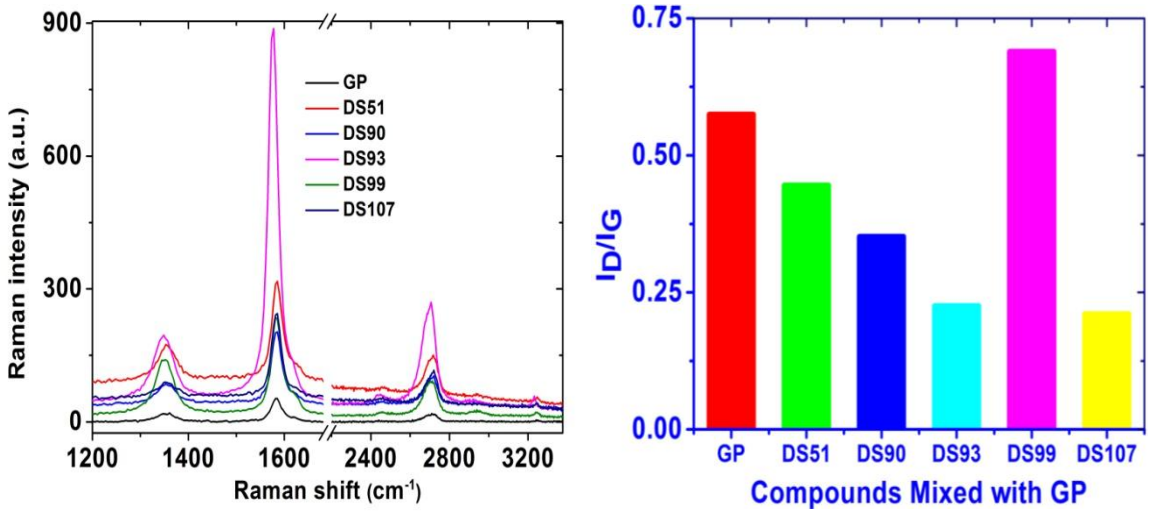

Figure 6.13: (a) Raman spectra (b) intensity ratios.

Table 6.8: Raman shift.

GP	GP+DS51	GP+DS90	GP+DS93	GP+DS99	GP+DS107
1361.01	1356.86	1352.72	1348.57	1352.72	1352.72
1585.77	1585.77	1585.77	1577.7	1581.74	1585.77
2440.6	2465.84	2455.03	2444.21	2458.64	2462.24
2710.24	2713.73	2720.73	2706.76	2706.76	2720.69
2882.49	2943.44	2943.44	2923.16	2943.44	2946.82
3240.95	3247.43	3244.95	3231.24	3244.19	3227.99

6.6. Conclusions

The time resolved photoacoustic spectra of wood black, graphite powder, and diesel soot have been successfully recorded using 532 nm, 30 ps pulses obtained from Nd: YAG laser systems. Due to higher band gap of TNT, it has no absorption at 532 nm, however, the Raman spectra of mixture of graphite and TNT explosive provides a downshift (~4 cm^{-1}) in the 'G' band of graphite as well as some shift in the other principal bands of TNT. This confirms the electron transfer mechanism between these samples due to the interaction of pi-orbitals. In addition, the double resonance peaks in PA spectra of graphite provides the phonon wave momentum transfer between graphite to the TNT molecules. Therefore, graphite is used as a sensor to identify the solid TNT molecules in terms of time resolved photoacoustic fingerprint spectrum. The selection of graphite as a potential candidate for getting strong photoacoustic spectra is also evaluated by means of data acquisition time, Q-factor and its response with respect to the incident laser energy as well as quantity of sample. The effect of percentile change in the weight of TNT in the graphite matrix has been examined to identify the potential use of the photoacoustic technique for identification of TNT with visible 532 nm wavelength. The minimum detectable quantity of TNT in graphite matrix is of the order of 7 %. The present study may open up a new channel for the detection of solid explosives using visible light without any chemical treatment. Based on the obtained results from PA and Raman spectra, we have extended this modality using 1064 nm wavelength. The laser wavelengths 532 nm, 1064 nm were also used to record the PA spectra of nitrogen-rich imidazole, 1, 2, 4-triazole and tetrazole-based solid compounds mixtures in graphite matrix. The presented results confirmed that graphite could be used as a sensing medium for recording time resolved photoacoustic spectra of solid explosives.

References

1. A. K. Chaudhary, G. C. Bhar, and S. Das, J. Appl. Spectrosc. **73**, 123 (2006).

2. D. D. Tuschel, A V Mikhonin, B. E. Lemoff, and S. A Asher, Xxii Int. Conf. Raman Spectrosc. **1267**, 869 (2010).

3. L. C. Pacheco-Londoño, J. R. Castro-Suarez, and S. P. Hernández-Rivera, Adv. Opt. Technol. **2013**, 1 (2013).

4. E. C. Meurer, H. Chen, L. Riter, I. Cotte-Rodriguez, M. N. Eberlin, and R. G. Cooks, Chem. Commun. (Camb). 40 (2004).

5. S. Wallin, A. Pettersson, H. Östmark, and A. Hobro, Anal. Bioanal. Chem. **395**, 259 (2009).

6. C. M. Wynn, S. Palmacci, R. R. Kunz, and M. Rothschild, *A Novel Method for Remotely Detecting Trace Explosives*.

7. K. S. Rao, A. K. Chaudhary, F. Yehya, and A. S. Kumar, Spectrochim. Acta Part A Mol. Biomol. Spectrosc. **147**, 316 (2015).

8. M. R. Leahy-Hoppa, M. J. Fitch, X. Zheng, L. M. Hayden, and R. Osiander, Chem. Phys. Lett. **434**, 227 (2007).

9. M. B. Pushkarsky, I. G. Dunayevskiy, M. Prasanna, A. G. Tsekoun, R. Go, and C. K. N. Patel, Proc. Natl. Acad. Sci. U. S. A. **103**, 19630 (2006).

10. M. Snels, T. Venezia, and L. Belfiore, Chem. Phys. Lett. **489**, 134 (2010).

11. A. V Deshmukh and A. Pandey, Malaysian J. Forensic Sci. **4**, 30 (2013).

12. N. Idros, M. Ho, M. Pivnenko, M. Qasim, H. Xu, Z. Gu, and D. Chu, Sensors **15**, 12891 (2015).

13. J. S. Caygill, F. Davis, and S. P. J. Higson, Talanta **88**, 14 (2012).

14. E. Erçağ, A. Üzer, and R. Apak, Talanta **78**, 772 (2009).

15. P. Mishra, S. Shukla, and S. Dutta, Ieee **3**, 3 (2011).

16. J. L. Anderson, A. A. Cantu, A. W. Chow, P. S. Fussell, R. G. Nuzzo, J. E. Parmeter, G. S. Sayler, J. M. Shreeve, R. E. Slusher, and M. Story, *Existing and Potential Standoff Explosives Detection Techniques* (National Academies Press, Washington DC, 2004).

17. W. O. Rivera, Standoff Raman Spectroscopy System for Detection of Explosives, Chemical Warfare Ajents Simulants and Toxic Industrial Compounds, 2008.

18. S. Botti, S. Almaviva, L. Cantarini, A. Palucci, A. Puiu, and A. Rufoloni, J. Raman Spectrosc. **44**, 463 (2013).

19. A. Mandelis and B. S. H. Royce, J. Appl. Phys. **50**, 4330 (1979).

20. A. Rosencwaig, J. Appl. Phys. **47**, 64 (1976).

21. A. Rosencwaig, Opt. Commun. **7**, 305 (1973).

22. A. Y. Watson and P. a Valberg, AIHAJ - Am. Ind. Hyg. Assoc. **62**, 218 (2001).

23. C. M. Long, M. A. Nascarella, and P. A. Valberg, Environ. Pollut. **181**, 271 (2013).

24. M. Douay and R. Nietmann, J. Mol. Spectrosc. **260**, 250 (1988).

25. R. W. Bergstrom, P. B. Russell, and P. Hignett, J. Atmos. Sci. **59**, 567 (2000).

26. Q. C. Campbell, *Graphite: Properties, Occurrences and Uses* (2013).

27. https://www.entegris.com/resources/assets/6205-7329-0513.pdf (2003).

28. A. ~B. Djurišić and E. ~H. Li, J. Appl. Phys. **85**, 7404 (1999).

29. A. C. Ferrari, Solid State Commun. **143**, 47 (2007).

30. R. Escribano, J. J. Sloan, N. Siddique, N. Sze, and T. Dudev, Vib. Spectrosc. **26**, 179 (2001).

31. J. Hodkiewicz, Sci. Thermo Fish. Appl. Note 51901.

32. M. Pimenta, Phys. Chem. Chem. Phys. **9**, 1276 (2007).

33. C. Pantea and T. W. Zerda, Carbon N. Y. **40**, 929 (2002).

34. X. Wang, S. Chang, J. Yang, J. Tan, H. Jia, H. Yin, X. Li, and G. Peng, in *Proc. SPIE 6622, Int. Symp. Photoelectron. Detect. Imaging 2007 Laser, Ultraviolet, Terahertz Technol. 662219 (February 22, 2008); doi10.1117/12.790827* (2007),662218–662219.

35. F. Yehya and A. K. Chaudhary, J. Mod. Phys. **02**, 200 (2011).

36. V. Kleiza, ACTA Phys. Pol. A **119**, 2 (2011).

37. T. Street, Phil. Trans. R. Soc. L. **362**, 2271 (2004).

Chapter 7

Terahertz generation, detection and its application in photoacoustic spectroscopy

Abstract

This chapter deals with the THz generation using optical rectification process in an indigenously grown organic salt 4-N, N-dimethylamino-4'-N'-methyl-stilbazoliumtoyslate (DAST) and commercially available zinc germanium phosphide ($ZnGeP_2$) crystals using optical parametric amplifier pulses of 60 fs, repetition rate 1 kHz. In addition, oscillator pulses of 150 fs duration, tunable between 800-850 nm were also employed to measure the output power of THz generated from DAST crystal. We have selected two rotational lines i.e. J= 19, 58 of pure N_2O gas and record the PA spectra of nitromethane and methanol vapor by using 0.5 and 1.5 THz band pass filters, respectively.

A part of the work presented in this chapter is published below journal:

[1] **K.S. Rao**, M. Venkatesh, K. Thirupugalmani, S. Brahadeeswaran and A.K. Chaudhary, *International Conference on Fiber Optics and Photonics*, OSA Technical Digest (online) (*Optical Society of America,* 2014), paper S2A.28.

[2] **K. S. Rao**, A. K. Chaudhary, M. Venkatesh, K. Thirupugalmani, and S. Brahadeeswaran, ***Curr. Appl. Phys.*,** 2016, **16**, 777–783.

[3] **Konda. Srinivasa Rao,** M. Venkatesh, S.P Tewari and A.K.Chaudhary "Generation of Terahertz Radiation in $ZnGeP_2$ by Difference Frequency Mixing Technique Using Femto Seconds Laser System" in *International Conference on Fibre Optics and Photonics*, Optical Society of America, Chennai, 2012, p. WPo.10.

7.1. Introduction

In recent years, the generation and detection of wide band terahertz (THz) radiation (0.1-10 THz) using optical techniques immerged as a new non-destructive tool for spectroscopic application. Moreover, it has potential use in the characterization of proteins, pharmaceuticals, explosives and narcotic drugs etc [1-5]. The generation of tunable THz radiation is achieved by means of different optical processes such as photo conductive (PC) antennas, electro optic (E-O) sampling, difference frequency generation (DFG) and optical rectification (OR) etc [6-13]. The OR is one of the effective techniques for the generation of powerful THz signal using ultrashort pulses. Some of the nonlinear crystals, which are suitable for THz radiation using OR process, is given in Table 7.1.

Table 7.1: Properties of some suitable nonlinear crystal used in optical rectification.

Material	Electro optic coefficient r (pm/V)	Nonlinear coefficient d (pm/V)	Optical ref. index n_{opt^*}	Group ref. index n_g^*	THz ref. index n_{THz}	Absorption coefficient α_{THz} (cm^{-1})	n_{THz}-n_{opt}
CdTe	4.5	81.8	2.92	3.73	3.23	4.8	0.31
GaAs	1.43	65.6	3.68	4.18	3.61	0.5	-0.07
GaP	0.97	24.8	3.18	3.57	3.34	1.9	0.16
ZnTe	4.04	68.5	2.87	3.31	3.17	1.3	0.3
GaSe	1.7	28	2.85	3.13	3.72	0.07	0.87
$LiTaO_3$	30.5	161	2.145	2.22	6.42	46	4.275
$LiNbO_3$	30.9	168	2.159	2.23	5.16	16	3.001
DAST	77	618	2.38	3.31	2.4	150	0.02

In the present case, we have generated the terahertz radiation from DAST crystal using optical parametric amplifier pulses tunable between 0.8-1.6 μm, range. Enhancement of THz signal in OR process can be achieved by matching the refractive index of generated THz radiation and corresponding group index of incident optical pump beam [14]. The phase velocity of THz and the group velocity of the optical pump beam are very close to each other due to low dielectric constant of the DAST crystal [15]. Therefore, it can generate efficient THz radiation, which is further used for the spectroscopic applications.

The organic crystal: 4-N, N-dimethylamino-4'-N'-methyl-stilbazoliumtoyslate (DAST) is one of the promising crystal for generation of terahertz generation using different types of nonlinear optical processes [16,18]. It has several interactive features such as large nonlinear optical susceptibilities (d_{11}>1000 pm/v), large electro-optic coefficients (r_{11}=92 pm/v) and wide spectral phase matching range for THz generation between 720 nm to 1650 nm [15,19-21]. The second order nonlinear coupling coefficient (d_{eff}) DAST is much higher than the other well known nonlinear crystals such as ZnTe, GaSe, CdTe [22,23]. Moreover, it has good transparence between mid to far infrared wavelength range [24]. We report the generation of efficient THz signal from indigenously grown organic nonlinear crystal DAST, which is grown along the direction of (001) plane. It belongs to

monoclinic space group Cc, point group m, with four molecules units for unit cell [25,26]. It is a positive biaxial crystal, which has high nonlinearity coefficient and broad transmission between 0.8 μm (infrared) to THz range (10 THz). Therefore, DAST crystal is treated as one of the promising candidate for generating wide band THz radiation using OR process [27-30].

The efficient THz radiation is generated by selecting suitable wavelengths in the near IR region where d_{eff} of the crystal has maximum value. Bosshard et al. reported the d_{eff} values of DAST crystal using Marker-Fringe experiment [31]. The d_{eff} values at 1.318 μm are d_{111} =1010±110, d_{122} =96±9 and d_{212}=53±12 pm/V, while for 1.542 μm it have d_{111}=290±15, d_{122} =41±3 and d_{212}= 25±3 pm/V, respectively. DAST is a positive biaxial crystal and its refractive indices are of the order of $n_x > n_y > n_z$. The principal XY plane behave like a positive uniaxial and YZ plane like a negative uniaxial crystal. In case of OR process, the extraordinary polarization is selected for pump beam, therefore the generated signal i.e. THz or second harmonic wavelengths are also extra ordinary polarised. The refractive indices of pump and generated wavelengths in XY principal plane are $n^e_{xy}(\lambda_p)$ and $n^e_{xy}(\lambda_{THz})$ respectively. The value of $n^e_{xy}(\lambda_{i=p,THz})$ is calculated using following expression for biaxial crystals,

$$n^e_{xy}(\lambda_i) = \left(\frac{\cos^2(\varphi)}{n_y^2(\lambda_i)} + \frac{\sin^2(\varphi)}{n_x^2(\lambda_i)} \right)^{-\frac{1}{2}} \tag{7.1}$$

φ is the phase matching angle. The refractive index of DAST crystal at different wavelengths are calculated using following sellmeier equation [32,33]

$$n^2(\lambda) = n_o^2 + \frac{q\lambda_o^2}{\lambda^2 - \lambda_o^2} \tag{7.2}$$

where, λ in μm. The values of n_o, q and λ_o parameter are selected along the X,Y, and Z- axis and listed in the Table 7.2.

Table 7.2: Values of n_o, q and λ_o.

	n_x	n_y	n_z
n_o	2.078	1.585	1.565
q	1.645	0.469	0.234
λ_o(μm)	0.533	0.504	0.501

Nitrous oxide (N_2O) commonly known as laughing gas is one of the green house molecules. It can be used as an oxidizer in a rocket motor. Robert Goddard proposed N_2O and gasoline as possible propellants for a liquid-fuelled rocket [34]. Plyler et al. reported the frequencies of the vibration-rotation spectrum of N_2O in the range of 4.405-5.464 μm [35]. Palik et al. presented the pure rotational spectra of N_2O between 100 and 600 microns [36]. Mittleman et al. demonstrated the

detection and identification of polar gases and gas mixtures based on the technique of terahertz time-domain spectroscopy [37]. Here, the generated terahertz radiation from the DAST crystal is used to record the time resolved photoacoustic (PA) spectra of N_2O using 0.5 and 1.5 THz band pass filters (BPF). The corresponding THz bands excites the rotational line J = 19, 58, respectively. Earlier, the same band pass filters were utilized to design of THz spectrophotometer using LT-GaAs photoconductive antennas, pyroelectric detector [38].

The DAST (001) crystal was successfully synthesized in the laboratory by adding the reactants 4-picoline, methyl 4-toluenesulphonate in equimolar ratio and using piperidine as a catalyst. The synthesized starting material was then purified by re-crystallization process several times before proceeding for the growth with methanol as solvent. The temperature of the bath (equipped with a controlled accuracy ± 0.01 ºC) was kept at 30 ºC at which the concentration of the solution was about 19.8 g/l. Later the temperature of the solution was increased to 40 ºC for complete dissolution and maintained this temperature up to 5 hours. Subsequently, the temperature of the solution was slowly lowered to 30 ºC with a cooling rate of 0.10 ºC/h. The growth was performed by isothermal slow evaporation technique at 30 ºC. Transparent single crystals of DAST were harvested after a period of about 10 days A typical DAST crystal (with a dimension of 3 x 3 x 0.28 mm^3) thus grown in the laboratory is shown in Fig. 7.1.

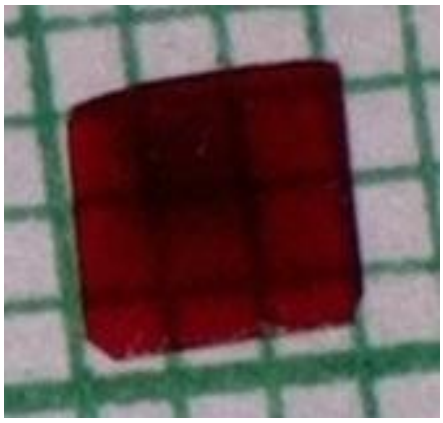

Figure 7.1: The picture of DAST crystal (001).

7.2. Experimental Details of THz based PA spectroscopy

The DAST crystal was then studied for its THz generation efficiency. The experimental layout employed for this study is shown in the Fig. 7.2. The required tunability of pump wavelength was obtained from an optical parametric amplifier (TOPAS-C, Coherent). The input wavelength for OPA was supplied from regenerative amplifier, which provides an output wavelength of 800 nm, pulse duration 40 fs and repetition rate 1 kHz. The tunable optical pump radiation obtained between 0.8-1.6 μm was vertically polarized and separated out from their corresponding idler and residual second harmonics using suitable wavelength separators. The tunable pump beam was directed to

incident on a 0.28 mm thick DAST crystal for generating the THz signal and its second harmonics. A Teflon sheet and silicon lens of thickness of 2 and 10 mm, respectively were used as filters for the residual incident unconverted and SHG signals. The power of generated THz signal was detected by employing pyroelectric detector (Gentec) which was placed 5.0 cm away from the crystal whereas second harmonic signal was detected in transmission mode using USB 4000 Spectrometer (Endor), which can detect the signal between 200 and 1100 nm range. The optical chopper is used to modulate the pump pulses at the rate of 25.4 Hz which acts as reference for pyroelectric detector (PED). The modulated pump beam was allowed to incident on the DAST crystal. The generated THz signal was detected with the help of a pyro-electric head (sensor) connected to a T-Rad system that consists of pre amplifier, lock-in amplifier, and used for the signal processing. Finally, the output of the T-Rad was fed to the personal computer (PC) for monitoring the power of the generated THz signal.

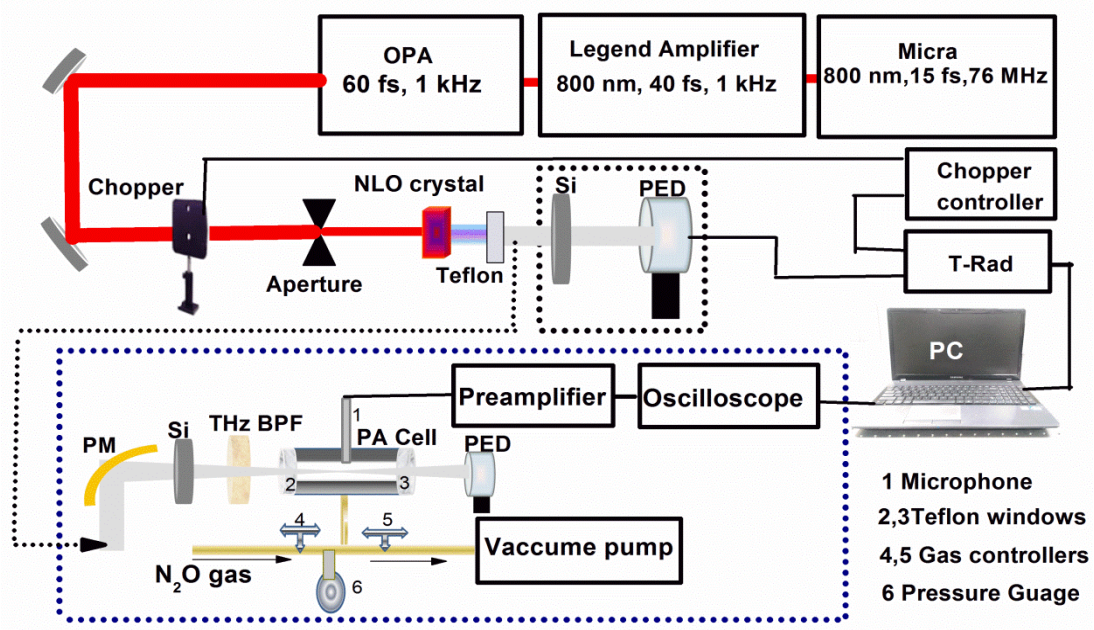

Figure 7.2: Experimental set up.

7.2.1. Photoacoustic spectroscopy arrangements

The PA spectrum of N_2O was recorded using a cylindrical resonator type PA cell of internal radius (R) of 7 mm and length (*L*) of 6.5 cm made of stainless steel. A Teflon, 25 mm diameter sheets and 1 mm thickness were used as a window of the PA cell. A Pre-polarized microphone (BSWA, China) of responsivity 50 mV/Pa was used to detect the generated acoustic signal. The output signal of the microphone was fed to a preamplifier, which was coupled to 200 MHz oscilloscope (Tektronix, U.S.A.). A silicon plate of 50 mm size and thickness of 2 mm was used to stop the residual unconverted pump pulses. A gold coated parabolic mirror (PM) was used to focus the THz beam at centre of the PA cell. Two band pass filters (BPF) of 0.5 THz and 1.5 THz (TYDEX) which are

equivalent to 600 and 200 μm wavelength, respectively were placed (one at a time) after the silicon plate. The PA cell was filled with pure N_2O gas at 1 atm pressure. Further details of optics used in the experiment are shown in Fig. 7.2.

7.3. Generated THz power

In the first step, the position of DAST crystal was optimized with respect to vertical orientation to achieve the maximum THz power. Fig 7.3(a) shows the variation of THz power with vertical rotation of crystal for the pump wavelength at 1.13 μm. It shows maximum power of the order of 0.56 μW at 180° compared to its original position. Fig 7.3(b) shows the generated power of THz for pump wavelength (λ_p) tunable between 0.8-0.9 μm, 0.93-1.14 μm and 1.15-1.6 μm range, respectively. These pulses of 60 fs duration are obtained at 1 kHz repetition rate. The diameter of the incident laser beam is reduced to 2.0 mm using a variable aperture.

The unfocused power of (*P*) =10 mW was used between 0.8-0.9 μm range, while in case of λ_p= 0.93-1.14 μm, range, the pump beam was focused on DAST crystal using quartz convex lenses of 10 cm focal length. The incident laser power between 1.15-1.6 μm range was fixed at 30 mW. We have used three different incident powers in three wavelength regions for the THz signal detection arrangement using pyro-electric detector, which was chopped between 25.1-26.1 Hz frequency range. It was observed that 10 mW power between 0.8-0.93 μm range is sufficient to generate the THz radiation. However, OPA systems (TOPAS-C) which was tunable between 0.94-1.14 μm range and did not provide power more than 10 mW after chopping at 25.3 Hz. As a result, the incident power provides very low THz radiation in this range, therefore, we have decided to focus the 10 mW power. In addition, between 1.15-1.6 μm wavelength range the OPA system provides 50 mW powers after chopping the pulses. Thus, instead of focusing we have increased the power of incident radiation up to 30 mW to get the higher generation without damaging the crystal.

The generated power of THz signal is directly dependent on incident pump wavelengths. The out power of THz for the pump wavelength tunable between 0.8-0.9, 0.93-1.14 and 1.15-1.6 μm range, is having 0.03-0.046, 0.02-0.465 and 0.83-4.82 μW respectively. The generated THz power shows linear growth in the wavelength domain 1.15-1.3 μm. After crossing the 1.3 μm, THz power start decreasing and this trend was continued up to 1.475 μm. The maximum power of the generated THz signal is of the order of 4.83 μW, which was recorded at 1.3 μm. The minimum power of the order of 0.83 μW was recorded at 1.475 μm. Once again, the power of generated THz signal starts growing between 1.5 and 1.6 μm, range. The highest generated THz power of the order of 0.113 μW was recorded at 0.85 μm (ν_{THz}=0.087 THz) between 0.8-0.9 μm, range. The output of the THz power shows linear growth between 0.93-1.14 μm, range. When ultrashort pulses entered into the nonlinear optical material, the phenominon of OR and SHG occurs simultaniously [19,39].

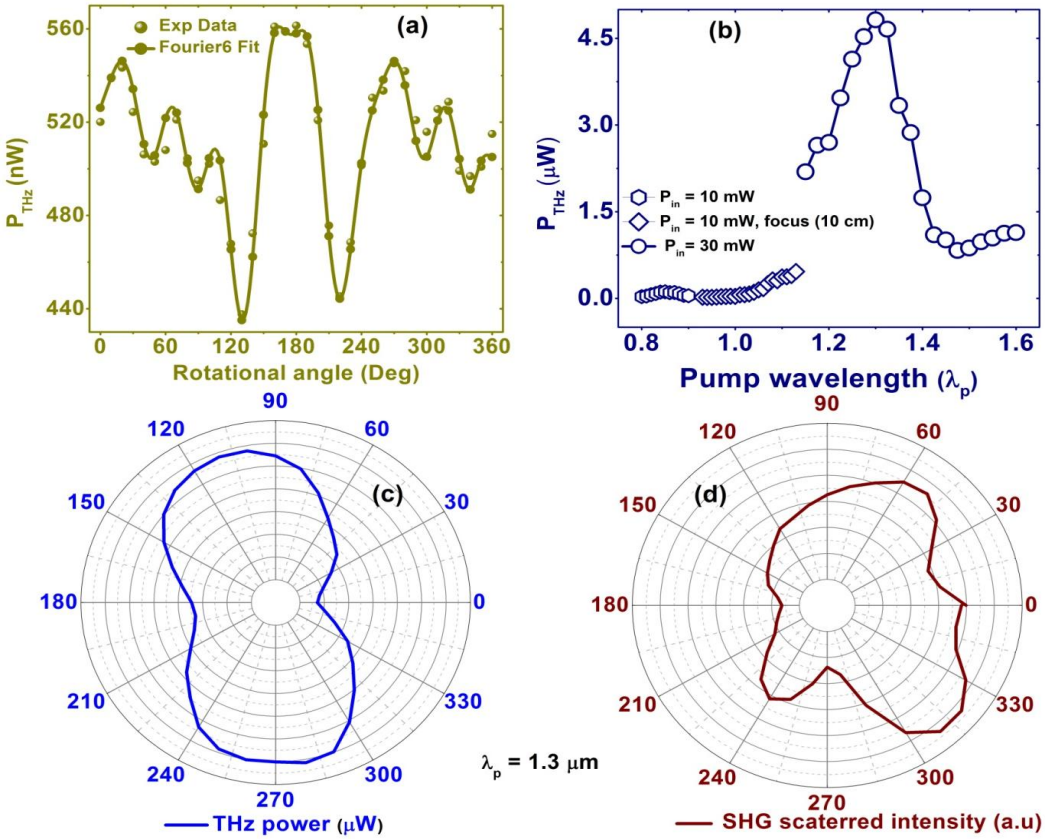

Figure 7.3: THz output power vs (a) at λ_p=1.13 μm with respect to rotation of crystal, (b) tunable wavelengths between 0.8-1.6 μm range and (c) THz power (d) SH signal intensity at 1.3 μm.

In the present case, we have also observed the similar process of THz generation along with second harmonic signal (SHS). Figure 6.3(c,d) shows the polar graphs of measured powers of THZ radiation and scatted SH signal respectively, with respect to crystal orientation at optical pump wavelength 1.3 μm having fluency of 0.668 mJ/cm^2. The generation of the THz and SH signal could be controlled by the rotating the crystal in its vertical plane for selecting the highest d_{eff} value of the crystal. Since, the pointing vector, which shows the direction of energy flow of generated signal, is affected by walk-off effect. In addition, the group velocity matching condition between THz pulses and optical pump pulses at 1.3 μm wavelength in DAST crystal is responsible for the efficient generation of THz signal [14][40].

This can be explained in the following way: the actual crystal thickness (length) is 0.28 mm. As per our calculation (using $\tau = l_{eff} \angle v_g$), the effective length (l_{eff}) of the crystal in XY plane for SHG (using λ_p=1.3 μm, λ_{SHS}= 0.65 μm) is 9.6 μm. This length is much smaller than the coherence length of the THz pulses (i.e. 0.28 mm). Consequently, the polarized waves of pump and second harmonics are not properly coupled inside the crystal due to group velocity mismatch (6.2484×10^3 fs/mm). Consequently, the generated SH signal is not efficient. However, in case of optical rectification, the velocity matching condition is fulfilled between optical and THz pulses. The measured power of

generated THz was of the order of 4.82 μW, with the experimental conversion efficiency (η) = 0.0161 %.

Fig. 7.3(c, d) clearly divulge the effect of generation of second harmonic signal with respect to the vertical rotation of the crystal. The polar graph is divided into four quadrants where the position of lobs shows the power of the generated signal. Fig. 7.3(c) shows that the power of THz signal is maximum at rotational angle between 90-130° and 250-290° range. Whereas Fig. 7.3(d) indicates that the intensity of SHS is comparatively higher at rotational angle 50 and 310°, respectively. Both radiations have comparatively less power at 180°. This confirms that the rotation of crystal plays a crucial role in the generation mechanism of output radiations. The difference in the rotational angle between maximum powers of both radiations is ~50°. However, the power of THz radiation is symmetrical in nature with respect to crystal rotation, whereas the SHS curve is unsymmetrical. Here, there is no loss in the emitted output power of THz, because THz radiation focused through the parabolic mirror on to the head of the pyro electric detector. Whereas, the crystal orientation affect the emitted intensity of SH signal because which is a scatted light spread in all directions from the crystal surface. The fiber coupled USB spectrometer was fixed at one particular position during the experiment. Therefore, there might be fluctuations in the intensity of SHS in the direction of USB spectrometer detector head. In the present case, we have measured the generated terahertz power with pyroelectric detector (which does not provide the temporal profiles of THz radiations). However, frequencies of generated THz are ascertained by selecting the crystal thickness (0.28 mm) which is equals to the coherence length (l_c).

7.3.1. Theoretical consideration for calculation of generated THz frequency

In the case of optical rectification process, the velocity matching condition between optical, terahertz pulses and coherence length (l_c) of the crystal is given by [20,41].

$$2(n_g(\lambda_p) - n_{THz}(\lambda_{THz}))l_c - \lambda_{THz} = 0 \tag{7.3}$$

Where, λ_{THz} (μm) is the wavelength of THz pulse, $n_g(\lambda_p)$ is the group index of pump pulse. If oherence length (l_c) of the crystal is greater than the length of the crystal (l) then it leads to generate the powerful THz radiation.

The λ_{THz} can be obtained by substituting the values of $n_g(\lambda_p)$, $n_{xy}(\lambda_{THz})$ and l_c i.e. 0.28 mm in Eq. (7.3) helps us to ascertain the generated THz frequency ($\nu_{THz} = c/\lambda_{THz}$) with respect to incident pump wavelength (λ_p) which is tunable between 0.8-1.6 μm range. This assumption is only applicable for the thin crystal where l_c and l are comparable.

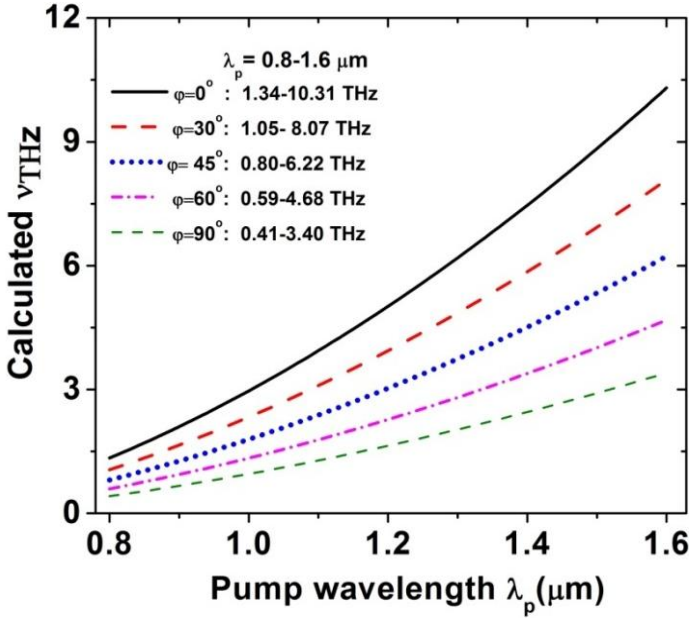

Figure 7.4: Calculated ν_{THz} at l_c=0.28 mm, the pump and generated pulses are extraordinary polarized.

Fig. 7.4 shows the calculated THz frequency at coherence length (l_c) = 0.28 mm for the incident pump wavelengths tunable between 0.8-1.6 μm, range. Here, the calculated values of THz frequency for extraordinary polarization are based on positive integer solutions of Eq. (7.3). The refractive index for extraordinary polarized THz wave n_{xy} (λ_{THz}) is calculated using Eq. (7.1) with respect to different values of φ. Where φ is the phase matching angle in XY principal plane, moreover, the optical rectification process is independent of φ. Here, the selection of arbitrary values of φ leads to ascertain the range of generated frequency, which lies in the THz domain. Therefore, theoretically we have tried to predict the probable range of THz generation with respect to different values of φ i.e. 0, 30, 45, 60 and 90°. Fig. 7.4 shows that the calculated ν_{THz} values are higher for low values of φ. The curve also highlights the linear behavior with different slope values which becomes maximum at φ=0°. This clearly indicates that at φ=0°, the frequency of the generated radiation extended up to 10.31 THz. Therefore, the higher range of ν_{THz} can be recorded for φ=0°, which reduces to minimum when φ becomes 90°. The frequency values as shown in Fig. 7.4 clearly show that the generated radiation lies in the terahertz domain. Therefore, this radiation utilized to record the PA spectra of N_2O by selecting the external band pass filters 0.5 and 1.5 THz, the rotational quantum numbers are associated with these bands discussed in the following section.

7.3.2. Assignment of rotational quantum number for N_2O

The vibrational frequency of pure rotational lines of N_2O is due to transitions between the ground vibrational state levels reported by Palik et al. [36],

$$v = 2B_o(J+1) - 4D_o(J+1)^2 \quad (7.4)$$

Where, B_o and D_o are the rotational constants of the ground state. J is the rotational quantum number. For N_2O, the constants of B_o and D_o are 0.41901 cm^{-1} and 0.19×10^{-6} cm^{-1}, respectively. The calculated rotational quantum numbers correspond to 0.5 and 1.5 THz bands are 19 and 59, respectively. Aenchbacher et al. measured the pure rotational lines and the THz absorption of N_2O between 0.69-1.18 atm pressure using terahertz time domain spectroscopy [42]. Furthermore, we have selected two specific rotational lines of N_2O for the recording of highly time resolved photoacoustic spectrum of N_2O molecules (at 1 atm pressure).

The probable frequency range of THz generated from DAST crystal is between 0.1-10 THz. However, detection of entire frequency range depends on types of detection arrangement. For example, if we detect the generated radiation using ZnTe crystals (Electro-Optic sampling) which can cover 0.1-10 THz, frequency range. Whereas, Si-GaAs antenna devices (photoconductive sampling) is limited up to 2.2 THz. However, in the present case we are using pyro-electric detector, which is an incoherent detection technique of measurement of power. Here, we are restricted to measure of the power of full-emitted radiation along with the 0.5 and 1.5 THz bands pass filters (procured from TYDEX, Russia). Therefore, the PA spectra of N_2O molecules recorded at broadband THz pulses i.e. full radiation (WBF), 0.5 and 1.5 THz lines.

7.3.3. THz PA spectra of N_2O molecules

The generated THz signal is employed for the recording of time resolved PA spectra of N_2O using pulsed photoacoustic technique. The PA cell made of stainless steel of dimensions L=6.5 cm and R=0.7 cm is used for recording the PA spectra. Some of the calculated longitudinal mode frequencies of the given PA cell are listed in Table 7.3.

Fig. 7.5(a) shows the presence of all excited modes due to broadband THz radiation, which covers the generated THz radiation including 0.5 and 1.5 THz range. Fig. 7.5(b,c) shows the PA spectra recorded at 1.5 and 0.5 THz frequencies using specific band pass filters. In addition, Fig. 7.5(d) shows the background signal recorded in N_2O molecules without any radiation source. The noise level of PA system for N_2O gas molecules is of the order of 300 μV. The corresponding right hand side PA spectra are recorded after subtracting the noise from the actual signal. It clearly provides the signature of different rotational lines of N_2O excited by individual THz frequencies in terms of PA signal. Therefore, PA spectra can be treated as a fingerprint of weak rotational lines of N_2O in acoustic domain for given PA cell. Moreover, this is the first report of recording of THz based PA spectra of N_2O at one atmospheric pressure. Some of the predominant acoustic modes without using band pass filters (WBF, i.e. complete generated THz radiation is allowed), and with 1.5 THz and 0.5 THz band pass filters are located at 46.4, 48.2, and 40.2 kHz. The corresponding strength of PA signals are 553.53, 477.49, and 428.92 μV.

Table 7.3: Longitudinal (q) resonance modes of the PA cavity.

q:	1	2	3	4	5	6	7	8	9	10	11
f(kHz):	2.6	5.3	7.9	10.6	13.2	15.8	18.5	21.1	23.7	26.4	29.0
q:	12	13	14	15	16	17	18	19	20	21	22
f(kHz)	31.7	34.3	36.9	39.6	42.2	44.9	47.5	50.1	52.8	55.4	58.1

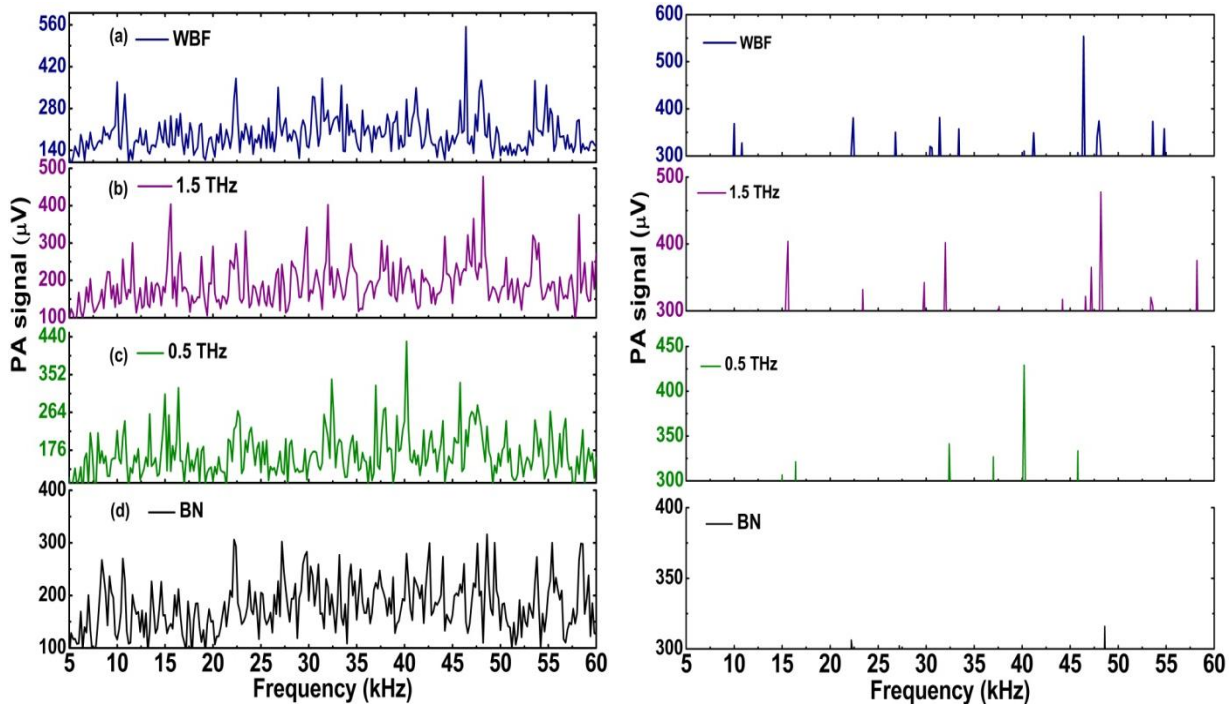

Figure 7.5: PA signal vs THz radiation without band pass filter, band pass filters and background noise.

It is observed that the strength of PA signal in THz domain lies in μV range. However, in case of UV-Visible region (using nanoseconds laser) in mV to V range [43,44]. It can be understood in following manner; the PA signal mainly depends on absorption of incident laser power which is much more stronger in case of UV-Visible range [45]. It is attributed to strong vibrational, rotational, and electronic transition. In addition, signal to noise ratio is of the order of 100-1000. Though in case of THz based PA spectroscopy the signal to noise ratio is of the order of 10 only but still we are able to record the signature spectra of weak rotation lines. It is only possible because the excited acoustic modes with THz radiation have sharp intense peak as compared to the modes of background noise spectra. Here data acquisition time plays very important role for the recording of time domain PA spectra. When, the experiment was performed with low power excitation wavelengths then 0.5 or 1.0 ms are identified as suitable data acquisition times. For this data acquisition time scale, the strength of PA signal which is not only strong in nature but also have the gap of the order of 200 Hz and 100 Hz respectively. However, in the present case if we select higher

data acquisition times i.e. t = 2.5 ms or 5.0 ms the PA signal coincided with the noise signal of PA system.

The PA spectra of N_2O recorded using BPF 1.5 THz has predominant acoustic mode at 48 kHz along with the other modes 33 and 15 kHz. These modes have similar strength of PA signal. However, for BPF 0.5 THz based PA spectra have strongest acoustic mode at 40.2 kHz and other additional modes are located at 15.0, 16.4, 32.4, 37.0, and 45.8 kHz respectively. All three PA spectra are different from each other but 33.0 kHz mode is one of the common modes present in the PA spectra of N_2O. Fig. 7.5 clearly shows that the number of excited acoustic modes and their corresponding intensities are higher for the generated THz frequency from the DAST crystal at 1.32 μm than 1.5 THz and 0.5 THz. Whereas 1.5 THz band shows higher number of excited acoustic modes than 0.5 THz. The output power of THz radiation was also measured with pyro electric detector at focused position of parabolic mirror. The average output power of THz radiation for WBF, 1.5 THz and 0.5 THz are 60, 42 and 29 nW respectively. This also confirms that the strength of the generated THz at 1.5 bands is strongest one.

However, the broadband experiment cannot include all peaks as shown in 1.5 THz and 0.5 THz experiments. Because, the photoacoustic cell has certain cavity eigenmodes, which are identified as longitudinal, radial and azimuthal modes respectively. As we know that the excitation mechanism of given gas depends on the incident radiation. Therefore, the predominant order of acoustic modes solely depends on the absorption properties of N_2O gas along with the intensity of incident laser pulses. Here, we have selected 600 μm and 200 μm wavelength which have corresponding frequency 0.5 and 1.5 THz and full radiation (WBF) to excite the N_2O gas molecules. Since, DAST is generating broad range of THz frequency i.e. 0.1-10 THz. As a result, many of the cavity modes are simultaneously excited, but they can also cancel each other due to interference of generated PA signal produced by THz pulses. In addition, the propagation velocity of generated PA signal varies from one wavelength to another wavelength. Therefore, all peaks for various rotation quantum modes (including J = 19 and 59) are difficult to identify in the PA spectra of without band-pass filter.

7.4. Generation of THz from DAST crystal using femtosecond oscillator

In this section, we have presented the generation of THz radiation from DAST crystal using the 140 fs oscillator pulses tunable between 800-850 nm. The generated THz pulse power is measured with the pyro electric detector and the profile of the generated pulse is detected with electro optic sampling technique using the ZnTe crystal. In addition, we have also studied the effect of polarization of input pump wavelength at 825 nm and the characteristic transmittance of 0.5 and 1.5

THz band pass filters are presented with respect to the generated THz radiation for the tunable pump wavelengths 800-850 nm range.

7.4.1. Generation of THz radiation with tunable wavelengths 800-850 nm

Fig. 7.6(a) shows the generated THz power using tunable wavelength 800-850 nm range. The curves show maximum THz power obtained at 820 and 830 nm, minimum at 800 nm for all the input laser powers lies between 25-125 mW. The power curves once again shows rise after crossing the 840 nm wavelength. The linear fit slopes values of the order of 0.068, 0.149, 0.159, 0.145, 0.079 and 0.075, respectively for the tunable wavelength between 800-850 nm range.

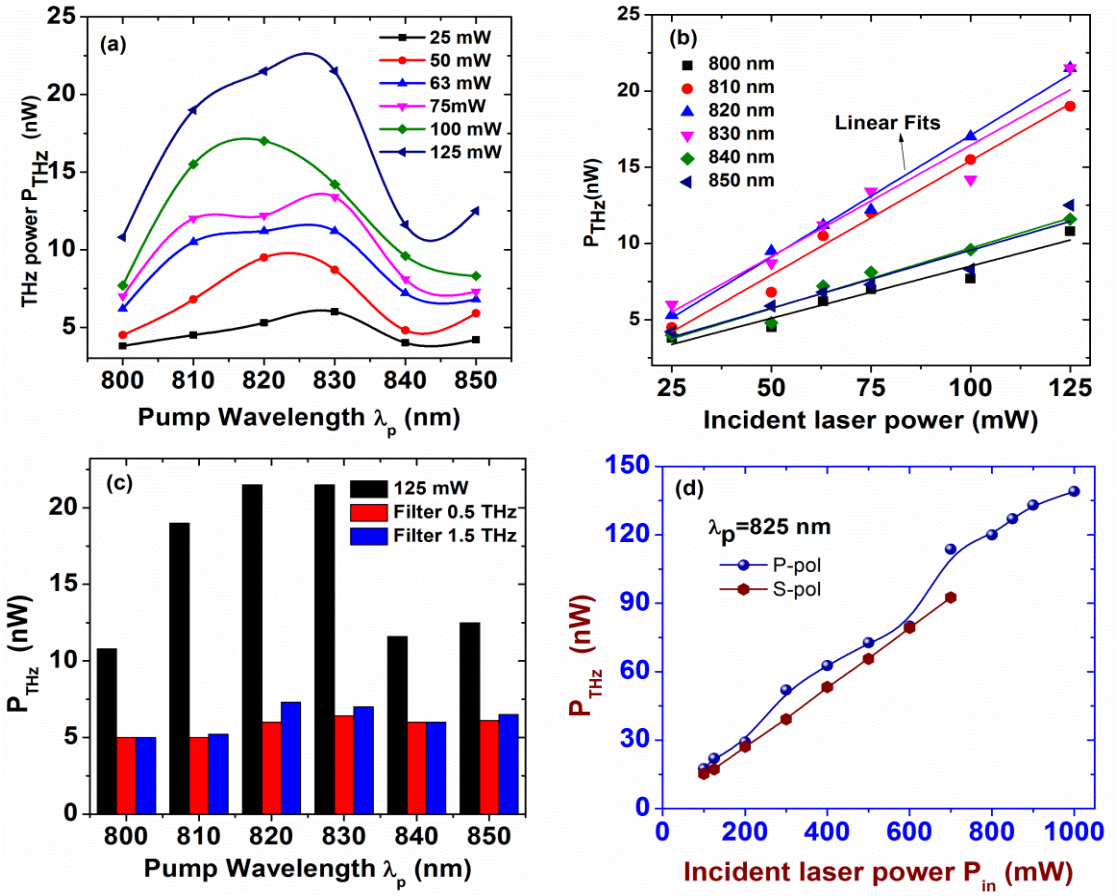

Figure 7.6: THz power vs (a) pump wavelength (b) incident laser power (c) at 125 mW w. r. to 0.5 and 1.5 THz band pass filters, and (d) for P and S polarized pulses.

In Fig. 7.6(c) the bar diagram shows the THz transmittance from 0.5 and 1.5 THz band pass filters, for the corresponding pump wavelength between 800-850 nm range, at input power P_{in} =125 mW. The black color bar graph shows the generated THz power for the similar range of wavelengths. The values of 1.5 THz band pass filter transmittance are comparatively higher than the 0.5 THz filter. Fig. 7.6(d) shows the characteristic percentage of transmittance of 0.5 and 1.5 THz band pass filters. The generated THz power of corresponding pump wavelength at 810,820 and 830 are high, but the percentage of transmittance of band pass filters at 0.5 and 1.5 THz are less. Fig.

7.6(d) shows the generated THz power with two different polarizations for pump wavelength 825 nm, with respect to different incident powers of pump wavelengths. The power of generated THz of P-polarized light is higher than the S-polarized light. In both cases the power of THz radiation increases linearly with respect to the incident pump power.

7.5. Generation of THz in $ZnGeP_2$ using DFG technique

The efficient monochromatic terahertz waves can be generated using phase matched difference frequency generation [46][47][48][49][50][51]. Some of the nonlinear crystals, which are frequently used of generation THz radiation through DFG process, are listed in **Table 7.4.**

Table 7.4: Linear, nonlinear optical properties of crystals most widely used for optical THz generation.

Crystal	GaAs	GaP	$ZnGeP_2$	GaSe	ZnTe	$LiNbO_3$	$LiTaO_3$
λ_{opt} (μm)	2.1	1.06	2.1	1.06	0.8	1.06	1.06
n_{opt}	3.33	3.11	3.15	2.8	2.85	2.16	2.14
n_{THz}	3.6	3.31	3.37	3.26	3.2	5.2	6.5
Δn	0.18	~0	0.17	0.34	~0	3.0	4.32
α_{THz} (cm^{-1})	1	3.3	1	2.5	9.9	21.7	95
r (pm/V)	r_{41}= 1.5	r_{41}= 0.94	r_{41} = 1.6	r_{22}= 1.58	r_{41} = 4	r_{33} = 28	r_{33} = 27.7
d (pm/V)	d_{14} = 46.1	d_{14} = 21.7	d_{36} = 39.4	d_{22} = 24.3	d_{14} = 66	d_{33} = 152.4	d_{33} = 145.2

Among them zinc germanium phosphide ($ZnGeP_2$) crystal is one of the promising crystal due to availability of sellmeir dispersion in the THz domain and higher values of nonlinear coupling coefficients. It is a chalcopyrite crystal with $\bar{4}2$ symmetry, positive uniaxial crystal ($n_e > n_o$), transparency range λ = 0.74-12 μm and non-hygroscopic in nature. In this section we have theoretically generated the THz radiation considering sellmeir given by Bhar et al for ordinary (n^o) and extraordinary (n^e) refractive indices [52]. The same sellmeier equations are also used by Wei shi et al. to generate the tunable terahertz using Nd:YAG laser where 1064 nm is used as a pump [47]. We have selected wavelength 800 nm as a pump and wavelengths tunable between 800-810 nm as a signal. In the case of femtosecond pulses, the effects of GVM and GVD plays very important role in coupling of pump energy to signal and idler waves inside the crystal. Therefore, the calculation of effective length of the crystal (L_{eff}) becomes very important and it also depends on temporal width of the incident pulses. The new sellmeier dispersion relation, for ZGP crystal, which is valid in THz range and shown in Eq (7.5) [47,52]

$$n_0^2(\lambda) = 10.93904 + \frac{0.60675\lambda^2}{\lambda^2 - 1600} \quad for\ \lambda > 60\ \mu m \tag{7.5}$$

7.5.1. Phase matching angle and angular bandwidth

The condition for phase matching for the collinear difference frequency generation (DFG) is given by

$$\Delta k = k(\omega_p) - k(\omega_s) - k(\omega_{THz}) \tag{7.6}$$

$$\frac{1}{\lambda_{THz}} = \frac{1}{\lambda_p} - \frac{1}{\lambda_s} \tag{7.7}$$

Where ω_p, ω_s and ω_{THz} are the pump, signal and generated (idler) THz frequencies. We have determined the phase matching angle for type II interaction where pump is treated as an extraordinary, signal and the generated wavelength (idler) are selected as an ordinary polarized. Therefore, using above relationship the phase matching angle for type II interaction (eoo:psi) is given by:

$$Sin^2(\theta_{pm}) = \frac{\lambda_p^{-2}\left(\frac{n_s^o}{\lambda_s} + \frac{n_{THz}^o}{\lambda_{THz}}\right)^{-2} - n_p^{o(-2)}}{\left(\frac{1}{n_p^{e2}} - \frac{1}{n_p^{o2}}\right)} \tag{7.8}$$

n_p^o, n_p^e and n_s^o, n_s^e ordinary and extraordinary refractive indices of corresponding pump and signal wavelengths.

Fig. 7.7(a) shows the calculated phase matching angles and Fig. 7.7(b) indicates the corresponding THz frequency for generated wavelength using DFG process. Whereas Fig. 7.7(c) exhibits the angular bandwidth of corresponding phase matching angle. We have selected pump wavelength as 800 nm and signal wavelength are tunable between 800.5-806 nm with variation of 0.25 nm. The generated wavelength increases with small for difference in pump and signal wavelengths are small which leads to lower the THz frequencies. Fig. 7.7(a,b) shows that the phase matching angle is increased with respect to higher frequencies. However, the angular bandwidth is low at phase matching angle 45°. This shows that at 45° is the optimum phase matching angle, if we can fix this angle cut and there is chance to generate tunable THz radiations with respect azimuthal orientation of the crystal.

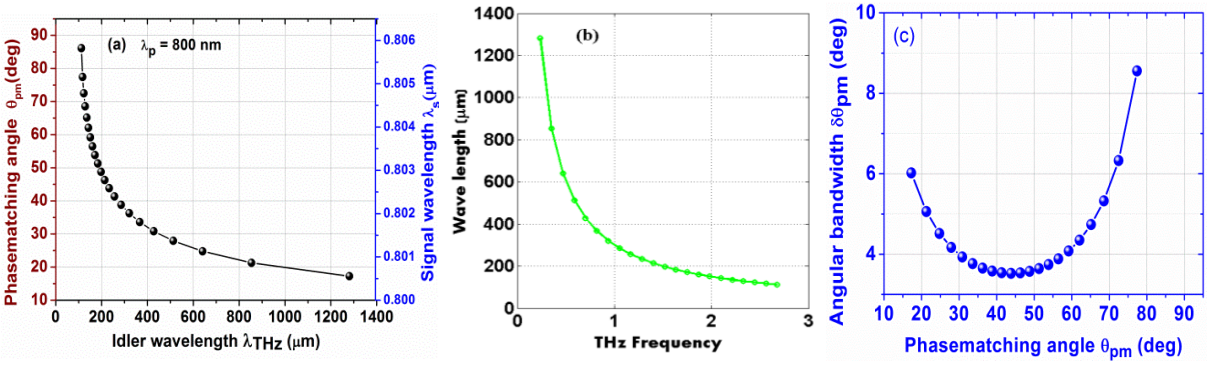

Figure 7.7: (a) required phase matching angle vs generated wavelength (b) wavelength in terms of THz frequency, (c) angular bandwidth of phase matching angles..

7.5.2. GVM and effective length of crystal between pump and signal-idler pulses

Fig. 7.8(a,b) shows the effective length of the crystals between pump wavelength to idler and signal wavelengths, respectively. It is clear that between idler pulses (generated wavelengths) to pump pulse the GVM is very high, therefore, it leads to lower the effective length of the crystal. Efficient THz radiation can generate when crystal length is lower than the effective length of the crystal. In this case the dispersion loss of optical and THz waves are nullified as a result strong THz radiation can emit from the crystal. The GVM of pulses decreases with respect to increases of the idler wavelength, while in terms of THz frequency the GVM is high for the higher order frequency.

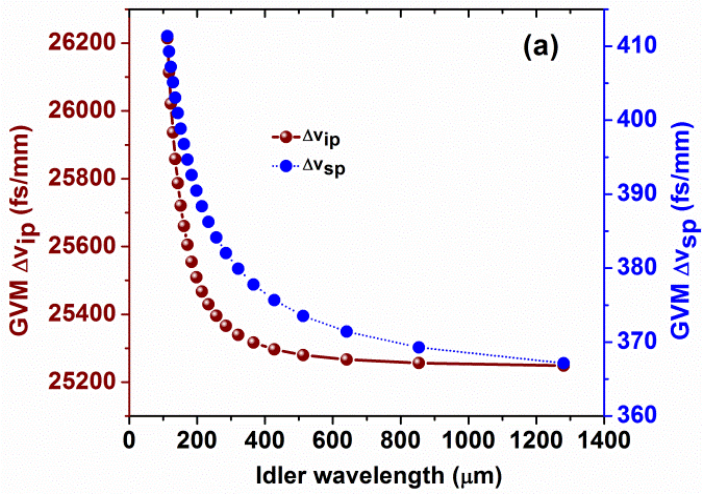

Figure 7.8 GVM between pump pulses to idler and signal pulses.

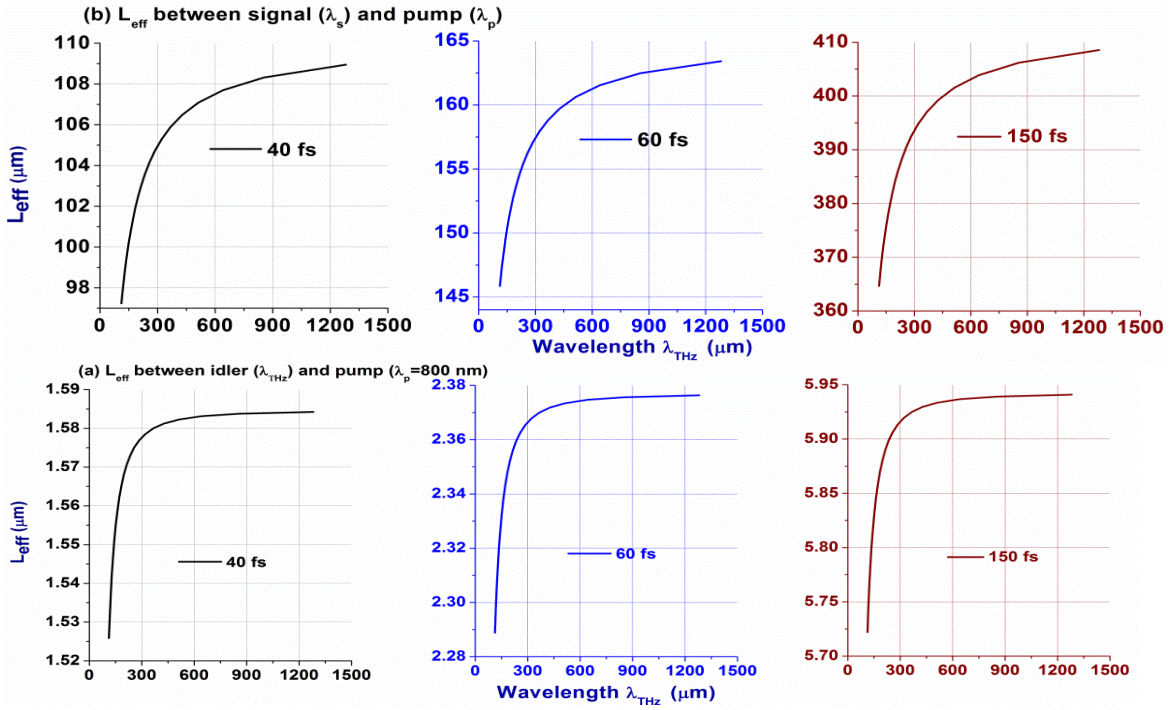

Figure 7.9: Effective length of the crystals between pump and idler, signals at 40, 60, 150 fs pulse durations.

Fig. 7.9 shows the effective length of the crystal between pump, signal and idler pulses measured 40, 60,150 fs for different incident laser pulse durations. The effective length of the crystal is directly proportional to the pulse duration. These pulse durations are available lasers in our laboratory durations i.e. regenerative amplifier, OPA and oscillator, respectively.

7.6. THz generation from $ZnGeP_2$ using optical rectification

In OR process the femtosecond laser pulses are easy to align and needs only single wavelength to generate the broadband THz radiation. While, in the case of DFG two laser wavelengths i.e. signal and pump beams are required. The broad band and narrow band THz pulses can be generate using $ZnGeP_2$ with various nonlinear optical process [47, 53-56]. It is well known that optical rectification is a second-order nonlinearity based optical process which generates a transient D.C. polarization, which typically creates THz radiation for short excitation pulses. Advances in broadband THz pulse generation technology by optical rectification have made significant enhancement in available pulse energy, which is applicable for communications [57], imaging and spectroscopy [58], coherent control [59], and chemical recognition [60]. Here, we report the generation of terahertz radiation from $ZnGeP_2$ by optical rectification process using optical parametric amplifier tunable between 1.15 -1.6 μm ranges of 60 fs pulses at 1 kHz repetition rate. The generated power of THz radiation measured using pyroelectric detector. It is utilized to record the time resolved pulsed PA spectra of methanol and nitromethane vapors at 0.5 and 1.5 THz band pass filters along with broadband THz radiation for the first time.

7.6.1. Measurement of THz power

Fig. 7.10 (a-c) shows the generated THz power with respect to full radiation (without band pass filters), with THz band pass filters at 0.5 THz and 1.5 THz, respectively. The output of the THz power is also measured after passing through the evacuated PA cell shown in Fig. 7.2. The maximum power for THz radiation obtained at pump wavelength 1.3 μm and it has approximately identical between the 1.275-1.35 μm range. The noise power of the pyro electric detector is 3-5 nW. The comparative results shows that generated THz signal power is highly absorbed by the atmosphere along with Teflon windows of the PA cell.

The 1.5 THz BPF has higher power than the 0.5 THz and follows the same trend of full radiation. Therefore, it confirms that most of the THz pulses possess 1.5 THz rather the 0.5 THz. However, the output power of the 0.5 THz BPF shows random variation, but the polynomial fit of order 5 follows the similar order to the full radiation with respect to pump wavelengths. Whereas the output power is comparatively lower than the 1.5 THz.

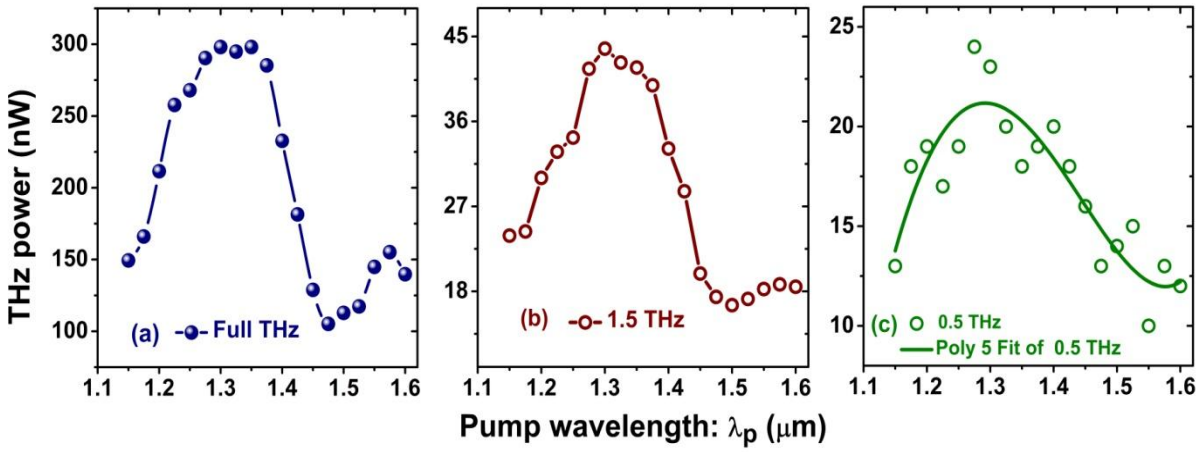

Figure 7.10: Power of THz radiation (a) Full Radiation, with band pass filters (b) 0.5 THz (c) 1.5 THz.

7.6.2. THz based PA spectra of Nitromethane and methanol

Fig. 7.11(a-c) and Fig. 7.11(d-f) shows that the PA spectra of methanol and nitromethane, respectively recorded at broad range of THz radiation, and at 0.5, 1.5 THz bands of the generated THz radiation. The background noise of the signal is 0.3 mV. Fig. 7.11(a) shows the PA spectrum of methanol vapor, which has the predominant acoustic modes present at 13.6, 15.0, 21.2, 34.2, and 56 kHz respectively at complete THz radiation generated by $ZnGeP_2$ crystal at 1.3 μm. Consequently, the major acoustic modes for 0.5 and 1.5 THz BPF are present at 13.6, 36.8, 39, 53.6 kHz and 13.6, 29, 36.8 and 40.2 kHz respectively. It is observed that the acoustic mode present at 13.6 kHz is the common mode present in the all spectra. The complete radiation has higher number of acoustic modes than 1.5 and 0.5 THz, among these bands 1.5 THz has higher number of modes than the 0.5 THz.

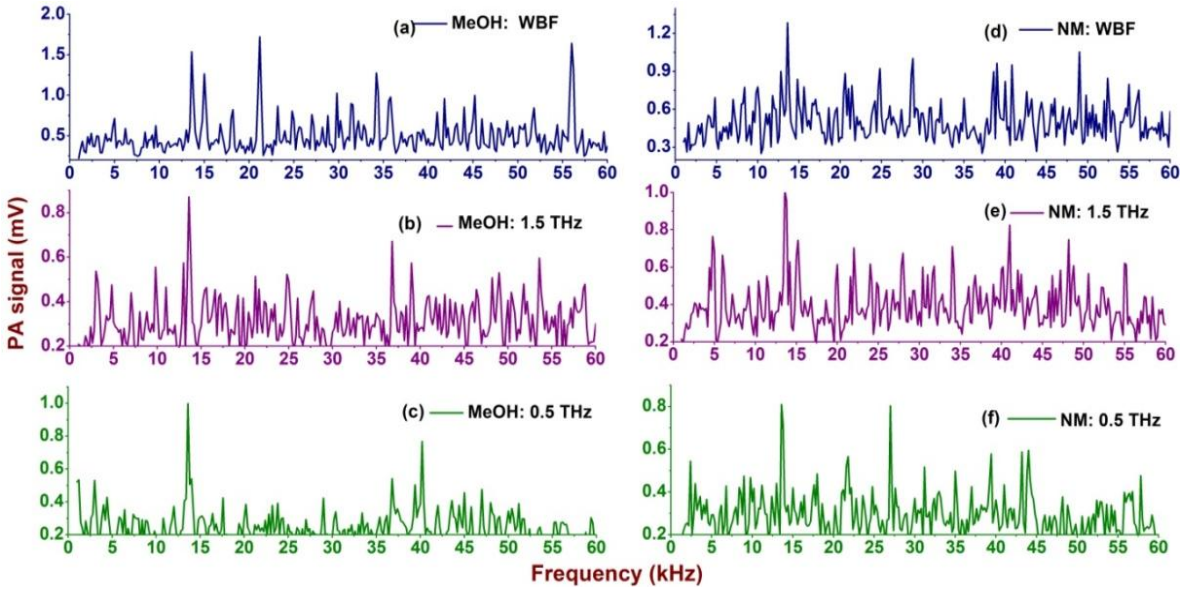

Figure 7.11: THz based PA spectra of methanol (MeOH) and nitromethane (NM).

Similarly, for nitromethane the major acoustic modes at broad band THz radiation present at 13.6, 24.8, 28.8 39 and 49 kHz, whereas for the band pass filters 1.5 and 0.5 THz are located at 4.8, 13.6,22.0,28.0,41.0,48.2 kHz and 13.6,21.8, 27.0, 39.4 and 44 kHz respectively. The calculated longitudinal modes are listed in Table 7.3. The same PA cell is used for recording the PA spectra NM and methanol.

7.7. Conclusions

We have reported the potential use of indigenously grown DAST crystal to generate efficient and wide range of THz signal using pump wavelength tunable between 0.8-1.6 μm ranges obtained by OPA. The effect of vertical rotation of crystal on the generation of SHS and THz signals has been demonstrated at 1.3 μm wavelength. These results exhibited the shuttling of electromagnetic radiation between THz to SHS. The higher efficiency of the generated THz signals could be attributed to the nonlinear coupling coefficients d_{eff} values of the DAST crystal. In addition, we correlated the coherence length of the crystal as a crystal length and calculated the ν_{THz} for the pump wavelengths tunability between 0.8-1.6 μm, range. In addition, the THz radiation was generated using $ZnGeP_2$ crystal using OPA pulses between 1.15-1.6 μm, range. For the first time, we have also recorded the time resolved PA spectra of N_2O, methanol and nitromethane using THz photoacoustic spectrometer at 0.5 and 1.5 THz. It confirms that the strength of 1.5 THz band is stronger than the 0.5 THz band.

References

1. M. Tonouchi, Nat Phot. **1**, 97 (2007).
2. J. F. Federici, B. Schulkin, F. Huang, D. Gary, R. Barat, F. Oliveira, and D. Zimdars, Semicond. Sci. Technol. **20**, S266 (2005).
3. Y. C. Shen, T. Lo, P. F. Taday, B. E. Cole, W. R. Tribe, and M. C. Kemp, Appl. Phys. Lett. **86**, 1 (2005).
4. Y. Sun, M. Y. Sy, Y.-X. J. Wang, A. T. Ahuja, Y.-T. Zhang, and E. Pickwell-Macpherson, World J. Radiol. **3**, 55 (2011).
5. M. C. Hoffmann and J. A. Fülöp, J. Phys. D. Appl. Phys. **44**, 83001 (2011).
6. S. B. Choi and D. J. Park, Curr. Appl. Phys. **16**, 109 (2015).
7. H. R. Zangeneh and M. A. F. Jahromi, Optik (Stuttg). **125**, 3098 (2014).
8. J. D. Rowley, J. K. Wahlstrand, K. T. Zawilski, P. G. Schunemann, N. C. Giles, and a. D. Bristow, Opt. Express **20**, 16968 (2012).
9. M. Venkatesh, K. S. Rao, T. S. Abhilash, S. P. Tewari, and A. K. Chaudhary, Opt. Mater. (Amst). **36**, 596 (2014).
10. J.-H. Jeong, B.-J. Kang, J.-S. Kim, M. Jazbinsek, S.-H. Lee, S.-C. Lee, I.-H. Baek, H. Yun, J. Kim, Y. S. Lee, J.-H. Lee, J.-H. Kim, F. Rotermund, and O.-P. Kwon, Sci. Rep. **3**, 3200:1 (2013).
11. B. J. Kang, I. H. Baek, J. H. Jeong, J. S. Kim, S. H. Lee, O. P. Kwon, and F. Rotermund, Curr. Appl. Phys. **14**, 403 (2014).
12. A. Schneider, IEEE Trans. Terahertz Sci. Technol. **4**, 605 (2014).
13. C. Vicario, C. Ruchert, and C. P. Hauri, J. Mod. Opt. **62**, 1480 (2015).
14. A. Schneider, I. Biaggio, and P. Günter, Opt. Commun. **224**, 337 (2003).
15. M. Jazbinsek, L. Mutter, and P. Gunter, IEEE J. Sel. Top. Quantum Electron. **14**, 1298 (2008).
16. S. Fan, F. Qi, T. Notake, K. Nawata, Y. Takida, T. Matsukawa, and H. Minamide, Opt. Express **23**, 7611 (2015).
17. J. Wook, Y. Lee, J. Park, D. Shin, G. Bok, J. Shin, S. Kim, C. Kee, and C. Kang, Curr. Appl. Phys. **15**, 1156 (2015).
18. J. El Haddad, B. Bousquet, L. Canioni, and P. Mounaix, TrAC - Trends Anal. Chem. **44**, 98 (2013).
19. A. Schneider, M. Neis, M. Stillhart, B. Ruiz, R. U. A. Khan, and P. Günter, J. Opt. Soc. Am. B **23**, 1822 (2006).
20. A. Schneider, M. Stillhart, and P. Günter, Opt. Express **14**, 5376 (2006).
21. C. P. Hauri, C. Ruchert, C. Vicario, and F. Ardana, Appl. Phys. Lett. **99**, 2013 (2011).
22. E. T. Sensors, Q. Wu, X. Zhang, and S. Member, IEEE J. Sel. Top. Quantum Electron. **2**, 693 (1996).
23. R. Huber, A. Brodschelm, F. Tauser, and A. Leitenstorfer, Appl. Phys. Lett. **76**, 3191 (2000).
24. Y. Toya, S. Yamamoto, T. Satoh, T. Shimura, K. Kuroda, S. Ashihara, Y. Takahashi, M. Yoshimura, Y. Mori, and T. Sasaki, in *Adv. Solid-State Photonics* (OSA, Washington, D.C., 2009), p. TuB2.
25. S. Brahadeeswaran, S. Onduka, M. Takagi, Y. Takahashi, H. Adachi, M. Yoshimura, Y. Mori, and T. Sasaki, J. Cryst. Growth **292**, 441 (2006).
26. Y. Takahashi, H. Adachi, T. Taniuchi, M. Takagi, Y. Hosokawa, S. Onzuka, S. Brahadeeswaran, M. Yoshimura, Y. Mori, H. Masuhara, T. Sasaki, and H. Nakanishi, J. Photochem. Photobiol. A Chem. **183**, 247 (2006).
27. P. Y. Han, M. Tani, F. Pan, and X.-C. Zhang, Opt. Lett. **25**, 675 (2000).
28. J. Liu, H. Schmutz, and F. Merkt, J. Mol. Spectrosc. **256**, 111 (2009).
29. K. Kawase, Opt. Express **25**, 1714 (2000).
30. B. Monoszlai, C. Vicario, M. Jazbinsek, and C. P. Hauri, Opt. Lett. **38**, 5106 (2013).
31. U. Meier, M. Bosch, C. Bosshard, F. Pan, and P. Gunter, J. Appl. Phys. **83**, 3486 (1998).
32. G. Knopfle, R. Schlesser, R. Ducret, and P. Gunter, Nonlinear Opt **9**, 143 (1995).
33. F. Pan, G. Knöpfle, C. Bosshard, S. Follonier, R. Spreiter, M. S. Wong, and P. Günter, Appl. Phys. Lett. **69**, 13 (1996).
34. R. H. Goddard, U.S. Patent 1,103,503 (14 July 1914).

35. E. K. Plyler, E. D. Tidwell, and A. G. Maki, J. Res. Natl. Bur. Stand. Sect. A Phys. Chem. **68A**, 79 (1964).
36. E. D. Palik and K. N. Rao, J. Chem. Phys. **25**, 1174 (1956).
37. D. M. Mittleman, R. H. Jacobsen, R. Neelamani, R. G. Baraniuk, and M. C. Nuss, Appl. Phys. B-Lasers Opt. **67**, 379 (1998).
38. V. Mottamchetty and A. K. Chaudhary, Indian J. Phys. (2015).
39. M. Manikandan, T. Chen, Z. Sun, S. Zhang, and J. Luo, INOCHE **61**, 165 (2015).
40. A. Schneider, I. Biaggio, and P. Günter, Appl. Phys. Lett. **2229**, 2002 (2008).
41. A. Nahata, A. S. Weling, and T. F. Heinz, Appl. Phys. Lett. **69**, 2321 (1996).
42. W. Aenchbacher, M. Naftaly, and R. Dudley, J. Opt. Soc. Am. B **27**, 1717 (2010).
43. K. S. Rao, A. K. Chaudhary, F. Yehya, and A. S. Kumar, Spectrochim. Acta Part A Mol. Biomol. Spectrosc. **147**, 316 (2015).
44. K. S. Rao, A. K. Chaudhary, N. Kommu, and A. K. Sahoo, RSC Adv. **6**, 4053 (2016).
45. K. S. Rao and A. K. Chaudhary, Thermochim. Acta **614**, 149 (2015).
46. W. Shi, Y. J. Ding, N. Fernelius, and K. Vodopyanov, Opt. Lett. **27**, 1454 (2002).
47. W. Shi, Y. J. Ding, and P. G. Schunemann, Opt. Commun. **233**, 183 (2004).
48. W. Shi, Y. J. Ding, N. Fernelius, and K. Vodopyanov, Opt. Lett. **27**, 1454 (2002).
49. Y. Sasaki, A. Yuri, K. Kawase, and H. Ito, Appl. Phys. Lett. **81**, 3323 (2002).
50. C. Staus, T. Kuech, and L. McCaughan, Opt. Express **16**, 13296 (2008).
51. N. E. Yu, K. S. Lee, D.-K. Ko, C. Kang, S. Takekawa, and K. Kitamura, Opt. Commun. **284**, 1395 (2011).
52. P. Kumbhakar, T. Kobayashi, and G. C. Bhar, Appl. Opt. **43**, 3324 (2004).
53. J. D. Rowley, J. K. Wahlstrand, K. T. Zawilski, P. G. Schunemann, N. C. Giles, and a. D. Bristow, Opt. Express **20**, 16968 (2012).
54. J. D. Rowley, D. A. Bas, K. T. Zawilski, P. G. Schunemann, and A. D. Bristow, J. Opt. Soc. Am. B **30**, 2882 (2013).
55. Y. S. Lee, *Principles of Terahertz Science and Technology* (2009).
56. J. D. Rowley, J. K. Pierce, A. T. Brant, L. E. Halliburton, N. C. Giles, P. G. Schunemann, and A. D. Bristow, Opt. Lett. **37**, 788 (2012).
57. J. Federici and L. Moeller, J. Appl. Phys. **107**, (2010).
58. P. U. Jepsen, D. G. Cooke, and M. Koch, Laser Photon. Rev. **5**, 124 (2011).
59. K. Yamaguchi, M. Nakajima, and T. Suemoto, Phys. Rev. Lett. **105**, 3 (2010).
60. B. Fischer, M. Hoffmann, H. Helm, G. Modjesch, and P. U. Jepsen, Semicond. Sci. Technol. **20**, S246 (2005).

Chapter 8

Conclusions and Future scope

Pulsed photoacoustic spectroscopy is one of the most efficient analytical technique to characterize the all phases of matter according to their absorption properties. Mostly, it is extended to the measurement of gaseous molecules in trace level. The UV-visible radiation leads to electronic, vibrational transitions in the molecule, while THz waves are responsible for heating of molecules due to vibrational-rotational lines. The selected HEMs are nitro rich compounds of benzyl and phenyl series 1,2,3-triazole derivatives. The thermal decomposition, stability and efficiency of these compounds are evaluated based on released quantity of byproducts during the controlled pyrolysis between 30-350 ^{o}C using pulsed photoacoustic technique. TG-DTA provides the basic information about the melting and decomposition temperatures. The results obtained from PA and TG-DTA techniques shows that benzyl series 1,2,3-triazoles are more efficient for rocket fuels, however, phenyl series compounds are more thermally stable compounds. The stability and efficiency of compounds directly depends upon the position of NO_2 groups. Also, the efficiency and stability of compounds controls due to presence of other groups such as methyl ($-CH_3$), methoxy ($-OCH_3$), amino ($-NH_2$) etc. We have attempted to study and identify the effect of these groups. The amino group leads to increase density, further it enhance the efficiency of compounds as a rocket fuel.

In addition, for the first time using solid PA cell, we have identified the graphite as a sensor for the identification of HEMs using visible (532 nm) - IR (1064 nm) wavelengths. Where, premier explosives molecules have no absorption bands. The pi-electrons of graphite and HEMs coupled with each other due to phonon waves momentum transfer and possess the double resonance Raman Effect. As a result the HEMs get excited in presence of graphite and generated the strong PA signal.

The broadband THz radiation was generated using DAST and $ZnGeP_2$ crystals. Band pass filters of 0.5 and 1.5 THz bands utilized to record the time resolved PA spectra of N_2O is one of green house gas major decomposition byproduct of HEMs. It is know that the decomposition products of HEMs and its molecule vapor has several rotational lines in the THz domain. Moreover, the reported compounds nitro rich triazoles release similar type of gaseous byproducts with different concentration according to their stability. Therefore, initially we have recorded the PA signal of N_2O

at 0.5 and 1.5 THz bands. The time resolved THz based PA spectra of nitromethane and methanol were recorded observe sufficient THz power get the PA signal.

Future scope

- By using tunable quantum cascade laser (QCL) laser in Mid-IR range will helps us to identify different types of individual gaseous species produced during the thermal decomposition.
- The photoacoustic imaging of solid HEMs using nanoseconds and picoseconds laser pulses.
- Designing and fabrication of suitable resonance windowless cell coupled with a quartz tuning fork or a quantum enhanced photoacoustic spectroscopy (QEPAS) sensors for low-level detection of HEMs vapors for standoff detection.
- Generation of efficient Terahertz radiations using nonlinear crystals coupled with a band pass filters and gratings to record the pulsed PA spectra of HEMs.
- Most of the HEMs possess several rotational lines, therefore, THz spectroscopy help us to recording the fingerprint spectra of these compounds. The time domain THz spectroscopy helps to buildup a library for the detection of HEMs.
- Windowless cell coupled with the suitable sensor for pollution monitoring in open system etc.
- Development of optical parametric oscillator (OPO) using DFG technique for efficient generation of tunable THz radiation.